A Study of Evolution of Microstructure through Modeling and Its Effect on Oxidation Behavior of Zr Based Alloys

By

Gargi Choudhuri

(ENGG01200804010)

Bhabha Atomic Research Centre, Mumbai, India

A thesis submitted to the Board of Studies in Engineering Sciences

In partial fulfillment of requirements

For the Degree of

DOCTOR OF PHILOSOPHY
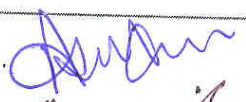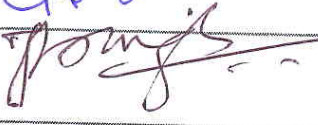
of

HOMI BHABHA NATIONAL INSTITUTE
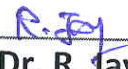
January 2015

Homi Bhabha National Institute

Recommendations of the Viva Voce Committee

As members of the Viva Voce Committee, we certify that we have read the dissertation prepared by Mrs. Gargi Choudhuri, entitled " A Study of Evolution of Microstructure through Modeling and Its Effect on Oxidation Behavior of Zr Based Alloys", and recommend that it may be accepted as fulfilling the thesis requirement for the award of Degree of Doctor of Philosophy.

Chairman	Dr. V. Kain		Date:16-01-2015
Guide / Convener	Dr. G.K. Dey		Date: 16-01-2015
Co-guide	Dr. D. Srivastava		Date: 16-01-2015
Technical Adviser	Shri B. K. Shah		Date: 16-01-2015
Member1	Dr. A. Awasthi		Date: 16-01-2015
Member2	Dr. A. Arya		Date: 16-01-2015
Member3	Dr. J. B. Singh		Date: 16-01-2015
Examiner	Dr. R. Jayaganthan		Date: 16-01-2015

STATEMENT BY AUTHOR

This dissertation has been submitted in partial fulfillment of requirements for an advanced degree at Homi Bhabha National Institute (HBNI) and is deposited in the Library to be made available to borrowers under rules of the HBNI.

Brief quotations from this dissertation may be permitted without special permission. But accurate acknowledgements of source is to be mentioned. Requests for permission for extended quotation from or reproduction of this manuscript in whole or in part may be granted by the Competent Authority of HBNI when in his or her judgment the proposed use of the material is in the interests of scholarship. In all other cases, however, permissions must be obtained from the author.

Date: 16. 1. 2015

Gargi Choudhuri

Declaration

I, hereby declare that the investigation presented in the thesis has been carried out by me. The work is original and has not been submitted earlier as a whole or in part for a degree / diploma at this or any other Institution / University.

Date: 16. 1. 2015

Gargi Choudhuri

List of publications arising from the thesis

1. "Phase Field Modeling of Microstructure Evolution in Zirconium Base Alloys," Choudhuri, Gargi, Chakraborty, Sibasis, Shah, B.K., Srivastava, D., and Dey, G. K., Zirconium in the Nuclear Industry: 17th International Symposium, STP 1543, Robert Comstock and Pierre Barberis, Eds., pp. 95‑117, doi:10.1520/STP154320130045, ASTM International, West Conshohocken, PA
2014.

2. "Influence of Fe content on Corrosion and Hydrogen pick up behaviour of Zr-2.5Nb pressure tube material", Gargi Choudhuri, Jagannath, M Kiran Kumar, V Kain, D Srivastava, S Basu, B K Shah, N Saibaba, G K Dey, Journal of Nuclear Materials 441 (2013) 178–189.

3. "Phase field modeling of Widmanstatten plate formation in Zr–2.5Nb material", G. Choudhuri, S. Chakraborty, D. Srivastava, G. K. Dey,Results in Physics 3 (2013) 7–13.

4."Precipitation and growth study of intermetallics and their effect on oxidation behavior in Zr–Sn–Fe–Cr alloy", G Choudhuri, S Neogy, D Sen, S Mazumder, D Srivastava , B K Shah , G K Dey, Journal of Nuclear Materials 430 (2012) 205–215.

Date: 16. 1. 2015

Gargi Choudhuri

Paper & poster presented in Conferences

1. *"Phase field modeling of Widmanstatten lath formation in Zr-base alloy",* [http://www.astm.org/COMMIT/B10_Zirc_Presentations/Presentations/1.1_dey_phase_field_modeling.pdf;](http://www.astm.org/COMMIT/B10_Zirc_Presentations/Presentations/1.1_dey_phase_field_modeling.pdf) *Gargi Choudhuri, S. Chakraborty, B K Shah, D Srivastava, G K Dey, 17th international symposium in Zirconium in nuclear industry, ASTM Committee B10 on Reactive and Refractory Metals and Alloys, held on February 3-7, 2013 , Hyderabad, India.*

2. *"Effect on Fe content on corrosion and Hydriding behavior of Zr-2.5Nb pressure tube material", International Conference on Advances in Nuclear Materials, 'ANM-2011' Mumbai, India.*

Date: 16. 1. 2015

Gargi Choudhuri

Dedicated to Maa, Babu

&

my Daughter

Acknowledgement

Contents

Chapter 4: Development of PFM to predict microstructure evolution in Zr-Nb alloy during diffusional phase transformation

Chapter 5: Precipitation and growth study of intermetallics and their effect on oxidation behavior in Zr-Sn-Fe-Cr alloys

Chapter 6: Influence of Fe content and β-phase on Corrosion and Hydrogen pick up behaviour of Zr-2.5Nb pressure tube material

Chapter 7: Effect of irradiation on Oxide

Chapter 8: Conclusions & Scope for further research

List of Figures

initial microstructure. The dark region in fig. 4. 14a indicates pre-nucleated allotriomorph α-Zr ($\varphi = 0$). $\varphi = 1$ in the region of β-Zr. Fig. 4.14b, 4.14c, 4.14d are microstructure at different non-dimensional time steps (.035, .0531, .0663 respectively). Planar front becomes unstable at 890 K. The colour code depicts the mole fraction of Nb in Zr-Nb binary alloy. The domain size is 1.57 μm x 5.14 μm. Black line denotes initial position of the interface.

in alloy 3, showing discontinuous β at α-α grain boundary as well as within α grain.

along with monoclinic structure of oxide as well as Zr_3O peak at 5° grazing angle of incidence heat treated alloy after exposure to accelerated steam at 415°C.

List of tables

List of Abbreviations used

BWR	Boiling water reactors
EBSD	Electron back scattered diffraction
EDS	Energy dispersive spectroscopy
FEM	Finite element method
FWHM	Full width at half maxima
GIXRD	Grazing angle X- ray diffraction method
PDE	Partial Differential Equation
PHWR	Pressurized heavy water reactor
PFM	Phase field model
PWR	Pressurized water reactor
SAD	Selected area diffraction
SANS	Small angle neutron scattering
SEM	Scanning electron microscopy
STEM	Scanning Transmission Electron Microscopy
TEM	Transmission Electron Microscopy
XRD	X-ray diffraction

Chapter 1

Introduction

1.1 Motivation

Three series of Zr alloys are currently being used for nuclear reactor core components. These include Zr-Sn alloys (Zircaloy-2, Zircaloy-4), Zr-Nb alloys (Zr-1Nb, Zr-2.5Nb) and Zr- Sn-Nb alloys (Zirlo, Alloy E-635). Zr alloys, in particular Zircaloy-2 and Zircaloy-4, Zr-1Nb have been widely used as fuel rod cladding material and Zr-2.5Nb for pressure tube material forthermal reactors. Zircaloy-2, Zircaloy-4, Zr-1Nb have shown satisfactory performance in PHWRs. New generation advanced reactors have more aggressive operating conditions (i.e. higher coolant temperature with partial boiling combined with higher burn up and longer residence time) and hence require a more protective adherent oxide which will prevent in reactor acceleration of corrosion and hydrogen intake. The alloy should also be more tolerant to flaws and more resistant to radiation-induced damages. Development of the new Zr base alloy will require optimization of chemical compositions, microstructure, texture and dislocation density. Role of various alloying elements and impurity elements in currently used alloys need to be reassessed with respect to the need for modifying the range of alloying elements, reducing the maximum limit of impurity elements and the introduction of new alloying additions.

In general, development of zirconium base alloy has been empirical. The development of Zr base alloys has occurred in following sequence: Zircaloy-1 (Sn: 2.5 wt.%); Zircaloy-2 (Sn: 1.20 - 1.70 wt. %, Fe: 0.07 - 0.20 wt. %, Cr: 0.05 - 0.15 wt. %, Ni: 0.03 - 0.08 wt. %, O: 900 - 1500 ppm; wherein, Fe + Cr + Ni: 0.30 wt. %); Zircaloy-3A (Sn: 2.5 wt. %, Fe: 0.25 wt. %); Zircaloy-3B (Sn: 0.5 wt. %, Fe: 0.4 wt. %); Zircaloy-3C (Sn: 0.5 wt. %, Fe: 0.2 wt. %, Ni: 0.2 wt. %); Zircaloy-4 (Sn: 1.20 - 1.70 wt. %, Fe: 0.18 - 0.24 wt. %, Cr: 0.07 - 0.13 wt. %, O: 900 - 1500 ppm, Ni: < 0.07 wt%., wherein Fe + Cr: 0.28 - 0.37 wt. %); and so forth. The above alloys, except for Zircaloy-2 and Zircaloy-4, have not been commercialized due to poor mechanical strength and corrosion resistance in the reactor. Another alloy system with good mechanical properties and corrosion resistance is Zr-Nb. When the entire Nb is in solid solution, the alloy shows poor corrosion resistance. With the precipitation of β-Nb during aging or stress relieving,

corrosion resistance improves significantly, but begins to deteriorate as these particles become coarser. Therefore selection of appropriate chemical composition is important. Optimization of fabrication route is also required to achievethe desired performance of the material.

It has been reported that Zircaloy-4 with low level of Sn has better corrosion resistance than the conventional Zircaloy-4. Sn is added to the Zr alloys to overcome the deleterious effects of N which is a common impurity in Kroll Zr. Due to technological advancement, N level in Kroll Zr alloys can easily be controlled below 30 ppm. It has been observed that the oxidation resistance in 400 °C steam improves with reduction of Sn from 1.41 to 0.09 wt. % in current Zr-Sn-Fe-Cr alloys. So the role of Sn in controlling the corrosion behaviors has to be relooked due to the above mentioned reasons. However, Sn substantially contributes in solid solution strengthening and creep resistance. Hence an optimum Sn content would be required to achieve the best of corrosion properties, strength and creep resistance. The largest test program with alternate Zr alloys with/without Sn and transition metals performed by Siemens, indicates that properly heat treated Zr-2.5 Nb has the best corrosion behavior and the behavior of the other alloys depends primarily on the Sn content. Based upon this study, Siemens selected at first a DUPLEX cladding with extra low Sn and enhanced Fe and Cr content in the outer part of the fuel clad wall. To counteract Li effect, Sn > 0.5 wt % is preferred in Zr-Nb-Sn-TM alloys.

Second phase precipitates in Zr-Sn-Fe-Cr series alloys play important role in controlling oxidation, hydriding and irradiation behavior of the alloys. Fine and uniform distribution of SPPs in Zr-Sn-TM alloy areessential in resisting nodular corrosion in BWR environment whereas slightly coarser precipitates arepreferred to resist uniform corrosion in PHWRs and PWRs environments.

Fe is an alloying element in Zr-Sn-Fe-Cr and Zr-Sn-Fe-Nb system, whereas, it is considered as an impurity in Zr-2.5 Nb pressure tube material and its specified limit is 650 ppm (max.).This limit has been specified on the premise that increased density of Zr-Fe intermetallic precipitates may increase the deuterium pick up rate. Recent in-service inspection results indicated lower axial elongation in pressure tubes which contained higher Fe impurities. Axial creep of 6.64 mm was observed during 3340 effective full power days in tubes containing mainly higher Fe content (> 800 ppm) as compared to 32.24 mm in tubes containing lower Fe content (< 300 ppm). Hence, the role of Fe in controlling the microstructure and oxide morphology in Zr-Fe-Nb

systemhas to be relooked to assess the scope of relaxation in Fe impurity limit in pressure tube materials.

The corrosion rate of the alloy is controlled by the characteristics of the oxide formed, which depends on the alloy composition, microstructure and texture and micro-texture of the base alloy. Though a large number of studies have been carried out, a more systematic study on the characteristic of oxide formed in different Zr alloys is required. Change in alloying or impurity elements or presence of precipitates in the matrix alters the phase fraction and stress distribution in oxides. To increase the life time of core components, a systematic study on the characteristics of oxide under irradiation is also required.

Development of desired microstructure with required texture in commercial Zr-Nb alloys have been achieved through empirical formulation and traditional trial and error method. But these are more expensive and much time consuming. Hence, models that characterize microstructural features with anisotropy and texture are required to design the process route. Over the last decade, phase-field method (PFM) has emerged as a powerful computational tool for modeling and predicting the meso-scale morphological and microstructure evolution during solid-liquid and solid-solid phase transformations. In PFM explicit tracking of interface is not required. However, quantitative modeling at real length and time scales requires that the fundamental model inputs be linked to thermodynamic and mobility databases. Extensive work has been done by Wang and Chen in developing and integrating thermodynamic modeling, mobility data base and phase field simulation to predict microstructural evolution in Ti base alloys mainly in Ti - 6Al-4V alloy [4. 18]. Loginova *et al.* [4. 19] have studied Widmanstatten ferrite plate formation in binary Fe-C interstitial solid solution system using a highly anisotropic interfacial energy. Limited work has been done in modeling of microstructural evolution in Zr-Nb alloy during various thermo-mechanical processing [4. 20, 4. 21]. The Phase field approach has been formulated for predicting microstructural evolution during athermal ω-phase transformation in Zr-Nb alloy system. There is a need for developing a phase field model for Zr-Nb substitutional solid solution system to predict morphological evolution during thermo mechanical processing using thermodynamic and mobility database.

1.2 Objectives of the work

The objective of the present dissertation is to develop better mechanistic understanding of microstructure evolution through modeling and experimentation and to study its effect on oxidation and hydrogen intake behaviour of important Zr base alloys. To improve the in-depth understanding of in-reactor oxidation behaviour of the alloy, understandings about the evolution of different phases in the oxide during irradiation and its dependency on matrix microstructure as well as microchemistry of the alloys are also important.

In order to achieve the aforementioned objectives, the following tasks have been identified.

Zr based commercial alloys may have various types of microstructures depending upon the heat treatment given. Development of a phase field model for Zr-Nb substitutional alloy system, utilizing Gibbs free energy functional and diffusional mobility database, to predict microstructure evolution during diffusional phase transformation and to investigate the generation of Widmanstatten morphology and allotriomorph α is one of the primary objectives of this work.

Experimental study of microstructural evolution mainly the change in size and distribution of second phase precipitates and their microchemistry in Zr-Sn-Fe-Cr alloy during various alpha annealing heat treatments is an important objective of this work.

In case of Zr-Sn-Fe-Cr alloys with different Sn content, development of a correlation between the precipitate size, its distribution and matrix microstructure with the oxidation behavior is another objective of this work.

For Zr-2.5Nb pressure tube, the effects of Fe addition in the range of 300-1250 ppm in cold worked stress-relieved alloy, on the oxidation and hydrogen pick up behaviour after 415°C steam autoclaving has been examined in detail.

One of the most important objectives of this study is to examine the effect of ion irradiation on the crystalline to crystalline phase transformation in the oxide of different Zr based alloys and to study the feasibility of correlating it with oxide formed in the actual fuel tube during neutron irradiation in PHWR with 7670 MWD/t burn up.

1.3 Organization of thesis

The outline of the thesis is as follows:

Chapter 2 gives a brief literature review of the topics directly pertinent to the present work.

This is followed by the details of the material used and experimental methods, characterization technique and computational technique used in the present study in Chapter 3.

Chapter 4 gives a detailed description of phase field model developed to predict the microstructure evolution in Zr-Nb alloys using Gibbs energy functional and diffusional mobility database. The incorporation of noise in the model to generate equilibrated nuclei has also been discussed.

Chapter 5 gives the results of microstructural and micro-chemical characterization of all the α annealed heat treated Zr-Sn-Fe-Cr alloys using optical microscope, scanning electron microscope (SEM) and transmission electron microscope (TEM), and small angle neutron scattering (SANS). The oxidation behaviour of various heat treated alloys is also described in this chapter. The oxide formed in all the alloys were characterized using grazing angle X-ray diffraction (GIXRD) and X-ray photoelectron spectroscopy (XPS) and the results of these investigations are described in this chapter.

 Chapter 6 gives a detailed account of the oxidation and hydrogen pick up behaviour of Zr-2.5Nb with different Fe content. The characterization of oxide using SEM, GIXRD and XPS is also described in this chapter.

Chapter 7 describes the effect of irradiation on oxides which were characterized by GIXRD. The crystalline to crystalline phase transformation in oxide induced by heavy ion irradiation is also discussed in this chapter and the results were compared with oxide formed in actual fuel tube irradiated in PHWR reactor after a burn up of 7670 MWD/t.

The main conclusions drawn are summarized in Chapter 8.

Chapter 2

Literature Review

2.1 Overview

This chapter gives a comprehensive review on alloying elements, impurity elements, uniform oxidation, localized corrosion and hydrogen intake behaviour of important Zr base alloys specially Zr-Sn-Fe-Cr, Zr-Nb and Zr-Sn-Nb series of alloys. The applicability of short term accelerated laboratory corrosion tests predicting long term performance in the reactor is also discussed. This is followed by a brief description of recent developments in modeling techniques for predicting microstructure evolution during solid state transformations.In the end, the effect of irradiation on the microstructure as well as oxide of Zr base alloys is discussed.

2.2 Microstructure and Microchemistry

2.2.1.1 Pure Zr:

The nuclear grade Zr is produced by Kroll process [2.1]. Crystal structure of pure Zr at room temperature is hexagonal closed packed (hcp α) with c/a 1.593. Lattice parameters are a = 0.323 nm, c = 0.515 nm [2.2]. c/a of α < ideal axial ratio makes a prismatic slip on $(10\bar{1}0)$ plane most predominant. Higher thermal expansion coefficient along the c direction implies that the c/a ratio tends towards the ideal ratio at higher temperatures. The anisotropy in thermal expansion coefficient and Young's modulus along the main crystallographic directions of the hcp lattice can induce the development of significant internal stresses or strong crystallographic textures during thermo mechanical treatment involved in the fabrication process. At 865°C, pure Zr undergoes an allotropic transformation from the low temperature hcp phase to body centered cubic (bcc β) phase. On cooling, the transformation is either martensitic or diffusional, depending on the cooling rate. But they always follow certain orientation relationship, i.e. $(0001)_\alpha \parallel (011)_\beta$ and $[11\bar{2}0]_\alpha \parallel [11\bar{1}]_\beta$ [2. 3]. This orientation relationship results in a coherent or semi-coherent

interface of very low energy. The melting of pure Zr occurs at 1860°C, and thus. Zr can be considered as a slightly refractory metal. Zr has a high reactivity with O, N and C as well as high solubility of these interstitial elements in α-phase. Low solubility of H in α phase causes hydride precipitation which could lead to serious embrittlement problem.

2.2.1.2 The Zr-O System:

Zirconium oxide (ZrO_2) is also an important ceramic material [2. 4]. The excellent optical, mechanical, electrical, chemical and photochemical properties of this material made it suitable for different applications such as, interferometric filter, coating, catalysis and sensors. The crystalline structure of ZrO_2 depends on temperature. Fig. 2. 1 is the phase diagram [2. 5] of Zr-O system at 1 atm. pressure. Monoclinic (α-ZrO_2) structure with Zr cations 7 fold coordinated by O anions' belonging to $P2_1$ /c group is the room temperature equilibrium phase (< 1170°C) [2. 6]. The tetragonal phase (β-ZrO_2) is stable between 1170 - 2370°C and high temperature cubic CaF_2 structure (γ-ZrO_2) is formed beyond 2370°C [2. 6]. In γ-ZrO_2, F.C.C sub lattice of cations form with anions at tetrahedral voids which lead to 8 fold coordinated cations and anions are 4 fold coordinated. To maintain CaF_2 structure, the ideal radius ratio of cations and anion (R+/R-) derived from crystal geometry must be greater than 0.732. Zr^{+4} is too small to form the 8 fold coordinated fluorite structure or too large for an efficiently packed rutile structure [2. 5]. β-ZrO_2 can be considered as a distorted cubic structure with displacement of oxygen ions along the <001> direction (c axis). The monoclinic to tetragonal phase transition is accompanied by a decrease in unit cell volume and increase in density by 4% as the 7 fold co-ordination of Zr changes to 8 fold. The β and γ phase belong respectively to the $P4_2$/nmc and Fm3m space groups [2. 5].
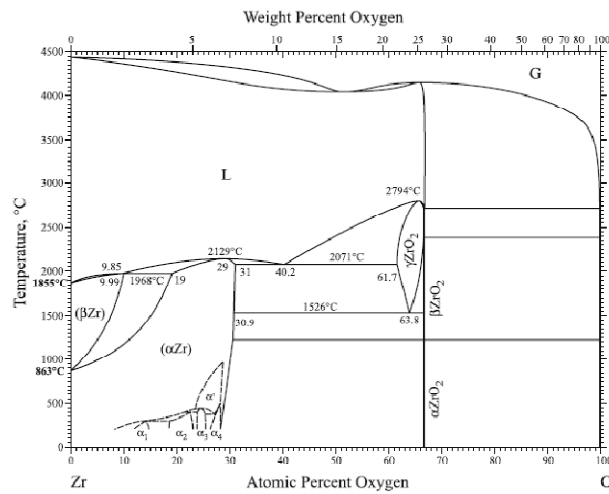
Fig. 2. 1: Zr-O phase diagram at 1 bar pressure [2. 5].

The optical, mechanical and spectroscopic properties are very much dependent on the crystalline structure of oxide. The tetragonal structure present high strength and toughness and is the key in the toughening transformation of ZrO_2 , since the β-ZrO_2 to α-ZrO_2 transformation can be stress-induced or strain induced under certain conditions [2. 4].

In case of Zr base alloy, the oxidation progresses by inward diffusion of the oxidizing species [2. 6]. Due to the high Pilling Bed-worth ratio (1.56 for zirconium), compressive stresses are developed in oxide whereas the metal near the metal oxide interface is under tension. According to the pressure - temperature phase diagram of Zirconia in fig. 2.2 [2.7] and based on measurement of stresses in oxide films, several authors [2.8-2.10] take these compressive stresses to be responsible for the tetragonal phase stabilization.

The tetragonal phase can also be stabilized by reducing the grain size [2.9, 2.11] to a critical value (20 - 30 nm depending on temperature) or by alloying addition [2. 12] (Y^{+3}, Ca^{+2}, Mg^{+2}, Fe^{+3}, Er^{+3}, Tb^{+3}). When reducing the grain size to a very low value, the surface energy term dominates and it reverts back to tetragonal phase from the equilibrium room temperature phase. The higher temperature phase can be stabilized by addition of larger cations (greater than Zr^{+4}, 0.84 Å) to expand the lattice or by doping with a lower valence cations (tri or bi-valent cations) to create oxygen anion vacancies or a combination of the two effects. The creation of oxygen vacancies modifies the average co-ordination number and facilitates the formation of oxygen sub-lattice towards cubic symmetry; this mechanism can be considered more effective than expanding the lattice.
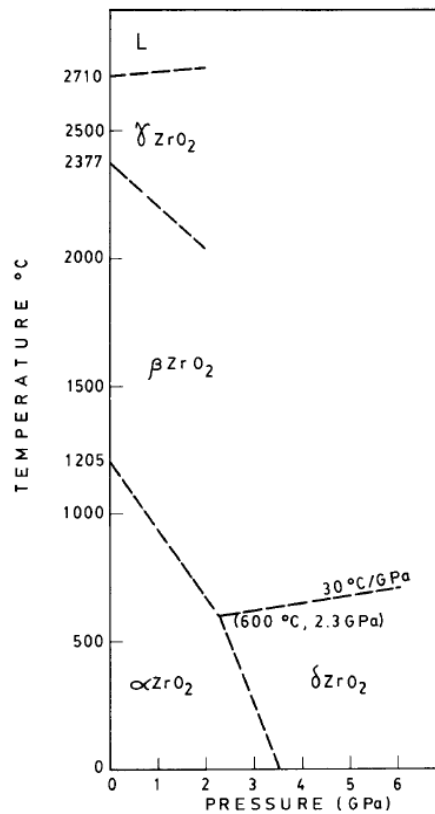
Fig. 2. 2: Pressure-Temperature diagram of ZrO_2 [2. 7].

During the growth of oxide by inward diffusion of the species, the fresh oxide which forms at the metal-oxide interface comes under compression, but in the earlier oxide, which is now far away from the interface, compressive stress which were present earlier decreases. The point where the stresses in the oxide have decreased below the critical stress to stabilize the tetragonal phase, a martensitic phase transformation occurs in which the tetragonal phase transforms to monoclinic. This is the reason for the decrease in the tetragonal fraction of the oxide with growing oxide thickness [2. 13] and its fraction is the highest near oxide-metal interface. The volume expansion during the transformation (β-ZrO_2 to α-ZrO_2) is approximately ~5% and micro-cracks and or pores form periodically. The morphology of the oxide is very much dependent on this crystalline to crystalline phase transformation.

2.2.2 Alloying elements of Zr based alloys:

The relative solubility of the various elements in the α and β phases as well as their neutron absorption cross sections are the criteria for the choice of additions as well as heat treatments to produce the alloys with desired properties for applications related to clad, pressure tube, garter-spring, fuel channel and spacer grid for the nuclear industry. Among the elements, oxygen and tin are α stabilizers i.e. these expand the region of the α phase diagram by formation of an interstitial or substitutional solid solution and Nb, Fe, Cr, Ni, Cu, Ta elements are β stabilizer.

Zr alloys are most widely used for fuel cladding and core components in the water cooled nuclear power reactors viz. BWRs, PWRs and PHWRs. The reasons for selecting Zr alloys as a nuclear core material are its low thermal neutron absorption cross-section, resistance to high temperature aqueous environments, optimum mechanical properties and resistance to radiation damage. Pure Zr corrodes much faster than the Kroll's Zr (1200 ppm Fe) in 415°C, 400°C steam and 360° C water because of the absence of second phase particles (SPPs) in pure Zr. Presence of SPPs in Kroll Zr improves uniform corrosion resistance [2.14]. The typical brittle, cracked white oxide forms in pure Zr after 415°C 10.3 MPa 72 hrs. exposure (fig. 2.3).
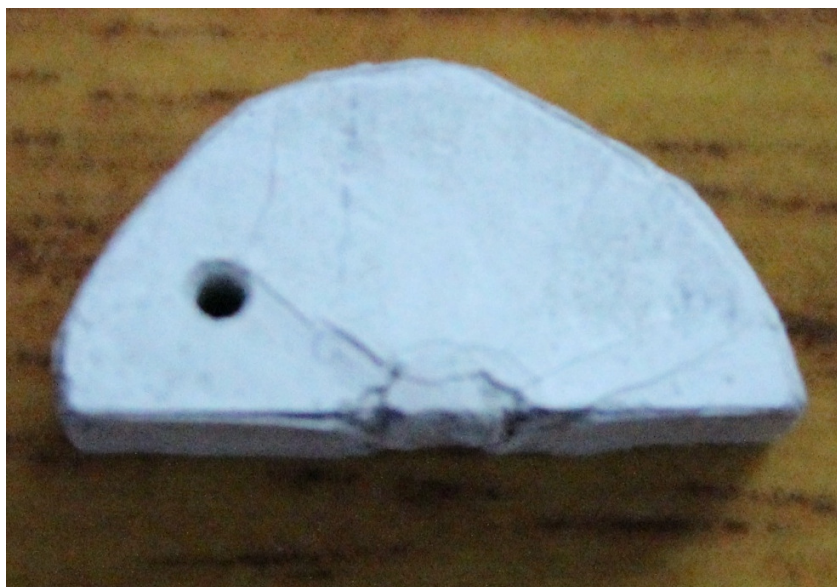
Fig. 2. 3 The typical cracked white oxide forms in pure Zr after 415° C 10.3 MPa 72 hrs. exposure at author's lab.

Two series of Zr alloys viz. Zr-Sn and Zr-Nb have been developed. Important alloys of Zr-Sn series are Zircaloy-2 (Zr - 1.5Sn - 0.1Fe - 0.1Cr - 0.05 Ni) and Zircaloy-4 (Zr - 1.5Sn - 0.2Fe - 0.1Cr). Zircaloy-2 is used as a fuel clad material in the oxygenated environment of BWRs to prevent uniform as well as localized corrosion where as Zircaloy-4 is used as fuel clad material in PWRs and PHWRs due to its low H pick up. Absence of Ni in Zircaloy-4 makes the alloy suitable for use in hydrogenated water environment. The exact mechanism of how Ni reduces H pick up is still not clear. Important alloys of Zr-Nb series are Zr-1Nb (fuel clad in VVERs), Zr-2.5Nb (pressure tubes in PHWRs) and Zr - 2.5Nb - 0.5Cu (garter springs in PHWRs). Of late, Zr - Sn - Nb series of alloys has been developed. These include ZIRLO (Zr- 1Sn- 1Nb- 0.1Fe) for extended burn up fuel clad in PWRs and EXCEL (Zr-3.5Sn- 0.8Nb-0.8 Mo) for creep resistant pressure tubes in PHWRs.

Sn is mostly present as solid solution in the Zr matrix of the alloys. It has a tetragonal lattice and exists in two vacancy states Sn^{+2} (ionic radius 1.02$\mathring{A}$) and Sn^{+4} (0.67 $\mathring{A}$). The binary phase diagram of Zr-Sn system is given in fig. 2.4 [2. 15]. At elevated temperatures, Sn is more soluble and solubility decreases to very small values below 300°C. The solubility is about 1.2 wt. % Sn at 500°C, 0.5 wt. % at 400°C and less than 0.1 wt. % at 300° C. The solubility of Sn in β zirconium increases to 21 wt. % at the eutectic temperature of 1590°C.

The accelerating effect of Sn upon the corrosion rate is rationalized on the basis of lattice defects [2. 16]. Sn enters the oxide, since the film formed on Zr-Sn alloy has different optical properties from those found in alloyed Zr. Presence of +2 ionisation state leads to the formation of anion vacanciesVO^{2-}. At lower temperature the mobility of this anion vacancy is less due to presence of immobile Sn^{+3} ion. At higher temperature, due to thermal activation, mobility of vacancy ion increases, leads to higher corrosion rate [2. 17]. There are contradictory studies on the effect of Sn on the stabilization of tetragonal oxide. Based on TEM study, Harda et al. [2. 18] showed that Sn stabilizes the monoclinic form of the oxide whereas studies by P. Barberis et al. [2. 19] and M. Preues et al. [2. 20] indicated that Sn is a tetragonal stabilizer. TEM investigations of the oxide morphology on standard Zircaloy-4 and extra low Sn (0.56 wt. %) Zircaloy have shown a somewhat higher fraction of equiaxed grains in the former alloy [2. 21]. Also Sn can form

intermetallic Zr_4Sn which is detrimental from deuterium pick up point of view. But Sn is beneficial [2. 22] when N is present in high amount from the corrosion point of view and it improves strength at both high and low temperatures. And it has excellent ductility and good impact strength. Zircaloy-2, Zircaloy-4 made from Kroll Zr, have a large amount of Sn, since it nullifies the negative influence of nitrogen. The influence of N on the corrosion resistance of Zircaloy-2 is negative because replacement of O by N (O ionic radius 1.36 $\mathring{A}$ and ionic nitrogen 1.48$\mathring{A}$) in the oxide lattice leads to expansion and thus affects the matching of oxide lattice with the lattice of metal.

With addition of Sn^{+4} in Zircaloy, due to size reduction, it causes contraction of crystal lattice of ZrO_2. If an ion of N happens to be in the vicinity of an ion of Sn, the dilating influence of N on the crystal lattice will be compensated by the contracting influences of Sn. Thus paradoxically two elements which individually have a negative influence, form an alloy with corrosion resistance higher than that of pure Zr.

The other alloying elements in Zr-Sn series are Cr, Fe and Ni. The solubility of these elements in α-Zirconium phase is very low [2. 3] and these form mostly second phase particles together with Zirconium $Zr(Fe, Cr)_2/Zr_2(Fe, Ni)$ which improve the corrosion resistance of the alloy. The binary phase diagrams for Zr-Fe, Zr-Cr and Zr-Ni are shown in fig. 2. 5, 2. 6 and 2. 7 [2. 15].

Fe crystallizes in a body centered cubic lattice and can exist as Fe^{+2} (0.8 Å) and Fe^{+3}(0.67 Å). Fe is a β stabilizer and promotes eutectoid decomposition of β phase - so called β eutectoid. In α phase Fe solubility is very low [2. 23], 120 ppm for Fe at maximum solubility temperature and precipitates out in α-phase as Zr_3Fe, Zr_2Fe, $ZrFe_2$ [2. 23 - 2. 33]. In β phase maximum solubility is 5.5 wt. % at 934°C [2. 15].

Cr crystallizes in a bcc lattice and it also forms β eutectoid. In α phase its solubility is very low and normally precipitates out as $ZrCr_2$ [2. 15]. It can form bi, tri, and hexa-valent ions having ionic radii 0.83, 0.64 and 0.35 Å respectively.
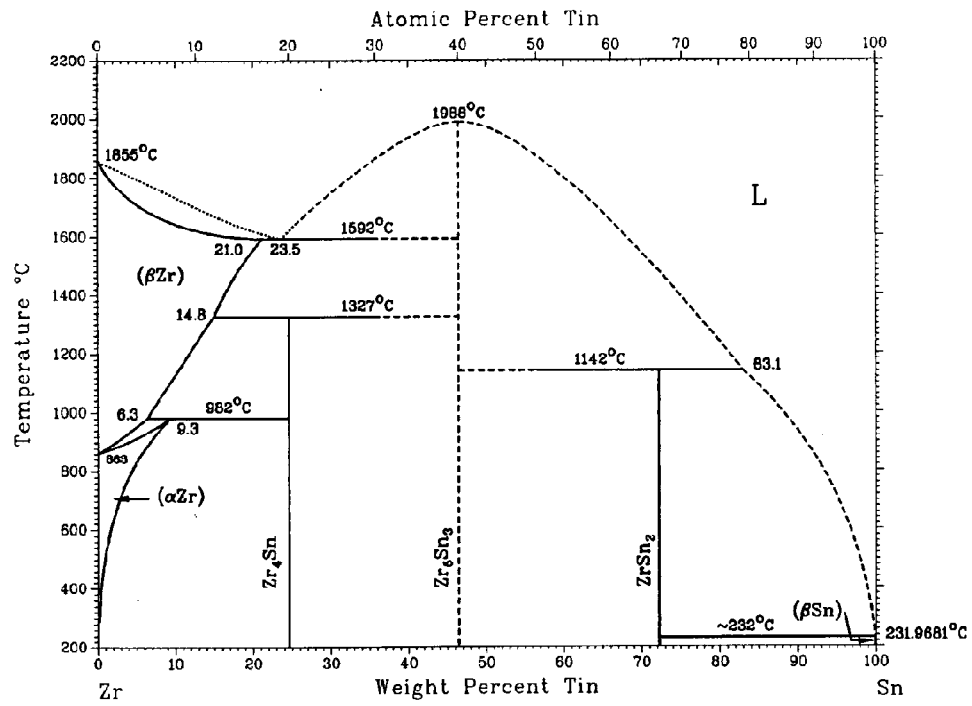
Fig. 2. 4 Binary Zr-Sn phase diagram [2. 15]
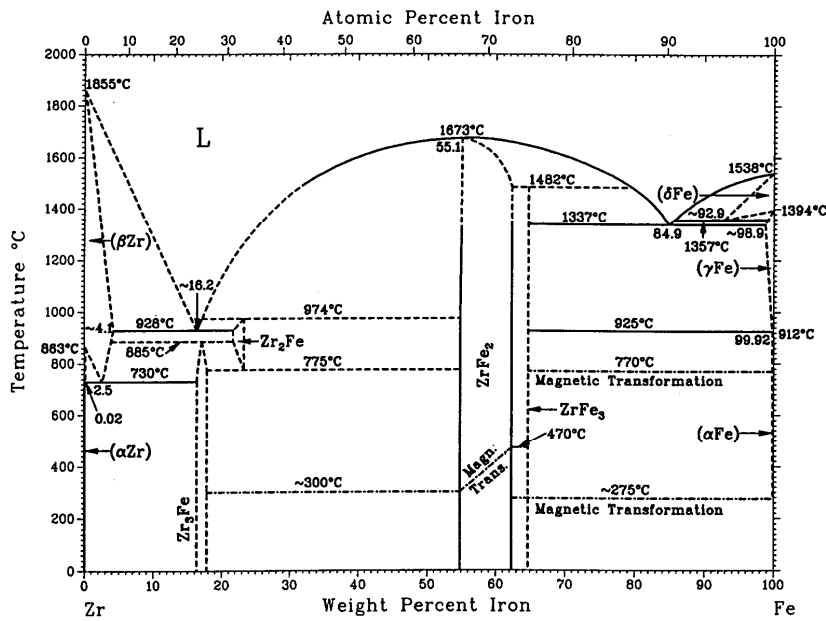
Fig. 2. 5 Binary Zr-Fe phase diagram [2. 15][D. Arias and J.P. Abriata, 1988.]
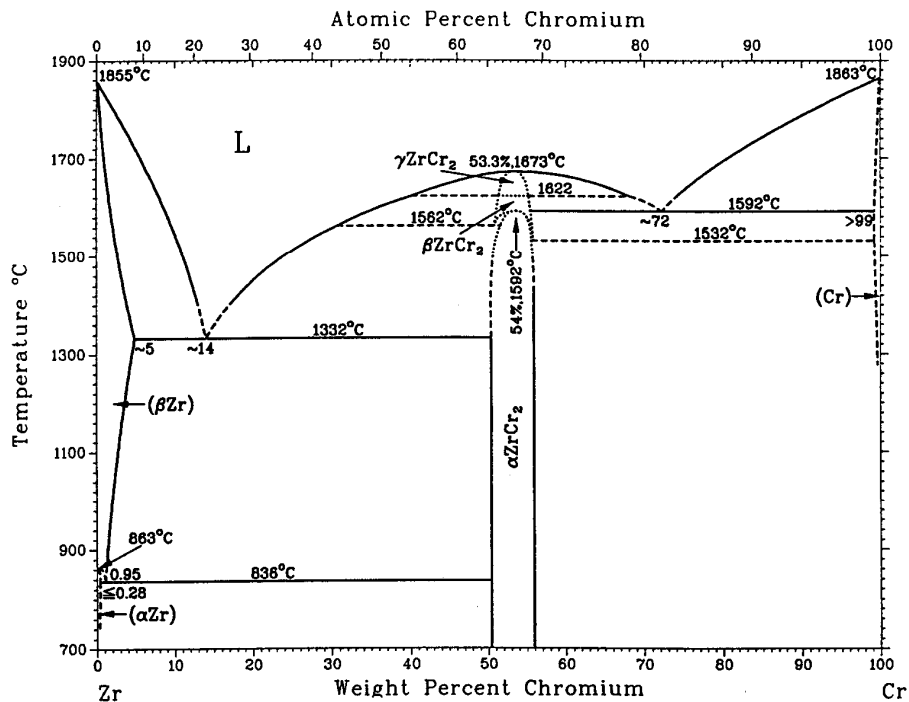
—— evaluated; - - - - probable; · · · · uncertain.

D. Arias and J.P. Abriata, 1986.

Fig. 2. 6 Binary Zr-Cr phase Diagram [2. 15]

The Zr - Ni binary phase diagram is given below in fig. 2.7 [2. 15]. Ni is a β stabilizer and they are fully soluble in β phase in the temperature range 835 - 845°C i.e. in the upper α + β range.

This element leads to eutectoid decomposition of the β phase. In α phase their solubility is very low. For Zr-Ni binary alloys, the stable form of the second phase is Zr_2Ni.
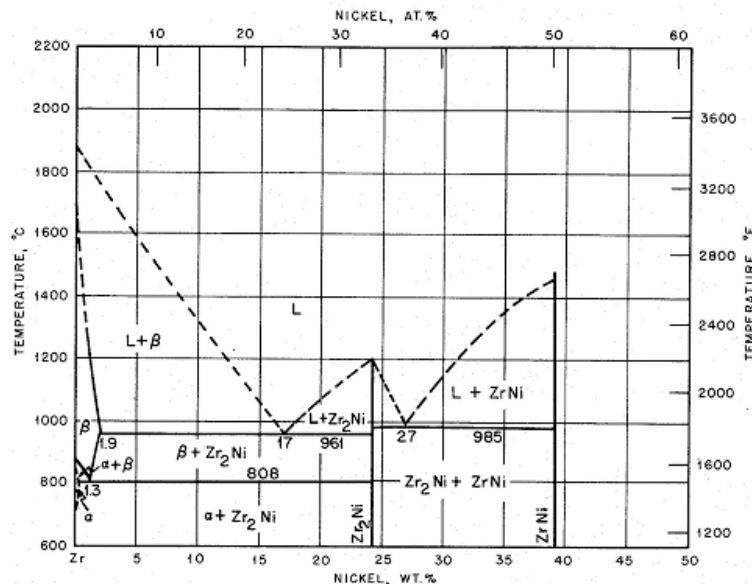
Fig. 2. 7 Binary Zr-Ni phase diagram [2. 15]

If Fe is present, then it substitutes for the corresponding transition metal and $Zr_2(Ni, Fe)$ intermetallic compound forms. These intermetallics are considered to play a vital role in the H-uptake mechanism by providing easy pathways for electron transfer from the metal substrate, through the barrier oxide layer to matrix phase.

O is considered as an alloying element in Zr base alloys rather than an impurity. It is added to the compact before melting as small additions of ZrO_2 powder. O is an α stabilizer, expanding the region of the phase diagram by formation of an interstitial solid solution. The usual O content is in the range of 900-1300 ppm and its purpose is to increase the yield strength by solution strengthening. A 1000 ppm O addition increases the yield strength by 150 MPa at room temperature. The effect is less pronounced at higher temperature (above 250ºC). At high concentration, O stabilizes the α-phase up to liquid temperature. During high temperature oxidation, a layer of O stabilized α Zr is found between the β quenched structure and the Zirconia. At normal operating temperature, the O diffusion layer ahead of the oxide front is very limited in thickness (< 1 μm at 400º C).

Nb is an important alloying element in Zr-Nb and Zr-Sn-Nb series alloys. Nb is a β stabilizer. From pure β Zr to pure Nb, there exists a complete substitutional solid solution at higher temperature [2. 34]. A monotectoid transformation occurs at about 620ºC at 18.5 wt.% Nb where β Zr transforms to Zr- α (2 wt. % Nb) + β Nb (83 wt. % Nb). By water quenching from the β or upper α + β region, the β phase (Nb rich) transforms by martensitic decomposition into an α' supersaturated hcp phase (up to about 8 wt.% Nb); subsequent heat treatment below the monotectoid temperature leads to the precipitation of β Nb precipitates at twin boundaries or lath boundaries of needles followed by transformation of α' to α [2. 35 - 2. 37]. It increases strength at room temperature and at higher temperature and also improves corrosion properties by formation of β Nb precipitates at reactor operating condition during aging. Nb exists in zirconium oxide as Nb^{+4} and Nb^{+5} ions with radii 0.67 and 0.66 Å respectively. These ionic radii are smaller than the radius of Zr^{+4}. Nb has a body centered cubic lattice. Thus Nb satisfies the conditions (volume reduction and favorably oriented distortion) necessary for matching of the lattice of the oxide and the metal and for the formation of an adherent protective oxide film. Another advantage of using Zr-2.5 Nb is the presence of Nb_2O_5 in Zirconia (ZrO_2) oxide layer resulting in a decrease of the solubility of proton thereby leading to low 'H' pick-up [2. 34].

2.2.3 Impurity elements:

In Zr-Sn series alloys most deleterious elements are C, Si, P, N, H, Cl, Mn, and Al. Others include Hf, B, Cd, Be, W, Mo, Cu, Ti, Pd, Co, U and V. C and Cl can form complex zirconium-carbide-chloride, (Zr_2Cl_2C) [2. 34] and or Zr-carbide and P can form Zr_3P and ZrP.These deposits have detrimental effect and can cause local decohesion under stress which can lead to reduction of fracture toughness of the components. These precipitates also can act as a short circuit path for easy H penetration. Al reduces the corrosion resistance of the alloy.

B, Cd, Co, Pb, Hf has poor neutron economy [2. 34]. Si can be added to Zr-alloys in considerable amounts, without sacrificing thermal neutron economy. It has been established that small amount of Si (up to 0.02 wt.%) addition is helpful if other impurities are present in limited amounts in increasing corrosion resistance of zirconium alloys in pre-transition region [2. 34] ; however, in the post transition region it produces a higher post transition slope and intercept. It was also

found that transition time also decreased as the silicon content is increased. Si also reduces the H pick up in the alloy.

Effect of Mn on aqueous corrosion resistance of Zr-base alloy depends on the valence state of Mn. Zr can absorb considerable quantities of H as a consequence of the corrosion reaction with water, as well as by other mechanisms [2. 34] and still show a metallic appearance. H has very limited solubility in Zr alloys, this being less than 1 ppm (wt. %) at room temperature, about 80 ppm at 300°C and about 200 ppm at 400°C.Whenever the solubility is exceeded a ZrH phase will be precipitated, and as this phase is brittle it affects adversely the mechanical properties of the alloy and reduce the fracture toughness of the material.

Effect of Cu on aqueous corrosion resistance of Zr-base alloy depends on the valence state of Cu. Cu can form monovalent and bivalent ions and has a face centered cubic lattice.The Zr-Cu binary phase diagram is a transitional $Fe-Fe_3C$ type, and is complicated by the presence of five intermetallic compounds, five eutectics and one peritectic. Cu is practically insoluble in α Zr since only about 0.2 wt. % dissolves, but it is much more soluble in β Zr, in which 1.6 wt.% Cu dissolves at the temperature of the eutectoid (822°C), increasing to about 3.8 wt.% Cu dissolved at the temperature of the eutectic (995°C) [2. 15].The intermetallic compounds are Zr_2Cu, $ZrCu$, Zr_2Cu_3, Zr_2Cu_5 (fig. 2.8). Formation of precipitates during aging makes the Cu bearing alloy as age-hardenable. One of the important age-hardenable alloy Zr-2.5Nb- 0.5Cu has been widely used as garter spring material in PHWRs which has high strength, excellent resilience and good corrosion resistance in CO_2 environment.
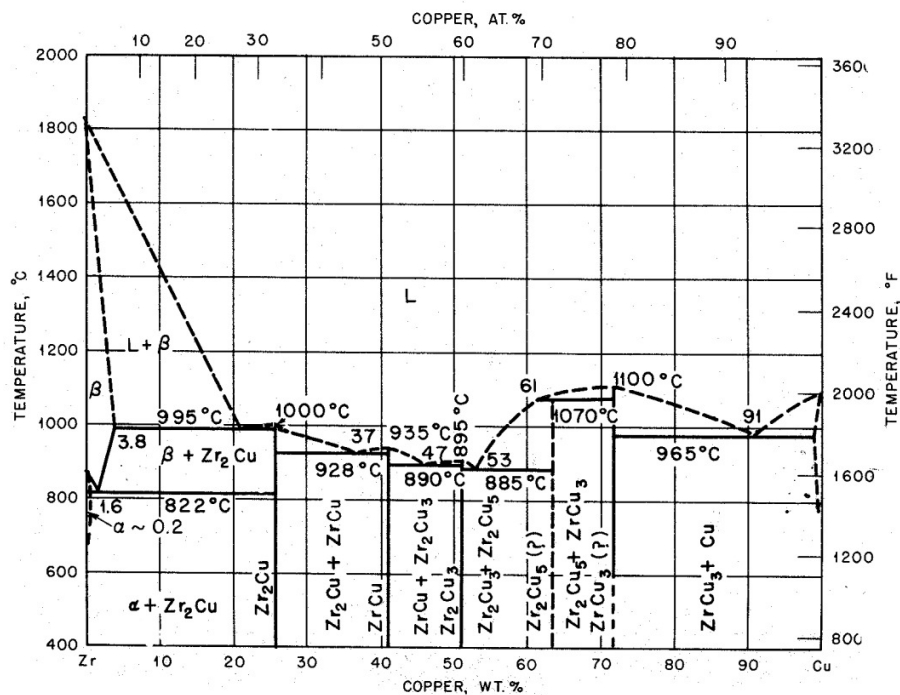
Fig. 2. 8 Binary Zr-Cu phase diagram [2. 15]

Mo has a bcc lattice so it should facilitate the distortion of the monoclinic oxide lattice bringing closer to cubic configuration. Mo can exit as Mo^{+4} and Mo^{+6} (ionic radius 0.68Å and 0.65Å respectively) and so it causes contraction of the lattice. Both these characteristics are favourable for matching of the lattices of the oxide and metal; consequently the protective properties of the oxide film should be better. It has been observed in practice that Zr-Mo alloys have a lower corrosion resistance at relatively low temperature. The corrosion resistance of Zr-Mo alloys is very much dependent on the heat treatment [2. 38] and the distribution of Mo. As Mo is a β stabilizer, the heat treatment which produces a significant amount of β-Zr, lead to poor corrosion resistance. When Mo is uniformly distributed, oxidation resistance improves. But non uniform distribution leads to poor oxidation resistance. The solubility of Mo in alpha Zr is less than 0.18 wt.%. At room temperature, it forms intermetallic compounds in the matrix. From these, Mo should pass into oxide film and become uniformly distributed throughout it. However Mo is fairly temperature resistance material and its diffusion rate is low and insufficient. The transfer of Mo to the oxide film leads to the formation of local Mo rich zones and this heterogeneous film will not provide reliable protection for the metal. At elevated temperature (450 - 500°C) Mo may

have a diffusion rate sufficiently high to produce a uniform distribution in the crystal lattice of the oxide film resulting in improvement in protective properties of the oxide film.

Be forms a eutectic with Zr at low melting point (950°C) and as a result, it is difficult to process the alloy with higher Be content.

2.3 Oxidation of Zirconium and its alloys

Two types of oxidation phenomena are observed in Zr and its alloys [2. 34]. The most common one is uniform oxidation which leads to growth of uniform protective oxide film formation. And the second one is localized oxidation viz. nodular corrosion, shadow corrosion. These are observed at different regions of temperature and environment.

2.3.1 Air Oxidation:

The solubility of O in α-zirconium is 28.6 at. % at 500°C and it increases to 35 at. % at 2065°C. Below 500°C marginal change in solubility of O in α-Zr is observed. Oxygen is more stable in the solid solution of Zr rather than as an oxide film [2. 34]. As a result of this, initially O is physisorbed on the surface metallic Zr and with continuousreactions, ultimately a thin oxide film formed. The thickness of the air formed film in all the Zr based alloys is around 2 – 5 nm. The nucleation rate of this thin oxide film is found to be significant and led to the formation of equiaxed oxide grains. The oxide grains have particular orientations with respect to the Zr matrix which reduce the stress generated during oxide formation [2. 39] (as the phase transformation from metal to oxide is related to the 56% volume expansion).This initial oxidation in O and the water vapour environment had been studied using Auger electron and XPS [2. 40]. The study indicates the presence of three sub-oxides of Zr_2O, ZrO, Zr_2O_3 along with ZrO_2. It had been observed that during air oxidation, ZrO_2 starts forming at 10^{-6} torr O partial pressure, whereas minimum 1 L water vapour exposure is required for its formation. The rate of formation of sub-oxide is lower in water vapor than in O environment. Presence of sub oxide is significant during the water vapour exposure in pure Zr rather than Zirclaoy2.

2.3.**2 Aqueous Corrosion:**

The chemical reaction of Zr with water results in the formation of zirconium oxide and H.

$$Zr + 2\ H_2O\ \rightarrow\ ZrO_2 + 2\ H_2$$
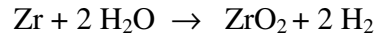
The above reaction can be divided into 3 partial reactions, viz.

Anodic Reaction at Zr/ZrO$_2$interface:

$$Zr + 2\ O^{-2} \rightarrow\ ZrO_2 + 2\ Vo^{++} + 8e^{-}$$
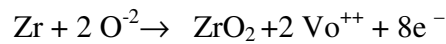
Cathodic Reaction at ZrO$_2$/H$_2$O interface :

$$Vo^{++} + 2e^{-} + H_2O \rightarrow 2\ H^{+} + O^{-2}$$
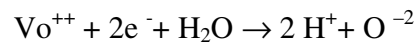
Proton discharge at ZrO$_2$/H$_2$O interface :

$$H^{+} + e^{-} \rightarrow H\quad,\quad H + H \rightarrow H_2^{\uparrow}$$
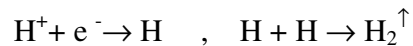
At elevated temperature thickening of the initial oxide film occurs although some fraction of oxygen dissolves in the matrix. The fraction of O dissolved depends upon a balance between the kinetics of the oxide growth and the kinetics of oxygen diffusing in to the metal. Kinetics of oxidation reaction are controlled by the diffusion of O ion from oxide-water interface, through the oxide film via anion vacancies, to oxide-metal interface. The difference in defect (anion interstitial or vacancies) concentrations at these two interfaces provides driving force for diffusion. The diffusion of these defects follows Fick's 1st law [2. 34] and is given by

$$J = -D\ \frac{dc}{dx}$$

where J is the flux of a particular defect at any position (x) in the oxide(where the x direction denotes the thickness direction and y and z is in the plane of the oxide/metal interface). D is the diffusion coefficient of the defects.

For Zircaloy, presence of alloying elements or impurities reduces the electrical resistivity of the oxide and widely separated SPPs generate localized electrical circuit. The electrical neutrality can be maintained, only through "coupled current" concept [2. 41].

Oxidation kinetics of Zircaloy exhibit three distinct stages: pre-transition, transition and post transition as shown in fig.2.9 [2. 34, 2. 42]. During Pre-transition period, oxidation rate follows the cubic rate law ($\Delta\omega = t^{\frac{1}{3}}$) and after transition linear rate law prevails. The inhomogeneous diffusion of defects through the SPPs or the crystal boundaries may be responsible for the deviation from the parabolic rate law as predicted by Wagner/Hauffe theory. Electron microscopy indicated microcrystalline nature of oxide and the mean crystallite size increases with thickening of oxide [2. 43]. Whether any crystal orientation grows preferentially from initial oxidation, or whether successive layers of crystallites nucleate and grow to different extents till remain to be resolved. Wanklyn [2. 44] has studied the oxide growth (upto 0.5 μm) on single crystals of Von Arkel zirconium as a function of crystal orientation, fig. 2. 10. He observed that different orientations of grains grow at different rates. Even of grain-boundaries oxidation rate differs from the grains and give rise to ridge formation.The oxide forms in Zr base alloys are always under compression as its formation is entirely by inward diffusion of oxygen and it has a high Pilling – Bedworth ratio (1.56). When the thickness of oxide reaches about 2 µm, the oxidation rate increases to a post transition, approximately linear rate. Transitional period can persist for longer duration and may exhibit multi-transitions before the onset of linear rate. After reaching 15-20 µm thickness, simultaneously accelerated corrosion and hydriding take place irrespective of bulk coolant chemistry.

Two mechanisms have been proposed for transition in oxidation kinetics: Crack Theory and Pore Theory. Crack theory predicts cracking of oxide film on reaching a certain critical thickness because of stresses set up by high Piling - Bedworth Ratio (1.56). Pore theory suggests that Nabarro - Herring creep of oxide crystallites occurs at elevated temperature and stress leads to pore-formation. Physical existence of the pores at transition has been confirmed by mercury
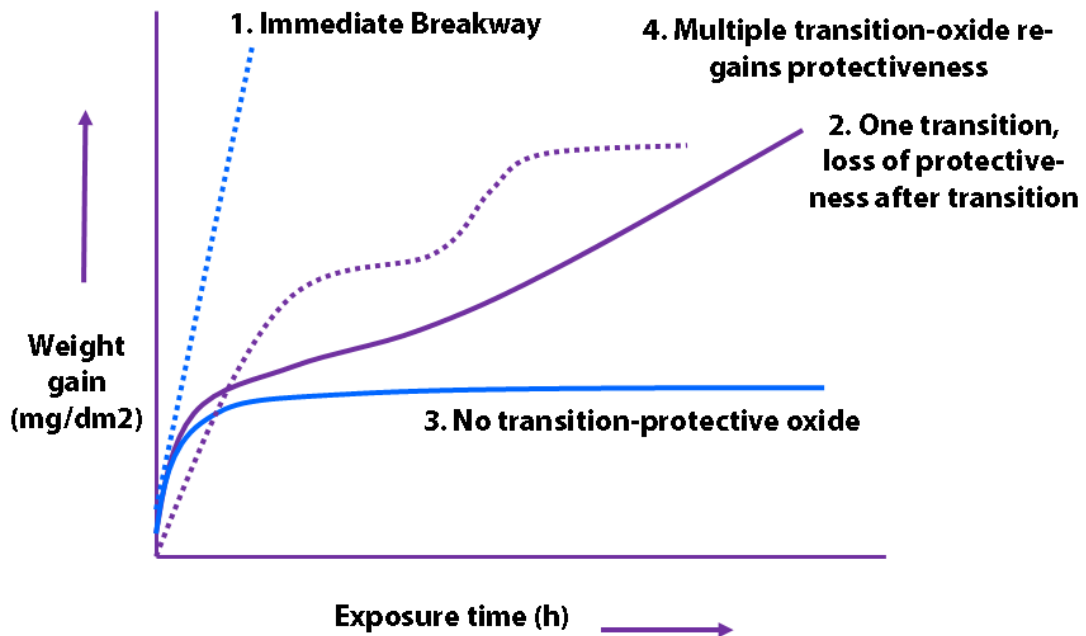
Fig. 2. 9: Schematic diagram of weight gain of different Zr alloys with exposure time for different oxidation regime.
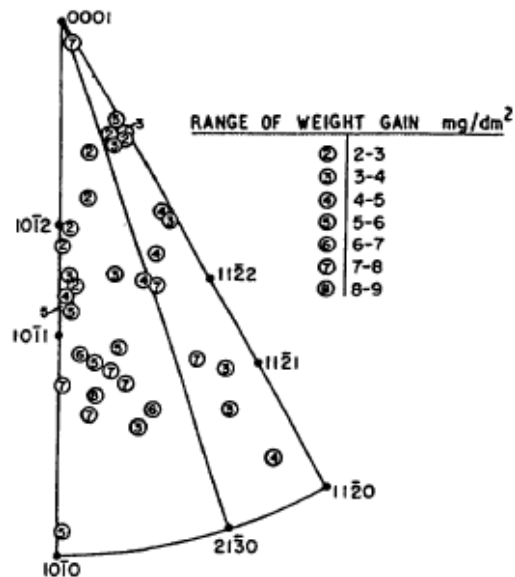
Fig. 2.10: Relation between weight gains on single crystals of van Arkel Zr (after 1min. at 500°C 1 atm. Pressure) with different crystal orientation [2. 44].

porosimeters, SEM [2. 45] and the presence of voids adjacent to second phase precipitates has been confirmed by TEM [2.46]. Acoustic emission monitoring during oxidation also confirms the pore theory and indicates that cracks develop after pores reach a certain critical size [2. 47].

Oxidation kinetics of Zr-Nb alloys is different from Zircaloys. In case of Zr-Nb alloys, no clear defined transition is observed. For Zr-2.5Nb alloys, the oxidation rate follows the parabolic rate law ($\Delta\omega = t^{\frac{1}{2}}$) in the PHWR water environment with no transition. In the presence of traces of oxygen, acceleration in corrosion rate is observed for Zr-Nb alloys compared to Zircaloys. As a result of this, Zr-1Nb alloy in an oxygenated mixture of water and steam undergoes heavy oxidation and can also result in nodular corrosion [2. 34]. Heavy oxidation in oxygenated environment may result in generation of the high amount of hydrogen, which can lead to the formation of hydride at or near surface. Use of these alloys is limited to reducing hydrogenated water chemistry.

2.3.2.1 Incorporation of SPPs in oxide:

Due to the poor solubility of alloying elements in α-Zr phase, most of the Zr base alloys contain SPPs. The crystal structure and microchemistry of these SPPs are dependent on the thermo-mechanical treatment given during fabrication.The fine and uniform distributions of the precipitates are desirable in BWRs environment, whereas slightly coarser precipitates are opted for PHWRs reducing environment. Although fine precipitates may dissolve during in reactor application. In order to understand the mechanism of improvement of oxidation and hydrogen intake, several microstructural studies have been done by STEM [2. 48, 2. 49, 2. 50]. These studies indicated that the precipitates were incorporated unoxidized in the surrounding dense oxide and slowly transformed. In case of Zircaloy, Zr and Cr are first oxidized and Fe remains as metallic particles. When oxygen potential is high enough, then only it allows Fe to oxidize and formation of tetragonal Zirconia is favoured locally. For Zr-Nb base alloys Nb rich precipitates are oxidized at the same rate as with Zr due to similar oxygen potential. But for thin oxide of Zr-2.5Nb [2. 51, 2. 52], β-Zr at crystal grain boundaries is found to oxidize faster than α-Zr and presence of amorphous ZrO_2, both at the oxide/metal interface and at columnar oxide crystallite boundaries is indicated. In case of Zr-1Nb no detailed studies of oxide structures near small precipitates of either β-Zr or β-Nb have been reported.

2. 3. 2. 2 Correlation of Autoclave Corrosion Testing to In-Reactor Uniform Corrosion Performance

The standard corrosion test in the nuclear industry for evaluation of uniform corrosion resistance of Zr based alloy is a steam autoclave test at 400°C for 3 days or 14 days with 10.3 MPa pressure as per ASTM G2. Evaluation criteria include weight gain and the visible appearance of oxide formed after autoclaving. The oxide should be black and lustrous and the weight gain in the cases of Zircaloy-2 and Zircaloy-4 should not exceed 22 mg/dm^2 or 38 mg/dm^2 after 3 days or 14 days respectively and for Zr-2.5Nb alloy 35 mg/ dm^2 or 60 mg/dm^2 respectively. The 14-day test is required only when the coupons have failed in the 3-days test. In a report it has been shown that some cladding materials have given acceptable results in the above test but they have not exhibited satisfactory in-reactor performance [2. 53]. They have conducted in-reactor corrosion measurements on a number of Zircaloy cladding tubes and the off-cuts of these tubes have been subjected to the extended period (100 days) steam autoclaving at 400° C or temperature of autoclaving raised to 415° C for 3 days. It has been seen that a better correlation to in-reactor performance has been reported when the test is conducted at 400° C for 100 days or at 415° C for 3 days. It is also shown that at 415° C, the test duration of 3 days [2. 53] is the best suited for ranking the alloys for in- reactor uniform corrosion performance since the extended time does not improve the correlation

2.3.2.3 Effect of Li on oxidation:

LiOH deteriorates corrosion resistance of all the Zr base alloys. With the addition of LiOH, onset of linear oxidation stage accelerates and porous zirconium oxides form. However, Zr-1Nb and Zr-2.5Nb are relatively more prone to accelerated corrosion in LiOH solutions than Zircaloys and Zirlo. Addition of 0.5 wt. % Sn in Zr-Nb alloys improves the corrosion resistance of these alloys in Li environment. Below approximately 400 ppm Li for Zircaloy-4 and below 60 ppm for Zr-2.5%Nb, no effect on corrosion kinetics in the pre-transition region has been observed [2. 54-2.56]. Following mechanisms [2.34] are proposed to explain the accelerating effect of LiOH.

> ➤ Li may incorporate in the oxide lattice replacing Zr $^{+4}$ ion (lithium zirconate) and can create additional anion vacancies which increase the rate of oxygen diffusion.

- Li may influence the re-crystallization process leading to a higher grain boundary area and increase the diffusion rate of O ion and hence a greater number of pores and cracks in the oxide.
- Li can also increase the number of pores by the preferential dissolution of inter-linked tetragonal or cubic sites in the lattice. The additional porosity then increases the corrosion rate by allowing the rapid transport of oxygen to the oxide/metal interface.

2.3.3 Localized Oxidation

Zr alloys can undergo various types of localized corrosion. Under oxygenated boiling water reactor environment, nodular corrosion [2. 57 - 2. 62], crud induced localized corrosion [2. 63 - 2. 70] and shadow corrosion [2. 71] are observed. The end plug weld regions of the fuel tube are susceptible to enhanced corrosion in the reactor environment if adequate precautions are not taken to prevent N [2. 72, 2. 73], O [2.73 - 2. 74], and H contamination during welding operation In case of Zr-2.5%Nb corrosion resistance is very much dependent on heat treatment, that is why fusion welding is not recommended in the end plug welding.

2.4.3.1 Nodular corrosion

Nodular corrosion [2. 14] or oxidation refers to formation of localized, lens-shaped white nodules (thickness of 30 -300 μm) on a black oxide film of uniform thickness (2-5 μm). This has been observed in clad (fig. 2.11a) of BWRs and is considered to result due to the synergistic effect of oxidizing water chemistry and neutron flux. Out of pile 500°C/24hrs. /steam test (fig. 2. 11b, c, d) is capable of giving a good correlation with observed material lot variability in-reactor. Development of a 2-step steam test (410°C/10.3 MPa steam/8hrs. followed by 510°C/10.3 MPa steam/16 hrs.) [2. 58, 2. 59] to evaluate the nodular corrosion susceptibility in BWR clad tubes is more suitable for ranking of nodular corrosion resistant clad.

Despite about 40 years of investigations, there is no agreement on the mechanism [2. 60, 2. 61] that cause nodular corrosion. All the models assumed that a negatively charged oxygen ion [O^{-2}] diffuses through the ZrO_{2-x} to the oxide-metal interface to oxidize Zr and release two electrons.

These electrons must diffuse back to the oxide until they meet a H containing radical, reducing the H^+ ion to $H°$. Location of the production of $H°$ in the oxide determines the susceptibility to nodule formation. If $H°$ is produced at or close to oxide/coolant surface, it gets liberated as H_2 to the coolant and oxide grows uniformly. If $H°$ is produced far into the oxide, it can damage or disrupt the oxide and metal comes in direct contact with the coolant and eventually excessive oxidation leads to formation of nodule. The differences in the models are embedded in the transport of electrons and H producing radicals through the oxide.

Fig. 2.11a Nodules formed in the fuel clad during exposure in BWR [2. 75] [Internal report, PIED, BARC]

Some models suggest that the nodules nucleate directly on second phase particles whereas some other models suggest that the solute depleted matrix in between the second phase particles are the nucleation points. Fig. 2.12 depicts the steps leading to nucleation of nodular oxide on Zircaloy.

Fig. 2.11b Nodules formed in the fuel clad during 500^0C autoclaving at 10.3 MPa pressure.
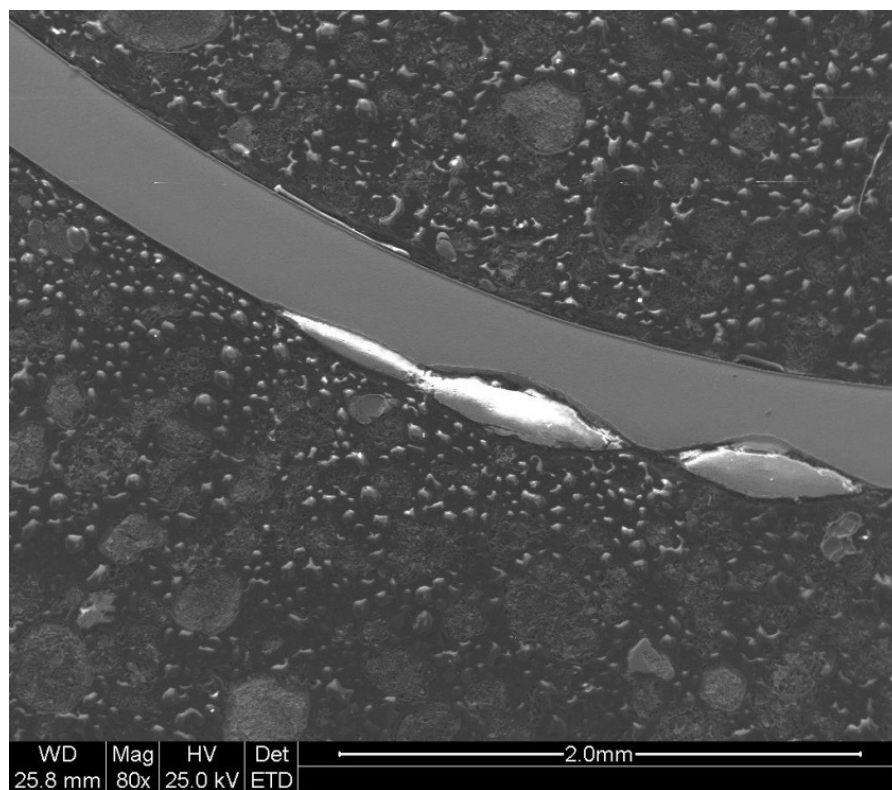
Fig. 2.11c Cross sectional view of lenticular shape of the nodules formed in the fuel clad during 500^0C autoclaving at 10.3 MPa pressure.
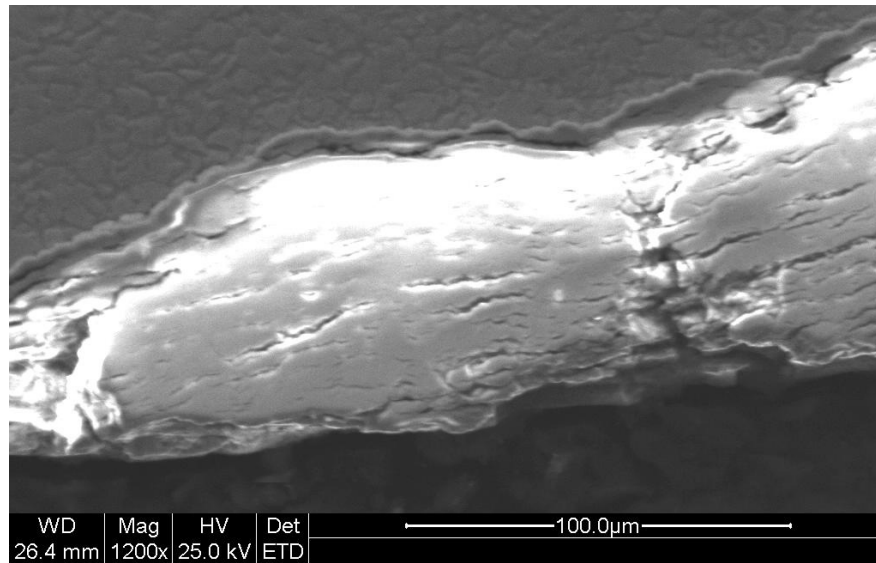
Fig. 2.11d Enlarged view of lenticular shape of the nodules showed presence of cracks parallel to metal oxide interface.
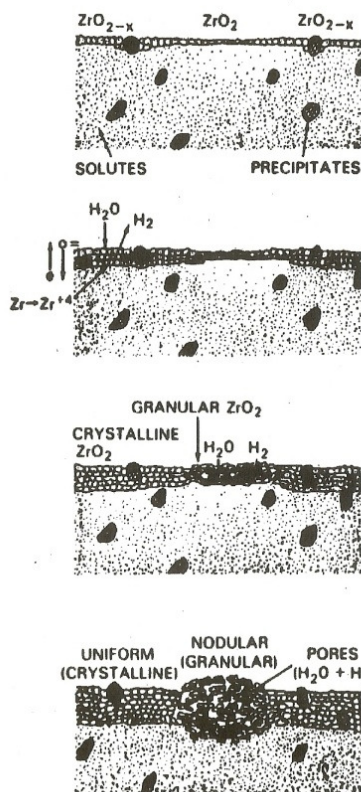
Step (a) Formation of initial uniform oxide, ZrO_2 or ZrO_{2-x}

Step (b) Thickening of initial uniform oxide

Step (c) Rupture of near stoichiometric ZrO_2 leading to direct access of H_2O to the interface.

Step (d) Repetitive formation and rupture of ZrO_2 leading to highly porous, granular ZrO_2, which retains corrosion hydrogen and prevents repassivation of the metal surface.

Fig. 2. 12 A schematic showing the steps leading to the nucleation of nodular oxide on Zircaloy [2. 90]

There are various factors which affect the nodular corrosion susceptibility viz:

(a) Precipitates size and distribution which can be represented after processing by

Cumulative Annealing Parameter $CAP = \sum_{i=1}^{N} A_i$, after beta quenching,

$$\sum_{i=1}^{N} A_i = \sum_{i=1}^{N} t_i \exp\left(\frac{-Q}{RT}\right)$$

Where t_i is the time in hrs. for an individual annealing operation performed at an elevated temperature T(K), Q is the activation energy, R gas constant. For individual annealing, Q/R value is taken as 40,000K which has been widely used.

Cumulative annealing parameter (CAP) controls the precipitate size and distribution. Higher value of CAP leads to coarser precipitate size and vice versa. It has been observed that if precipitates are fine (below 0.2 μm) and uniformly distributed in the fuel tubes, it will lead to nodular corrosion resistant clad. To get nodular corrosion resistant fuel tube, prescribed value of the cumulative annealing parameter should be below 2x 10^{-18} hrs. But in PHWR, as nodular corrosion is not a concern and to improve uniform corrosion resistance, relatively coarser intermetallic precipitates are required. So the best range of CAP for BWR and PHWR cladding appears to be within 2 x 10^{-18} to 50 x 10^{-18} hrs. and correspondingly precipitates size should be in the range of 0.1 - 0.2 μm (fig. 2.13). But till now there is no consensus on the mechanism on how precipitates size and its distribution control the oxidation kinetics in different environments.

(b) Alloy composition,

Chemical composition [2. 62] is another important factor in controlling the nodular corrosion resistance as it has an effect on the oxide electron conductivity. It was seen that alloys with high Sn, low (Fe + Cr) and a high level of impurities (Si, C, and P) show nodular corrosion susceptibility whereas O, Ni, Fe, Cr improve the resistance to nodular corrosion. Uniform distribution of alloying element is also essential for improved resistance. The depletion of solute elements is the cause of poor nodular corrosion resistance.

Zircaloy-2 shows higher resistance to nodular corrosion than Zircaloy-4. Because it contains Zr(Fe, Cr)$_2$ and Zr$_2$(Ni, Fe) precipitates, whereas Zircaloy-4 contains only Zr(Cr, Fe)$_2$ precipitates. Zr$_2$(Ni, Fe) is more corrosion resistant than Zr(Fe,Cr)$_2$. Fine uniform distribution of

Zr$_2$(Ni,Fe) precipitates provides the short circuit path for electron to traverse from the oxide metal interface to the oxide coolant interface. Subsequently H$^+$ is reduced closer to oxide coolant interface where it can be liberated from the oxide and prevent nodule formation.
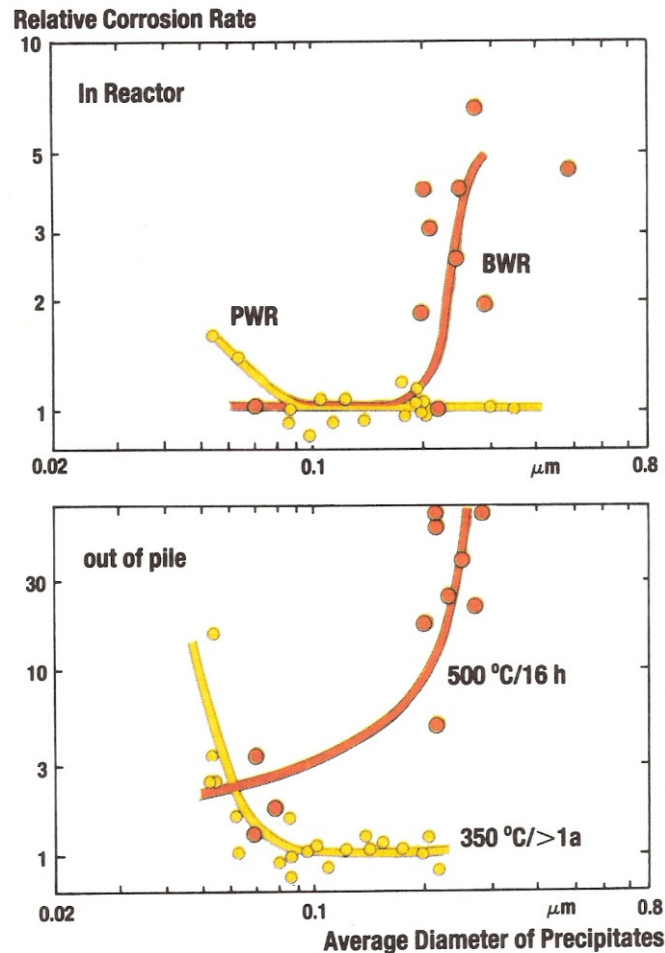
Fig.2.13 Correlation between relative corrosion rates to the mean diameter (μm) of second phase particles in Zircaloy fuel sheath in reactor [2. 34].

(c) Water chemistry and Irradiation

The phenomenon of nodular corrosion is relevant to BWR water chemistry where water radiolysis and boiling, allow oxygen to accumulate in water at 300° C. Reducing water chemistry will not lead to the formation of nodules. Out of pile 500°C/24hrs. /steam test shows nodule formation, but the mechanism of nodule formation at this high temperature is not clear. Couple

of studies indicated that the nodule nucleation occurs in precipitates free areas. Our own studies [2. 57] also indicated that the regions of the fuel tube where very less SPPs are present become susceptible to nodular corrosion compared to the regions where a large number of uniformly distributed fine precipitates are present.Zr-l wt.%Nb alloy cladding undergone nodular corrosion in an out-reactor loop in the presence of added O. Adamson et.al [2. 76] showed that high dose of neutron irradiation causes the dissolution of $Zr(Fe,Cr)_2$ precipitate and subsequently enrichment of Fe and Cr into the solid solution of Zircaloy which reduces the nodular corrosion.

(d) Texture & Residual Stress

Texture is an important factor in controlling nodular corrosion resistance. Correlation of texture with nodular corrosion weight gains was analysed by Wang et al. [2. 60]. It was seen that higher the value of f_n, the better was the nodular corrosion resistance in samples of same size and annealing history. According to Kuwae et al. [2. 61], H diffuses slower parallel to rather than perpendicular to the (0001) plane. Thus a hydrogen build up may occur and cause cracking at the metal/oxide interface on planes which exhibit low f_n values. This leads to oxygen access to the interface and acceleration of the corrosion rate. Compressive residual stress is supposed to improve the resistance to nodular corrosion.

2.4 Hydriding of Zr and its alloys

Normally Zr base alloys after fabrication, contain H content around 5-10 wt.ppm. These alloys absorb H mainly as a consequence of the corrosion reaction with water. H has limited solubility in Zr alloys. At any temperature this solubility is called Terminal Solid Solubility (TSS) and can be written as

$$C_H = 9.9 * 10^4 * \exp\left(\frac{-8250}{RT}\right) \ ppm \ (R = 1.987 \frac{cal.}{mol.K})$$

At 400°C TSS is about 200 ppm, at 300°C, it is about 60 ppm but at room temperature it is less than 1 ppm [2. 77- 2. 80]. Once H concentration exceeds the solubility limit, ʹHʹ in excess of TSS forms hydride precipitates. At room temperature, practically all the hydrogen precipitates out as Zr hydride platelets. This phase is brittle and lowers the mechanical properties of the alloys. The extent to which this embrittlement of the alloy occurs depends on the volume fraction

of hydride present, its orientation within the alloy and the degree of interconnection of the hydride platelets. These hydride precipitates occurs either as plates or needles, and three types of structures and compositions are possible.

γ-hydride (ZrH) with face centered tetragonal structure(a=b=4.5957Å, c= 4.9686Å)

δ-hydride (ZrH$_{1.6}$) with face centered cubic structure (a=b=c=4.781 Å) and

ε-hydride (ZrH$_2$) with face-centred tetragonal (a=b=4.9789 Å, c=4.4508 Å)

The phase diagram of Zr-H is given in fig.2.14.

Zr-H Phase Diagram
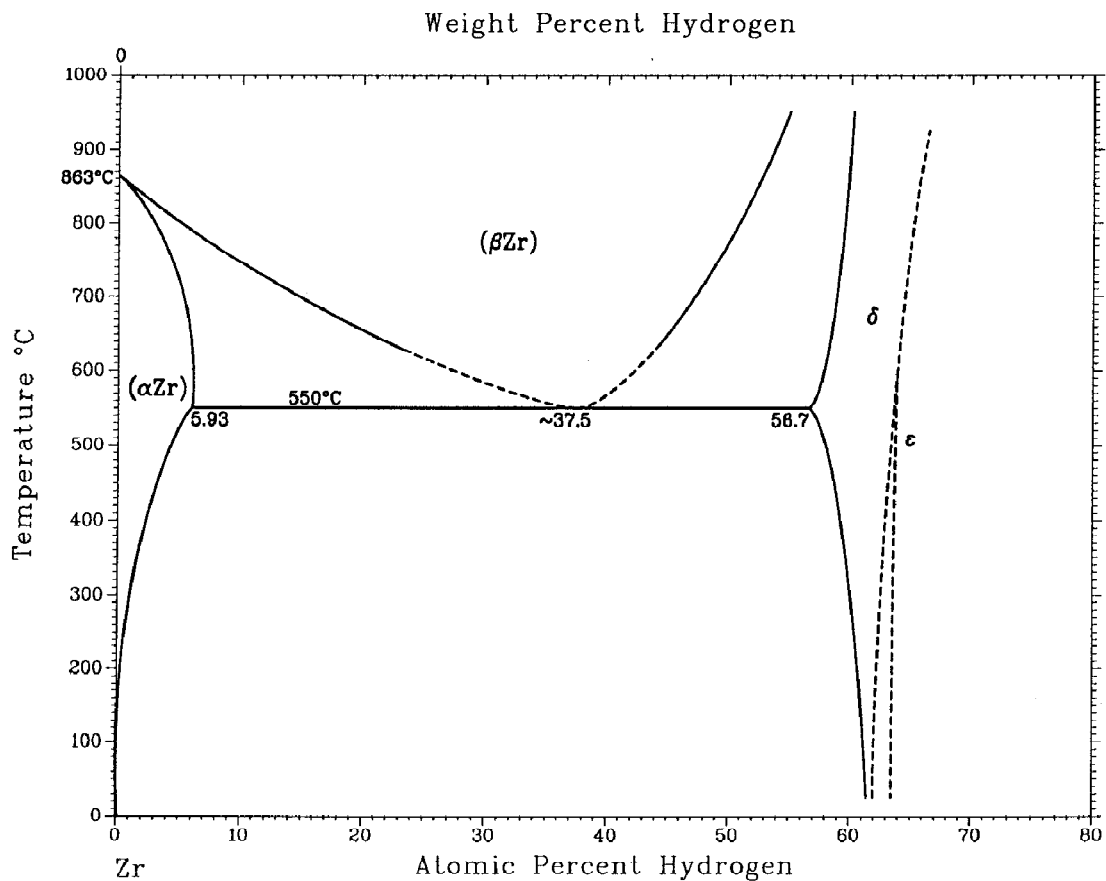
Fig.2.14 Binary Zr-H phase diagram [2. 15]

Few studies [2. 81, 2. 82] indicated that the influence of H on the oxidation behaviour. Heavily corroded zirconium normally shows presence of high levels of H in the matrix. TEM investigation [2. 83] showed similar morphology of oxide, both in a pre-hydrided and a reference sample after oxidation tests. But the oxide of pre-hydrided samples have shorter periodicity of cracks and have a higher crack density.

H, when in solution in Zr alloys can be driven in certain directions within the alloy under the action of a number of gradients, viz., thermal, stress and concentration. H moves down the temperature gradient, up the stress gradient and down the concentration gradient. Its movement under thermal gradient leads to hydride blistering when the local bulk concentration exceeds a threshold value. And its migration up a tensile stress gradient near a flaw tip, ultimately leads to delayed hydride cracking (DHC). The major steps in DHC are: 1) Formation of hydride once local concentration exceeds the terminal solid solubility, 2) Accumulation of hydrides and 3)Finally fracture of hydride once the local stress is high enough. Fracture of hydride leads the flaw tip to ductile matrix and there is no further crack growth. Now the extended flaw results in still higher stress concentration and provides still higher driving force for hydrogen to diffuse to flaw tip. This whole sequence of process is then repeated and the flaw grows in a discontinuous mode in a series of steps. Hence the term delayed is used to characterize this mode of cracking.

The important sources of hydrogen are:

(i) Aqueous corrosion reaction : $(Zr + 2H_2O \rightarrow ZrO_2 + 4H)$
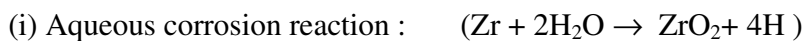
"H" atoms produced by the aqueous corrosion reaction, either recombine and release as hydrogen gas in the coolant or enter into the metal. These atoms can diffuse preferentially through intermetallics or uniformly over the surface. At present, the question of whether hydrogen migrates uniformly through the oxide or locally via defects or intermetallics is unresolved.

(ii) H overpressure in the coolant.

(iii) Radiolytic decomposition of water.

(iv) By reaction of gaseous hydrogen.

Absorption of gaseous H from the annulus gas of a CANDU reactor pressure tubes was a contributing factor in the failure of Pickering-2G16 pressure tube [2. 34].

(v) By the diffusion of H through a galvanic couple of dissimilar metals. Diffusion of deuterium from the end fitting through the metallic contacts at rolled joints, into the CANDU pressure tube was noticed during the investigation of early DHC of Zr-2.5Nb pressure tube in Pickering 3 and 4.

(vi) By cathodic polarization of zirconium in an electrolyte.

The presence of dissolved O or other oxidizing species accelerates the removal of discharged protons from the ZrO_2 surface and hence reduce the percentage H uptake.

Corrosion experiments performed using tritium doped water have shown that "H"dissolved in the coolant is not trapped by the matrix, but that radicals obtained during the reduction of water are necessary for hydrogen pick up. That is why H pick up is always expressed as the ratio of hydrogen entering the metal to that released by the corrosion reaction during the same period $f_H = \frac{H_{absorbed}}{H_{generated}}$. It is not a unique property of an alloy, but depends on the alloy chemistry, fabrication and exposure condition.

2.5 Microstructure modeling during phase transformation

The computational modeling has two main purposes. Primarily it gives in-depth understanding of mechanistic aspects of a process or transformation from one state to another. Secondly,it ensures more accurate prediction of complex phenomena. Many researchers [2. 21-2.32, 2.35-2.38] have studied the phase transformation of Zr-Nb system with experimental techniques using different analytical tools like TEM, STEM, HRTEM, SEM, XRD etc. But to design microstructure of Zr-Nb alloy with desired physical properties, computational modeling is required to find out key parameters behind those transformations and quantification of these parameters will help in controlling the microstructure.

The main features of solid state transformations are:

(1) The solid state transformation starts from an inhomogeneous microstructure and normally it consists of segregation bands, dislocation tangles, secondary and tertiary precipitates etc.

(2) The nucleation of product phase happens on the grain boundaries of the parent phase or twin boundaries or at a stacking fault, i.e. nucleation is predominantly heterogeneous in nature.

(3) A large numbers of dissipation mechanisms are active, like internal friction, retarded partitioning in para-equlibrium, plastic relaxation etc.

(4) The complexity of solid-solid transformation increases due to the presence of high anisotropy of the interfacial energy. The diffusivity of atoms in the solid state is in the range of 10^{-12} - 10^{-15} m^2/sec.

2.5.1 Evolution of Phase Field Modeling in solid state:

For the last two decades phase field modeling has become an important mathematical technique for multiscale modeling. The phase field equation was first introduced by van der Walls nearly a century ago [2. 84] and almost 40 years ago again by Cahn and Hilliard [2. 85, 2. 86]. Cahn and Hilliard in their paper on spinoidal decomposion, described free energy functional as a function of non-conservative phase field variable and its gradient terms. Their non-linear PDE mathematically describes local inhomogeneities of the system. The similar approach was taken by Allen-Chan (time-dependent Ginzburg-Landau) [2. 87, 2. 88] on the problem of moving anti-phase boundary for order-disorder type of system. Then Langer [2. 89] and Fix [2. 90] used phase field concept for first order transformation. Collins and Levin [2. 91] used the diffuse interface concept to model solidification.Then two major contributions came from Kobayashi [2. 92] and Wang [2. 93]. Kobayashi calculated dendritic structure in three dimensions and Wang [2. 93] was first to show that phase field variable is thermodynamically consistent.

In solid-solid phase transformation the driving force for grain growth comes from reduction in bulk free energy and minimization of surface energy. The application of the phase field concept has happened in two ways, first one to describe facetted growth [2. 94] and the second one to describe structural change during solid-solid phase transition [2. 95]. A number of researchers have applied the phase field method to study grain growth. First, Chen and Young [2. 96] had proposed a model consisting of a set of non-conserved order parameter fields to describe grain growth. Another grain growth model was proposed by Steinback [2. 97] where an additional

constrain was incorporated. Later Kobayashi presented further improved model by introducing another parameter which describes grain orientations [2. 98, 2. 99]. This grain orientation parameter helps in simulating grain rotation. Granasy et al. [2. 100, 2. 101] have incorporated nucleation and growth in the phase field model. First time, Widmanstatten plate growth was explored through phase field modeling by Loginova et al. on interstitial Fe-C alloy [2. 102].

Very few works have been done in microstructure modeling in Zr-Nb alloy system. Zr-Nb base alloys are used as critical components in the nuclear industry. The fabrication flow sheets of the components have been mostly made by traditional trial and error method which is expensive and time consuming. Prediction of microstructure through modeling is inexpensive as well as provides better in depth understanding of the process. Widmanstatten plate growth in Zr-Nb substitutional system has been modeled using Calphad type Gibbs free energy functional and diffusional mobility. Loginova et al. [2. 102] had used ad-hoc nucleation process which was further improved by using explicit and implicit nucleation events in the model by G. Choudhuri [2. 103] during this thesis work.

2.6 Effect of Irradiation:

The energetic particles like electrons, protons, neutrons and heavy ions cause damage in materials through the process of electronic excitation, ionization and by displacement of atoms from their lattice position [2. 104]. The damage profiles created by light ions are homogeneous in nature, whereas the damage caused by high energy, neutron or heavy ion through the primary knock on leads to formation of highly localized regions containing vacancies and interstitials. Formation of non equilibrium defects and the process of dissipation of energy during irradiation can modify the strain field of surrounding area and ultimately lead to changes in structure and properties of the materials. Therefore the entire damage profile caused by neutron in the reactor is often simulated in the short term by varying irradiation conditions (the light or heavy ions irradiation, energy of the particle etc.). The advantages of ion bombardment are as follows:

(1) Higher displacement rate leading to shorter irradiation duration for creating the same amount of damage;

(2) Less reactivation & ease of handling,

(3) Precise control of irradiation conditions,

(4) A lower cost of irradiation than that of neutron irradiation

The characteristic of the oxide formed in Zr base alloys are very much dependent on chemical composition, microstructure mainly size, type and distribution of second phase and second phase precipitates [2. 34, 2. 105] and its micro-chemistry. The behaviour of these intermetallic precipitates under irradiation has been studied in great details and investigations were mainly focused on the analysis of radiation damage in terms of mechanical properties and correlating the in reactor corrosion behaviour of the alloys with amorphization of precipitates [2. 106, 2. 34]. Depending upon their composition and crystal structure, some of these intermetallic precipitates are radiation resistant whereas some are prone to amorphization when these are irradiated by neutrons and ions such as Kr and He, and the transformation is believed to be due to the defect accumulation [2. 107 - 2. 117]. The intermetallic precipitates viz. Laves phase $Zr(Fe, Cr)_2$ which exist over a narrow composition range are prone to amorphization. $Zr_2(Fe, Ni)$ precipitates are susceptible to dissolution rather than amorphization [2. 118 - 2. 120].

In case of Zr-Nb alloy with two phases α-Zr and β-Zr microstructure, irradiation induced precipitation of fine β Nb (80-85 at. % Nb) particles occurs with the concomitant reduction of the Nb concentration in the α-Zr. This precipitation reaction is believed to be responsible for improving the in reactor corrosion resistance of Zr-2.5Nb pressure tube material [2. 34, 2. 121].

Another issue is how the precipitates either in crystalline form or in amorphous form get incorporated in the oxide. Pêcheur et al. [2. 110] showed that the oxidation of amorphous precipitates is similar to oxidation of unirradiated precipitates. They found a higher fraction of tetragonal/cubic zirconium oxide at the oxidized microcrystalline precipitate. This high temperature phase may be stabilized due to presence of Fe.

Effect of fast neutron irradiation on the matrix microstructure has also been studied [2. 122- 2. 123]. Supersaturation of vacancies and interstitials formed during irradiation is responsible for the evolution of dislocation loops as well as a network structure. In Zr base alloys, predominantly the <a>-type dislocations evolve during irradiation, but, at high irradiation doses in addition of <c>-[2. 123] component dislocations, network structures are also evolved. Formation of <c>-component dislocation marks the beginning of steady state irradiation growth in the recrystallized material whereas for the cold worked material, supersaturation of point defects leads to steady state growth from the early period.

Radiation destroys the protective properties of the oxide film by the formation of additional anion vacancies in the oxide. It can also induce the transformation to the high temperature phase in the oxide [2. 124 - 2. 2. 129]. Irradiation can enhance the redistribution of Fe in Zirconia [2. 130] and a higher fraction of tetragonal phase may also be expected due to Fe induced chemical stabilization of the tetragonal phase, but this had not been studied in detail.

2. 7 References:

2.1. Ganguly C, Advances in Zirconium technology for nuclear reactor application, Proceedings of the Symposium Zirconium 2002, 11-13 September 2002, BARC, Mumbai.

2.2. Lustman B and Kerze F, The metallurgy of Zirconium, McGraw Hill, N.Y. (1955).

2.3. Banerjee S. and Mukhopadhyay P. , Diffusional Transformation, Phase transformations: Examples from Titanium and Zirconium Alloys, Pergamon Materials Series, Vol. 12, pp. 555-716.

2.4 H. J. Beie, A. Mitwalsky, F. Garzarolli, H. Ruhmann, H.-J. Sell, ASTM STP 1245 (1994) 615-641.

2.5 J.P. Abriata and J. Garcés, Bulletin of Alloy Phase Diagrams Vol. 7 No. 2 1986, 116-123.

2.6 Victor Milman, Alexander Perlov, Keith Refson, Stewart J Clark, Jacob Gavartin and BjoernWinkler, J. Phys.: Condens. Matter 21 (2009) 485404 - 485415.

2.7. P. Barberis, J. Nucl. Mater. 226 (1995) 34-43.

2.8. J. Godlewski, ASTM-STP 1245 (1994) 663-683.

2.9. R. C. Garvie, J. Phys. Chem., 60 (4) (1966) 1238-1243.

2.10. W. Córdova-Marťnez, E. De la Rosa-Cruz, L.A. Díaz-Torres, P. Salas,A. Montoya , M. Avendaño , R.A. Rodyŕguez, O. Barbosa-Garćia, Optical Materials 20 (2002) 263– 271.

2.11. E. Polatidis, P. Frankel, J. Wei, M. Klaus, R.J. Comstock, A. Ambard, S. Lyon, R.A. Cottis, M. Preuss. J. Nucl. Mater. 432(1-3) (2013) 102-112.

2.12. P.Mukherjee, P. M. G. Nambissan, P. Barat,Pintu Sen, S. K. Bandyopadhyay, J. K. Chakrabartty, S. L. Wadekar, S. Banerjee, S. K. Chattopadhyay, S. K. Chatterjee, M. K. Mitra, J. Nucl. Mater. 297 (2001) 341-344.

2.13. F. Garzarolli, R. Schumann and E. Steinberg, Zirconium in the Nuclear Industry, ASTM STP 1245, 1994, 709-723.

2. 14. "Zirconium Alloy Corrosion" - A Review Based on an IAEA Meeting at Portland, Ninth Int. Symposium on Zirconium in Nuclear Industry, ASTM-STP-1132 (1991), pp. 3-32.

2.15. T. B. Massalski, "Binary Alloy Phase Diagrams", Second Edition, ASM International.

2.16. C. M. Eucken, P. T. Finden, S. Trapp-Pritsching and H. G. Weidinger, Zirconium in the Nuclear Industry, ASTM STP1023, 1989, 113-127.

2.17. A. M. Garde, S. R. Pati, M. A. Krammen, G. P. Smith and R. K. Endter, Zirconium in the Nuclear Industry, ASTM STP 1245, 1994, 760-778.

2.18. M. Harada, M. Kimpara and K. Abe, Zirconium in the Nuclear Industry, ASTM STP 1132, 1991, 368-391.

2.19. P. Barberis, J. Nucl. Mater., 226, 1995, 34-43.

2.20. Philipp Frankel , J. Wei, E. Francis, S. Lyon, R.A. Cottis, M. Preuss,N. Ni, S. Lozano-Perez, C. R. M. Grovenor, R. J. Comstock, L. Hallstadius, A. Ambard, M. Blat-Yrieix , 17th International Symposium on Zirconium in the Nuclear Industry, 03-08 February 2013, Hyderabad, India.

2.21. O Gebhardt, A Hermann, G Bart, H Blank, F Garzarolli and I L F Ray, Zirconium in the Nuclear Industry, ASTM STP1295, 1996, pp. 218-241

2.22. K Takeda and H Anada, Zirconium in the Nuclear Industry, ASTM STP 1354, 2000, 592-608.

2.23. Borrelly R., Merle P., Adami L., J. Nucl. Mater., 170 (1990) 147-156.

2.24. B.D. Warr, M.W. Hardie, V.F. Urbanic and D.O. Northwood, Proc. Pacific Corrosion '87 November 1987, Vol. 1.

2.25. M. Griffiths, J. Nucl. Mater. 159 (1988) 190-218.

2.26. X. Meng and D. O. Northwood, ASTM-STP 1023 (1989) 478-486.

2.27. M. Griffiths and R.A. Holt, ASTM-STP 1132 (1992) 172-176.

2.28. C.K. Chow, C.E. Coleman, R.R. Hosbons, P.H. Davies, M. Griffiths and R. Choubey, ASTM-STP 1132 (1991) 246-275.

2.29. A. Perovic, V. Perovic, G.C. Weatherly, G.R. Purdy and R.G. Fleck, J. Nucl. Mater. 199 (1993) pp. 102-111.

2.30. V. Perovic, A. Perovic, G.C. Weatherly, L.M. Brown,G.R. Purdy, R.G. Fleck and R.A. Holt, J. Nucl. Mater. 205 (1993) pp. 251-257.

2.31. O.T. Woo, G.J.C. Carpenter, J.A. Sawicki and S.R. MacEwen, J. Nucl. Mater. 172 (1990) pp. 71-76.

2.32. M. Griffiths, R W Gilbert and V. Fidleris, ASTM-STP1023 (1989) pp. 658-677.

2.33. D.O. Northwood, X. Meng-Burany and B.D. Warr, ASTM-STP 1132 (1992) 156-172.

2.34. IAEA TECDOC-996, 'Waterside Corrosion of Zirconium Alloys in Nuclear Power Plants', IAEA, 1998.

2. 35 Dey G. K., Banerjee S., J. Nucl. Mat. 125 (1984) 219-227.

2. 36 Dey G. K., Singh R. N., Tewari R., Srivastava D., Banerjee S., J. Nucl. Mat. 224 (1995) 146-157.

2. 37 Tewari R., Srivastava D., Dey G. K., Chakravarty J. K., Banerjee S., J. Nucl. Mat. , 383, 1-2, (2008) 153-171.

2.38 J.H. Lee, S.K. Hwang,J. Nucl. Mat. 321 (2003) 238–   248.

2.39. Cox B, "Oxidation of zirconium and it alloys", Adv. in Corr. Sci. and   Tech. , Vol. 5, Edited by Fontana M G, Staehle R. W., Plenum N. Y., (1976) 173- 391.

2.40. Y. Nishino, A. R. Krauss, Y. Lin, D. M. Gruen, J. Nucl. Mater, 228 (1996) 346-353

2.41. Fromhold A. T., Theory of Metal Oxidation-vol. I, Fundamentals, North Holland, Amsterdam 1976.

2.42. G. Choudhuri, K. R. Gurumurthy, B. K. Shah, J. Met. Mater. & Process, (2006)18 (1) 95-106.

2.43. Ploc R. A., J. Nucl. Mater. 28 (1968) 48-60.

2.44. J. N. Wanklyn, Corrosion of Zirconium Alloys, 1963, ASTM STP 368, 58-75.

2.45. Cox B.,J. Nucl. Mater., 148 (1987), 332-343.

2.46 Pia Tejland, Hans-Olof Andrén, Gustav Sundell, Mattias Thuvander, Bertil Josefsson, Lars Hallstadius, Maria Ivermark and Mats Dahlbäck, 17th international

symposium in "Zirconium in nuclear industry", ASTM Committee B10 on Reactive and Refractory Metals and Alloys, February 3-7, 2013 , Hyderabad, India.

2.47. Gaur B.K., J. of Acoustic Emission (USA), Vol. 7, No. 3, 1988, 13-17.

2.48. Pecheur D, Lefebvre F, Motta A T, Lemaignan C, Wadier J F, J Nucl Mater. 189 (1992) 318-332.

2.49. Garzarolli F., Seidel H., Tricot R., Gros J. P., Zirconium in the Nuclear Industry: 9th Int. Symp., ASTM-STP-1132, (Eucken C M., Garde A. M., Eds.), American Society for Testing and Materials, W. Conshohocken, PA. (1991) 395-415.

2.50. Pecheur D., Lefebvre F., Lemaignan C., J de Physique IV, C7, (1993) 503-507.

2.51. Warr B. D., Rasile E. M., Brennenstuhl A. M., Proc. IAEA Tech. Comm. Mtg. on the Fundamental Aspects of Corrosion on Zirconium Base Alloys in Water Reactor Environments, Portland, OR., USA, IWGFPT/34, IAEA, Vienna, Austria, (1989) 124-134.

2.52. Warr B. D., Elmoselhi M. B., Newcomb S. B., Mcintyre N. S. , Brennenstuhl A. M., Lichtenberger P. C. , Zirconium in the Nuclear Industry 9th Int. Symp. , ASTM-STP-1132, (Eucken, C M, Garde, A M, Eds.), American Society for Testing and Materials, W. Conshohocken, PA. (1991) 740-757.

2.53 Perkins R. A., Shih-Hsiung Shann, Proc., Application of Accelerated Corrosion Tests to Service Life Prediction of Materials, ASTM-STP-1194(1994) 239.

2.54. Mcdonald S. G. , Sabol G. P. , Sheppard K. D. , Zirconium in the Nuclear Industry 6th Int. Symposium , ASTM-STP-824, (Franklin D , Adamson R B, Eds.), American Society for Testing and Materials, W Conshohocken, PA (1983) 519-530.

2.55. Ramasubramanian N., Balakrishnan P. V., Zirconium in the Nuclear Industry 10th Int. Symp. ASTM-STP-1245, (Garde A M , Bradley E R , Eds.), American Society for Testing and Materials, W Conshohocken, PA (1994) 378-399.

2.56. Polley M. V., Evans H. E., Proceedings of Water Chemistry of Nuclear Reactor Systems 6, British Nuclear Energy Society, London, (1992) 61-66.

2.57. G. Choudhuri, R. S. Dutta, K. R. Gurumurthy, B. K. Shah, Proceeding of Zirconium-2002, ZIRC 2002, (11-13 September 2002) 411-419,.

2.58. Cheng B., Proc., Seventh Int. Symposium on 'Zirconium in Nuclear Industry, ASTM-STP-939, 239.

2.59. Schemel J. H., Zirconium in the Nuclear Industry, Seventh International Symposium, ASTM STP 551, 1987, 243-256.

2.60. Chun T. Wang, Craig M. Eucken, Ronald A. Graham, Zirconium in the Nuclear Industry, Ninth International Symposium, ASTM STP1132, Philadelphia, 1990, 319-345.

2.61. Kuwae R., Sato, K. Higashinakagawa, E. Kawashima J. and Nakamura S., J. of Nucl. Mater. , 1983, Vol.119, 229-239.

2.62. E. R. Bradley, J. H. Schemel and A. L. Nystrom, Zirconium in the Nuclear Industry, Ninth International Symposium, ASTM STP1132, Philadelphia, 1990, 304-316.

2.63. Lohner H., Blaser W., and Zwicky H. U., "Water Chemistry and Fuel Performance," Enlarged Halden Programme Group Meeting, Lillehammer, Norway, 15-20 March 1998.

2.64. Anderson B. and Zwicky H. U., "Enhanced Spacer Shadow Corrosion Phenomenon," Jahrestagung Krntechnik, 1999.

2.65. Zwicky H. U., Loner H., Andersson B., and Hardbottle J., "Enhanced Spacer Shadow Corrosion on SVEA Fuel Assemblies in the Leistadt Nuclear Power Plant," ANS International Topical Meeting on Light Water Reactor Fuel Performance, 10-13 April 2000, Park City. Utah.

2.66. Anderson B., Ballinger R., Hauso E., Johnsen T., Limbäck M., Nystrand A., Wikmark G., "Test Reactor Studies of the Shadow Corrosion Phenomenon ", Zirconium in nuclear Industry:13th International Symposium, STP 1423.

2.67. Hem J. S. F. "Observations of Shadow Phenomena on Zirconium Alloys", ANS Topical Meeting on LWR Fuel Performance, 1994, 309.

2.68. Lemaignan C., J. of Nucl. Mater., 187 (1992) 122-130.

2.69. T. Kelen, K. Lundgren and B. Andersson, "Fuel corrosion and activity build up in BWRs –Impact from metal balance", 103-110.

2.70. B. Cox, J. of Nucl. Mater., 336(2005) 331-368.

2.71. Strasser A., Sunderland D., IAEA TECDOC-709, 1993, 17-25.

2.72. Liv Lunde, (Special features of External Corrosion of Fuel Cladding in boiling water reactors.) Nuclear Engineering and Design 33 (1975) 178-195.

2.73. J. Delafosse and Poeymenge, Proceedings of Conference on the use of Zirconium Alloys in Nuclear Reactors, Maraushe Lazue (1966).

2.74. A. Garlick, J. Nucl. Mater. 45 (1972/73).

2.75 PIED, BARC Internal report.

2.76B. Cheng and R. B. Adamson, Zirconium in the Nuclear Industry, ASTM STP 939, 1987, 387-416.

2.77. J. J. Kearns, J. Nucl. Mater., vol. 22, 1967, 292-303.

2.78. B. F. Kammenzind, D. G. Franklin, H. R. Peters and W. J. Duffin, Zirconium in the Nuclear Industry, ASTM STP 1295, 1996, 337-370.

2.79. W. H. Erickson and D. Hardie, J. Nucl. Mater., vol. 13, 1964, 254-262.

2.80. A. Sawaatzky, and B. J. S. Wilkins, J. Nucl. Mater., vol. 22, 1967, 304-310.

2.81. M. Garde, Zirconium in the Nuclear Industry, ASTM STP 1132, 1991,566-594.

2.82. A. M. Blat and D. Noel, Zirconium in the Nuclear Industry, ASTM STP 1295, 1996, 319-337.

2.83. M. Blat, L. Legras, D. Noel and H. Amanrich, Zirconium in the Nuclear Industry, ASTM STP 1354, 2000, 563-591

2.84 Van der Waals J. D., 1894. Z. Phys. Chem.13:657.

2.85. J. W. Chan and J. E. Hilliard, J. Chem. Physics, 28, 1958, 258-267.

2.86. Cahn J. W., 1961, Acta Metall. 9: 795–801.

2.87. Allen S. M., Cahn J. W. 1977. J. Phys. 38: C 7–51.

2.88. S. M. Allen and J. W. Chan, Acta Metallurgica, 27, 1979, 1085-1095.

2.89. Langer J. S. 1986, Models of pattern formation in first order phase transitions, Directions in Condensed Matter Physics, ed. G Grinstein and G Mazenko (Singapore: World Scientific) 165.

2.90. J. George Fix, Theory and Applications, vol. 2, ed. A. Fasano and A. Primicerio (Boston, MA: Pitman) 580.

2.91. J. B. Collins and H. Levin, Physical review B, 31, 1985, 6119.

2.92. R. Kobayashi, Physica D 63, 1993, 410 - 423.

2.93. S. L. Wang, R. F.Sekerka, A. A. Wheeler, B. T. Murray, S. R. Coriell, R. J. Braun and G. B. McFadden, Physica D, 69, 1993, 180-200.

2.94. Ingo Steinback, Oleg Shchyglo, Current Opinion in Solid State and Material Science 15(2011) 87-92.

2.95. Matthias Militzer, Current Opinion in Solid State and Material Science 15(2011) 106-115.

2.96. L. Q. Chen, W. L. Wang, Physical Review B, 50, 1994, 15752.

2.97. I. Steinbach, F. Pezzolla, B. Nestler, M. Seebelberg, R. Prieler, G. J. Schmitz, J.L.L. Rezende, Physica D 94, 1996, 135-147.

2.98. R. Kobayashi, J.A. Warren and W.C. Carter, Physica D, 140, 141-150 (2000).

2.99. J. A. Warren, R. Kobayashi and W. C. Carter, J. Crystal Growth, 211, 18-20 (2000).

2.100. L. Granasy , T. Borzsonyi and T. Pusztai, Phys. Rev. Lett.88, 2002, 206105.

2.101. L. Granasy , T. Borzsonyi and T. Pusztai, J. Crystal Growth , 237-239, 1813-1817 (2002).

2.102. I. Loginova, J. Ågren and G. Amberg,Acta Materialia, Volume 52, Issue 13, 2 August 2004, 4055-4063.

2.103. G. Choudhuri, S. Chakraborty, D. Srivastava, G. K. Dey, Results in Physics, 3, 2013, 7-13.

2. 104. A.T. Motta, F. Lefebvre and C. Lemaignan, C.M. Euken and A.M. Garde (eds), Zirconium in the Nuclear Industry. : 9th International Symposium, Kobe, Japan, 1990, ASTM STP 1132(1991) 718.

2. 105. Y. Etoh, S. Shimada, K. Kikuchi, J. Nucl. Sci. Tech. 29 (12) (1992) 1173.

2. 106. W.J.S. Yang, J. Nucl. Mater. 158 (1998) 71.

2. 107. M. Griffiths, J. Nucl. Mater. 170 (1990) 294.

2. 108. F. Lefebvre, C. Lemaignan, J. Nucl. Mater. 171 (1990) 223.

2. 109. Idem, J. Nucl. Mater. 165 (1989) 122.

2. 110. D. Pecheur, F. Lefebvre, A. T. Motta, C. Lemaignan and D. Charquet, J. Nucl. Mater.,vol. 205, 1993, 445-451

2. 111. G.Y. Tang, B.H. Chio, W. Kim, K.S. Jung, H.S. Kwon, S.J. Lee,J.H. Lee, Surf. Coat. Technol. 89 (1997) 252.

2. 112. J. Xu, X.D. Bai, F. He, S.G. Wang, X.Z. He, Y.D. Fan, J. Nucl.Mater. 265 (1999) 240.

2. 113. J.H. He, X.D. Bai, C.L. Ma, H.M. Chen, Nucl. Instru. Meth. B 100 (1995) 59.

2. 114. X.D. Bai, S.G.J. Wang, F. He, H.M. Chen, Y.D. Fan, Chin. J. Nucl.Sci. Eng. 16 (3) (1996) 243.

2. 115. A. T. Motta and C. Lemaignan, J. Nucl. Mater., vol. 195, 1992, 277-285

2. 116. Y. Etoh and S. Shimada, J. Nucl. Mater., vol. 200, 1993, 59-69

2. 117. M. Griffiths, R. W. Gilbert and B. A. Cheadle, Atomic Energy of Canada, AECL-8852, 1985.

2. 118. M. Griffiths, R. W. Gilbert and G. J. C. Carpenter, J. Nucl. Mater., vol. 150, 1987, pp. 53-66

2. 119. C.D. Cann , C.B. So, R.C. Styles and C.E. Coleman , J. Nucl. Mater., 205 (1993) 267-272.

2. 120. M. Griffiths, J. F. Mecke and J. E. Winegar, Zirconium in the Nuclear Industry, ASTM STP 1295, 1996, 580-602

2. 121. L. Tournadre , F. Onimus , J. L. Béchade, D. Gilbon, J.-M. Cloué , J.P. Mardon , X. Feaugas ,O. Toader , C. Bachelet, J. Nucl. Mater., 425 (2012) 76–82.

2. 122. A. Benyagoub, Nuclear Instruments and Methods in Physics Research B 206 (2003) 132–138.

2. 123. D. Simeone , G. Baldinozzi , D. Gosset , S. Le Cae¨r, Nuclear Instruments and Methods in Physics Research B 250 (2006) 95–100.

2. 124. D. Simeone , D. Gosset , J.L. Bechade, A. Chevarier, J. Nucl. Mater., 300 (2002) 27–38.

2. 125. James A. Valdez , Ming Tang, Zhenhuan Chi , Maria I. Peters, Kurt E. Sickafus, Nuclear Instruments and Methods in Physics Research B 218 (2004) 103–110

2. 126. Jeremy Cheng , Fritz B. Prinz, Nuclear Instruments and Methods in Physics Research B 227 (2005) 577–583.

2. 127. C. Gibert-Mougel, F. Couvreur, J.M.Costantini, S. Bouffard, F. Levesque, S. Hemon, E. Paumier, C. Dufour, J. Nucl. Mater., 295 (2001) 121–125

2. 128. X. Iltis, F. Lefebvre, C. Lemaignan, J. Nucl. Mater., 224 (1995) 121-130.

2. 129. M. Li, M.A. Kirk, P.M. Baldo, D. Xu, B.D. Wirth, Phil. Mag. 92 (16) (2012) 2048–2078.

2. 130. Y. Idrees , Z. Yao , M.A. Kirk, M.R. Daymond, J. Nucl. Mater., 433 (2013) 95–107.

Chapter 3

Materials and Methodology

This chapter describes details of materials used, experimental methods and characterization techniques used during this study. The computational technique used for modeling microstructure evolution during diffusional phase transformation is also discussed.

3.1 Material

Two series of Zr base alloys were used. The alloys of Zr-Sn-Fe-Cr series, were triple arc melted ingot which were manufactured at Nuclear Fuel Complex (NFC) Hyderabad. One alloy containing 1.53 wt. % Sn and the other one having 1.35 wt. % Sn with transition elements as given in table 3.1. These were having composition of optimized Zr-Sn-Fe-Cr series alloy and designated as alloy 1, alloy 2 respectively in the thesis.

Table: 3.1 Chemical composition of two Zr-Sn-Fe-Cr alloys

Sl.No.	Sn* (wt.%)	Fe* (wt.%)	Cr* (wt.%)	Fe+Cr (wt.%)	O# (ppm)	C** (ppm)	Si** (ppm)	N** (ppm)	H** (ppm)
Alloy1	1.53	0.20	0.10	0.30	1007	100	65	39	5
Alloy2	1.35	0.19	0.09	0.28	1064	78	42	30	4

* Error in estimation 0.1%

 # Error in estimation 1%

** Error in estimation ±1 ppm

Another series of alloy chosen is Zr-Nb series. Cold worked stress relieved Zr-2.5Nb pressure tubes fabricated at NFC, Hyderabad, were used in this study. The fabrication flow-sheet [3.1] of pressure tube is given in fig. 3.1. Coupons sliced from tubes just after autoclaving were used as

starting material and are referred to as-received material. To study the effect of Fe content in Zr-Nb-Fe alloy on microstructure and precipitates characteristics and in turn its oxidation and hydrogen pick up behavior of the alloy, three different compositions (table 3.2) of Zr-2.5Nb pressure tubes were selected. These alloys were having Fe-content of 300 ppm, 800 ppm, 1250 ppm and were designated as alloy 3, alloy 4 and alloy 5 respectively.

```
┌─────────────────────────────────────┐
│   Zr-2.5Nb Quadruple melted ingot    │
└─────────────────────────────────────┘
                  │
                  ▼
      ┌──────────────────────────┐
      │   Hot Extruded (800°C)    │
      └──────────────────────────┘
                  │
                  ▼
   ┌────────────────────────────────┐
   │  Machining, cutting & Deep hole │
   │     drilled hollow billet        │
   └────────────────────────────────┘
                  │
                  ▼
       ┌──────────────────────┐
       │  beta quenched (1000°C) │
       └──────────────────────┘
                  │
                  ▼
     ┌──────────────────────────┐
     │ Hot Extruded (800°C) hollow│
     │          blank            │
     └──────────────────────────┘
                  │
                  ▼
      ┌─────────────────────────┐
      │  Vacuum Stress Releived  │
      │     (480°C/3 hrs.)       │
      └─────────────────────────┘
                  │
                  ▼
   ┌─────────────────────────────────┐
   │  Two stage pilgering with        │
   │  intermediate vacuum annealing   │
   │        (560°C/6hrs. )            │
   └─────────────────────────────────┘
                  │
                  ▼
 ┌──────────────────────────────────────┐
 │            Inspection                  │
 │ (UT, ECT, Dimensional, boroscopy,      │
 │         pressure testing               │
 └──────────────────────────────────────┘
                  │
                  ▼
  ┌──────────────────────────────────┐
  │ Steam Autoclaving (400°C/36       │
  │       hrs./10 atm.)               │
  └──────────────────────────────────┘
                  │
                  ▼
        ┌──────────────────────┐
        │    Final Inspection   │
        └──────────────────────┘
```

Fig. 3. 1 Fabrication flow sheet for production of seamless Zr-2.5%Nb pressure tubes for PHWR at NFC, Hyderabad [3. 1]

Table: 3. 2 Chemical Compositions of the Zr-Nb series

Alloy	Nb (wt%)	Fe (ppm	O (ppm)
Alloy-3	2.60	300	946
Alloy-4	2.47	800	950
Alloy-5	2.49	1250	1003

3.2 Sample preparation and different characterization techniques:

3.2.1 Fabrication of coupons and thermo mechanical treatment:

Samples from triple melted ingot of Zr-Sn-Fe-Cr were initially 30% cold rolled and 10-15% cross rolled to break the previous cast structure. Then these samples were cut into small pieces and encapsulated in glass tube under helium environment. Solution annealing was carried out at 1050° C for 30 min and immediately glass capsules were transferred and broken into water to achieve high cooling rate. Quenched samples were again encapsulated in quartz glass tube with helium gas filled at 100mm Hg pressure and α annealing heat treatment was carried out at 700°C and 800° C for 15 mins, 1hr. and 10 hrs., respectively to study size, size distribution and nature of the SPPs. To observe the effect of annealing at α+β phase field, annealing of some samples was carried out at 850°C for 1 hr.

A mathematical parameter which is a combination of time and temperature of each annealing heat treatment to sum up effect of all applied heat treatment in the αphase region of zirconium during fabrication, is described as Cumulative Annealing Parameter (CAP) [3.2],

$$CAP = \sum_{i=1}^{N} A_i = \sum_{i=1}^{N} t_i \exp\left(\frac{-Q}{RT}\right)$$ ---------------- 3.1

taking Q/R =40000 K. A wide range of CAP (in hrs.) values were calculated (Table 3.3) for each annealing heat treatment.

Table: 3. 3 CAP values for each alpha annealed heat treated condition

Sl. No.	Annealing Condition	CAP in hrs.(Calculated)
1.	700° C for 15 mins.	0.35×10^{-18}
2.	700° C for 1 hr.	1.4×10^{-18}
3.	700° C for 10 hrs.	14×10^{-18}
4.	800° C for 1hr.	64.6×10^{-18}
5.	800° C for 10 hrs.	646×10^{-18}

To study the influence of β phase on corrosion and hydrogen intake behaviour of Zr-2.5Nb alloy higher volume fraction of β(Zr) phase was generated in the as received samples (alloy 5) after soaking the material at 680°C for 2 hrs. i.e. above monotectoid temperature and followed by air cooling. The heat treatment was carried out in 'He' environment keeping the samples in encapsulated quartz glass tube. This sample is designated as β-heat treated alloy 5.

3.2.2 Autoclaving:

For oxidation study five coupons from each heat treated condition of alloy 1 and alloy 2 were pickled according to ASTM G2 for autoclave testing. Accelerated Autoclaving at 415° C, 10.3 MPa pressure for three days period [3.3] was done to observe the oxidation behavior of the differently heat treated alloy. The weight before and after accelerated autoclaving of the coupons

was taken on a balance of 0.01 mg accuracy and dimensions were measured with 0.05 mm accuracy as specified by ASTM G2.

Autoclaving of few samples was carried out at 500°C 10.3 MPa for 3 days to simulate nodular corrosion observed in boiling water environment of nuclear reactor.

For Zr-2.5Nb pressure tube material, three samples from each Fe level were taken and autoclaved oxide layer was removed by using emery paper. After that these samples were also pickled and following which autoclaving at 415° C, 10.3 MPa pressure for 3 days period was carried out.The weights before and after accelerated autoclaving of the coupons were measured. The thicknesses of the oxide layers formed on the samples as a result of autoclaving was determined by SEM.

3.2.3 H pick up measurement:

To measure hydrogen pick up during autoclaving, as received samples and samples after accelerated autoclaving were cut using a cut-off wheel and carbon tetrachloride as coolant. The autoclaved oxide layer was removed by dry grinding on coarse emery paper. After that the samples were cleaned in tetrachloride solution, dried and weighed. H content was determined using inert gas fusion technique [3.4]. Hydrogen measurement of standard Ti samples having H $16\pm2ppm$ and $27\pm2ppm$ respectively was done before and after testing of each coupon. The microstructures of the autoclaved samples were also examined to establish if hydrides had formed.

3.2.4 Optical Microscopy:

For optical microscopy work, samples of Zr-Sn-Fe-Cr series were polished mechanically and then chemically in 45 % HNO_3-45% H_2O-10% HF solution.

3.2.5 Scanning Electron Microscopy:

Specimens for scanning electron microscopy (Camscan CS3200L) were prepared by mechanical grinding and subsequent etching in a glycerine: Hf : HNO_3 (6 : 2 :1) solution for nearly 20 sec to reveal second phase particles in Zr-Sn-Fe-Cr alloys. For Zr-Nb series alloys, samples were prepared by mechanical grinding and subsequent etching in HF : HCl: HNO_3 (2: 2:1) solution to reveal the second phases.

3.2.6 Transmission Electron Microscopy:

For transmission electron microscopy, 100 μm thick discs with 3 mm diameter were made and electro polished in a solution of 20% perchloric acid and 80% methanol at -50° C using jet-thinning apparatus. These electron transparent foils were examined at 160KV using JEOL transmission electron microscope. Elemental analyses were performed using an energy dispersive spectrometer (EDS) attached with STEM.

3.2.7 Cross sectional TEM sample preparation technique:

For observation of oxide in the cross section, samples with small transverse cross-sections of tubing that were prepared according to the following procedure. Two samples having axial segments ofabout 1.5 mm width and 10 mm height were cut from the autoclaved oxidized Zr-2.5Nb pressure tube material and oxidized Zr-Sn-Fe-Cr alloys. Then the two pieces were glued together such a way that the oxide surfaces were facing each other. Then this joined piece was inserted into a slot having width 1.1mm and is made on 2.5 mm (diameter) x 12mm (height) Mo rod. Then the whole assembly was placed inside a brass tube having outer diameter 3mm and inner diameter 2.5mm. This attachment was bonded in place using Devcon (R) epoxy resin with hardener. Slices about 0.5 mm thick were then cut from the brass tube to provide 3 mm diameter disks with the oxide cross-section located near the center of the disk. The disk samples were ground on 600 grit silicon carbide paper on both sides until the thickness was approximately 100 μm. These disks were then dimpled by using dimple grinder with the dimple centered near the oxide–oxide interface. The dimple was made by using progressively finer diamond abrasives followed by a final polish using0.05 μm alumina. Dimples were made on both sides ofthe disk with the final thickness of the disk at the bottom of the dimple is around 40μm. After that GATAN ion milling at 4.3 kV was carried out for sufficient time such that electron should

transmit through the oxide. Throughout the sample preparation and polishing, care was constantly exercised to avoid sample deformation and to remove the damaged oxide from the cutting operation because of the sensitivity of the oxide to develop lateral cracks during preparation.
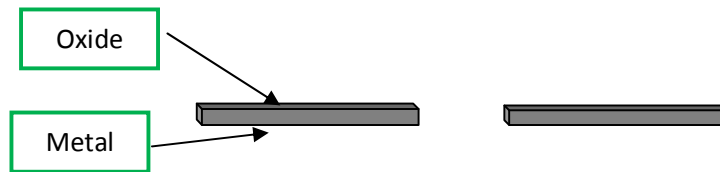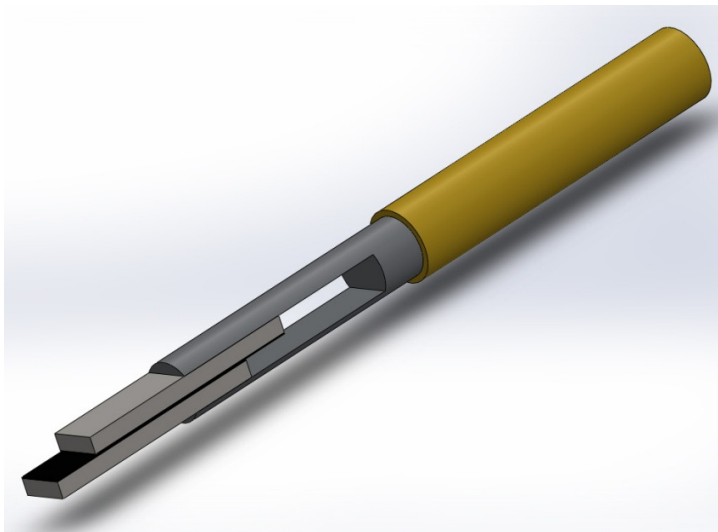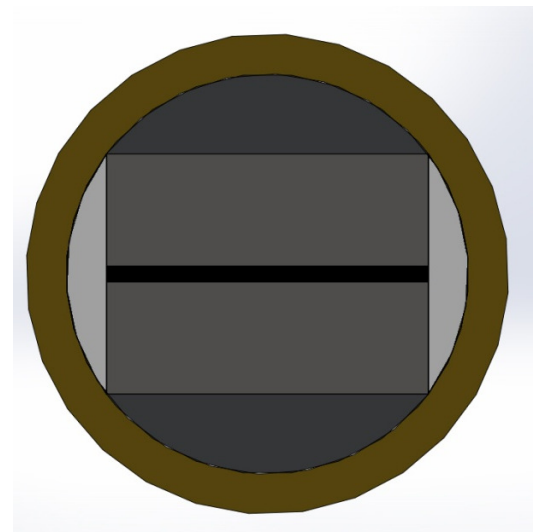
Fig. 3. 2 Steps involved in making cross sectional sample (diagram not in scale).

3.2.8 Micro-hardness measurement:

Vickers hardness measurements using 300 gm load with 10 s dwelling time were carried out on all the annealed samples heat treated at two different temperatures for various lengths of time. For Zr-2.5Nb pressure tube material with different Fe content, Vickers hardness measurements were carried out in a plane containing longitudinal-transverse directions. Eleven measurements on each samples were done to get the hardness of the alloys.

3.2.9 Small Angle Neutron Scattering (SANS):

Small angle scattering (SAS) is a powerful nondestructive technique to investigate structural features (size or size distribution, shape, inter-particle spacing) of the in-homogeneities (second phase precipitates or particles or pores in porous medium) or the density fluctuations in condensed matter [3.5, 3.6], on a length scale ranging from one nanometer up to one micron in a large specimen without any special sample preparation. Small angle scattering refers to the scattering at small wave vector transfer and is caused by the variation of scattering length density over a distance exceeding the normal inter-atomic distances in condensed systems. SAS differs from Bragg or diffuse scattering in the sense that it refers to scattering at small magnitude of wave vector transfer compared to the smallest reciprocal lattice vector in crystalline material or to that first maximum of the structure factor in non crystalline materials. So study of gross scale structural properties of a medium overlooking the specific details over inter-atomic distances is possible. Generally X-ray or neutrons are used as incident radiation for SAS investigations and the techniques are named as Small angle X-ray scattering (SAXS) or Small angle neutron scattering (SANS) respectively. In SAXS, as X-rays get scattered by electrons, it investigates inhomogeneities in electron density whereas SANS probes inhomogeneities in nuclear scattering length density. It is worthy to mention that SANS [3.7] is an useful nondestructive tool to obtain statistically averaged morphological information about inhomogeneities that are present in an alloy. It is to be mentioned that SANS and TEM are complementary in nature. TEM provides direct information on localized zone while SANS gives statistically averaged information from bulk.

SANS measurements were carried out to find the size and distribution of second phase precipitates in Zr-Sn-Fe-Cr series alloy in a thick specimen to get good statistical averaged information and have been performed using a double crystal based medium resolution small-angle neutron scattering instrument (MSANS) [3.7] at the guide tube laboratory of DHRUVA reactor, India. The scattered intensities [I(q)] have been recorded as a function of wave vector transfer function q [= $4\pi\sin(\theta)/\lambda$, where 2θ is the scattering angle and λ (= 0.312 nm.) is the incident neutron wavelength for the present experiment]. The specimens (~2 mm) were placed on a sample holder with a circular slit of 1.5 cm diameter. The SANS data were corrected for background, transmission and instrument resolution effects [3.8].

3.2.10 X-ray photo Electron Spectroscopy:

X-ray photo-electron spectroscopy (XPS) [3.9] is a surface sensitive quantitative spectroscopic technique that measures the elemental composition at the parts per thousand range, chemical state and electronic state of the elements that exist within material. The XPS spectra are obtained by irradiating a material with a beam of X-rays while simultaneously measuring the kinetic energy and the number of photo electrons that escape from the top 0 to 10 nm of the surface. Very high vacuum or ultra vacuum is required. Fig.3.3 depicts the principles of XPS technique. A typical XPS spectrum is a plot of the number of electrons detected versus binding energy of the electrons detected. The binding energy of the electron can be determined by using an equation that is based on the work of Ernest Rutherford [3.10].

$$E_{binding} = E_{Photon} - \left(E_{Kinetic} + w_\varphi\right) ----- 3.2$$

where $E_{binding}$ is the binding energy (BE) of the electron, E_{Photon} is the energy of the X-ray photon being used, $E_{Kinetic}$ is the kinetic energy of the electron as measured by the instrument and w_φ is the work function of the spectrometer.

Each element produces a characteristic set of XPS peaks at characteristic binding energy that directly identify each element present in or on the surface of the material analyzed. These characteristic spectral peaks correspond to the electron configuration of the electrons within the

atoms, e.g., 1s, 2s, 2p, 3s, etc. The number of detected electrons in each of the characteristic peaks is directly related to the amount of element within the XPS sampling volume. To generate atomic percentage values, each raw XPS signal must be corrected by dividing its signal intensity (number of electrons detected) by a "relative sensitivity factor" (RSF), and normalized over all of the elements detected. Since hydrogen is not detected, these atomic percentages exclude hydrogen. This technique is also called as Electron spectroscopy for chemical analysis (ESCA).
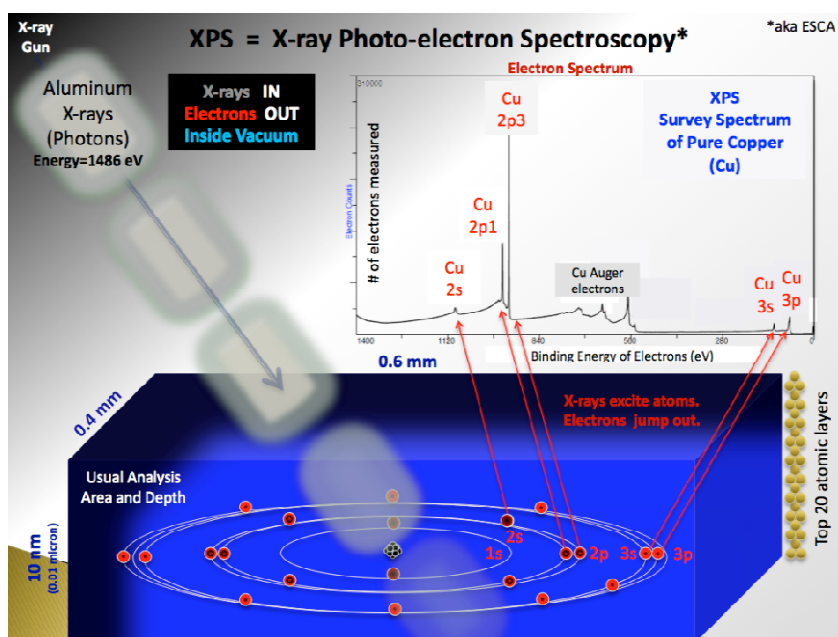
Fig.3. 3: Schematic Diagram of principles of X-ray photo electron spectroscopy technique where probing beam is Al X-ray having 1486 eV energy (internet source).

To establish the chemical state of elements in the oxide film the outermost surface of all the alloys were analyzed with XPS using hemispherical Thermo VG Clam2 analyzer. Detailed scans of C 1S, Zr 3d, Nb 3d, Fe, O 1S were obtained with monochromatic Mg Kα X- ray source. The area of analysis was approximately 100 mm^2. The binding energy of O1s, Zr 3d and Nb 3d was correctedtaking C 1S peak at 284.5 ev.

3.2.11 Grazing Incidence X-ray Diffraction (GIXRD):

Grazing Incidence X-ray diffraction technique is used to record the diffraction pattern of thin films, with minimum contribution from substrate. It is a nondestructive surface sensitive

technique. Since the angle of incidence (α) of X-ray beam decreases, so that the refractive index is less than unity, total external reflection of X-rays occurs below critical angle of incidence α_c. The diffracted and scattered signals at the angle 2θ arise only from the limited depth from surface depending upon angle of incidence. While the detected signal is Bragg-diffracted at a lattice plane directed perpendicular to the surface, the method possesses the capabilities of measuring residual stress or phase analysis across the depth. The experimental set up for carrying out GIXRD is shown in fig.3.4. GIXRD was performed using a rotating anode X-ray diffractometer with Cu Kα radiation in order to obtain information about the oxide structure from the specimens so that the normal direction to their surface corresponded to the radial direction of the pressure tube. The grazing incident angles of 0.5°,1°, 5°and 10°were used to study the oxide structure along the thickness direction.
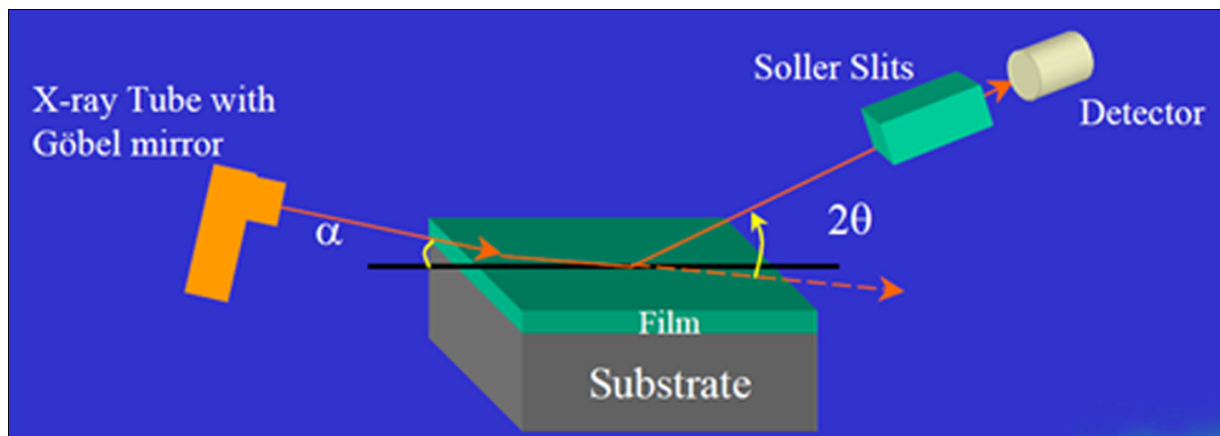
Fig. 3. 4 Schematic Diagram of Grazing Incidence X ray Diffraction principle where parallel monochromatic X-ray beam falls on a sample surface at a fixed angle of incidence (α) so that signal comes mostly from the oxide film, not from substrate and the diffraction profile is recorded by detector (internet source).

The linear absorption coefficient (μ) of ZrO_2 oxide is 581.84cm^{-1} [3. 11] and for Zr it is 898.46 cm^{-1} . The depth of penetration (τ) was calculated using the following relationship at 0.5°,1°, 5° and 10° and are given in table 3.4 .

$$\tau = \frac{\sin \alpha}{\mu} - - - - - 3.3$$

Table 3.4: Depth of penetration at different grazing angle in Zr metal and its oxide

Grazing angle (α)	Depth of penetration	
	ZrO_2(nm)	Zr (nm)
0.5°	150	97
1°	300	194
5°	1498	970
10°	2984	1933

3.2.12 Ion and neutron Irradiation:

The oxide surface of the Zr-2.5Nb alloy and alpha annealed (700°C for 10 hrs.) Zr-Sn-Fe-Cr alloys were irradiated with 306 KeV Ar^{+9} ions at a dose of $3X10^{19}$ Ar^{+9} /m^2. To compare the effect of heavy ion irradiation with proton irradiation, oxide surface of αannealed (800°C for 10 hrs.) Zr-Sn-Fe-Cr alloy was irradiated with 3.5MeV proton using the beam at the Variable Energy Cyclotron Centre (VECC), Calcutta, at dose of $5x10^{20}$ proton/m^2. The samples for irradiation were mounted in a target holder flange, made of aluminum. The dose accumulating to the target material (sample) was measured from the total charge of projectile particles i.e. protons falling on the sample. Water is allowed to flow to the target flange to minimize the heat generated during irradiation. The temperature did not rise above 313 K, as monitored by a thermocouple sensor placed inside a groove of the flange in close proximity to the sample [3.12]. The displacements per atom (dpa) in both the case was obtained using TRIM programme. The irradiated oxides were characterized using GIXRD and XPS technique.

The fuel tube which was irradiated upto 7600MWD/T burn up was received. After decladding, a slice of 2 mm x 5 mm was made and inner side was ground to move the fuel contamination. During sample preparation proper care was taken so that no damage occurred in the outer surface of the tube. After ultrasonic cleaning it was taken out for GIXRD study.

3.2.13 Computational technique:

For prediction of microstructure evolution during diffusion controlled phase transformation in Zr-Nb substitutional alloy system, phase field technique has been adapted. This phase field

technique which is based on diffuse interface concept, features large scale separation. The interface is of the order of nanometers while characteristic features of microstructure present on a scale of micrometers. This scale separation can pose main computational drawback often preventing results to be quantitative. This problem can be overcome by using adaptive meshing as the variations of the phase field and diffusion fields are localized over the interfacial region. This adaptive grid would follow the migration of the phase boundary and give high accuracy. Adaptive Finite Element method in combination with the phase field model has been used to simulate diffusional phase transformation in Zr-Nb alloy system.

3.3 References:

3.1 C. Ganguly, Advances in Zirconium Technology for Nuclear Reactor Application, Proceedings of the Symposium Zirconium-2002, 11-13 September, Bhabha Atomic Research Centre, Mumbai.

3.2 Waterside corrosion of zirconium alloys in nuclear power plants, IAEA TECHDOC- 996, 124-169.

3.3 Perkins R.A., Shih-Hsiung Shann, Proc., Application of Accelerated Corrosion Tests to Service Life Prediction of Materials, ASTM-STP-1194(1994) 239.

3.4 Dennis Lawrenz, John Hawkinswww.leco.com/resources/application.../O-N%20209-141-003.pdf.

3.5 Martin J. Hollamby, Phys. Chem.Chem.Phys, 2013, 15, 10566.

3.6 S. Mazumder, D. Sen, T. Sarvanan, P.R. Vijayraghavan, J. Neutron Res. 9 (2001) 39.

3.7 J. A. Lake, Acta Cryst. (1967). 23, 191-194.

3.8 Aschroft, N. W.; Lekner, J. Phys. Re . 1966, 145,83 90.

3.9 C. D. Wagner, W. M. Riggs, L.E.Davis, J. F. Moulder, G. E. Muilenberg, Handbook of X-ray photo electron spectroscopy, Perkin Elmer Corporation.

3.10 http://en.wikipedia.org/wiki/X-ray_photoelectron_spectroscopy.

3.11Jianlong Lin , Hualong Li, Cheol Nam, Jerzy A. Szpunar, J. Nucl. Mater., 334 (2004) 200–206.

3.12 P. Mukherjee, P.M.G. Nambissan, P. Barat, Pintu Sen, S. K. Bandyopadhyay, J. K. Chakravartty, S. L. Wadekar, S. Banerjee, S. K. Chattopadhyay, S. K. Chatterjee, M.K.Mitra, J. Nucl. Mater., (2001) 341-344.

Chapter 4

Development of PFM to predict microstructure evolution in Zr-Nb alloy during diffusional phase transformation.

This chapter gives a detailed description of development of phase field model for Zr-Nb alloys using Gibbs free energy functional and diffusional mobility to predict evolution of Allotriomorph α and Widmanstatten lath α through phase field concept.

4.1 Introduction

Zirconium-Niobium (Zr-Nb) alloys exhibit a wide variety of phase transformations. Depending upon the diffusion length of atomic species, different types of diffusional transformation are encountered in Zr based alloys which lead to generation of wide range of morphological products [4.1, 4.2, 4.3, 4.4]. In Zr-Nb alloys, Nb acts as a β stabilizer. At higher temperatures complete solubility exists between Zr and Nb in the β phase. At 620° C (893 K)
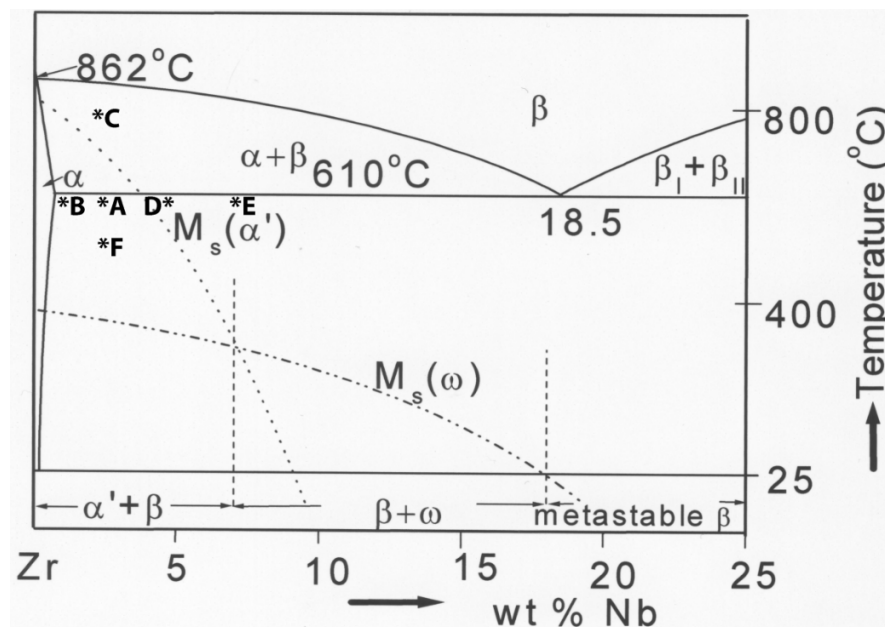
Fig. 4. 1: Zr-Nb phase diagram. The points A, B, D, E, F specify the operating points i.e. the alloys with corresponding simulating temperature for Widmanstatten plates and C for planar growth respectively.

(fig. 4.1), the β -Zr containing 18.5 wt.% Nb (BCC) transforms into equilibrium products α-Zr (HCP) and β-Nb (BCC).

During fast cooling β -Zr undergoes martensitic transformation up to about 8.0 at. % Nb [4.5, 4.6, 4.7]. During intermediate or slow cooling rate, mainly two distinct morphologies of α -Zr phase are found. One is allotriomorph α (fig. 4.2) formed during slow cooling or at lower undercooling. Another one is lath shaped product (fig. 4.2 and fig. 4.3a, b, c) called Widmanstatten plate [4.2].
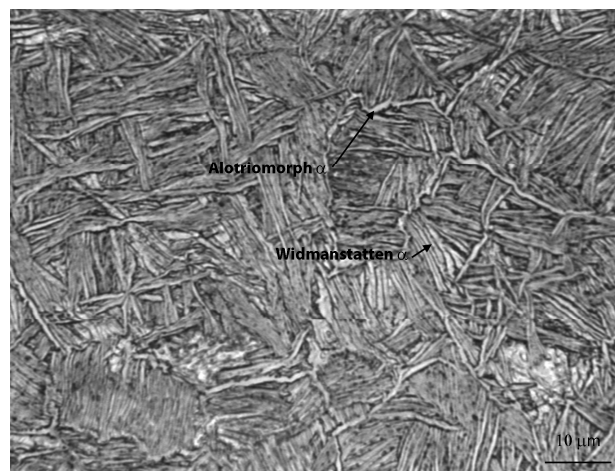
Fig. 4. 2 Typical grain boundary α Allotrimorph observed surrounding the prior β grain along with lath shaped product formed in Zr-Nb alloy during cooling from β phase [4. 62].
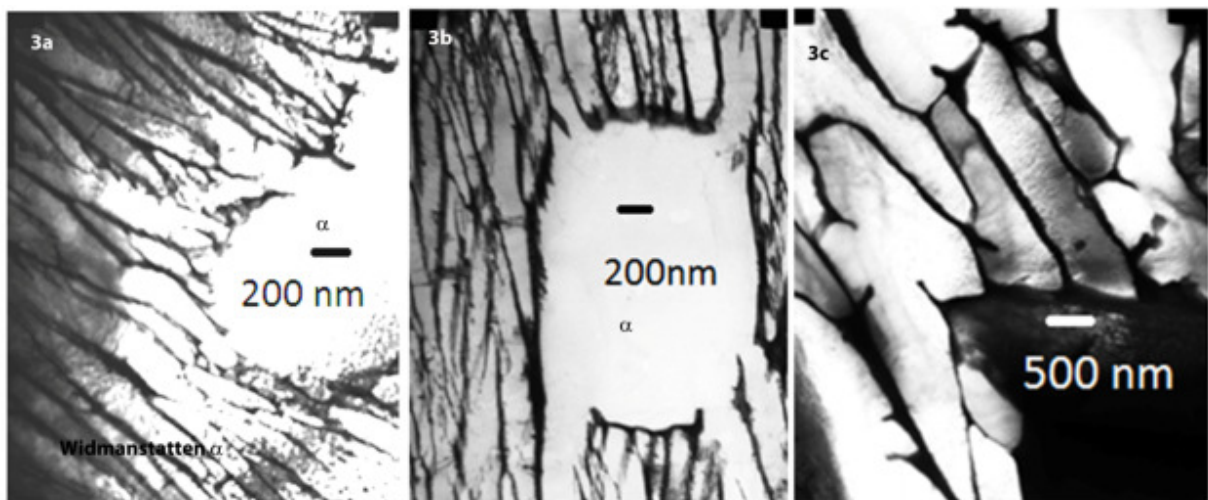
Fig. 4. 3 Typical Widmanstatten lath found in Zr-2.5 Nb alloy during gas quenching from $\alpha + \beta$ phase [4. 63].

This plate morphology is formed when the dilute Zr-2.5 Nb alloy is step quenched from β -phase and heat treated isothermally at 550°C (823 K) or during intermediate cooling rate [4.6]. The α zirconium phase nucleating in beta phase always follows the Burger orientation relationship ((0001) hcp ∥ (011) bcc, (1$\bar{1}$00) hcp ∥ (2$\bar{1}\bar{1}$) bcc and [11$\bar{2}$0] hcp ∥ [11$\bar{1}$] bcc) irrespective of whether the transformation is diffusional or martensitic [4.1, 4.7]. This orientation relationship is responsible for formation of very low energy α/β interface in certain orientations. In Zr-2.5Nb alloys α/β interfaces consist of closely spaced (a) type dislocations [4.7]. The interface structure of β phase in the α matrix of Zr-2.5Nb alloy has been studied by W. Z. Zhang etal. [4.8]. The misfit at the habit plane is accommodated by a single set of dislocations lying along the invariant line. At other side, the facet planes consist of two or three different sets of dislocations. These dislocations are required to relieve the misfit strain.

Several researchers [4.9, 4.10] have studied pattern formation to design microstructures during crystal growth in a dynamical system. Widmanstatten plate growth is a type of pattern formation problem during solid-solid phase transformation in both interstitial and substitutional metallic alloys. The diffusion controlled growth of unstable planar surface generates pattern due to interplay among surface tension, bulk volume free energy and kinetic phenomena like diffusion. The investigations about Widmanstatten plate formation will remain incomplete if the nucleation event along with growth process is not considered. Although many researchers find a close relationship with the Mullin –Sekerka (M-S) type instability theory [4.11, 4.12, 4.13], the second school of thought is the strain induced sympathetic nucleation theory [4.14, 4.15]. Experimental techniques like Laser Confocal Microscopy [4.16] had been used to corroborate sympathetic nucleation theory of plate growth. While in sympathetic nucleation theory strain plays a major role, for phase transformations which are purely diffusion controlled in nature, the M-S instability theory can be used in the nucleation stage to perturb the phase boundary before progressing into the growth stage ignoring the strain energy contribution.

Over the last decade, phase-field method (PFM) has emerged as a powerful computational tool for modeling and predicting the meso-scale morphological and microstructure evolution during solid-liquid and solid-solid phase transformations [4.17]. In PFM for predicting microstructure evolution at real length and time scales requires that the fundamental model inputs be linked to thermodynamic and mobility databases. Extensive work has been done by Wang et al. [4.18] in

developing and integrating thermodynamic modeling, mobility data base and phase field simulation to predict microstructural evolution in Ti base alloys mainly in Ti -6Al-4V alloy. Loginova et al. [4.19] has studied Widmanstatten ferrite plate formation in binary Fe-C interstitial solid solution system using a highly anisotropic interfacial energy. To circumvent the ill-posed phase field equation due to highly anisotropic nature of interfacial energy, regularization method was adopted in the non-differential domain of interfacial energy.

Limited work [4.20, 4.21] has been done in modeling of microstructural evolution in Zr-Nb alloys during various thermo-mechanical processing. Phase field approach has been formulated for predicting microstructural evolution during athermal ω-phase transformation [4.22] in Zr-Nb alloy system. In the starting of the chapter, phase field model [4.23] had been formulated for β Zr (BCC) →α Zr (HCP) phase transformation. Morphological evolution had been studied for Zr-2.5Nb pressure tube material using pre-nucleated protrusion. Later the formation of plate morphology during β Zr (BCC) →α Zr (HCP) phase transformation has been modeled using stochastic nucleation event and followed by deterministic growth using highly anisotropic interfacial energy [4.19]. The nucleation phenomenon has been incorporated both implicitly and explicitly [4. 24 - 4.31]. The time dependent evolution of the spatially dependent field variables is studied by solving the Allen-Cahn equation [4.32] for non conserved order parameter and Cahn–Hilliard equation [4.33] for conserved concentration parameter. Using Gibbs free energy functional and diffusional mobility, different morphology of α Zr phase evolution has been simulated in different Zr-Nb binary alloys. Based on this model the growth rate and morphology selection have been investigated by varying the supersaturation, i.e., temperature and Nb content in different Zr-Nb alloys.

4.2   Phase Field model formulation

Phase Field model (PFM) is based on diffuse interface description developed by Vander Walls [4.34] and subsequently by Cahn - Hilliard [4.33] and Cahn - Allen [4.32]. The nature of the interface in PFM is different from the conventional approaches for microstructure modeling which take mathematically sharp interface. PFM applies a continuum field, *i.e.* a phase field characterized by a set of conserved and non-conserved phase field variables. Conserved variables like concentration or mole fraction (c) satisfy the mass conservation condition. The non-conserved variables like order parameter (φ) contains information of local crystal structure or

orientation of different domains.These order parameters in phase field models may or may not have macroscopic physical interpretations.

In the solid phase transformation, the non conservative continuously varying phase-field variable (φ) can be 0 in one phase and 1 in other phase. The spatial range over which φ changes from 0 to 1 is the width of the interface. This concept of a continuous non-conserved phase-field for distinguishing two coexisting phases was introduced by Langer [4.35]. The single-phase-field representation in combination with a composition field has been applied to study growth of Widmanstatten side plate in Zr-Nb substitutional system.

4.3   Free Energy Functional

The formation of α-Zr plate from β -Zr occurs by nucleation-growth mechanism [4.1] which is a first order transformation. The thermodynamic basis of model is depicted through free energy functional [4.36]

$$G = \int_v \left(\frac{g(\varphi, c, T)}{Vm} + \frac{\varepsilon_c^2}{2} |\nabla c|^2 + \frac{\varepsilon_\varphi^2}{2} |\nabla \varphi|^2 \right) dv \quad - - - - 4.1)$$

with $g(\varphi, c, T)$, the homogeneous free energy density at a given temperature (T K) is a function of phase field variables, *viz.,* order parameter φ (non conservative) and concentration c (conservative). Concentration (c) is expressed in terms of mole fraction of Nb. The molar volume (Vm) is assumed to be constant for both the phases and ε_φ and ε_c is the gradient energy coefficient for order parameter and concentration inhomogeneities respectively. Temperature (T K) is taken as constant due to rapid heat conduction.

This free energy density, $g(\varphi, c, T)$, associated with bcc to hcp phase transformation in Zr-Nb system can be constructed according to the symmetry changes from Landau free energy functional [4.37]. But getting a Landau free energy consistent with experimental equilibrium free energy data as well as the temperature and composition dependent parameters in the Landau free energy expansion is a tedious task.

Alternate approach, developed by Wang et al. [4.38], is using a phenomenological order parameter that considers different values for different phases. The local free energy is then obtained using the equilibrium free energy of individual phases. In this approach, the

homogeneous free energy density consists of an interpolation function $fp(c, \varphi, T)$ and a double-well function $k(\varphi)$.

$$g(c, \varphi, T) = fp(c, \varphi, T) + k(\varphi) - - - - 4.2)$$

The interpolation function fp combines the free energy expressions of the coexisting phases $G\alpha(c, \varphi, T)$ and $G\beta(c, \varphi, T)$ into one free energy expression, which is a function of the phase field variables c and φ, using a weight function p(φ):

$$fp(c, \varphi, T) = \big(1 - p(\varphi)\big)G\alpha(c, T) + p(\varphi)G\beta(c, T) - - - - - 4.3)$$

In this case φ is set to 0 in hexagonal closed packed (HCP) α phase and 1 in body centered cubic (BCC) β phase. c is the mole fraction of Nb. The functions $G\alpha(c, T)$ and $G\beta(c, T)$ are the homogeneous free energy expressions for the composition and temperature dependence of the α phase and the β phase. In our simulations these were taken from a paper titled "Thermodynamic analysis of stable phases in Zr-Nb system and calculation of phase diagram" by Armando Fernandez Guillermet [4.39] and SGTE database for pure element by AT Dinsdale [4.40].The complete expressions are given in Appendix A.

$p(\varphi)$ is a smooth function that equals 1 for $\varphi = 1$ and 0 for $\varphi = 0$ and has local extrema in between $\varphi = 0$ and $\varphi = 1$. Mostly, the following function [4.40]
$p(\varphi) = \varphi^3(10 - 15\varphi + 6\varphi^2)$ is used, for which p'(φ) $= 30q(\varphi)$. And is shown in fig. 4.4.
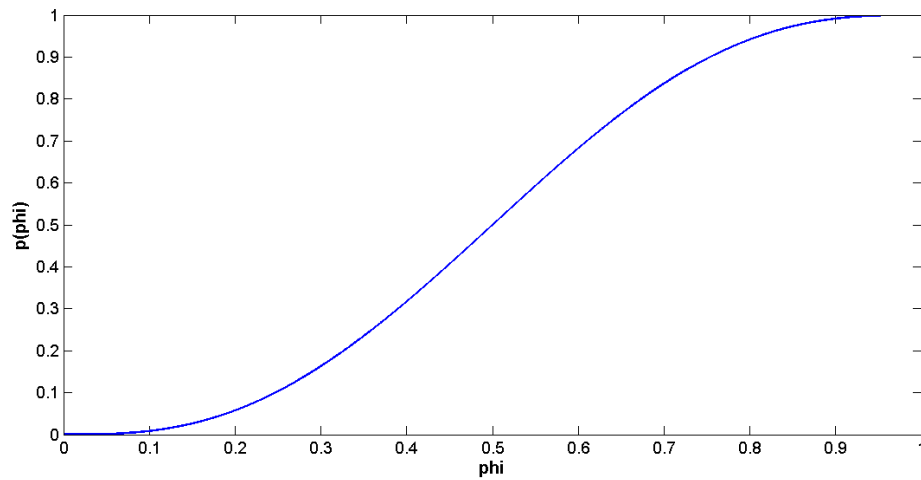
Fig. 4. 4 Variation of the function $p(\varphi)$ w.r.t. φ is plotted.

The k(φ) in equation 4. 2 can be represented by

$$k(\varphi) = w * q(\varphi) = w * (\varphi^2 - 2\varphi^3 + \varphi^4) - - - - 4.4)$$

Where w is the kinetic barrier between the two minima in the double well free energy density representation and can be adjusted to fit the desired interfacial energy.

And $q(\varphi) = (\varphi^2 - 2\varphi^3 + \varphi^4)$ and is shown in fig.4.5. At φ=0 and 1 q(φ)=0 and it has maximum value at φ=0.5.
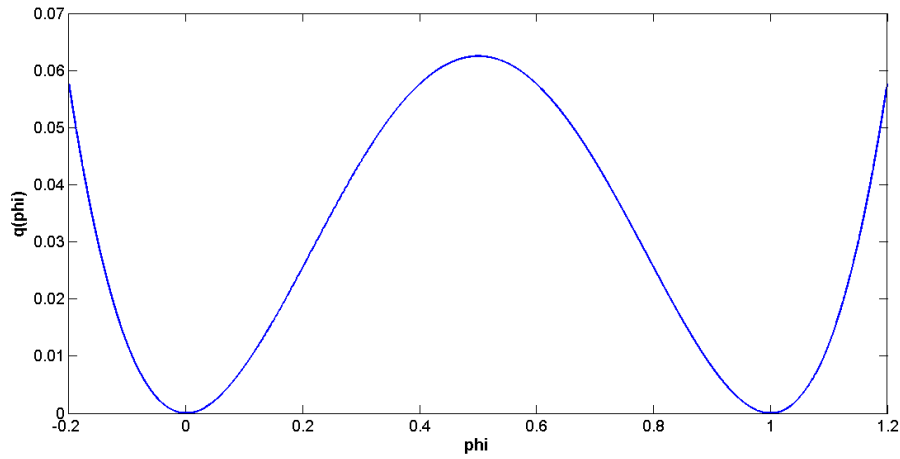
Fig.4. 5 Variation of the function $q(\varphi)$ w.r.t. φ is plotted.

The interface thickness is a balance between two opposing effects. The interface tends to be sharp in order to minimize the volume of material where φ is varying in between 0 and 1 and q(φ) is large. While, the interface tends to be diffuse to reduce the energy associated with the gradient of φ as described by ε_φ in Eqn. 4. 4. For pure material interface thickness (δ) is related with (ε_φ) and w by the expression, $\delta = \frac{\varepsilon_\varphi}{\sqrt{2w}}$[4.41] and interfacial energy (σ) is related to them as $\sigma = \varepsilon_\varphi\sqrt{\frac{w}{18}}$ [4.41]. Combining the above two expression, w becomes$\frac{3*\sigma}{\delta}$. For alloys apart from ε_φ, the thickness of diffuse interface is also depends on the properties of phase diagram. Selzer *et al.* [4.36] showed that the thickness of interface in phase field solution remains almost unchanged with $\varepsilon_\varphi$when there is large difference in equilibrium concentration of the phases. When the difference in equilibrium concentration of the phases is not significant, thickness of diffuse interface is directly related to ε_φ . In the present model, for simplification ε_φ and w were assumed as independent of temperature and composition and $\varepsilon_c = 0$. In case of spinoidal

decomposition $\varepsilon_c \neq 0$ but for isobar-thermal $\beta(b.c.c\ Zr) \rightarrow \alpha(h.c.p\ Zr)$ transformation ε_c can be assigned to zero as this will not affect the kinetics of Widmanstatten plate formation significantly.

4.4 Evolution Equations

The evolution of non conserved and conserved phase field variables in a phase-field model can be obtained by solving the Allen-Cahn equation and the Cahn-Hilliard diffusion equation taking the above mentioned total free energy (G) of the microstructure.

$$\dot{\varphi} = -M_\phi \frac{\delta G}{\delta \varphi} \quad ----4.5)$$

$$\dot{c} = \nabla . L'' \nabla \left(\frac{\delta G}{\delta c}\right) -----4.6)$$

Where Mφ is the order parameter mobility and can be directly related to interface mobility (M) in sharp interface approach as $M_\varphi = 0.0235 M/\delta$ [4.42] which ensure diffusion controlled process and L˝ is related to the diffusional mobility of Nb atom (M_{Nb}) through $L'' = c(1-c)M_{Nb}$ [4.43, 4.44] . As diffusivity of Nb in h.c.p and b.c.c phase is different [4.45-4.50], M_{Nb} can be represented by phase field parameter, $M_{Nb} = (M_{Nb}^{hcp})^{1-p(\varphi)} M_{Nb}^{bcc\ p(\varphi)}$, where $M_{Nb}^{hcp} = \frac{D_{Nb}^{hcp}}{RT}$ and $M_{Nb}^{bcc} = \frac{D_{Nb}^{bcc}}{RT}$.

To get interfacial mobility, Turnbull's model [4.47] for the mobility of incoherent grain boundaries in a single phase material is considered. This model assumes that the atoms are transferred individually across the interface by a process related to diffusion and it yields the following type of relationship, $M = \frac{\delta_0 D_{eff} V_m}{b^2 RT}$, where δ_0 is the width of the incoherent boundary and b is the distance between atoms. D $_{eff}$ is the effective diffusivity of the atoms in this process . In this case, it is taken as $D_{eff} = (D_{Nb}^{hcp^{0.5}} + D_{Nb}^{bcc^{0.5}})^2$. D_{Nb}^{hcp} and D_{Nb}^{bcc} are the lattice diffusivity of α and β phase [4.46,4.50] respectively and are given in table 4.1.

4.5 Anisotropy in Interfacial Energy

Interfacial energy is the free energy associated with the compositional and/or structural in-homogeneities presence at interfaces. Since in a phase-field method the interface is diffuse in

nature, the proper incorporation of interfacial energy is of utmost important. The extent of anisotropy in interfacial energy determines the morphology of the phase [4.51].

The β → α transformation in Zr based alloys follows the Burgers Orientation relation almost exactly, irrespective of whether the transformation is diffusional or martensitic [4.1], *i.e.*, $(0001)_{hcp}$ ‖ $(011)_{bcc}$, $(1\bar{1}00)_{hcp}$ ‖ $(2\bar{1}\bar{1})_{bcc}$ and $[11\bar{2}0]_\alpha$ ‖ $[11\bar{1}]_\beta$. This orientation relationship results in a coherent or semi-coherent interface of very low energy. α phase nucleated at β phase grow along specific crystallographic direction which depends on the relative orientation of the crystalline lattices of the two adjacent grains and also on the orientation of the phase interface. As β→ α transformation in Zr based alloys follows the Burgers Orientation relation, it has been assumed that in the simulation thin β and α plates are following the same orientation relationship. In the case of Widmanstatten plates, the broad sides of the parallel plates are coherent in nature with minimum interfacial energy whereas the tip of the plate is incoherent in nature with highest interfacial energy. This anisotropy in interfacial energy in solid state transformation can be introduced by using a function, $\eta=(\theta)$ where $\theta = \arctan(\frac{\varphi_y}{\varphi_x})$ which is nearly equal to the angle between interface normal and x axis. The thickness of the interface also varies due anisotropy. Thickness of coherent interface is much smaller than incoherent interface. It has been proposed by G. B. McFadden *et al.* [4.52], that the diffuse interface thickness (δ) and the interfacial energy (σ) follow the same anisotropy. The relationship of interfacial energy and interface thickness with orientation can be written as follows.

$$\sigma = \sigma_0 * \eta(\theta) \; ; \quad \delta = \delta_0 * \eta(\theta) \; ;$$

where σ_o and δ_o are the maximum interfacial energy and maximum interface width which are the input parameters of the model, $\sigma_o = 0.3$ J/m^2 (typical value for incoherent phase interfaces) and $\delta_o = 5$ nm . Using the above relationships ε_φ becomes $\varepsilon_\varphi^2 = 6 * \sigma_0 * \delta_0 * \eta(\theta)^2$.

Anisotropy in interfacial energy and thickness is introduced by the following cosine function of θ, *i.e.*, $\eta = \frac{(1+\gamma|\cos(\theta-\theta_0)|)}{(1+\gamma)}$ [4.19] . Where θ_0 is the angle between the interfacial plane having good crystallographic fit and x axis. γ is the extent of anisotropy. This function would give maximum interfacial energy (σ$_0$) when θ=θ_0 and minimum interfacial energy (σ$_0$ / (1+ γ)) when $\theta - \theta_0 = \pi/2$. So extent of γ controls the interfacial energy of coherent interface. i.e. γ +

1 becomes ratio of interfacial energy of incoherent interface (maximum interfacial Energy) to the coherent interface having minimum interfacial energy. Very high value of γ ensures very low interfacial energy of coherent interface which emphasizes perfect match in between α and β phases. During growth, in our model we have considered to have a good crystallographic fit along an interfacial plane having the angle $\theta_0 = 0^0$ with the x axis. If a plate with coherent sides develops it would grow with that angle (0^0) toward the x axis.

To assure Gibbs Thomson remains positive anisotropy function is regularized using a smooth function near $(\theta - \theta_0) = n*\pi/2$ as introduced by Loginova $et\ al.$ [4.19].

For anisotropic interface

$$\frac{\delta G}{\delta \varphi} = -\varepsilon_\varphi{}^2 \nabla^2 \varphi + \frac{\partial}{\partial x}\left(\varepsilon \varepsilon_\theta' \frac{\partial \varphi}{\partial y}\right) - \frac{\partial}{\partial y}\left(\varepsilon \varepsilon_\theta' \frac{\partial \varphi}{\partial x}\right) + \frac{\partial g(\varphi, c, T)}{\partial \varphi} \quad ----4.7)$$

And using

$$\frac{\partial g}{\partial \varphi} = p'(\varphi)\frac{G\beta - G\alpha}{V_m} + q'(\varphi)\frac{w}{V_m} ------4.8)$$

Thus the evolution equation 5 becomes

$$\frac{\partial \varphi}{\partial t} = M_\varphi\left[\varepsilon_\varphi{}^2 \nabla^2 \varphi - \frac{\partial}{\partial x}\left(\varepsilon \varepsilon_\theta' \frac{\partial \varphi}{\partial y}\right) + \frac{\partial}{\partial y}\left(\varepsilon \varepsilon_\theta' \frac{\partial \varphi}{\partial x}\right) + p'(\varphi)\frac{G\alpha - G\beta}{V_m} - q'(\varphi)\frac{w}{V_m}\right] ----4.9)$$

Similarly

$$\frac{\delta G}{\delta c} = \frac{\partial^2 g}{\partial c\, \partial \varphi} \nabla \varphi + \frac{\delta^2 g}{\delta^2 c} \nabla c \quad ----4.10)$$

And using the expression of $L^{"}$ and M_{Nb}, the evolution equation for conservative phase field variable becomes

$$\frac{\partial c}{\partial t} = \nabla.[c(1-c)\left(M_{Nb}^{hcp}\right)^{1-p(\varphi)}\left(M_{Nb}^{bcc}\right)^{p(\varphi)}\left(\frac{\partial^2 g}{\partial c\, \partial \varphi}\nabla \varphi + \frac{\delta^2 g}{\delta^2 c}\nabla c\right)] ----4.11)$$

4.6 Non-dimensionalization & Finite element method

For convenience equations 4.9 and 4.11 were non dimensionalized using reference length

$$l = .9\delta_0 \text{ and diffusion time } \tau = \frac{t * RT * M_{Nb}^{\alpha}}{l^2} .$$

The other phase field parameters become $\widetilde{M}_{\varphi} = M_{\varphi} * \dfrac{l^2}{M_{Nb}^{\alpha} V_m}, \tilde{\varepsilon}_{\phi} = \dfrac{\varepsilon}{l * \sqrt{\dfrac{R*T}{Vm}}} ,$

$\tilde{\varepsilon}_{\theta}' = \dfrac{\varepsilon_{\theta}'}{l * \sqrt{\dfrac{R*T}{Vm}}} \widetilde{G} = \dfrac{G}{RT}, \widetilde{w} = \dfrac{w}{RT}$, respectively.

The dimensionless forms of the equations are given below.

$$\frac{\partial \varphi}{\partial \tau} = \widetilde{M}_{\phi} \left[\tilde{\varepsilon}_{\varphi}^2 \widetilde{\nabla}^2 \varphi - \frac{\partial}{\partial \tilde{x}} \left(\tilde{\varepsilon} \tilde{\varepsilon}_{\theta}' \frac{\partial \varphi}{\partial \tilde{y}} \right) + \frac{\partial}{\partial \tilde{y}} \left(\tilde{\varepsilon} \tilde{\varepsilon}_{\theta}' \frac{\partial \varphi}{\partial \tilde{x}} \right) \right] + \widetilde{M}_{\varphi} \left[p'(\varphi) \frac{\widetilde{G}\alpha - \widetilde{G}\beta}{V_m} - q'(\varphi) \frac{\widetilde{w}}{V_m} \right] - -$$

$$- - - - - - - - - - 4.12)$$

$$\frac{\partial c}{\partial \tau} = \widetilde{\nabla}. \left[c(1-c) \left(\frac{M_{Nb}^{bcc}}{M_{Nb}^{\alpha}} \right)^{p(\varphi)} \left\{ \frac{\partial^2 \tilde{g}}{\partial c^2} \, \widetilde{\nabla} c + \frac{\partial^2 \tilde{g}}{\partial c \, \partial \phi} \widetilde{\nabla} \varphi \right\} \right] - - - - - - - 4.13)$$

These two coupled PDEs are solved by finite element method using implicit time stepping and adaptive unstructured grid. The phase field equation shows very stiff gradient at the interface region and with realistic interface thickness of few nanometers the tasks of solving it becomes challenging. Due to requirement of huge computational power, we have taken incoherent interface thickness δ_0 as 5 nm and in non dimensional space the interface regions (fig. 4.6) have been discretized using five grid points and the rest of the region with large triangles optimizing the computational load and accuracy of the solution. Zero flux Neuman boundary conditions were applied.
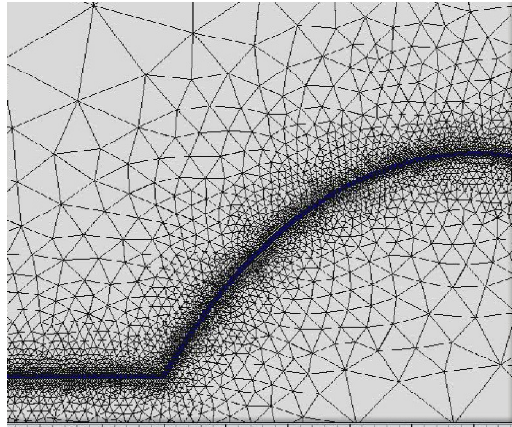
Fig. 4. 6 Adaptive meshing where the interface regions have been discretized using five grid points and the rest of the region with large triangles.

4.7 Initial Microstructure

The Zr rich portion of Zr-Nb equilibrium phase diagram is given in fig. 4.1 [4.39]. The simulations were carried out at different temperatures and for different Nb contents in Zr-Nb alloys. Initial state was homogeneous β with a very thin layer of α Zr. In all simulations the composition of the thin layer of *α* Zr was taken from the equilibrium phase diagram. In some simulations, the initial protrusion of α was made on the planar surface had amplitude 6l and length 15l. In other simulations phase boundary was perturbed using explicit nucleation algorithm. And all other simulations implicit nucleation method has been incorporated.

4.8 Phase-field simulations of growth of single protrusion of grain-boundary α

Phase-field simulations of growth of single protrusion of pre-nucleated α in β-Zr phase of Zr-2.5Nb alloy were performed at different temperatures. These temperatures were indicated in phase diagram of Zr-Nb (fig. 4.1). The A and F specify the simulations temperatures for Widmanstatten plates formation and C for planar growth respectively. Initial state was homogeneous β (with 0.025 Nb) with a very thin layer of α having a Nb concentration of 0.007 (mole fraction) for A. The initial protrusion of α on the planar surface had amplitude 6*l* and length 15*l*. In our simulations, we observed that Widmanstatten plate grows from the initial grain boundary protrusion of α, in Zr-2.5Nb alloy in the temperature range of 800 - 890K when interfacial energy of coherent interface is 1/21th interfacial energy of incoherent interface,

corresponding to γ=20. Otherwise initial perturbation decays and planar surface of grain-boundary allotrimorphs grows. So higher value of γ is responsible for growth of Widmanstatten plate in this temperature range. This is similar to the result obtained for the growth of grain boundary ferrite [4.19] in Fe-C system.

With increase in γ from 20 to 120, the lengthening rate (increase of length per unit time) of the single Widmanstatten side plate (after omitting few initial steps) increases (fig. 4.7) whereas the widening rate (increase in width per unit time measured after few initial steps) of the plate reduces (fig. 4.8). With further rise in γ, no further change in widening rate is observed. Higher values of γ lead to reduction of interfacial energy of two parallel coherent side and lengthening of these two side becomes more energetically favorable compare to widening of the plate and lead to formation of plate with high aspect ratio. To generate side plates with high aspect ratio, larger value of γ is required.
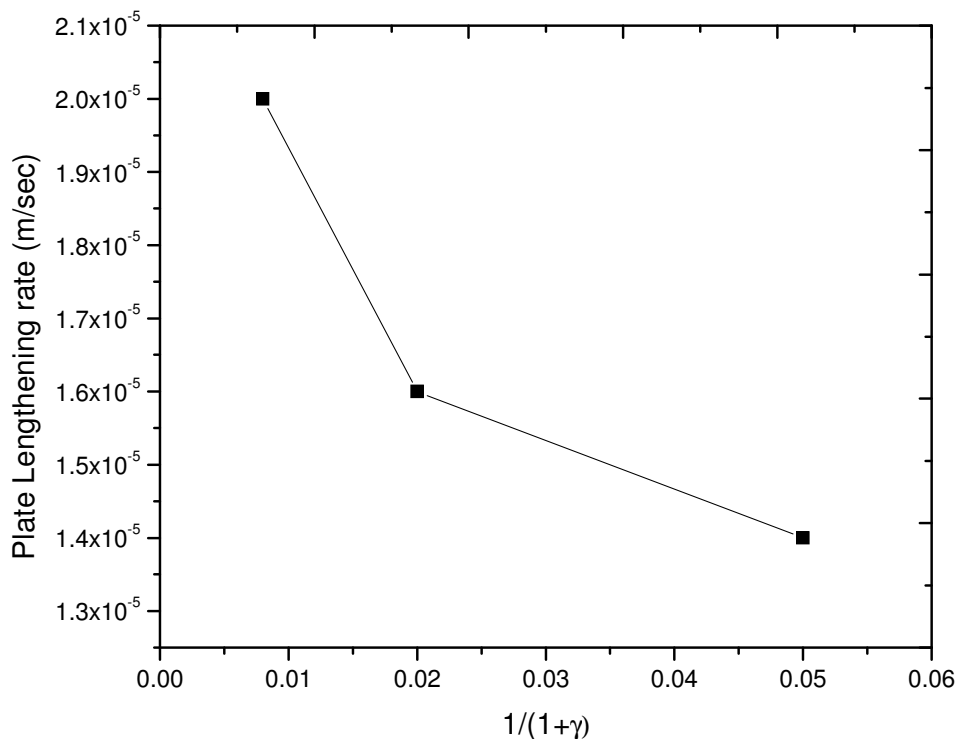
Fig. 4. 7. Effect of γ parameter on the side plate lengthening rate
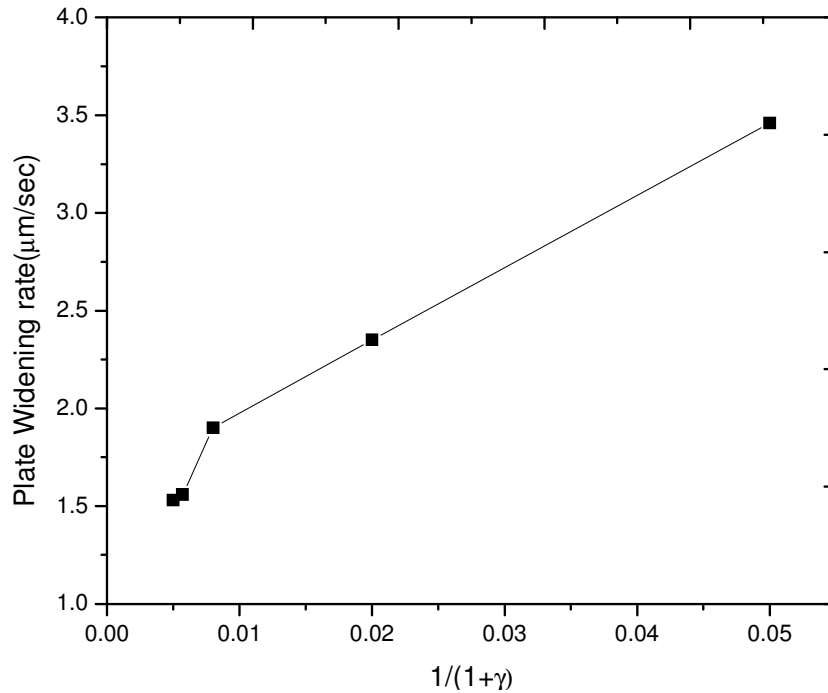
Fig. 4. 8 Effect of γ parameter on the side plate widening rate

From an interfacial energy stand point, it is always favorable for a second phase precipitate to be surrounded by low energy coherent or semi coherent interfaces. If the crystal structure of the second phase is different from parent one, getting common lattice plane is difficult. Nevertheless, there may be one plane that is identical in each crystal and with choosing correct orientation relationship a low energy coherent or semi coherent interface can form which must be bounded by high energy incoherent interfaces as usually no other plane of good matching present. From the γ plot of the interfacial energy, the Wulff theorem would predict the equilibrium shape to be a disc with a thickness/diameter ratio of γ_c/γ_i where γ_c and γ_i are the energies of the (semi) coherent and incoherent interfaces [4.53]. Deviation from equilibrium shape may be due to constraints imposed by the relative mobility of coherent/semi-coherent and incoherent interface as well as presence of misfit strain energy effects. In phase field model, this aspect can also be incorporated by making the mobility or relaxation parameters anisotropic.

It was also observed from the model that the lengthening rate of single protrusion from grain boundary α depends on the relative velocity of tip with respect to planar surface of pre-nucleated

α. The movement of the planar surface of pre-nucleated α is restricted due to accumulation of solute atoms in front of it. The movement of the tip of Widmanstatten plate depends on how fast the excess solute atoms diffuse away from the tip. And it goes through a maximum as the radius of curvature increases. This is due to the fact that a smaller tip radius allows the excess solute atoms to diffuse away from the tip more rapidly and it also increases surface to volume ratio which leads to increase in requirement of energy in creating the surface.

From the simulations, it was observed that the tip of the lath grows linearly after initial few steps. For $\gamma = 120$, $\delta_0 = 5$ nm, taking boundary as isoline of $\varphi = 0.5$ the tip velocity of Widmanstatten plate for Zr-2.5Nb alloy at 890 K is 20 μm/sec. The width of the single lath grows slowly compared to tip and its growth rate in initial stage is around 1.5 μm/sec for the same γ. The single lath formed from pre-nucleated α can be divided into 3 regions, *viz.*, tip region, parallel sides and planar region. The tip region is incoherent characterized by the linear growth velocity. Parallel broad sides are coherent in nature. The velocity of these two parallel interfaces is parabolic in nature. The planar region of pre-nucleated α is incoherent in nature, although having parabolic velocity profile.

When simulations were performed at higher temperature 1054K (point C in fig. 4. 1) with γ greater than 20, the initial protrusion of grain boundary α does not grow into β to form a lath morphology, but it decays and the entire planar α grows and leads to formation of allotrimorphs α. At higher temperature due to higher diffusivity of solute atoms, solute pile up at the interface is less and rejected solutes from α phase build up more or less uniformly ahead of the entire interface including tip region (fig. 4.9a). The tip of the protrusion could not attain higher relative velocity with respect to planar interface of pre-nucleated α and the protruded region decays and the growth of entire planar interface take place. This is a classical diffusion controlled phase transformation. As temperature is lowered, movement of the planar surface of pre nucleated α is restricted due to accumulation of solute in front of it and the lower mobility of solute atoms helps in maintaining the difference in solute concentration at tip and at the planar interface of pre nucleated α (fig. 4.9b) and favored the growth of single lath (point A in fig.4.1).
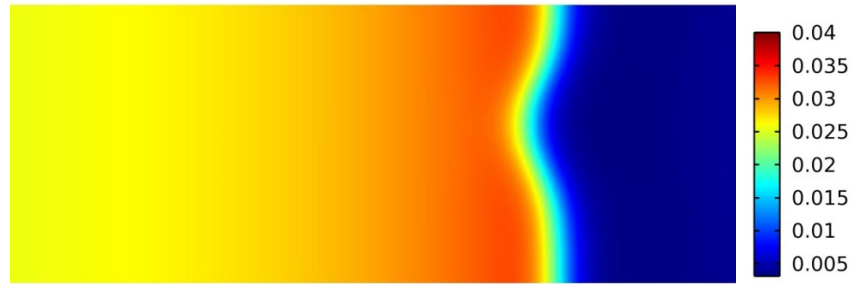
Fig. 4. 9a. More or less uniform distribution of concentration field (mole fraction of Nb) across the entire interface leads to planar growth. The domain size is 3.88 μm x 1.5 μm.
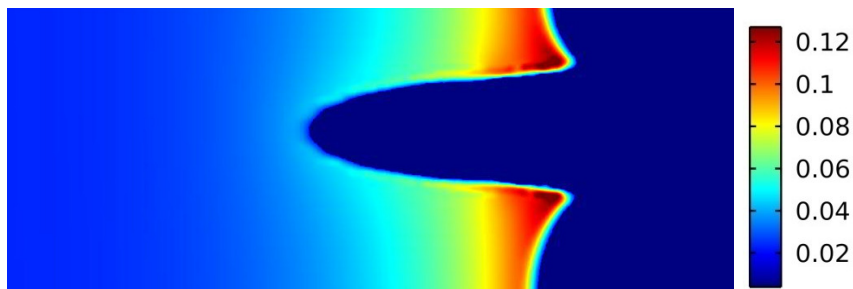
Fig. 4. 9b. Distribution of concentration field (mole fraction of Nb) during lath formation. Movement of planar interface is restricted due to solute accumulation and growth of tip leads to lath formation. The domain size is 3.88 μm x 1.5 μm.
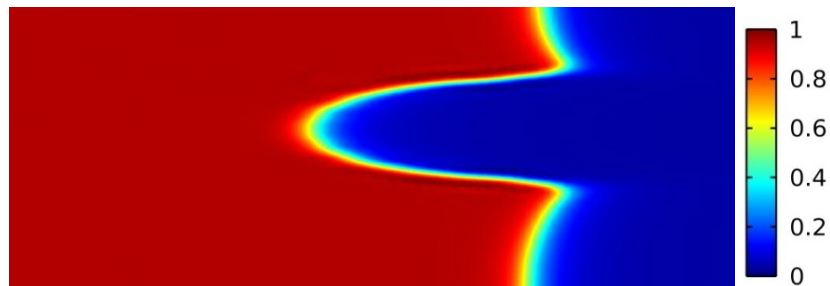
Fig. 4. 9c. Distribution of phase field variable (phi) during lath formation. The domain size is

3.88 μm x 1.5 μm.

The distribution of non conservative phase field variable phi (fig. 4.9c) deserved special attention. The large variation of interface width along the phase change boundary can be explained by the fact that interface thickness follows the same anisotropy function, as interfacial

energy mentioned by G. B. McFadden et al. [4.52]. The two parallel sides of a single lath are coherent in nature whereas the tip is incoherent and the coherent interface is much thinner than incoherent interface. For perfect coherent interface, thickness is zero.

4.9   Phase-field simulations of multiple protrusions in grain boundary α

In the case of multiple side plates formation from grain boundary α, interaction of diffusion field of neighbouring protrusions change the morphology of the growing phase. To simulate the formation of multiple plates from grain boundary α, protrusions of same size are generated at particular distance in the domain of 3.5 μm x 1.5 μm.

The evolution of multiple side plates from grain boundary α with initial Nb concentration c = 0.007 was simulated at 890 K (point A in fig.4.1) using γ=120. With increasing time it can be seen (fig. 4.10) that the inter lath location becomes rich in solute content as the diffusion field of neighboring laths overlapped and prevents further widening of each lath. Depending on the position of the neighboring lath the width of each lath achieves a constant thickness which is lower than when the simulation is performed with single lath. Further growth of the lath in width direction is restricted.
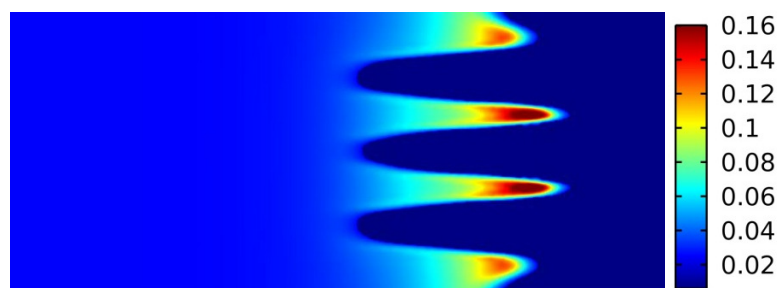
Fig. 4. 10. Distribution of concentration field (mole fraction of Nb) during growth of multiple lath from allotrimorph α at 890 K. The domain size is 3.5 μm x 1.5 μm.

When initial microstructure contains protrusions of various sizes (fig. 4.11a), it was observed that the initial protrusions which were wider grow faster than other ones (fig. 4.11b). Certain protrusions do not grow at all due to interaction of diffusion field of neighboring ones.
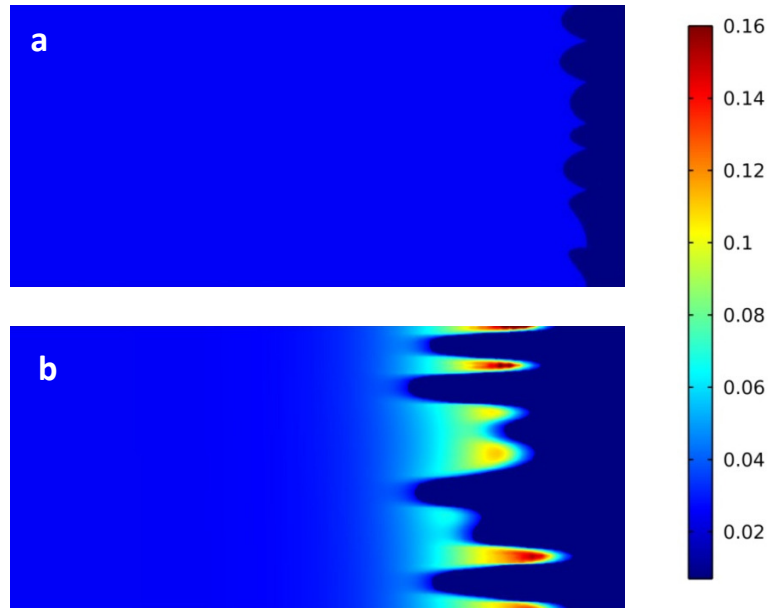
Fig. 4. 11(a) Distribution of concentration field (mole fraction of Nb) in initial microstructure having various size of protrusions of grain boundary α in a matrix of β
(b) Evolution of microstructure during growth of grain boundary α at 890 K.
The domain size is 3.28 μm x 1.5 μm.

Simulations were also performed with higher number density of protrusions in unit length of interface in a domain of 2.4 μm x1 μm. It was observed that as temperature is lowered (870 K) (point F in fig. 4.1), Widmanstatten plate width decreases. At lower temperature, diffusion of excess solute atom from two broad surface of Widmanstatten plate becomes difficult and higher numbers of protrusions in unit length of interface are able to grow independently without overlapping of diffusion field, giving lath with lower thickness (fig. 4.12a). At higher temperature (890 K) if closely spaced protrusions are present, then due to overlapping of diffusion field of neighbouring laths in front of the tip of in between protrusion, growth of in between protrusion may not take place at all leading to lesser number of coarser side plates (fig. 4.12b). After large numbers of simulations were performed at different temperature with various sizes of initial perturbation, it was observed that higher temperature leads to formation of coarser lath irrespective of position of neighbouring protrusions. So the lath width is very much sensitive to the temperature of transformation.
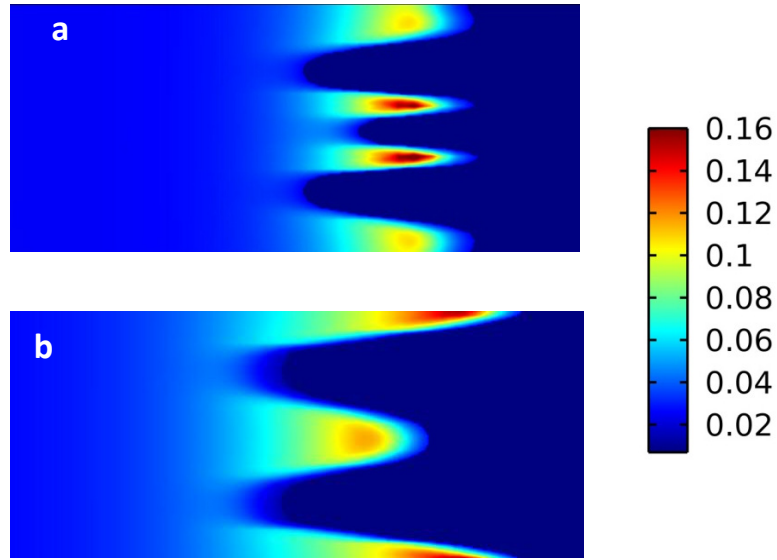
Fig. 4.12. Distribution of concentration field (mole fraction of Nb) during development of α phase of different morphology from the initial protrusions of grain-boundary α,
(a) lower temperature and (b) higher temperature lath morphology. The domain size is 2.4 μm x 1 μm.

Simulations were also performed for multiple nuclei at 1054 K (point C in fig. 4.1) with high value of γ (120). The starting microstructure consists of thin layer of domain of α with Nb content c= 0.004 in a matrix of β with Nb content c = 0.025. After simulations all the initial protrusions irrespective of their positions on grain boundary α, decay and planar interface moves in classical diffusion controlled process (fig. 4.13).
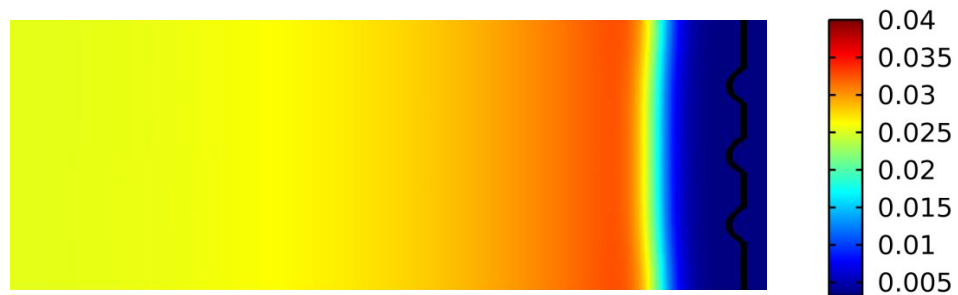
Fig. 4. 13 Distribution of concentration field (mole fraction of Nb) during development of allotrimorphs α from the protrusions of grain-boundary α at 1095 K, The black line denotes the initial position of the interface. The domain size is 2.80 μm x 1 μm.

4.10   Incorporation of nucleation event implicitly and explicitly

In order to account for nucleation in a meta-stable system, it is necessary to consider fluctuations in the local driving forces for the reaction to occur. This can be done by adding Langevin noise term $\xi_\varphi(r,t)$ [4.54] in eq. 4.5. $\xi_\varphi(r,t)$ is taken to be Gaussian distributed and its correlation properties should meet the requirement of the fluctuation - dissipation theorem.

$$< \xi_\varphi(r,t), \xi_\varphi(r',t') > = 2k_B T M_\varphi \delta(r-r')\delta(t-t') ----4.14)$$

Where k_B is the Boltzmann constant.

In our implicit nucleation and growth model, we incorporate the stochastic noise in a simple form to stimulate fluctuations at the planar interface of α-Zr. It is introduced by a function which incorporates fluctuations in the local driving forces using order parameter only.

$$\xi_\varphi = \alpha r_n 16\,k(\varphi)M_\varphi \left[p'(\varphi)\frac{G^\beta - G^\alpha}{V_m} + q'(\varphi)\frac{w}{V_m} \right] ----4.15)$$

Where r_n is a random number between 0 and 1, α in equation 4. 15, is the amplitude of fluctuation. However, coarse graining in mesoscale average out Langevin noises fluctuations of finer scale. As the process of nucleation happens in lower time and length scale, it is computationally difficult to simulate nucleation and growth process in a single simulation and at the outset it can be said that in mesoscale one can only simulate nucleation event (i.e. only equilbriated nucleus can be generated) not the physical process of nucleation. This is done by artificially allowing the noise terms (ξ_φ in eq. 4. 15) to have a large amplitude at the beginning of the simulations to form a suitable number of viable nuclei and subsequently turning off this noise term (ξ_φ) to observe the growth.

The explicit nucleation algorithm developed by Simmons et al. [4.55] is another way to allow nucleation event to occur depending on a criterion of nucleation rate derived from the classical theory. From the classical theory [4.56], the nucleation rate is

$$J^* = ZN\beta^* \exp\left(-\frac{\Delta G^*}{kT}\right)\exp\left(-\frac{\tau}{t}\right) -----4.16)$$

where Z is the non-equilibrium factor due to Zeldovich, N is the number of atoms in each phase field cell, β* is the frequency factor, ΔG^* is the activation free energy necessary to form a stable nucleus, k is Boltzmann's constant, τ is an incubation time, and t is time. For simplicity, the nucleation rate can be approximated using the classical nucleation theory without considering incubation.

In a 2- dimensional model ΔG^* is determined from following relationship [4.55] where γ is the interfacial energy (assumed as independent of temperature) and ΔG_a is the free energy change per unit area due to transformation.

$$\Delta G^* = \frac{\pi \gamma^2}{\Delta G_a} - - - - - 4.17)$$

The expectation value of number of nuclei that form in Δt time period is $J^* \times \Delta t$. The probability of a nucleation event occurring can be approximated by

$$P_n = 1 - \exp(-J^* \times \Delta t) - - - - 4.18)$$

Where $\exp(-J^* \times \Delta t)$ is the zero event probability of a Poisson distribution.

In our model nucleation event is explicitly incorporated by generating a uniform random variable at the α/β interface and comparing its value with P_n. If it is more than P_n, nuclei formed; otherwise it did not.

4.11   Implicit nucleation and subsequent growth

In all simulations with implicit source term, a thin layer of α-Zr with planar interface was put along with β-Zr (fig. 4.14a). The initial composition of α-Zr was taken from the equilibrium phase diagram.

4.11.1 Effect of temperature or undercooling

At 890 K and below, simulations with a stochastic source term shows that the planar interface in Zr-1Nb, Zr-2.5Nb, Zr-5Nb and Zr-7Nb becomes unstable and undulations generate in the α/β diffuse interface. These undulations are having favorable length scale grow and lead to the formation of stable protrusions (fig. 4.14b) shown for Zr-2.5Nb). The formation of the stable

protrusion causes solute to be rejected laterally and pile up of solute at the root of the protrusion occurs which restricts the further movement of the adjacent planar interface and growth of Widmanstatten lath is favored. The tip velocity of the lath depends on how fast solute atoms diffuse away from the interface. A smaller tip radius allows the excess solute atoms to diffuse away from the tip more rapidly but also increases surface to volume ratio which leads to energy penalty in creating the surface. At an optimum radius tip will grow with a maximum growth velocity. The earliest model for lengthening of a plate was given by Zener [4.57] and further modified by Hillert [4.58]. The essential feature of the model was the assumption of a constant tip radius which will give maximum growth rate (v) for a needle crystal [4.51] where

$$v = \frac{dr}{dt} = 2 * \frac{D}{r} * \frac{C_0 - C_\alpha}{C_\beta - C_\alpha} = 2D\frac{\Omega}{r} ----4.19)$$

Where C_α and C_β are the equilibrium composition at particular temperature and D is the diffusivity of the solute in the alloy having composition C_0. Ω is the dimensionless supersaturation, described by $\frac{C_0 - C_\alpha}{C_\beta - C_\alpha}$. After including the surface free energy effect [4.51], the above equation becomes

$$v = \frac{dr}{dt} = 2 * \frac{D}{r} * \frac{C_0(r) - C_\alpha(r)}{C_b(r) - C_\alpha(r)} = 2D\frac{\Omega}{r} --- 4.20)$$

For a plate-like crystal the equivalent expression given by Ivantsov [4.51] is:

$\Omega = \pi P^{.5} \exp(P) \operatorname{erf}(P^{.5}) --- 4.21)$, where P is the Peclet Numer $P = vr/2D$

Livingston and Cahn [4.59] observed that the tip radius was larger than that expected to give the maximum growth rate. As a result the growth rate was, of course, less than the expected maximum velocity.
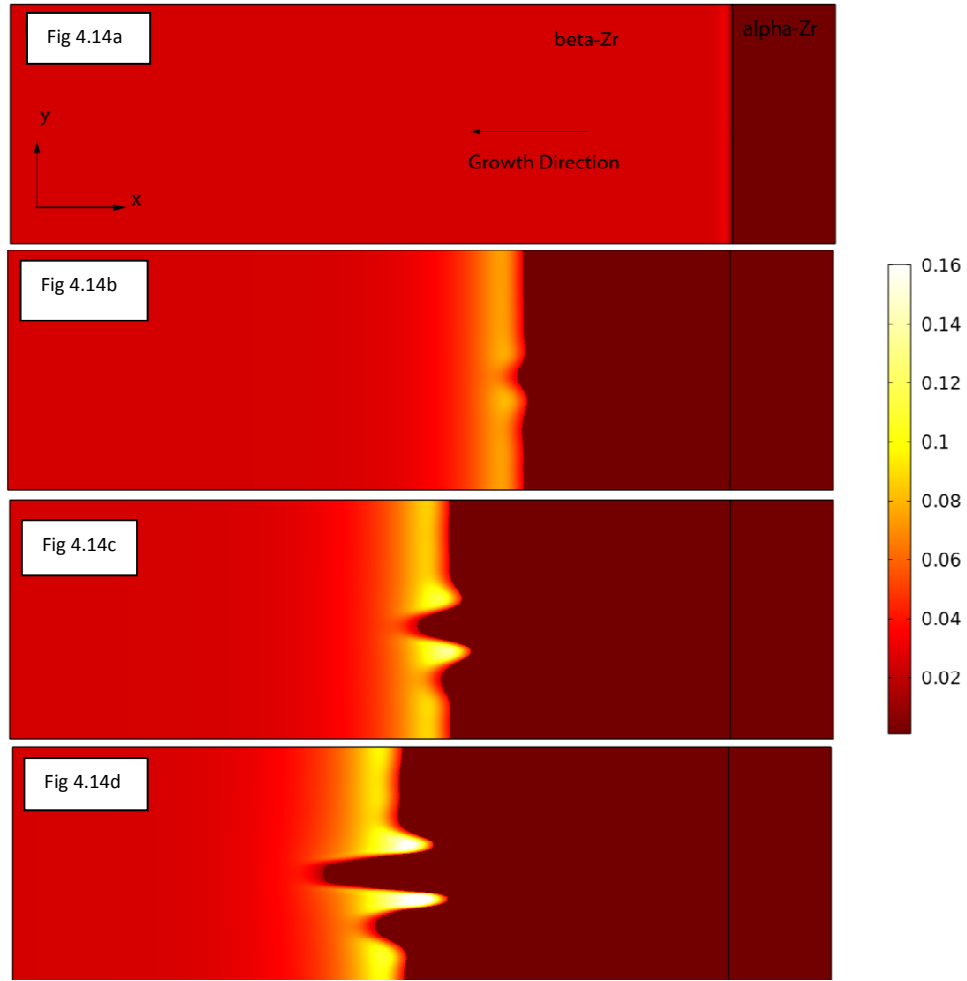
Fig. 4.14 Development of Widmanstatten lath morphology from planar front of allotriomorph α-Zr in Zr-2.5Nb alloy using implicit nucleation. Fig. 4.14a is the initial microstructure. The dark region in fig. 4.14a indicates pre-nucleated allotriomorph α-Zr ($\varphi = 0$). $\varphi = 1$ in the region of β-Zr. Fig. 4.14b, 4.14c, 4.14d are microstructure at different non-dimensional time steps (.035, .0531, .0663 respectively). Planar front becomes unstable at 890 K. The colour code depicts the mole fraction of Nb in Zr-Nb binary alloy. The domain size is 1.57 μm x 5.14 μm. Black line denotes initial position of the interface.

In this model there is no need to specify tip radius, or tip velocity. Depending upon operating temperature, composition of the alloy and degree of anisotropy, the tip of undulation attains a characteristic velocity. When the degree of anisotropy (γ) reduces below 20, lath morphology

does not develop at or below 890 K and a planar front is retained. $\gamma + 1$, which is the ratio of interfacial energy of incoherent interface to the coherent interface, plays a vital role in formation of Widmanstatten lath morphology. A higher value of γ favours the formation of lath morphology at higher undercooling. With increasing γ, the plate lengthening rate increases while the widening rate reduces as discussed earlier section. Beyond $\gamma = 120$ no further change in widening rate is observed for single lath growth. That is why in our simulations the γ value has been fixed at 120.

The diffusion field surrounding the initial protrusion (fig. 4.14c) triggers the formation of other neighbouring protrusions and subsequently the entire planar interface becomes unstable and the simultaneous growth of protrusions develops into parallel laths giving rise to side plate morphology (fig. 4.14d). With decreasing temperature simulations show the formation of α-Zr side plates with finer and finer spacing. As temperature is lowered the interaction of diffusion field of neighbouring protrusions is less which allows growth of a large number of protrusions leading to a finer lath width. With increasing undercooling the tip velocity increases (fig. 4.15).
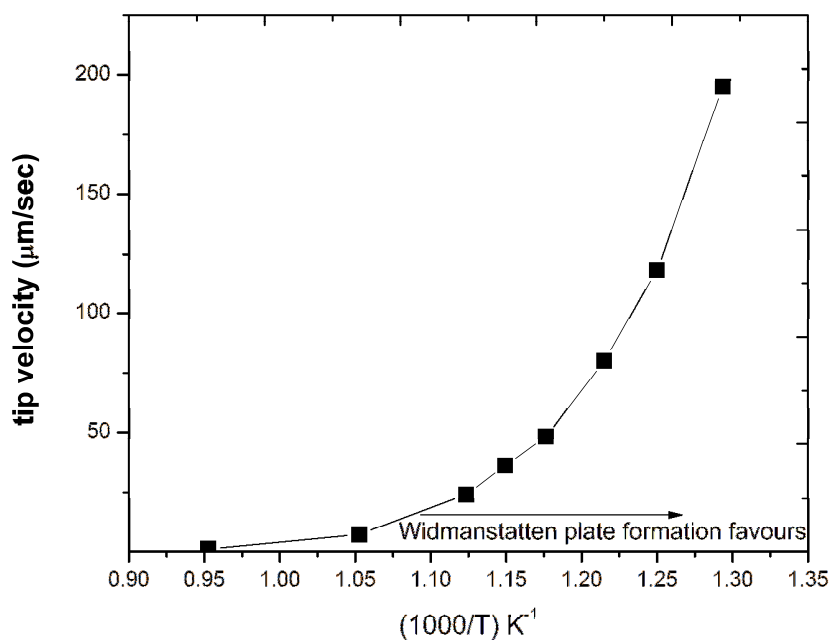
Fig. 4.15. Tip velocity as a function of undercooling in terms of (1/T) multiplied by 1000. Lower temperature i.e. higher undercooling favoured Widmanstatten lath morphology.

When simulations were carried out at a higher temperature, i.e. with lower undercooling (1054 K), no instability of planar interface is formed during the whole simulation process and the entire interface moves in classical diffusion controlled way giving the formation of allotriomorphs α (fig. 4.16a and fig. 4.16b). At higher temperatures due to higher diffusivity, solute atoms get distributed more or less uniformly at the tip as well as at the root of the protrusion giving a uniform velocity of the entire interface and planar growth is favored. With time, build up of Nb concentration has been observed ahead of the entire planar interface.
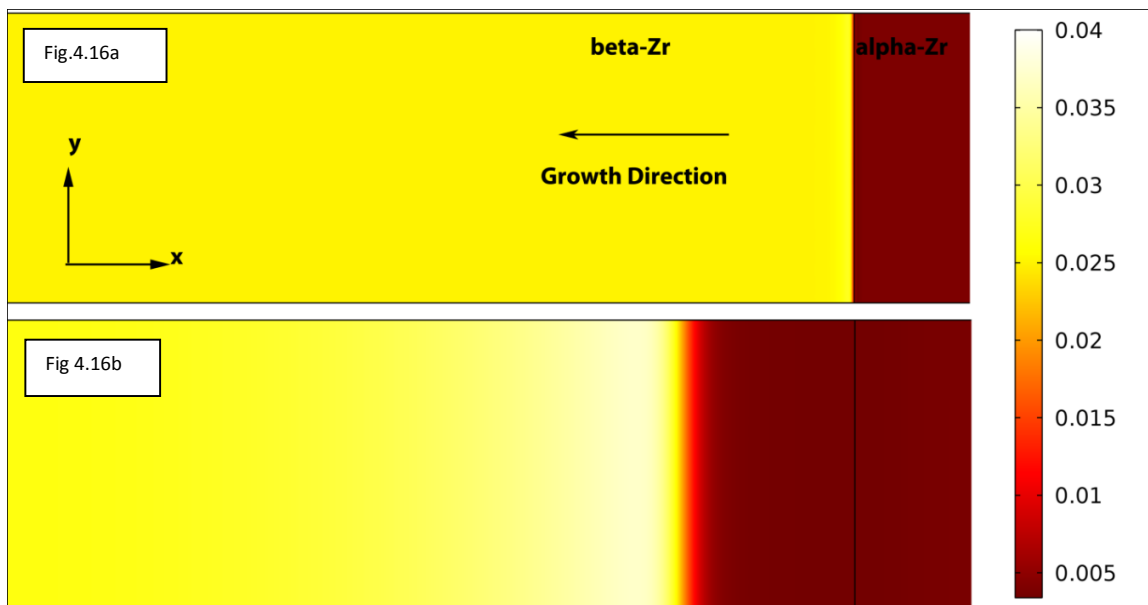
Fig. 4.16 Stable planar front grows from pre-nucleated allotriomorph α-Zr of Zr-2.5Nb alloy at 1054 K. No stable perturbation has been formed at this temperature. The dark region in fig. 4. 16a indicates pre-nucleated allotriomorph α-Zr. The images (fig. 4. 16a and fig. 4. 16b) were taken at 0.0, 0.107 non-dimensional time steps. The colour code depicts the mole fraction of Nb in Zr-Nb binary alloy. Black line in fig. 4.16b denotes initial position of the interface. The domain size is 1.57 μm x 5.08 μm.

4.12   Explicit nucleation event and subsequent growth

In the case of an explicit nucleation event, different numbers of equilibrated nuclei were generated (fig. 4.17a) on the α/β interface by generating a uniform random variable. During growth with stochastic source term $\xi = 0$, these equilibrated nuclei have been grown into side

plate morphology (fig. 4.17b). Development of this morphology is due to the interplay between temperature, interfacial energy and the degree of anisotropy in interfacial energy.
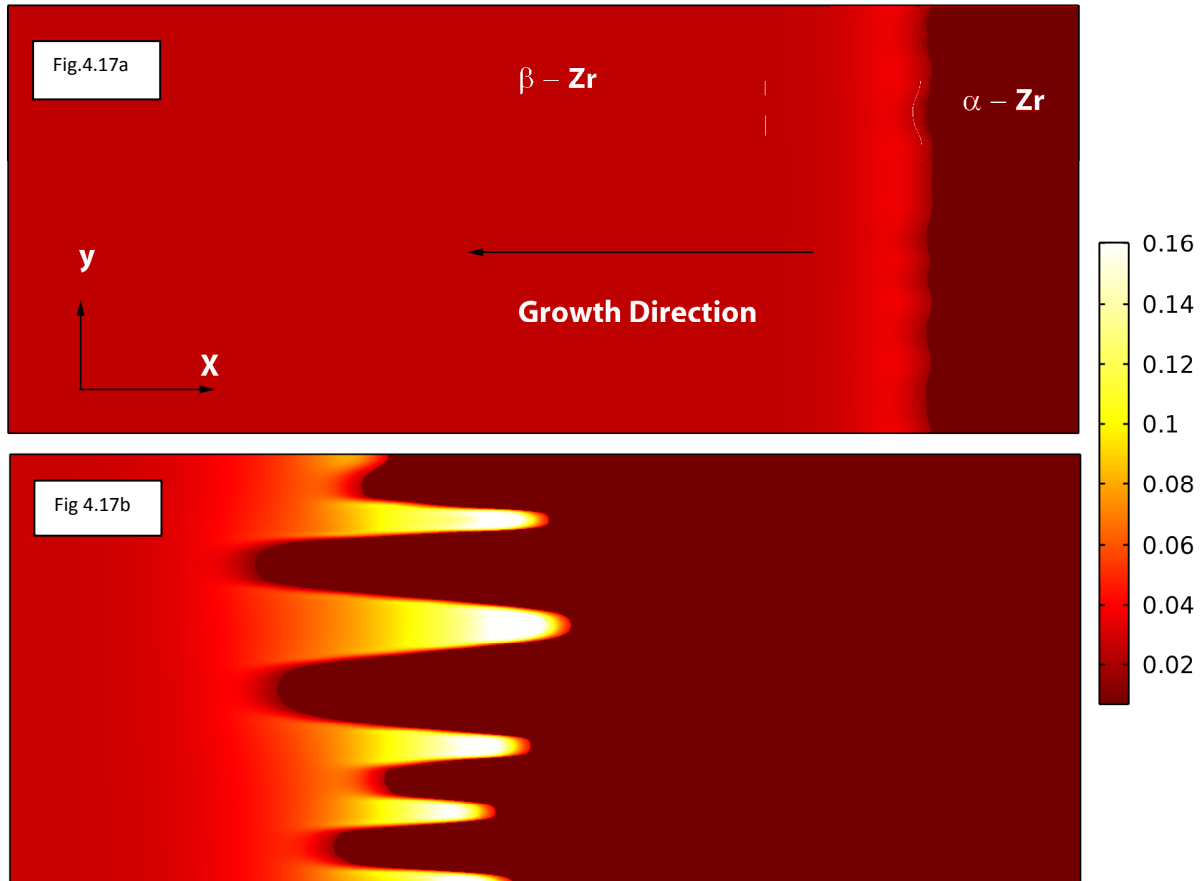
Fig. 4.17 Development of Widmanstatten lath morphology at 890 K from allotriomorph α- Zr in Zr-2.5Nb alloy using explicit nucleation. 4. 17a is the initial microstructure and 4. 17b is the microstructure at 0.0814 non-dimensional time step. The grayscale colour code depicts the mole fraction of Nb in Zr-Nb binary alloy. The domain size is 1.8 μm x 4.26 μm.

4.12.1 Interface velocity

The α/β interface position has been fixed on the iso-line of $\varphi = 0.5$. In case of Zr-2.5Nb alloy at 890 K, the plot of tip position (fig. 4.18) at different time shows a linear trend for Widmanstatten plate growth, i.e. a constant velocity profile and corresponding tip velocity is 20 $\mu m/sec$. A constant lengthening rate is also experimentally found [4.60].
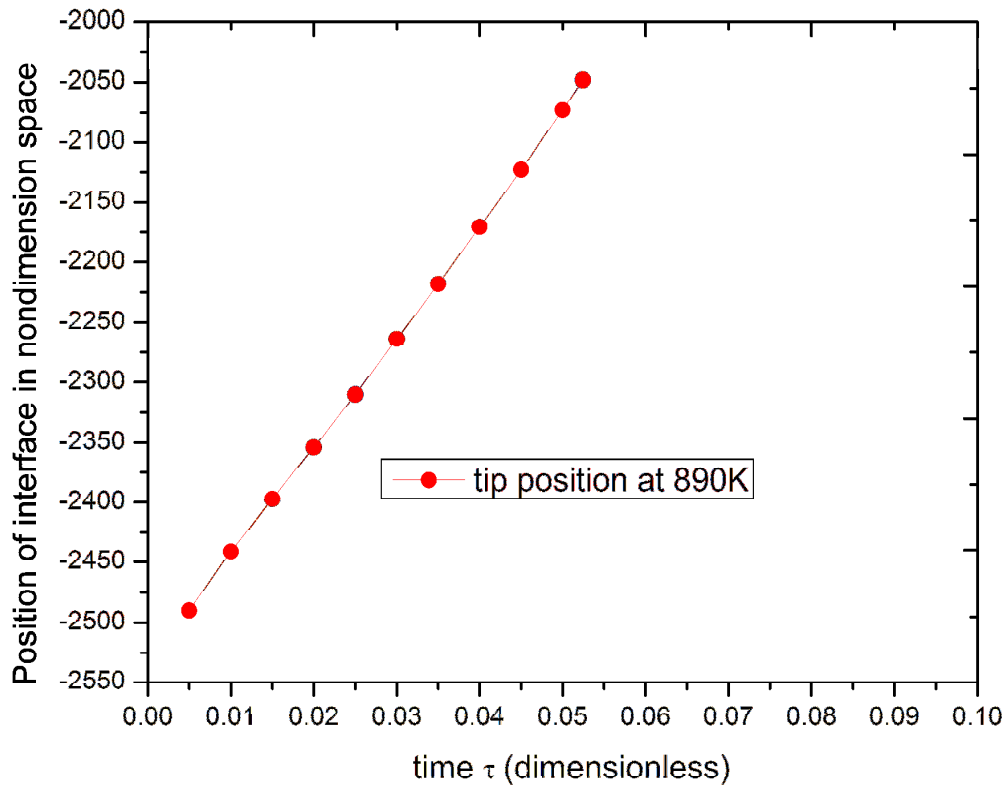
Fig. 4.18. Position of interface at different instant (dimensionless) for Widmanstatten plate growth at 890 K indicate linear lengthening rate.

The width of the single lath grows slowly compared to tip and its growth rate in the initial stage is around 1.5 $\mu m/sec$ for the same γ. The reason behind the low growth rate in width direction is that the broad faces of each lath have a very good atomic fit with parent lattice and due to difficulty in joining of individual atoms on the habit plane, thickening of the plates is restricted giving a very low values of mobility. These broad faces move forward by sideways motion of ledges. It was indicated by Aaronson that ledged interfaces would always show interface-controlled or mixed controlled growth and it grows more slowly than expected for diffusion control. And its tips grow linearly maintaining a constant radius of curvature. But for classical planar growth at 1054 K, the interface position shows (fig. 4.19) a parabolic profile with diffusion time (τ) and the velocity of the interface is essentially proportional to $\tau^{-1/2}$.
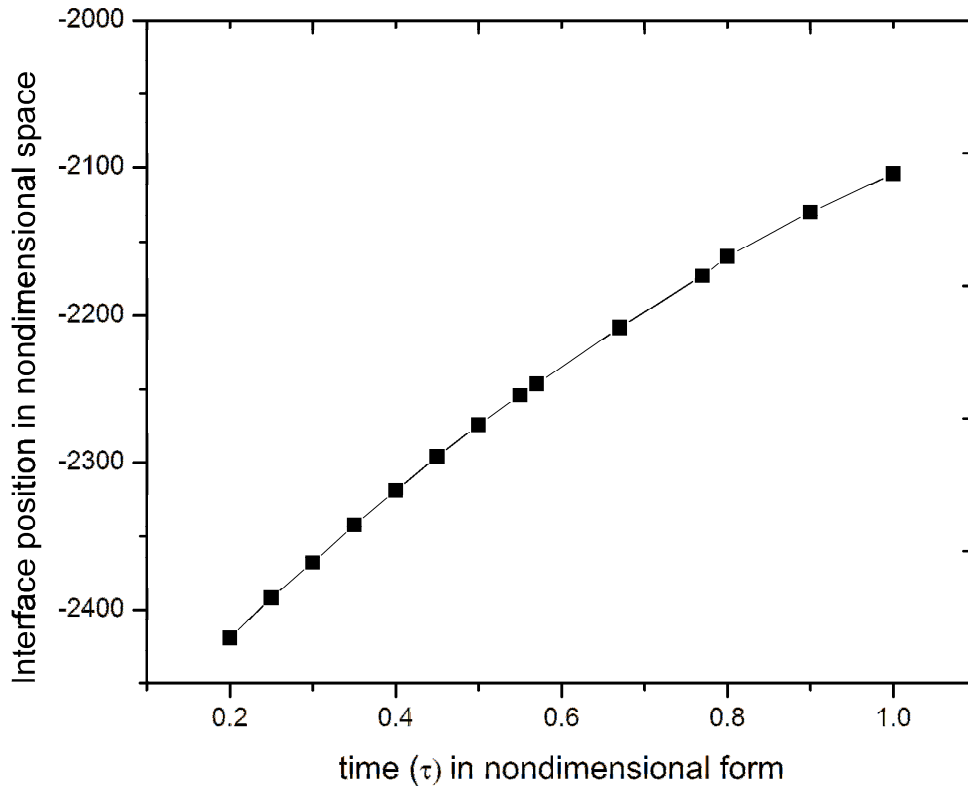
Fig. 4. 19. Position of interface at different instant (dimensionless) for diffusion controlled planar growth at 1054 K. Interface position was taken the location where $\varphi = 0.5$ at different instant.

4.13   Effect of supersaturation on growth velocity

The supersaturation of the alloy is defined as $\Omega_0 = \frac{c^{\beta/\alpha\,eq} - c^o}{c^{\beta/\alpha\,eq} - c^\alpha}$, where $c^{\beta/\alpha\,eq}$ is the equilibrium concentration of solute at the β/α interface, c^α is the solute concentration of the growing α phase and c^o is the initial alloy composition. It also may be noted that the effective supersaturation at the interface deviates from Ω_0 depending upon solute concentration on the two sides of the interface which are determined by local equilibrium at the interface. Fig. 4.20 shows the dependence of tip velocity with supersaturation (Ω_0) for Zr-0.8Nb, Zr-1Nb, Zr-2.5Nb, Zr-3.5Nb, Zr-5.5Nb, Zr-7Nb alloys at 890K.
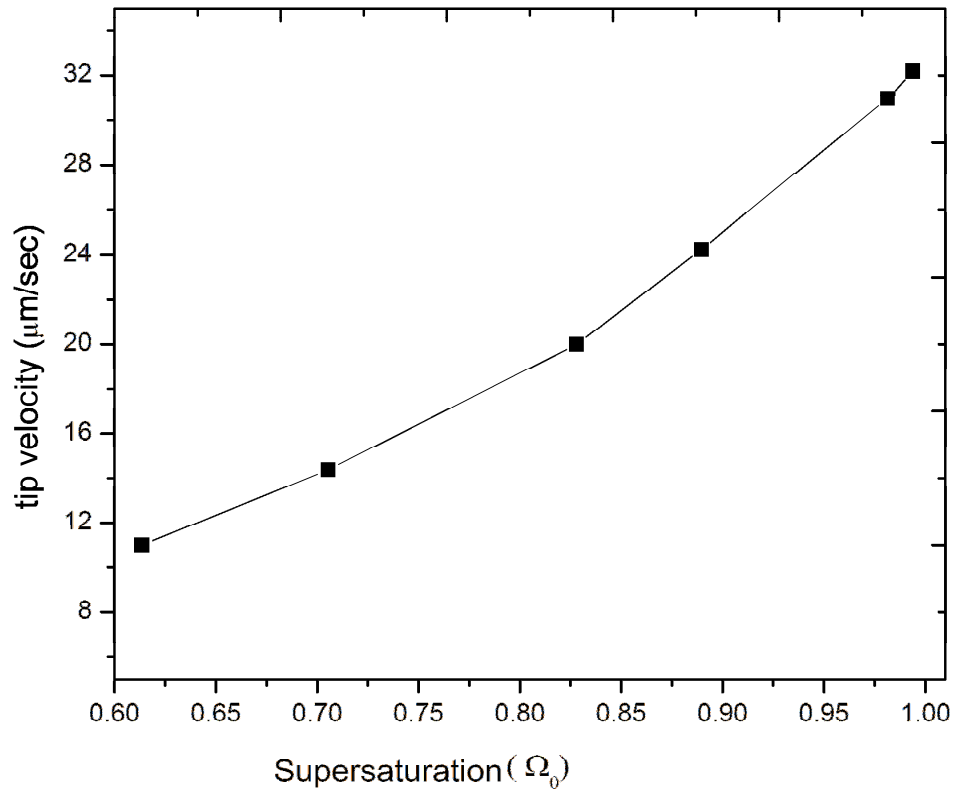
Fig. 4.20. Tip velocity as a function of supersaturation Ω_0 at 890 K. At very high supersaturation steeper slope presents and transition was observed at Ω_0 0.83.

The tip velocity increases steadily with the increase in supersaturation. At high super-saturation, the growth velocity approaches a linear dependence with Ω_0. The work of Hillert [4.61] discusses the appropriateness of the solutions of Zener-Hillert, Liu-Ågrenand Trivedi at different supersaturation. The Trivedi's solution is only valid at very high supersaturation ($\sim\Omega_0 = .99$) i.e. close to 1. The Zener-Hillert proposes a velocity profile which follows two different slopes (one from $\Omega_0 = 0.6 - 0.88$ and another from 0.88 - 1). In our case the velocity profile is close to what was found by Zener-Hillert. The velocity profile has a lower slope up to supersaturation 0.83 and a steeper slope is seen thereafter. So there is a transition in slope of growth velocity with supersaturation. The increase in tip velocity with supersaturation signifies that solute can easily be removed from the tip region at higher supersaturation to favor plate growth. Simulations also show that in pure Zr containing 200 ppm Nb or less, lath morphology does not develop at 890K and the initial protrusions gradually decays and the formation of a planar interface is favoured with very high γ (fig. 4.21).
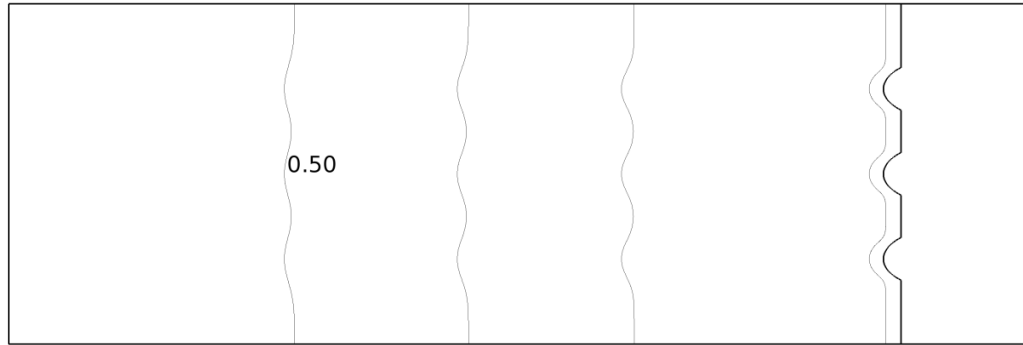
Fig. 4.21 Contour plot of $\varphi = 0.5$ showing interface position at different instant. For Zr with less than 200 ppm Nb, lath morphology does not develop and initial protrusions decay and a planar interface formation is favored with very high value of γ (120).

Due to very low concentration of solute atoms in the alloy, solute pile up at the tip of the protrusions as well as at the root of the protrusions is more or less same. The tip of the protrusion could not attain higher relative velocity with respect to planar interface of pre-nucleated α and the protruded region decays and the growth of entire planar interface takes place. This also established the fact that the influence of the concentration field ahead of α / β interface is responsible for the growth of a group of α lath of identical orientation giving parallel plate morphology.

Table.4.1 Simulation parameters for Phase Field Model

Parameters' Name	Symbol (unit)	Expression/Value
Molar Volume	V_m (m^3/mol)	$1.4060 * 10^{-5}$
Distance between atoms	b (Å)	3.23
Incoherent Interface Thickness	δ_0 (nm)	5
Interfacial Energy of incoherent interface	σ_0(J/m2)	0.3
Extent of anisotropy	γ	120
Nb diffusion coefficient in α-Zr	D_{Nb}^{hcp}(m^2/sec)	$6.6 * 10^{-10} * e^{-\frac{15851.4}{T}}$ [4.46]
Nb diffusion coefficient β-Zr	D_{Nb}^{bcc} (m^2/sec)	$9 * 10^{-9} * (\frac{T}{1136})^{18.1} * e^{-\frac{(25100+35.5*(T-1136)}{1.98*T}}$ [4.50]

4.14 Summary

➢ The growth of α-phase from equilibrated nucleus has been modeled using phase field method for Zr-Nb series alloys with different Nb content. Using this simulation the microstructure evolution during β to α diffusional phase transformation can be predicted for Zr-Nb substitutional alloy system.

➢ The effect of nucleation events has been incorporated through the introduction of noise term both implicitly and explicitly.

➢ The equilibrium and kinetic data for the model input has been taken from the literature and simulations were carried out at different isothermal temperatures.

➢ The anisotropic surface tension has a pronounced effect on the morphology development apart from the mobility parameters.

➢ For Zr-2.5%Nb with low under-cooling, the driving force for plate growth decreases and at 1054 K it shows formation of allotriomorphs α through classical diffusional transformation. Higher undercooling favours Widmanstatten lath formation. The growth velocity of the Widmanstatten plate is constant. The change in alloy composition changes the effective super-saturation at the α/β interface and leads to a different tip velocity.

➢ When Nb content reduces below 200 ppm, lath morphology does not develop and the interface remains planar only.

4. 15 References

[4.1] Banerjee S., Mukhopadhyay P.," Diffusional Transformation, Phase transformations: Examples from Titanium and Zirconium Alloys", Pergamon Materials Series, Vol. 12, 2007.

[4.2] Holt R. A., J. Nucl. Mat. 35 (1970) 322-334.

[4.3] Perovic V., Perovic A., Weatherly G. C., Brown L. M., Purdy G. R., Fleck R. G., Holt R. A.,J. Nucl. Mat.205 (1993) 251-257.

[4.4] "Waterside corrosion of zirconium alloys in nuclear power plants", IAEA TECHDOC-996, IAEA,VIENNA (1998) 124-169.

[4.5] Dey G. K., Banerjee S., J. Nucl. Mat. 125 (1984) 219-227.

[4.6] Dey G. K., Singh R. N., Tewari R., Srivastava D., Banerjee S., J. Nucl. Mat. 224 (1995) 146-157.

[4.7] Tewari R., Srivastava D., Dey G. K., Chakravarty J. K., Banerjee S., J. Nucl. Mat. , 383, 1-2, (2008) 153-171.

[4.8] Zhang W. Z., Perovic V., Perovic A., Weatherly G. C. and Purdy G. R., Acta mater. 46(10) (1998) 3443-3453.

[4.9] Langer J. S., Review of modern physics, 52, (1980), 1-28.

[4.10] Pelcé P., Libchaber A., Academic Press, New York, 1988.

[4.11] Mullins W. W., Sekerka R. F., J. Appl. Phys. 35 (1964), 444-451.

[4.12] Mullins W. W., Sekerka R. F., J. Appl. Phys. 34 (1963), 323-329.

[4.13] Saarloos Wim V., Physics Reports 301 (1998) 9-43.

[4.14] AaronsonH. I., Spanos G., Masamura R. A., Vardiman R. G., Moon D. W., Menon E. S. K., Hall M. G., Mater. Sci. and Eng. B, 32, 3(1995) 107-123.

[4.15] Shewmon P. G., Trans. TMS-AIME, 233 (1965), 736-748.

[4.16] Phelan D., Stanford N., Dippenaar R., Mater. Sci. and Engg. A : 407, 1-2 (2005), 127-134.

[4.17] Chen L.Q., Annu. Rev. Mater. Res. 32(2002), 113–140.

[4.18] Wang Y., Ma N., Chen Q., Zhang F., Chen S. L., Chang Y. A., JOM (2005), 32–39.

[4.19] Loginova I., Ågren J., Amberg G., Acta Mater., 52(13) (2004), 4055–4063.

[4.20] Dunlop J. W. C., Bréchet Y. J. M., Legras L., Zurob H. S., J. Nucl. Mat. 2007, 366 , 178–186.

[4.21] Massih A.R. , Jernkvist L. O., Comp. Mat. Sci. (2007), 39, 349– 358.

[4.22] Tang Bin , Cui Y. W., Chang Hui , Kou Hongchao , Li Jinshan, Zhou L, Computational Materials Science 53 (2012), 187–193.

[4.23] Choudhuri G., Chakraborty S., Srivastava D., Dey G. K., Results in Physics, (2013), 3, 7-13.

[4.24] Karma A. , Rappel W. J., Phys. Rev. E 60 (1999) 3614-3625.

[4.25] Elder K. R., Drolet F., Kosterlitz J. M., Grant M., Phys. Rev. Lett. 72 (1994) 677-680.

[4.26] Pavlik S. G. , Sekerka R. F., Physica A 268 (1999) 283-290.

[4.27] Pavlik S. G. and. Sekerka. R. F., Physica A 277 (2000) 415-431.

[4.28] László Gránásy, Tamás Börzsönyi, and Tamás Pusztai, Journal of Crystal Growth 237–239 (2002) 1813-1817.

[4.29] Jou H. J ,Lusk M. T., Physical review B, (1997) 55, 13: 8114-8121.

[4.30] Castro M., Physical review B, (2003) 67, 035412(1-8).

[4.31] Junjie Li, Wang J., Yang G., Journal of Crystal Growth 309 (2007), 65–69.

[4.32] Allen S. M., Cahn J. W., Acta Metall. (1979) 27, 1085–1095.

[4.33] Cahn J. W., Hilliard J. E., J Chem Phys. (1958), 28, 258–267.

[4.34] Van der Waals J.D., Z Phys Chem 1894; 13:657.

[4.35] Langer J.S. In: Grinstein G, Mazenko G, editors. Directions in condensed matter physics, Singapore: World Scientific; 1986, 165–186.

[4.36] Selzer M., Nestler B., Danilov D., Math Comput. Simul. 2010; 80:1428–1437.

[4.37] Provatas N., Elder K., Wiley-VCH (2010), Verlag GmbH & Co KGaA, Germany-printed in Singapore.

[4.38] Wang S. L., Sekerka R. F., Wheeler A. A., Murray B. T., Coriell S. R., Braun R. J., McFadden G. B., Physica D, 69 (1993) 189-200.

[4.39] Guillermet A. F., Z. Metalkundu, (1991) 478-487.

[4.40] Dinsdale A.T., CALPHAD, 15(4), 1991, 317- 425.

[4.41] Boettinger W., Ann Rev Mater Res 2002; 32:163–194.

[4.42] Loginova I., Odqvist J., Amberg G., Ågren J., Acta Mater 2003;51:1327–1339.

[4.43] Singer H. M., Singer I., Jacot A., Acta Mater. 2009; 57:116–124.

[4.44] Ågren J,J. Phys. Chem. Solids 43, 5 (1982) 421-430.

[4.45] Tiwari G.P., Sharma B.D., Raghunathan V.S., Patil R.V., J Nucl Mater 1973;46:35–40.

[4.46] Dyment F., Libanati C. M., J. of Mat. Sci. 3 (1968) 349-359.

[4.47] Turnbull D. Trans AIME 1951; 191:661.

[4.48] Piotrkowski R., Dyment F., J Nucl Mater 1986; 137:94–9.

[4.49] Piotrkowski R.,J Nucl Mater 1991; 183:221–5.

[4.50] Federer J. I., Lundy T. S., Trans of Met. Society, AIME 227 (1963) 592-597.

[4.51] Doherty R.D. In: Cahn R.W., Haasen P., ed. Physical metallurgy, vol. 2. 4th revised and enhanced ed. North Holland: Elsevier Science B.B.; 1996.

[4.52] McFadden G B, Wheeler A A, Braun R J, Coriell S R, Sekerka R F,, Phys. Rev. E 1993;48:3, 2016-2024.

[4.53] Porter D.A., Easterling K.E., Phase transformation in metal and alloys, 2nd ed. Chapan & Hall; 1996.

[4.54] Gunton J. D., Miguel M. S., Sahni P. S., In: Phase transitions and critical phenomena, Vol. 8, edited by Domb C and Lebowitz J L, Academic Press London, 1983.

[4.55] Simmons J. P., Wen Y., Shen C., Wang Y. Z., Mater. Sci. and Engg. A 365 (2004) 136-143.

[4.56] Aaronson H. I., Lee J. K., In: Aaronson H I (Ed.), Lectures on the Theory of Phase Transformations, TMS, New York, (1975).

[4.57] Zener C., Transactions of the American Institute of Mining and Metallurgical Engineers 167(1946) 550–5o95.

[4.58] Hillert M., Metallurgical Transactions A 6(1975) 5-19.

[4.59] Livingstone J. D. and Cahn J. W., Acta Metall. 22, 4(1974) 495-503.

[4.60] Aaronson H. I., Enomoto M., Lee J. K.," Mechanisms of diffusional phase transformation in metals and alloys", CRC Press, 2010.

[4.61] Hillert M., Höglund L., Ågren J., Acta Mater. 51 (2003), 2089-2095.

[4.62] Prerana Misra, unpublished work.

[4.63] N. Saibaba, S. K. Jha, S. Tonpe, Kumar Vaibhaw,V. Deshmukh, S. V. Ramana Rao, K. V. Mani Krishna, S. Neogy, D. Srivastava, G. K. Dey, R. V. Kulkarni, B. B. Rath, E. Ramadasan, and S. A. Anantharaman, proceedings of 16th International Symposium on " Zirconium in the Nuclear Industry", ASTM STP 1529, Magnus Limbäck and Pierre Barbéris, Eds., May 9-13, 2010, Chengdu, Sichuan Province, China , 349-360.

Chapter 5

Precipitation and growth study of intermetallics and their effect on oxidation behavior in Zr-Sn-Fe-Cr alloys

This chapter gives detailed description of microstructure evolution through various α-annealing heat treatments and its effect on out of pile oxidation behaviour of the alloy.

The evolution of second phase precipitates and their microchemistry in Zr-Sn-Fe-Cr alloy during α-annealing heat treatments have been investigated by transmission electron microscopy and energy dispersive spectrometer attached with scanning transmission microscopy. Size distribution of the precipitates was also estimated from small angle neutron scattering. The effects of precipitate size, its distribution, matrix microstructure, oxide morphology, chemical state as well as phases of oxide on the oxidation behavior of the alloy have been studied during accelerated autoclaving.

5.1 Introduction

Zirconium based alloys, in particular, Zircaloy-2 and Zircaloy-4, Zr-1Nb have been widely used as fuel cladding material for thermal reactors. Zircaloy-4 has shown satisfactory performance in pressurized heavy water reactors (PHWRs). However, present nuclear plants are being designed for higher coolant temperature with partial boiling combined with higher burn-up and longer residence time. Thus, an alloy with optimized chemical composition and microstructure is desired for higher burn-up applications [5.1].

The principal alloying elements in Zircaloy-4 are Sn, Fe, Cr and their total amount is restricted to less than 2 wt. %. Sn is primarily added in Zircaloy to overcome the deleterious effects of nitrogen and also to improve mechanical property, especially in reactor creep of the alloy [5.2]. Sn possesses tetragonal crystal structure and it is an alpha stabilizer. At elevated temperatures, Sn is more soluble and its solubility decreases sharply below 300°C. The solubility of Sn in Zr is about 1.2 wt. % at 500°C, 0.5 wt. % at 400°C and less than 0.1wt. % at 300°C. At room temperature Sn has negligible solubility in α-Zr. The excess Sn precipitates mostly as Zr_4Sn. The solubility of Sn in β-Zr increases to 21wt. % at eutectic temperature of 1590°C.

The poor corrosion resistance of Sn in Zr based alloys is rationalized on the basis of lattice defects. Thus, when Sn enters in Zr oxide as Sn^{+4}, it disturbs the required distortion of the monoclinic lattice of ZrO_2 that is necessary for matching with Zr lattice. It also increases the number of anion vacancies. The mobility of these anion vacancies increases with temperature which leads to high corrosion rate of Zr-Sn alloy at high temperature in water steam [5.3, 5.4, and 5.5] environment. In addition, Sn can form intermetallics Zr_4Sn which enhances the deuterium pick up in reactor environment. So Sn composition in optimized Zr-Sn-Fe-Cr series alloy is restricted to 1.2-1.5 wt. % with tighter control on C, N and Si.

As the solubility of these alloying elements in α Zr is significantly small, they tend to form second phase precipitates (SPPs). Although the volume fraction of the precipitates remains small enough, these SPPs play an important role in controlling oxidation, hydriding and irradiation behavior [5.6, 5.7]. Fine and uniform distribution of the precipitates improve nodular [5.8- 5.13] corrosion resistance in BWRs. However, during high burn up application, they show poor irradiation stability. The coarser precipitates are required to improve uniform corrosion resistance in PHWRs and PWRs [5.3]. Matrix microstructure and its micro-constituents are also very important in controlling the oxidation, hydriding and irradiation behavior of the alloy. Quenched and aged at different temperature would produce variety of microstructures which play important role in controlling their properties.

Crystal structure of these SPPs [5.3], their size, distribution in the matrix and their morphology depend on the alloy composition, thermo-mechanical treatment and irradiation dose. However, full mechanistic understanding of the micro-structural evolution and their influence on oxide formation for high burn up application has not been achieved so far.

In this work, we have studied microstructural evolution, mainly the formation and growth of SPPs and their microchemistry, morphology, size and distribution in Zr-Sn-Fe-Cr alloy during various alpha annealing heat treatments by transmission electron microscopy (TEM)/scanning transmission electron microscopy (STEM) and small-angle neutron scattering (SANS) [5.14, 5.15].

The triple melted ingot with two different compositions of Zr-Sn-Fe-Cr alloys were subjected to a series of thermo mechanical treatments (section 3.2.1) to break the cast structure and had finally undergone β-quenching. Subsequently α annealing heat treatment was carried out at 700°C and 800°C for 15 mins. , 1hr. and 10 hrs. as well as at 850°C for 1 hr. to generate different types of microstructure having different magnitude of cumulative annealing parameter, from 0.35×10^{-18} to 646×10^{-18}.hrs. Effect of different types of α-annealed microstructure and precipitates on the oxidation behavior of the alloy has been studied by accelerated autoclaving at 415°C,1500 psi for 72 hrs. . The samples for autoclaving was prepared as per ASTM G2.

5.2 Results:

5.2.1 Microstructure Characterization:

Microstructure of triple arc melted ingot of alloy-1 is shown in fig. 5.1. It shows Widmanstatten structure with parallel α lath growing from grain boundary towards the grain interior and β enriched in solute content remains in between two laths. This type of structure forms due to anisotropy in surface energy. The broad faces of each lath have a very good atomic fit with parent lattice and due to difficulty in joining of individual atoms on the habit plane, thickening of the plates is restricted giving very low values of mobility whereas the tip grow linearly with high mobility. Presence of randomly fine precipitates within the matrix can act as a site for nucleation and give rise to formation of intragranular α plate. The formation and growth of groups of parallel intragranular plates called packet give rise to generation of basket weave morphology.

Fig. 5. 1: Basket weave micro structure of as received triple arc melted ingot of Zr-1.53 Sn-Fe-Cr alloy.

40% cold rolled samples were showing elongated deformed grains, unlike as cast sample's widmanstatten structure, no exact structure pattern has been seen in deformed sample.

5.2.1.1 Cold rolled and as quenched microstructure: In as-quenched condition optical microstructure revealed basket weave morphology (fig. 5.2a). Presence of precipitates in as-quenched condition was not evident from the SEM micrograph. TEM microstructure of alloy-1 (fig. 5.2b) in as quenched condition confirmed mostly precipitate free lath. The width of the laths which made up a packet or colony of lath was varying from 0.4 µm to 2 µm.
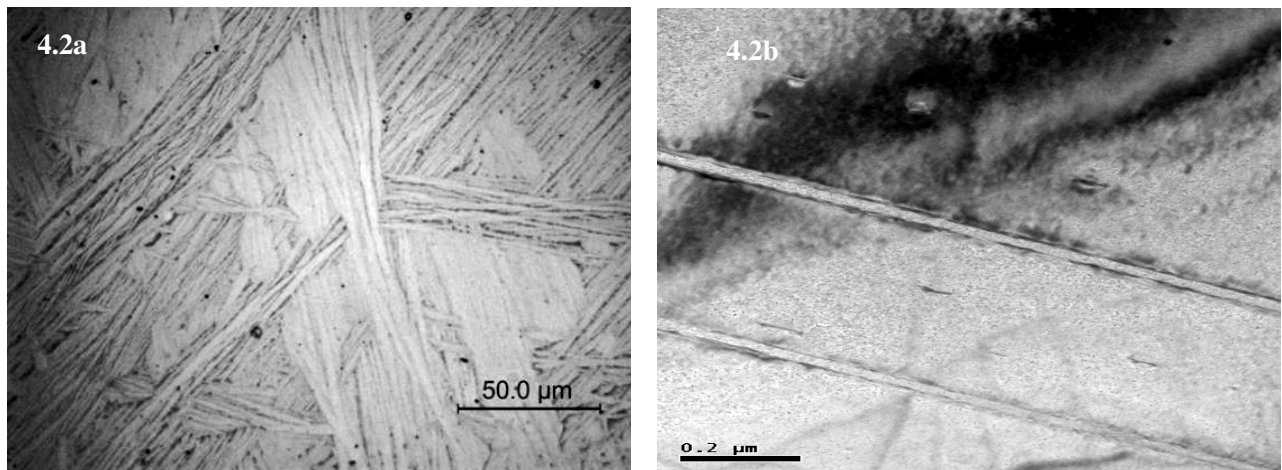
Fig. 5. 2: Cold worked and quenched microstructure of Zr-1.53Sn-Fe-Cr alloy, a) Basket weave microstructure observed in optical microscope, b) TEM microstructure of single lath .

5.2.1.2 Annealing at 700°C for 15 min: Optical microstructure after 15 minutes annealing at 700°C did not show appreciable change (fig. 5.3a). Few precipitates were observed under SEM that were clustered in certain grains (fig. 5.4a).
.
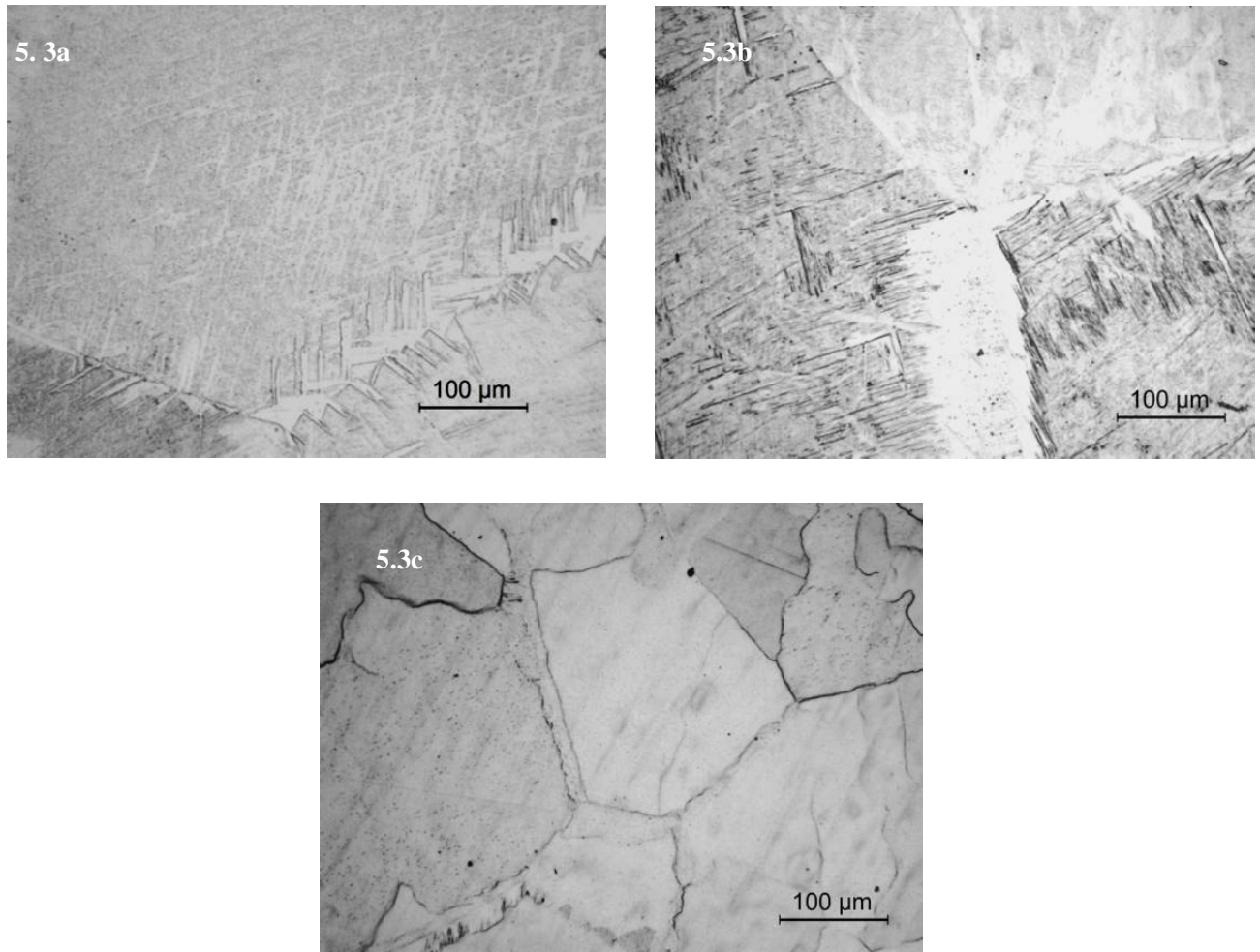
Fig. 5. 3: Optical micrograph of alloy 1 annealed at 700°C for a) 15 minutes, b) 1hr. and c) 10 hrs..

5.2.1.3 Annealing at 700°C for 1hr. : Optical microstructure did not show any appreciable change even after 1 hr. annealing at 700°C. Widmanstatten laths were seen under microscope. But with annealing for longer duration (1 hr.), precipitates were seen under SEM (fig. 5.4b) to be distributed all over the microstructure.
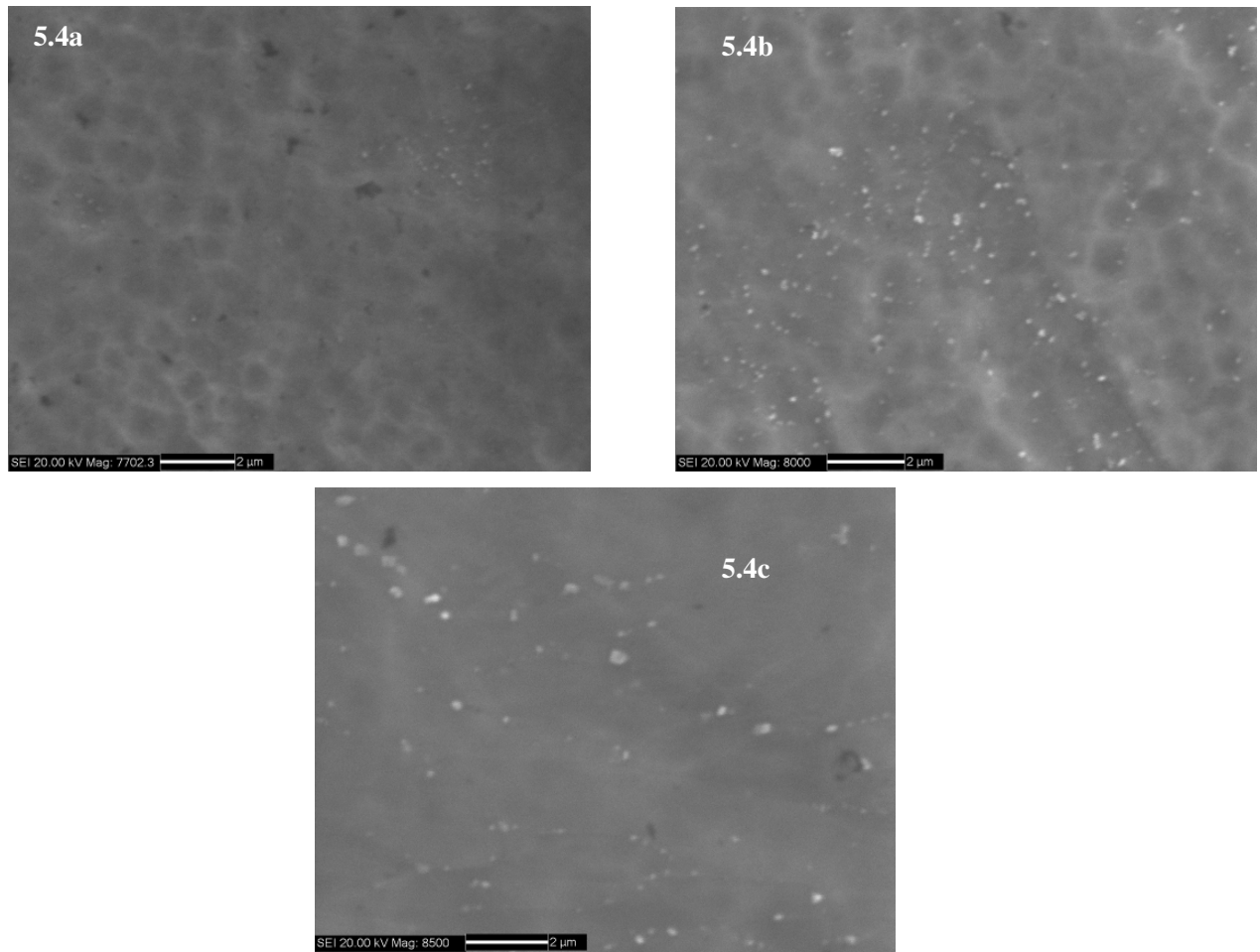
Fig. 5. 4: SEM micrograph alloy 1 annealed at 700°C for a) 15 mins. , b) 1hr. and c) 10 hrs. .

TEM micrographs of alloy-1and alloy-2 after 1hr. of annealing at 700°C showed both grain body and grain boundary precipitates (fig. 5.5a). These were uniformly distributed. Grain boundary precipitates were observed on low angle lath boundaries (fig. 5.5a).The morphology of the precipitates were globular and in the shape of parallelepipe.The volume fraction (assumption: volume fraction is same as area fraction) of the SPPs was found to be significantly small (0.6%) and inter-particle spacing was large. Average diameter of globular precipitates was around 30 nm (fig. 5.5b) in alloy 2. The average width of the parallelepiped precipitates was nearly 33 nm (fig. 5.5c) with length around 100 nm. Aspect ratio which is a ratio of longer side to the shorter side of parallelepiped precipitates was in the range of 2.5 to 3.
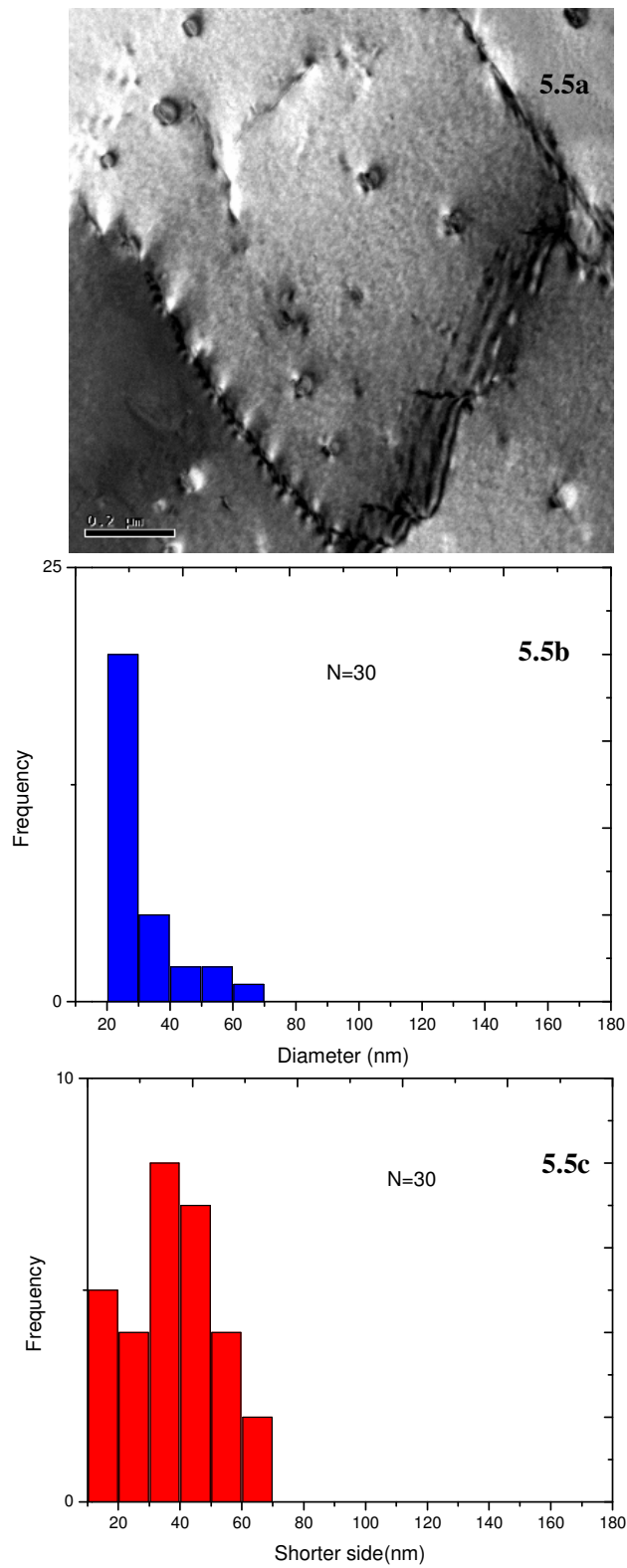
Fig. 5. 5: a) TEM micrographs showing both grain body and grain boundary precipitates, size distribution of b) globular precipitates and c) smaller side of parallelepiped precipitates (with aspect ratio around 2.5) after annealing at 700° C for 1 hr. The number of particles analyzed is given as N.

5.2.1.4 Annealing at 700°C for 10 hrs.: Recrystallized microstructure observed after 10 hrs annealing at 700°C (fig. 5.3c).Volume fraction of the SPPs was increased with annealing for longer duration at 700°C (fig. 5.4c). For globular precipitates it was approximately 0.8% (fig. 5.6b) and for parallelepiped precipitates, it was around 2.8 % (fig. 5.6c). Precipitates were more closely and uniformly spaced. Avg. diameter of globular precipitates was around 33 nm. Most of the parallelepiped precipitates were having width in the range of 30 - 80 nm with aspect ratio at around 3.5. 700°C 10 hrs. annealing resulted in highest volume fraction of the closely spaced parallelepiped precipitates.

After annealing at 700°C for 10 hrs. in alloy 2, matrix is α Zr with Sn content in the range of 1.25-1.56 wt.% with no detectable Fe or Cr. The EDS profile of the matrix taken in 200 KeV STEM is given in fig. 5.7a.
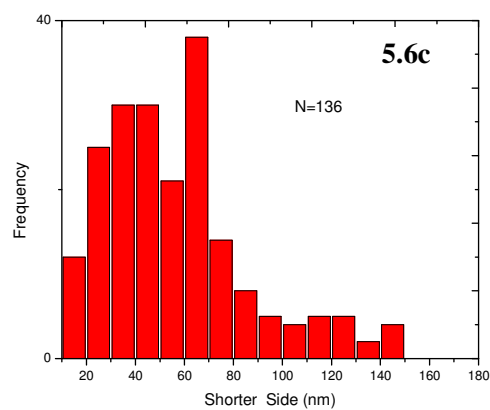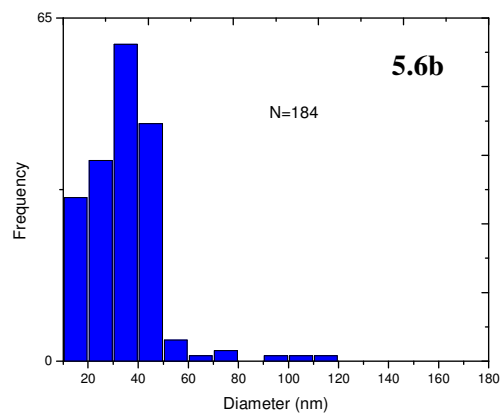
Fig. 5.6: a) TEM micrographs showing both grain body and grain boundary precipitates, size distribution of 5.6b) globular precipitates and 5.6c) smaller side of parallelepiped precipitates (with aspect ratio around 3.5) after annealing at 700° C for 10 hrs..
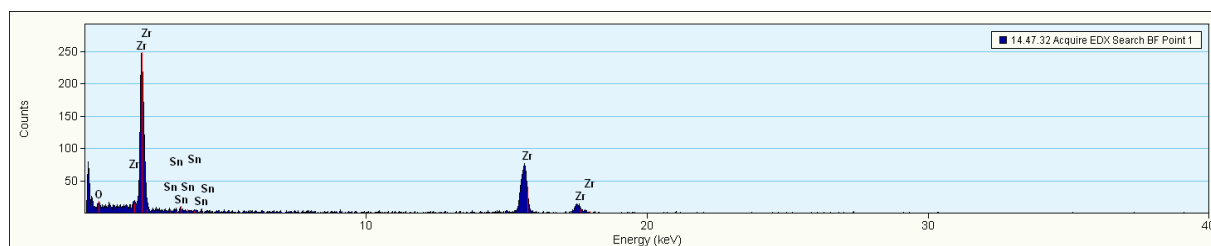
Fig. 5. 7a: EDS profile of matrix shows presence of Sn after annealing at 700°C for 10 hrs..

Matrix near certain smaller size parallelepiped precipitates indicated absence of Sn. EDS analysis of these precipitates confirmed that they were Zr and Sn rich. These precipitates were found to be straining the matrix (fig. 5.7b) and contained around 3 - 6 wt.% Sn. They were 20-40 nm wide and 40 - 90 nm long.

EDS analysis shows that most of the parallelepiped precipitates, are Fe and Cr rich and contain Fe : 31.71 (0.75%) at.%, Cr : 16.43 (0.48%) at.%, O : 13.38 (0.46%) at.% and balance Zr with uncertainty in measurement given in bracket (fig. 5.7c). It is $Zr(Fe_{0.6}Cr_{0.4})_2$ type. Most of the parallelepiped precipitates analyzed after various alpha annealing heat treatments were $Zr(Fe_x Cr_{1-x})_2$ type with x<0.8. EDS profile of one of these precipitates is given in fig. 5.7c. As 700°C 10 hrs. results in highest volume fraction of $Zr(Fe_{0.6}Cr_{0.4})_2$, this α-annealing treatment does result in considerable relief of the super saturation of the solute elements by precipitating them out in the form of precipitates.

Precipitates with aspect ratio near to 1 were Zirconium rich. EDS profile of these precipitates is given in fig. 5.7d. EDS analysis indicated the composition of one of these type of precipitates in at. % is as follows with uncertainty in measurement given in bracket. Zr : 62.16 (1.33 %) at. %, Fe : 24.38 (0.42%) at. % ,Cr :10.18(0.25) at. % & O: 3.25(0.15%) at. %. It is $Zr_2(Fe_{0.7}Cr_{0.3})$ type. Atomic fraction of Fe of these SPP was always less than <0.8.
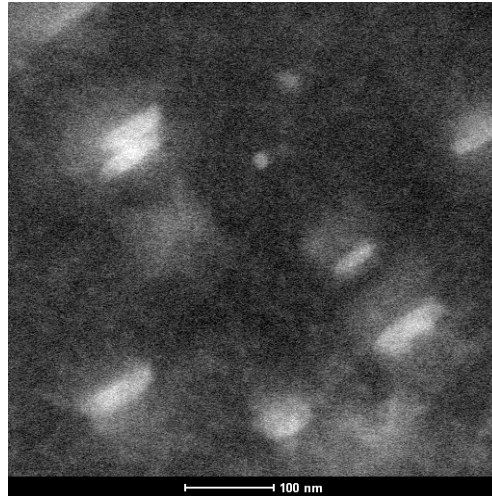
Fig. 5. 7b: Zr-Sn rich parallelepiped precipitates were seen to strain the matrix.
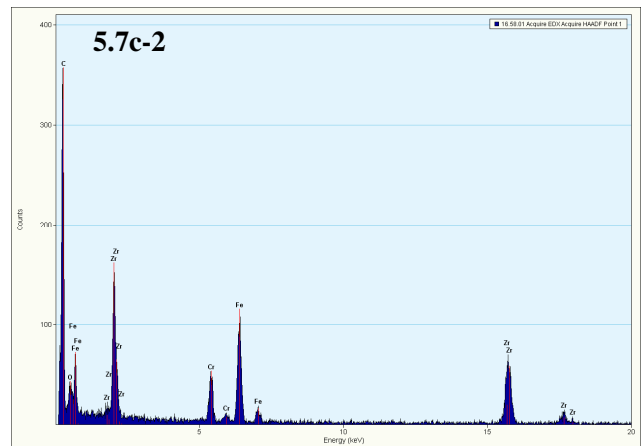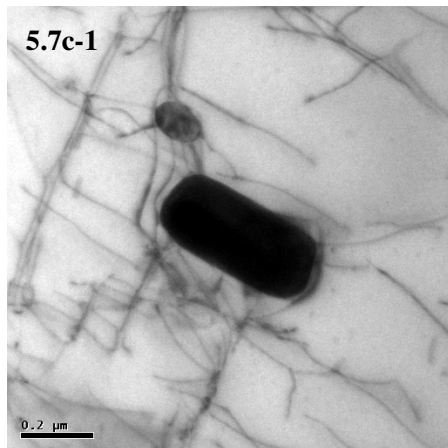
Fig. 5. 7c: EDS profile (5.7c-2) at larger precipitates (5.7c-1) indicates it is Zr lean, $Zr(FeCr)_2$ type.
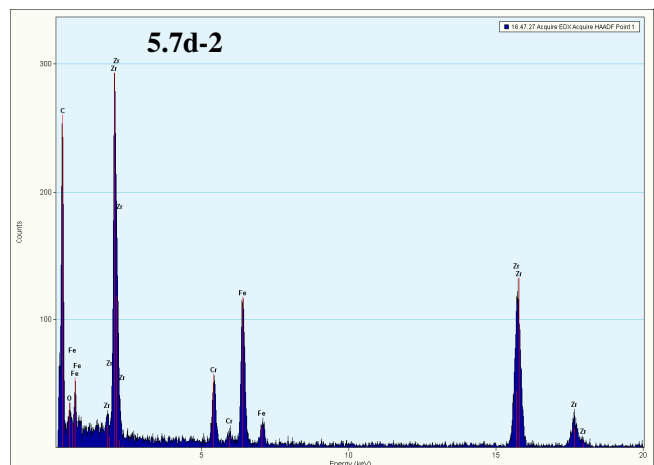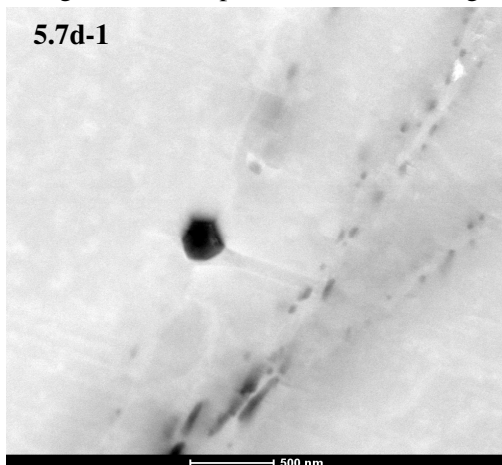
Fig. 5. 7d : EDS profile(5. 7d-2) of precipitates(5. 7d-1)with aspect ratio one indicates it is Zr rich, $Zr_2(FeCr)$type.
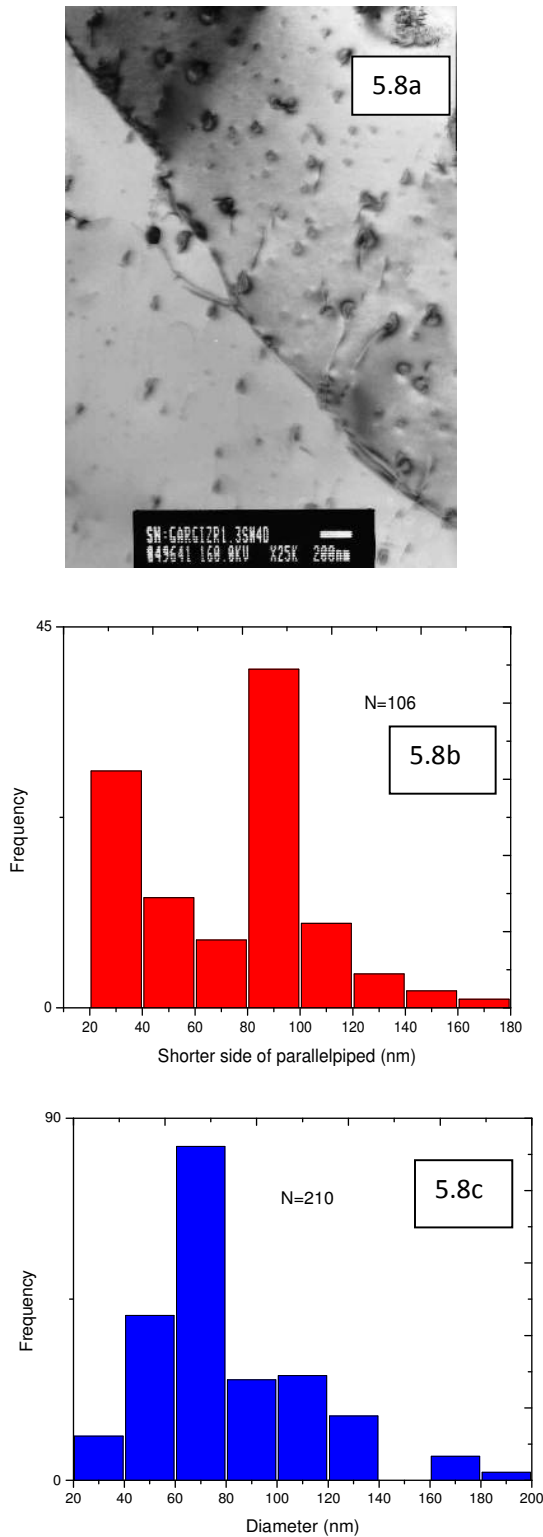
Fig. 5. 8: a) TEM micrographs showing both grain body and grain boundary precipitates in alloy 2 after annealing at 800°C for 1 hr. with b) Distribution of globular precipitate and c) Distribution of parallelepiped precipitates (smaller side and aspect ratio 2 to 5).

5.2.1.5 Annealing at 800°C for 1hr.: TEM micrograph after 1hr. annealing at 800° C is given in fig. 5.8a. With annealing coarser precipitates formed. Volume fraction of precipitates with aspect ratio 1 was increased to 2.5% and for parallelepiped precipitates, it reduced to 1 %. Wide size ranges of globular precipitates were found with average diameter at around 80 nm (fig. 5.8b). Bimodal distribution of parallelepiped precipitates was noticed. Width of smaller parallelepiped precipitates was at around 30 nm and the bigger one at around 100 nm (fig. 5.8c). Aspect ratio of these precipitates was varying from 2 to 5.

5.2.1.6 Annealing at 800°C for 10hrs. : After annealing at 800°C for 10 hrs no significant change in relative fraction of globular and parallelepiped precipitates were observed. Average diameter of globular precipitates was around 80 nm (fig. 5.9a). The fine globular particles dissolved and these particles were having narrow size range. Whereas parallelepiped precipitates grow in size and were widely spaced. The bimodal distribution of the parallelepiped precipitates was maintained (fig. 5.9b). Width of smaller size parallelepiped precipitates was at around 35 nm and the bigger one was at 125 nm. Aspect ratio of these precipitates did not change much after soaking for longer duration.
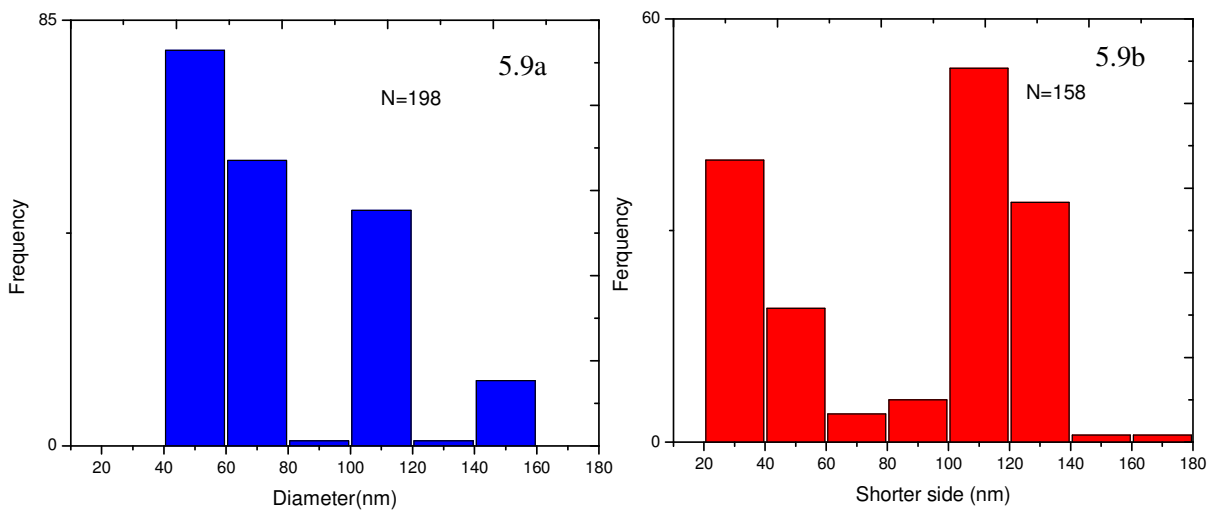
Fig. 5. 9: a) Distribution of globular precipitatein alloy 2 after annealing at 800°C for 10 hrs. and

b) Distribution of smaller side of parallelepiped precipitates (with aspect ratio around 2.5) in alloy 2 after

annealing at 800°C for 10 hrs.

5.2.1.7 Annealing in α+ β phase field (850°C/1hr.): After annealing in α+ β phase field the precipitates were seen to decorate the boundaries. The composition of these SPP is as follows: Zr: 86.64, Fe: 6.77, Cr: 1.88 & O: 4.76 at.%. The EDS profile of this type of precipitates indicated that these were Zr rich, $Zr_4(Fe_xCr_{1-x})$ type with x at around 0.7.

5.2.2 Micro-hardness Study:

The alloy in as quenched condition have hardness in the range of HV 241-246. With annealing at 700° C for 1 hr. of alloy 1, hardness reduced to HV 209 - 219 (fig. 5.10a). After 10 hrs. of
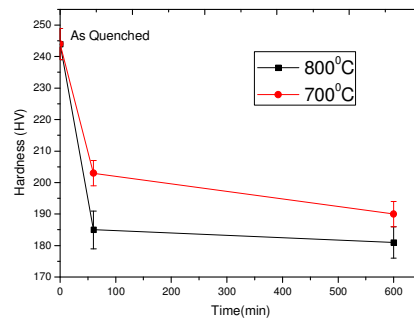
Fig. 5. 10a: Variation of hardness with annealing time in Vicker's Scale using 300 gm load in alloy-1.
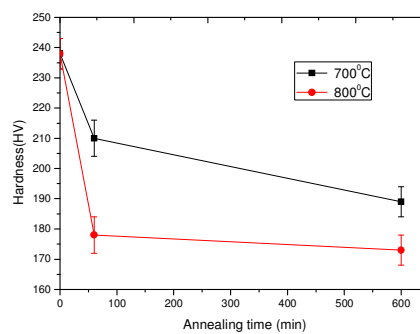
Fig. 5. 10b: Variation of hardness with annealing time in Vicker's Scale using 300 gm load in alloy-2.

annealing, it decreased to HV 186 - 197. Similar trend was observed with alloy-2 (fig. 5.10b). With annealing as-quenched microstructure transformed into equilibrium phases α Zr and second phase precipitates (SPPs). The size of these SPPs increased with time. As these precipitates were bigger in size, these were not taking part in strain hardening the material.

5.2.3 Small Angle Neutron Scattering:

SANS profiles from all the α annealed samples are depicted in fig. 5.11. If looked carefully, it is evident from the fig. 5.11a that the SANS profiles can be broadly sub-divided in three distinct zones; namely Zone-I, Zone-II and Zone-III. From TEM micrographs, it is discernible that precipitates with two different morphologies, parallelepiped and spherical, were present in the system. SANS also confirmed this. In fact, the precipitates with parallelepiped morphology were present in two widely separated length scales. It is important to mention that for the specimens annealed at $700^{\circ}C$, 15 min and $700^{\circ}C$, 1 hr. scattering signal was primarily concentrated in Zone-I. However, a tendency towards a slight increase in the scattering intensity in Zone-II was observed unlike the cases of the rest of the specimens that were annealed at higher temperature or for higher annealing time.
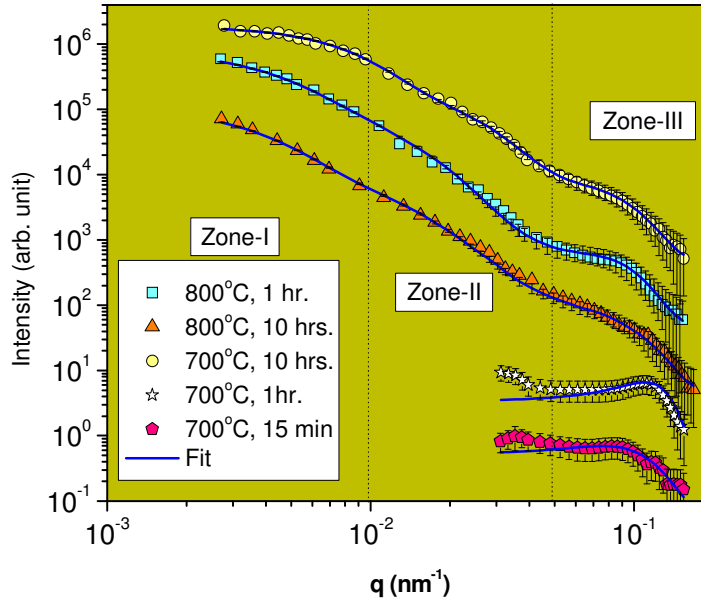
Fig. 5. 11a : Scattered points showing extracted SANS profiles from various alpha annealed heat treated samples. The solid line represents the fit of the model.

As supported by TEM results, a scattering model with additive scattering contributions from different precipitates was assumed to explain the present experimental data. Scattering intensity I(q) was expressed as

$$I(q) = N_{prl\_big} I_{prl\_big}(q) + N_{prl\_small} I_{prl\_small}(q) + N_{sph} I_{sph}(q) \qquad (5.1)$$

I_{prl_big}(q) and I_{prl_small}(q) represent the scattering intensity from parallelepiped like precipitates at larger length scale and smaller length scale, respectively. I_{sph} represents the scattering intensity from the spherical precipitates.

$$I_{prl}(q) = N_{prl} \int_0^\infty D(a) V^2(a, \beta) P_{prl}(q, a, \beta) da \qquad (5. 2)$$

P_{prl}(q, a, β) is the form factor of a randomly oriented parallelepiped with edge 'a' and height 'βa'. V represents the volume of the parallelepiped. D(a) represents the distribution of the edge size. It

is to be noted that for making the problem simpler, as the form factor involve two integration to take into account the orientation average, the edge and the height is coupled with an aspect ratio 'β'. $N_{prl}$is proportional to the number of parallelepiped precipitates.

For the third term of the equation (5. 1), similar distribution was assumed but for the radius of the spheres and form factor for the sphere was considered. A lognormal type distribution

$$D(R) = \frac{1}{\sqrt{2\pi\sigma^2 R^2}} \exp\left[-\frac{[\ln(R/R_0)^2]}{2\sigma^2} \right]$$
(5. 3)

was assumed, where R_o and σ represent median and poly-dispersity index, respectively. A hard sphere type correlation [5.16] between the spheres was needed to be considered and was used under the local mono-disperse approximation [5.17]. The estimated parameters from the SANS analysis are tabulated in the Table - 5.1.
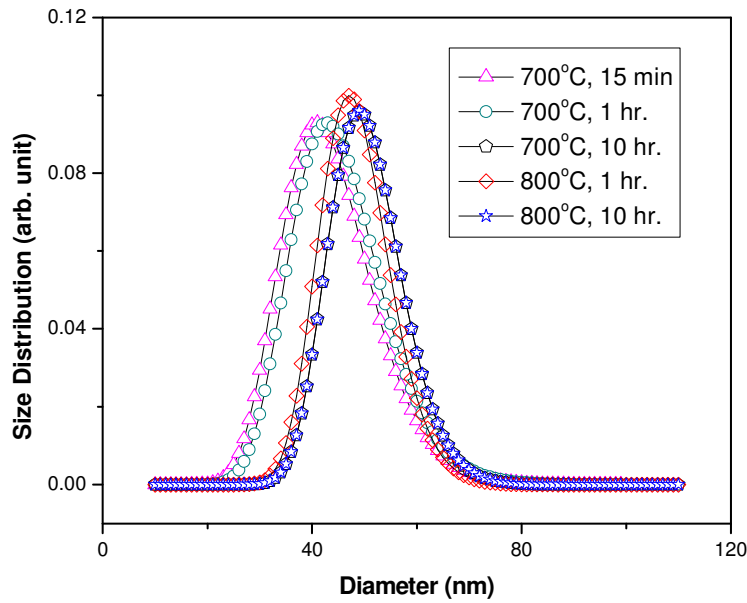
Fig. 5. 11b: Estimated size distributions of diameter of the precipitates present in different annealed conditions assuming spherical particle model.
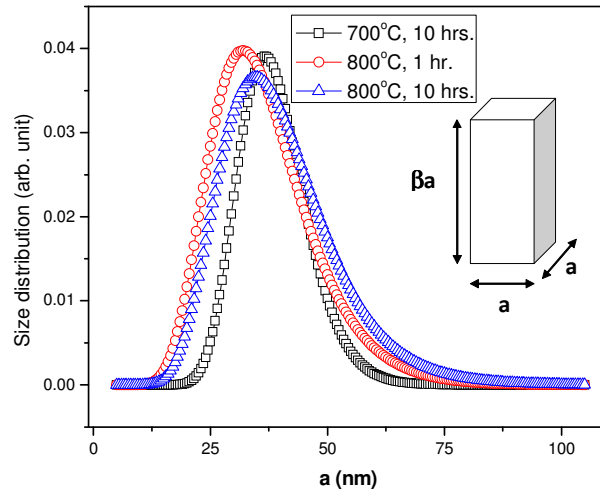
Fig. 5. 11c: Estimated size distributions of smaller length scale parallelepiped precipitates present in different annealed conditions.
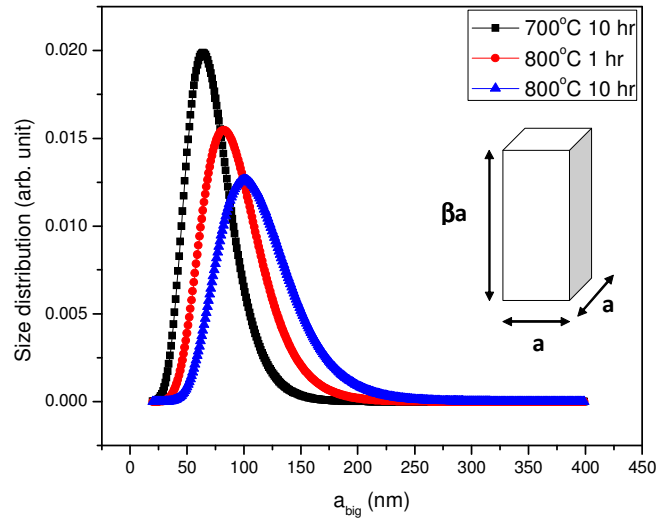
Fig. 5. 11d : Estimated size distributions of larger length scale parallelepiped precipitates present in different annealed conditions.

Table 5. 1: SANs results for different annealed conditions.

	700°C,15 min.	700°C,1hr.	700°C, 10hrs.	800°C, 1hr.	800°C, 10hrs.
a_{big} (nm)	-	-	70	90	110
σ_{big}	-	-	0.3	0.3	0.3
β_{big}	-	-	3.5	3.9	3.9
a_{small} (nm)	-	-	38	35	38
σ_{small}	-	-	0.3	0.25	0.3
β_{small}	-	-	2.5	2.5	2.5
N_{small}/ N_{big}	-	-	22.5	27	100
R_{sph} (nm)	21	22	25	24	25
σ_{sph}	0.20	0.20	0.14	0.14	0.14
ϕ_{sph}	0.12	0.12	0.12	0.12	0.12
N_{sph}/ N_{big}	-	-	12.5	15	75

5.2.4 Oxidation Study:

After accelerated autoclaving of differently heat treated alloys at 415°C, 10.3 MPa pressure for 72 hrs., weight gains of five samples for each condition were measured and the minimum and the maximum values were discarded and the average weight gain was found out from the remaining three values which are given in table 5.2. Both the materials which were annealed for shorter

duration (15 minutes) at 700°C, showed the highest weight gain or poor oxidation resistance With increasing annealing duration at 700°C, oxidation resistance during 72 hrs. autoclaving improved (fig. 5.12a). Similar oxidation behavior during accelerated autoclaving was observed in 800°C annealed samples. The oxide-metal interface was observed in SEM. The interface is wavy in nature. The amplitude of waviness is varying in wide range, around 75-175 nm in all the α-annealed samples. Periodicity is around 525 nm and it reduces with increase in oxide thickness. The relationship between weight gain and respective CAP values are plotted in fig. 5.12b.

Table: 5. 2 Weight gain vs CAP for different annealed conditions.

Sl. No.	Sample Condition	CAP(hrs.)	Alloy-1 Weight Gain(mg/dm^2)	Alloy-2 Weight Gain(mg/dm^2)	Remarks
1.	As Quenched	-	21.32	21.77	Black Lustrous Oxide
2.	700° C/15 mins.	0.35×10^{-18}	28.00	27.14	
3.	700° C/1hr.	1.4×10^{-18}	21.01	18.19	
4.	700° C/10hrs.	14×10^{-18}	16.79	11.08	
5.	800° C/1hr.	64.6×10^{-18}	22.79	17.34	
6.	800° C/10hrs.	646×10^{-18}	15.41	16.86	
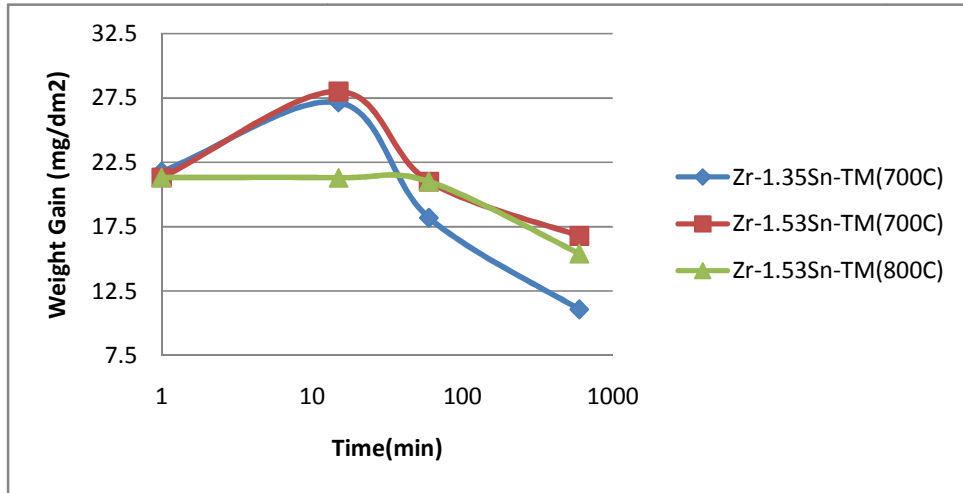
Fig. 5. 12a: Oxidation behavior of the alloy 1 (Zr-1.53Sn-TM) and alloy 2 (Zr-1.35Sn-TM) at 415°C 10.3 MPa for 3 days which were annealed at 700°C & 800°C for with different duration.
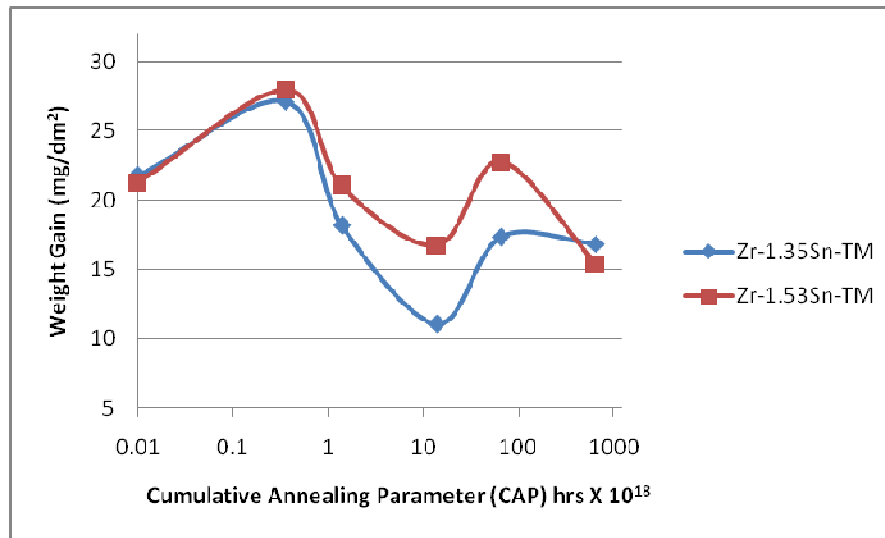
Fig. 5. 12b: Oxidation behavior after autoclaving at 415°C 10.3 MPa for 3days of alloy 1 (Zr-1.53Sn-TM) and alloy 2 (Zr-1.35Sn-TM) with different annealing conditions represented by CAP values.

It has been observed that in alloy 2

1. Highest oxidation resistance or lowest weight gain occurredat a CAP of 14×10^{-18} hrs. .
2. After that weight gain increased moderately up to CAP of 64.6×10^{-18} hrs. After that itagain reduced till 646×10^{-18} hrs CAP.

3. Higher weight gain or poor oxidation resistance was measured with very low value of CAP ($< 0.35X10^{-18}$). Similar behavior was observed for alloy 1 having 1.53 wt. % Sn. So a threshold level of CAP is required to achieve a good uniform oxidation resistance of α annealed heat treated alloy.

4. Alloy 2 shows better oxidation resistance compared to alloy 1 during α annealing treatment although in as quenched condition similar behaviour is observed.

5.2.4.1 GIXRD study: 0.5° grazing angle reflection of oxide in as quenched alloy 2 showed peaks of monoclinic ZrO_2 oxide of $(001)m$, $(\bar{1}11)m$, $(200)m$ and $(002)m$ at 17.4°, 28.3° , 34.12°and 35.3° respectively (fig. 5.13a). Very small characteristic peak $(101)t$ of tetragonal ZrO_2 peaks was found at 30.12°. Peaks at 32.2° , 36.8° and 57.3° correspond to peaks of hexagonal Zr_3O as α-Zr peaks of (100)α-Zr, (101)α-Zr and (110) α-Zr are at 31.95°, 36.51° and 56.94° respectively. Average oxide thickness is around 1.17 μm as measured in SEM and penetration of X-ray at 0.5° grazing angle is only 150 nm as discussed in section 3.2.11. So there is no probability of getting peaks of α-Zr with shift of 0.3°. 1° grazing angle reflection shows similar reflection pattern (fig. 5.13b). With increasing grazing angle to 5° peaks of matrix α-Zr at 31.95° and 36.51° were found (fig. 5.13c). The $(200)m$ plane in oxide is nearly perpendicular to the oxide metal interface as majority of oxide reflection comes from $(200)m$ in grazing angle reflection geometry.

When Sn content increased to 1.5 wt.%, 0.5° grazing angle reflection of oxide in alloy 1 in as quenched condition showed monoclinic reflection and 1° grazing angle reflection shows relatively higher fraction of tetragonal reflection compared to earlier one (fig. 5.13d). The maximum intensity ratio of $(101)t$ to $(\bar{1}11)m$ peaks (R) was 12% obtained at 1° grazing angle reflection.

When annealing is carried out at 700° C for 15 mins. in as quenched samples, poor oxidation resistance was obtained. In this condition both the alloys show maximum oxide thickness and the lowest fraction of tetragonal phase was found as revealed from R value, (maximum 10% at 5° grazing angle). The 0.5° and 1° grazing angle reflection shows only reflections from oxide (fig. 5.13e) which includes Zr_3O reflection. 5° grazing angle showed reflection from matrix along with oxide reflections which include tetragonal reflection (fig. 5.13f).
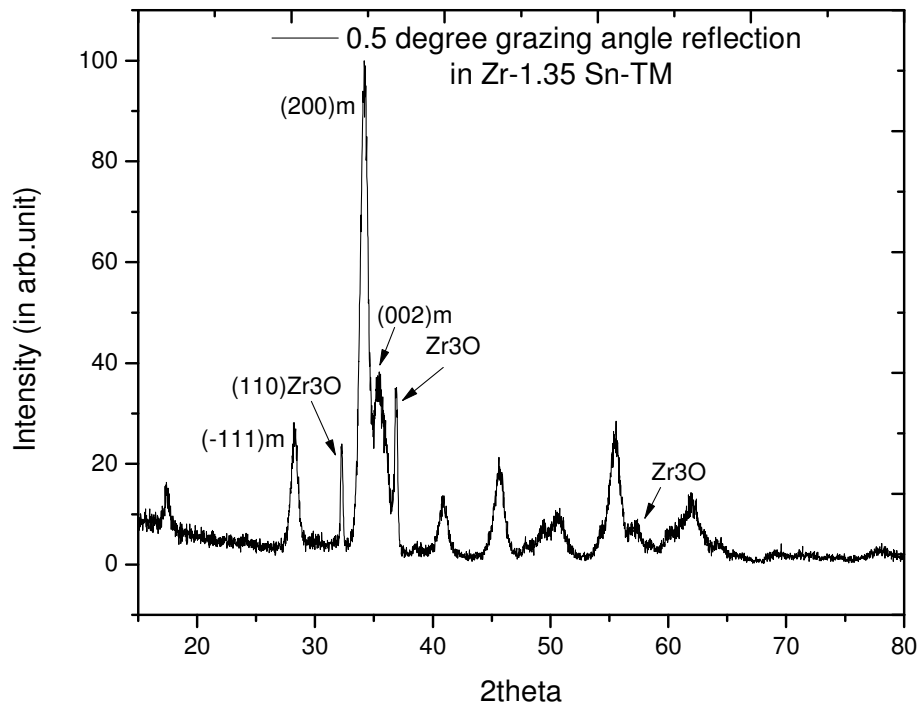
Fig. 5. 13a: 0.5° grazing angle reflection from oxide of as quenched Zr-1.35Sn-TM alloy, shows reflection from monoclinic phase, hexagonal Zr_3O reflection and very small (101) tetragonal reflection.
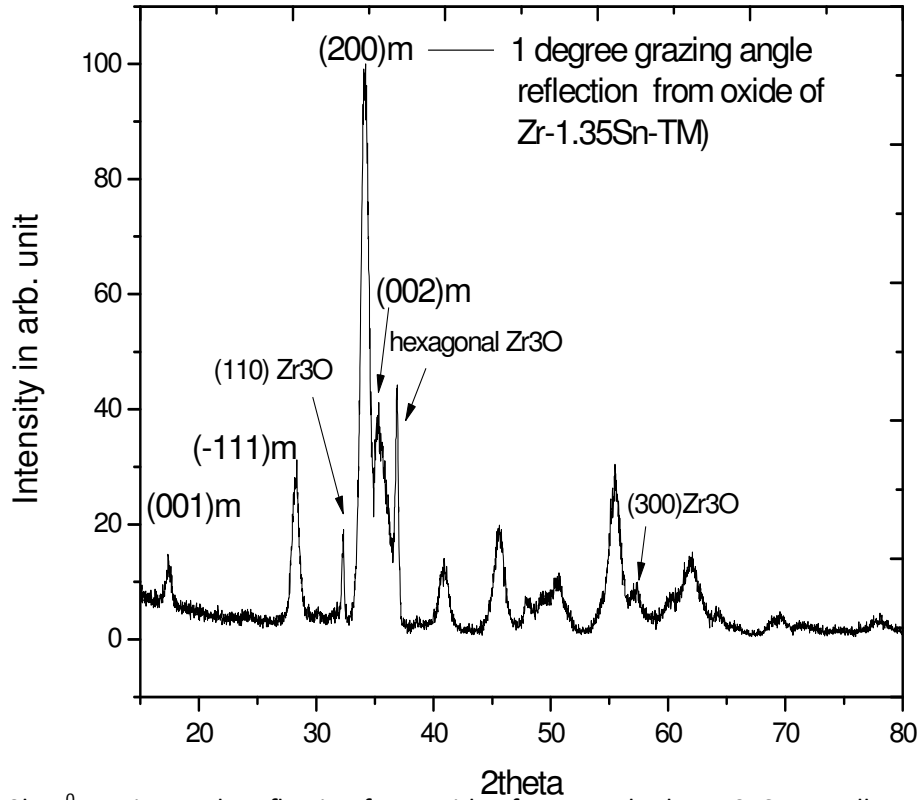
Fig. 5. 13b: 1^0 grazing angle reflection from oxide of as quenched Zr-1.35Sn-TM alloy, shows reflection from monoclinic phase, (101) hexagonal Zr_3O reflection .
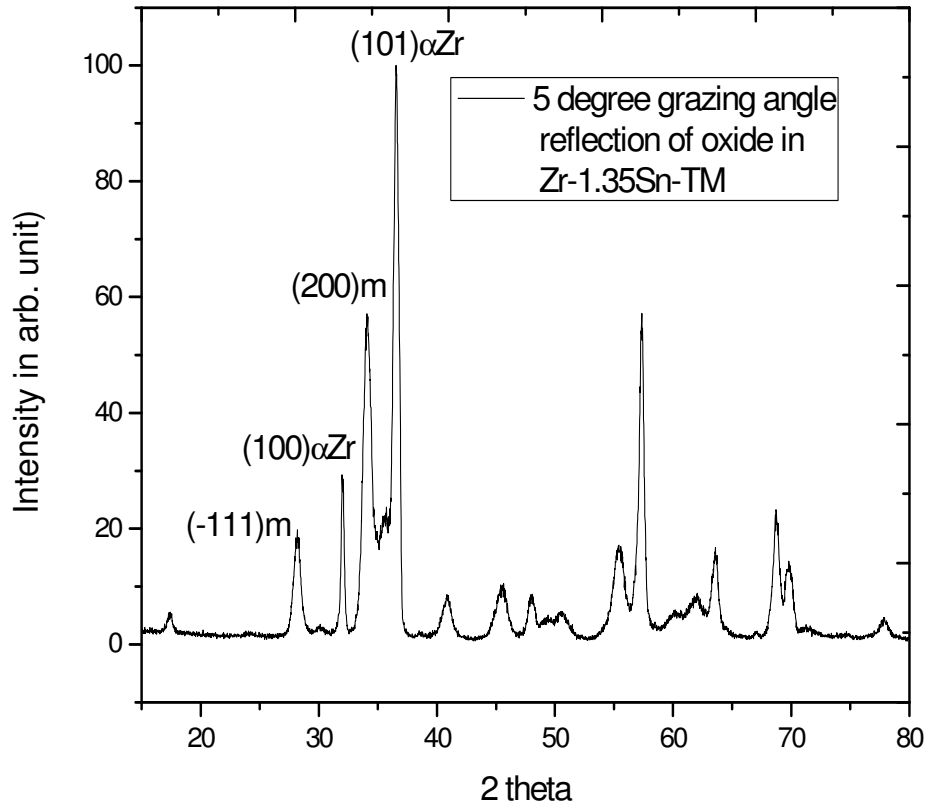
Fig. 5. 13c: 5° grazing angle reflection from oxide of as quenched Zr-1.35Sn-TM, shows majority of reflection from matrix α-Zr along with oxide.
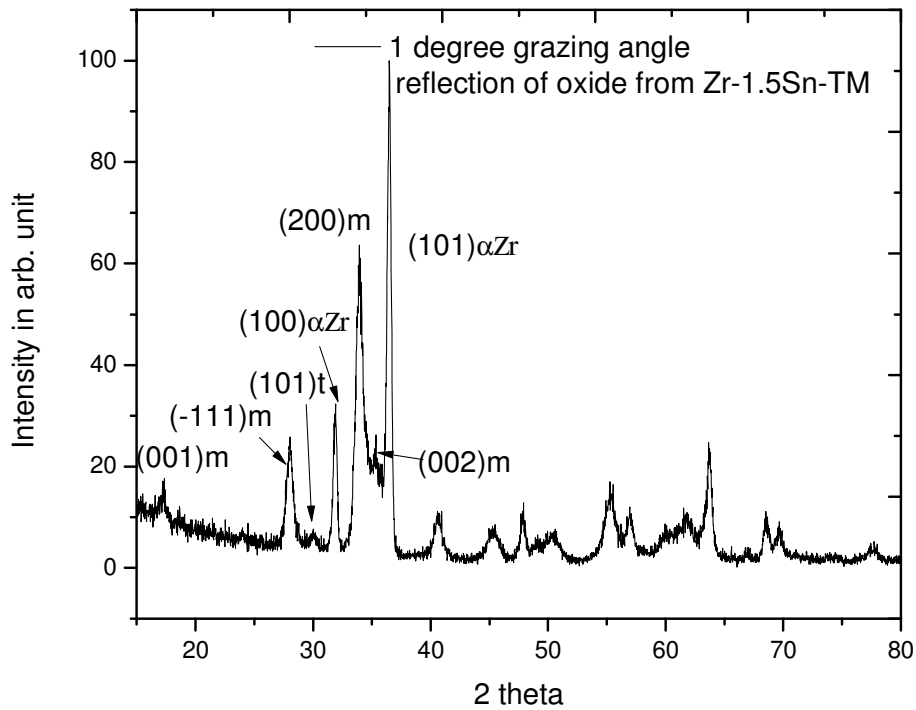
Fig. 5. 13d : 1° grazing angle reflection from oxide of as quenched Zr-1.5Sn-TM alloy, shows majority of reflection from matrix α-Zr along with monoclinic and tetragonal reflection.
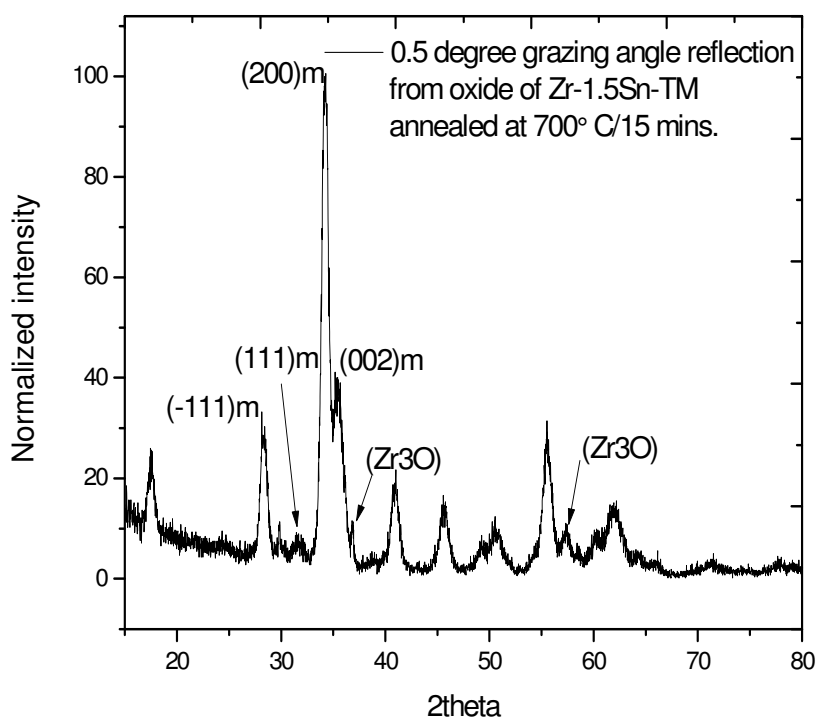
Fig. 5. 13e :0.5° grazing angle reflection from oxide of Zr-1.5 Sn-TM alloy in 700°C/15 mins. annealed condition, shows majority of reflection from monoclinic and reflection from Zr$_3$O was found.
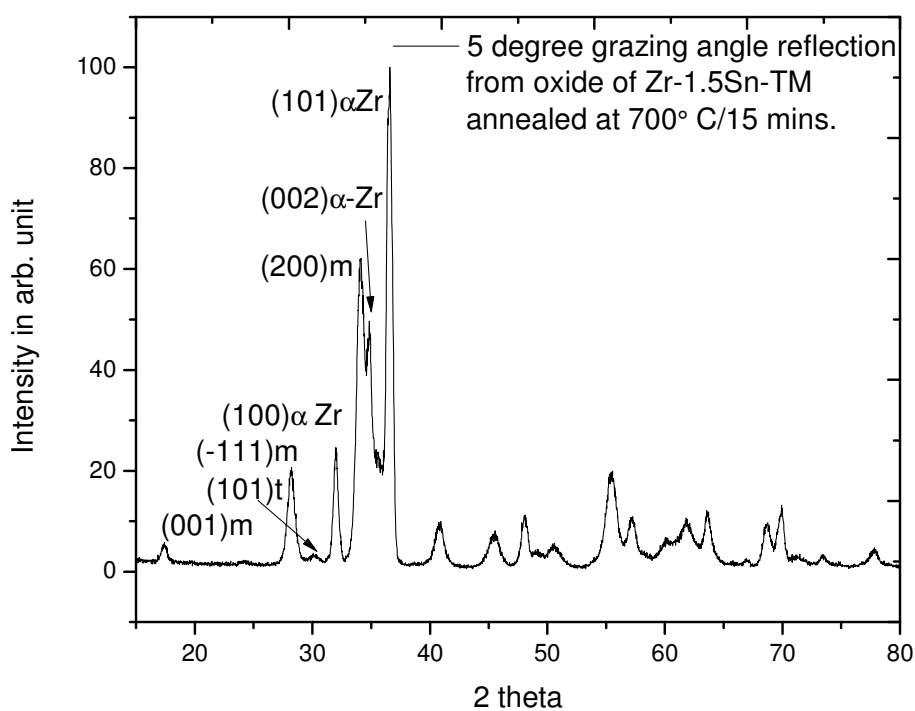
Fig. 5. 13f: 5° grazing angle reflection from oxide of Zr-1.5 Sn-TM alloy in 700°C/15 mins. annealed condition, shows majority of reflection from matrix α-Zr along with monoclinic and tetragonal reflection.

When longer duration annealing 10 hrs. was carried out, the fraction of tetragonal reflection increases as compared to shorter duration annealing (15 mins.) and maximum R value obtained was 16%.

Black oxide formed on inner surface of the fuel tube during accelerated autoclaving at 500° C 1500 psi for 24 hrs., shows monoclinic reflection upto 5° grazing reflection and at 10° reflection small peak of tetragonal reflection was present. Highest reflection is from $(\bar{1}11)m$ at 28.17°. in all the grazing angles which indicates that orientation of oxide is different compared to 415°C steam autoclaving.

The outer surface of the fuel tube which shows nodular corrosion, up to 10° reflection, no tetragonal peak was observed. The maximum reflection from monoclinic oxide is at 33.91° of $(002)m$ along with significant reflection from $(\bar{1}11)m$. Reflection from $(\bar{1}02)m$ at 35.74° is also present.
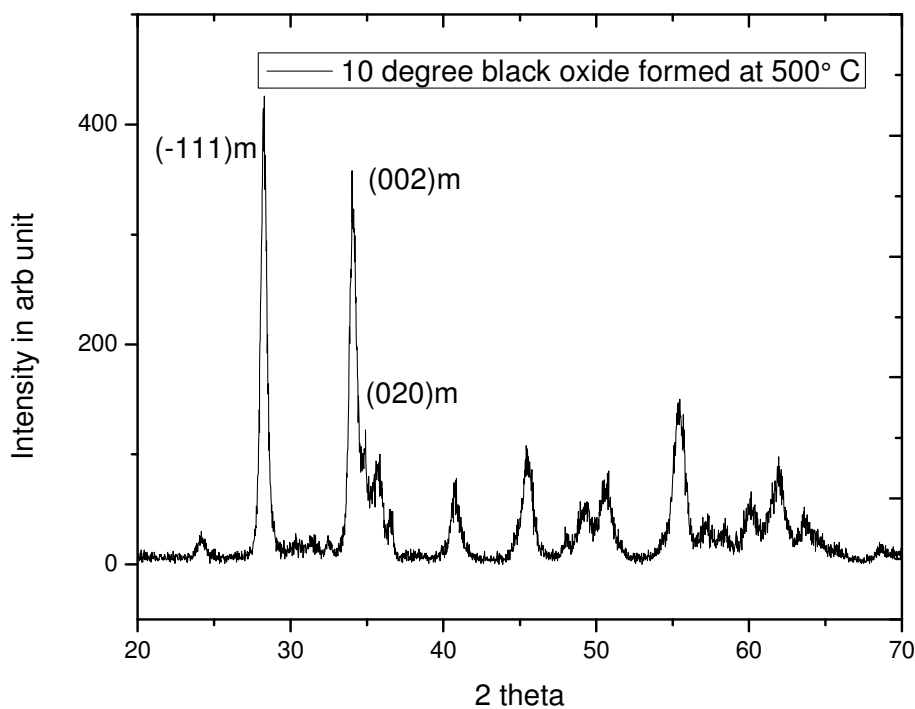
Fig. 5. 13g :10° grazing angle reflection from black oxide of fuel tube formed at 500°C autoclaving, shows majority of reflection from monoclinic ZrO_2 oxide.

5.2.4.2 XPS Analysis: XPS analysis indicated the presence of Zr and O in the surface of oxide which formed during 415° C autoclaving in all the α-annealed samples (fig. 5.14a). No peaks corresponding to chemical state of Sn, Fe, Cr was found at the outer surface of the oxide during 415° C autoclaving. The peak corresponds to 182.19 eV indicated +4 oxidation state of Zr as binding energy of Zr 3 d 5/2 comes at 182.2 eV. The doublet is separated by 2.4eV.
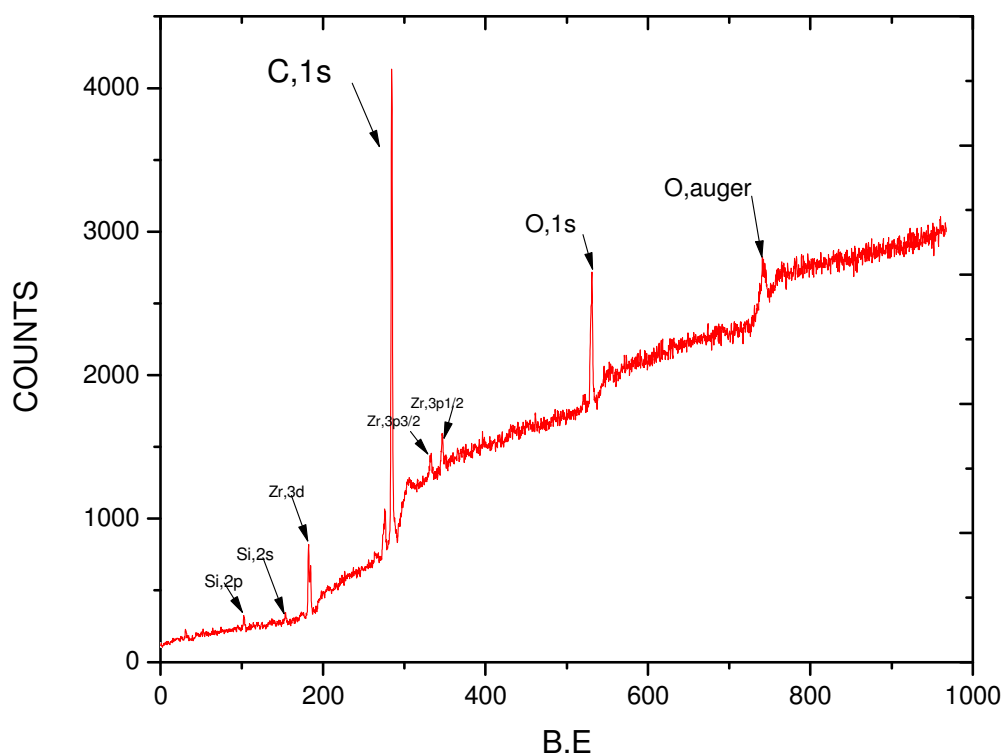
Fig. 5. 14a: Intensity of XPS lines spectra of the oxide formed during autoclaving at 415° C on α-annealed (700° C/1h.) Zr-1.3Sn-TM alloy showing Zr 3d5/2 binding energy peak at 182.1 eV. No 3d peak of Sn was found.

When autoclaving temperature was raised at 500° C 1500 psi for 24 hrs., the black oxide mostly formed in the inner surface of the fuel tube material where as outer surface showed white nodular oxide (fig.2.10b and c). XPS analysis of the black lustrous oxide as well as white nodular oxide both showed presence of Sn in the outer surface of oxide layer (fig. 5.14b and fig. 5.14c). Zr 3d 5/2 peak was observed at 182.38 eV and Sn 3d 5/2 peak was found at 485.9 eV for white oxide. For black oxide Zr 3d5/2 peak was observed at 182.22 eV and Sn 3d 5/2 peak at 486.1 eV.

The 3d 5/2 peak of zero valence state of Sn is at 485.0 eV with a std. deviation of 0.5 eV. Whereas 3d5/2 for Sn+2 is at 486.5 with 0.6 eV std. deviation and for Sn^{+4}, it is at 486.7 with a std. deviation 0.3 eV. [http://www.xpsfitting.com/2012/02/tin.html] This observation clearly emphasis the fact that higher temperature (500° C) autoclaving oxidizes Sn to a large extent to Sn^{+2} state in the both white as well as black oxide of Zr-Sn-Fe-Cr alloy and XPS analysis on the outer surface analysis can identify it. Outer surface of oxide contains Zr in +4 ionization state irrespective of temperature of oxidation.
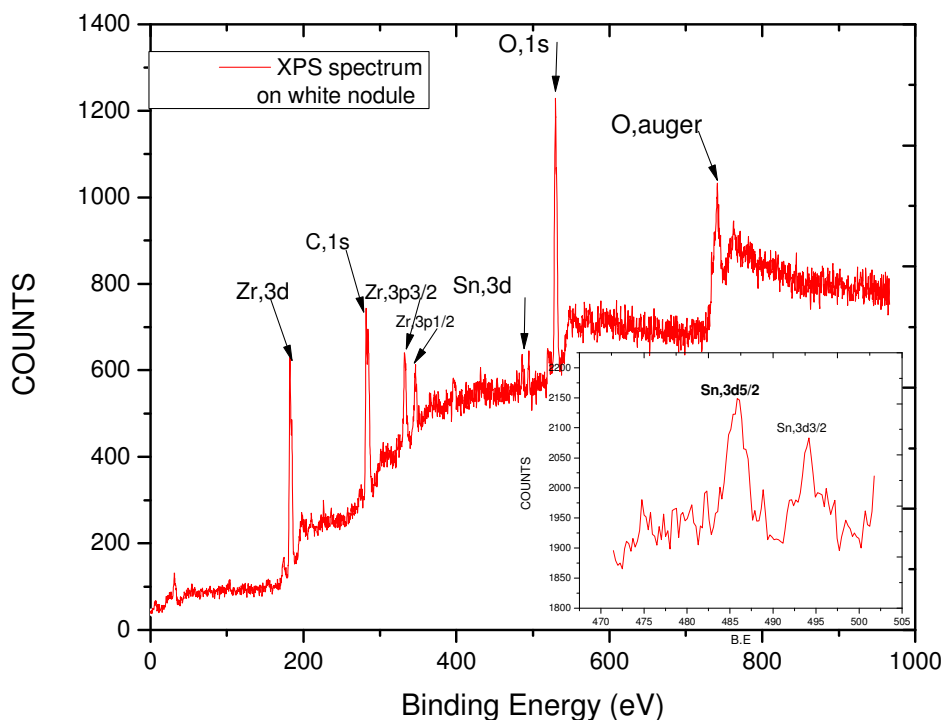
Fig. 5.14b: Intensity of XPS lines spectra of the white nodular oxide formed during autoclaving at 500°C on Zircaloy-4 fuel tube showing Sn 3d5/2 binding energy peak at 485.9 eV.
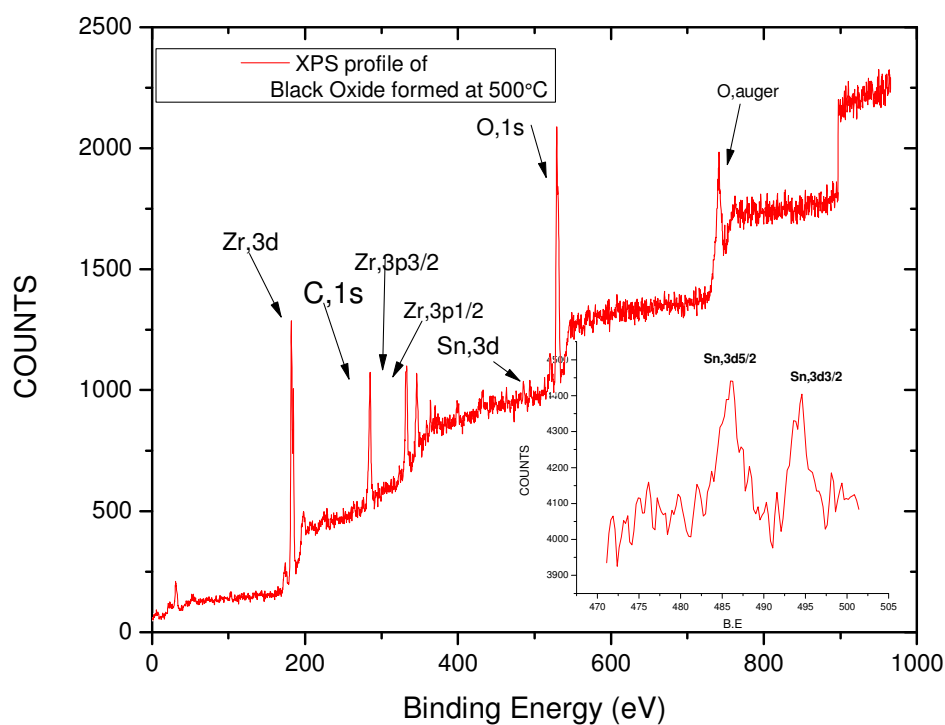
Fig. 5.14c: Intensity of XPS lines spectra of the black oxide formed during autoclaving at 500°C on inner side of Zircaloy-4 fuel tube showing Sn 3d5/2 binding energy peak at 486.1 eV.

5.2.4.3 Cross Sectional TEM:

The bright field and dark field images of oxide in cross sectional sample are shown in fig. 5.15a and fig. 5.15b respectively. The dark field images clearly indicate presence of columnar grain in the direction perpendicular to the metal oxide interface. Typical ring pattern fig. 5.15c was found in SAD image taken in oxide near metal oxide interface. This indicates that the oxide is nano-crystalline.
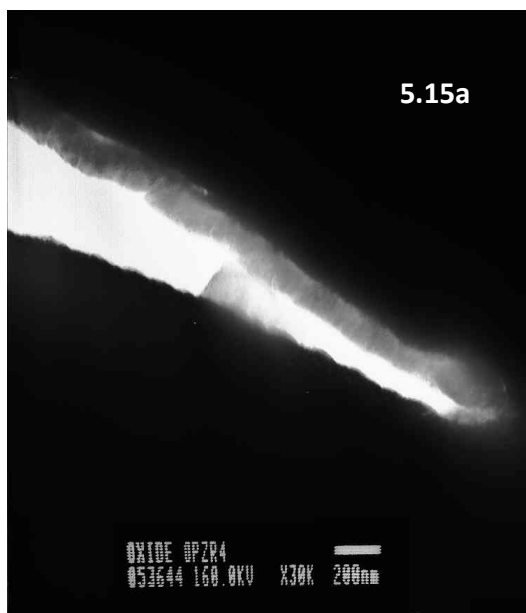
Fig. 5. 15 a. Bright field TEM image of oxide in cross sectional sample.

b. Dark field TEM image of oxide in cross sectional sample indicating columnar grains, c. Selected area diffraction pattern of oxide near oxide metal interface indicates presence of nanocrystalline grains.

5.3 Discussions:

As quenched microstructure of both Zr-Sn-Fe-Cr alloys consists of combination of several martensite packets within each beta grain and basket weave microstructure. Under polarized light each packet exhibits a separate contrast, indicating that the orientation within a given packet is nearly the same. Under TEM a number of laths which are stacked in parallel array were observed. Each lath is separated by low angle grain boundaries i.e. the misorientation between the adjacent laths is <1.5°. This lath martensite is normally observed when the transformation temperature (M_s) is relatively high and the alloy is dilute [5.18, 5.19]. When a martensite lath forms at high temperature where the matrix β phase remains relatively soft, the stain associated with formation of a lath is primarily accommodated by the plastic flow of matrix. So stress assisted nucleation of other martensite variants around the first generation laths is restricted. But the surface provided by the first formed laths acts as favorable nucleation sites for new generation laths having habit plane close to that of first formed laths and orientations are either close to or twin related with the former. As critical resolved shear stress for slip is less than twining at higher transformation temperature [5.18], promotes the operation of the slip mode at high temperature. So lath dislocated martensite is commonly observed at higher transformation temperature. Mostly precipitates free lath martensitic microstructure in as quenched condition ensures proper cooling rate. Normally very high cooling rate ensures needle type martensitic microstructure whereas intermediate cooling rate gives rise to basket weave nature where diffusion is involved and the transformation is reconstructive in nature [5.18].

From the morphology of the precipitates, mainly two types of precipitates were observed during alpha annealing heat treatment. Their EDS analysis indicated that

1. Globular precipitates of nearly $Zr_2(Fe_{.7}Cr_{.3})$ type
2. Parallelepiped precipitates mostly $Zr(Fe_{.6}Cr_{.4})_2$ type.

Some of the parallelepiped precipitates of 20 - 40 nm wide and 40 - 90 nm long, were rich in Sn content and its composition is nearly (Zr_4Sn) and it strained the matrix.

When annealing was carried out up to 1hr. at 700°C, globular precipitates of diameter around 30 nm were observed. Average size of these globular precipitates was not found to change much during holding for longer length of time (10 hrs.) at 700°C. But very few precipitates with coarse size (70 - 120 nm) were formed in the matrix after 10 hrs. annealing which were totally absent

initially. Similar behavior was observed for parallelepiped precipitates. Aspect ratio of this type of precipitates was raised with longer duration of holding at 700°C which confirmed that these were growing more at length direction.

When temperature is raised to 800°C, globular precipitates grow appreciably in size. The average diameter of these precipitates increased to 80 nm and some precipitates were observed with a diameter of 160 - 200 nm. With further annealing (10 hrs.) at same temperature, smaller globular precipitates less than 40 nm dissolved and coarser precipitates grew in size. In case of parallelepiped precipitates, when temperature is raised to 800°C, bimodal distribution of precipitates was observed. Further annealing for 10 hrs., this bimodal distribution of the parallelepiped precipitates was maintained.

For the specimens annealed at 700°C for 15 mins. and 1hr., scattering intensities were primarily concentrated in Zone-III. Size distribution of the precipitates was estimated from these SANS profiles considering poly-dispersed spherical particle model. Diameter distribution showed a mode at around 40 nm. It is to be mentioned that for these two specimens, no significant scattering signal was observed at lower q region although a slight increasing trend was observed at the boundary of zones-III and II. This suggests a presence of some bigger precipitates, with small enough number density. In fact, some bigger parallelepiped type precipitates was indeed observed from TEM micrograph. Microstructure under TEM showed presence of a very small fraction of parallelepiped precipitates with size in same length scale with aspect ratio varying from 2.5 to 3.

In case of samples annealed at 700°C for 10hrs., 800°C for 1hr. and 10 hrs., respectively, SANS profiles give bimodal type distribution of parallelepiped precipitates. The average edge-size of the finer parallelepiped precipitates in all the cases has been found to be nearly 40 nm with aspect ratio (β_{small}) 2.5 while that for the larger parallelepiped precipitates, has been 70, 90, 110 nm respectively with aspect ratio (β_{big}) 3.5 - 3.9. SANS also supported the presence of (diameter) finer precipitates in all the above three alpha annealed heat treated samples. Assuming the morphology of these precipitates as spherical (as observed from TEM), the distribution of these precipitates were estimated from SANS data. A growth in precipitate radius was found for all the above three specimens in comparison to that of the samples annealed at 700°C for 15 mins. and 1 hr. In the former samples the average diameter has been found to be nearly 40 nm while that for the later samples were nearly 50 nm. From TEM, presence of precipitates with 80 nm was also

observed. It is worthy to be mentioned at this juncture that slight difference in the radius obtained from TEM and SANS is due to the fact that SANS gives statistically averaged information from bulk unlike that is observed in local zones in TEM. TEM and SANS (table 5.1) both data indicate that 700°C/10 hrs. annealing heat treatment which is corresponding to CAP value 14×10^{-18} gives highest number density of big parallelepiped precipitatesas compared to other heat treatments. When annealing is performed at higher temperature, number density of parallelepiped precipitates reduces but they grow in size.These precipitates are Zirconium lean $Zr(Fe_{0.6}Cr_{0.4})_2$ and the structure is C14. $Zr(Fe, Cr)_2$ precipitates can be either h.c.p or fcc crystal structure depending on composition and heat treatment and usually show the characteristic stacking fault. Both the structures are Laves phases. Shaltiel et al. [5.20] in a study using X-ray diffraction established criteria for the crystal structure of Zirconium precipitates. For $Zr(Fe_xM_{1-x})_2$ (M = V, Cr, Mn; 0 < x < 1), the precipitateis predicted to be hexagonal (hcp) when x < 0.8 and (cubic) fcc when x > 0.9. The observation cubic $Zr(Fe_{0.1}Cr_{0.9})_2$ precipitates in Zr base alloys extends the condition that $Zr(Fe_xCr_{1-x})_2$ is cubic when x < 0.1 or x > 0.9. EDS analysis of all the parallelepiped precipitates observed after alpha annealed heat-treatment shows that the x value is always less than <0.8 (0.6-0.7) and accordingly these are having hcp crystal structure. Presence of $Zr_2(Fe, Cr)$ precipitates in alpha annealed Zircaloy-4 had also been reportedby other author [5.21]. Volume fraction of these $Zr_2(Fe, Cr)$ precipitates is enhanced with high α annealing compared to $Zr(Fe, Cr)_2$.

When annealing is carried out in the α+ β phase field due to reduction in driving force for precipitation, precipitates are mostly seen to decorate the grain boundaries and at low angle grain boundaries. These precipitates are having composition near to $Zr_4(Fe_{.7}Cr_{.3})$. This phase has a face-centered cubic crystal structure [5.21].

The variation in the morphology and chemistry of the second phase particles as a function of heat-treatment in Zr-Sn-Fe-Cr base alloys was addressed by very few previous studies. Earlier studies [5.22- 5.23] emphasized on identification of second phase particles in certain heat-treatments. Vandersande and Bement [5.23] identified the second phase particles in annealed Zircaloy 4 sample to be primarily the hexagonal, Laves $Zr(Fe Cr)_2$ type. Mukhopadhyay et al. [5.24] observed fine precipitates mostly cubic $ZrCr_2$in β-quenched Zr-1.9 wt. % Cr alloy. Later, Kuwae et al. [5.9] studied the intermetallic particles in α annealed heat treated and α + β quenched Zircaloy-4. They observed elemental Sn in both the samples in addition to Zr-Cr-Fe

intermetallic particles. While the intermetallic particles in the α-annealed sample have been concluded to be the hexagonal Zr(Cr, Fe)$_2$ the nature of these particles in the a + β quenched sample has not been conclusively established. In the present study, no evidence for elemental Sn was found but formation of very small fraction of Sn rich precipitates with surrounding region lean in Sn was noticed which indicated that it might precipitate out from matrix during cooling from α annealing temperature as these were absent in as quenched condition. In as quenched condition Sn content in matrix is found to vary in close range. As regards the intermetallic particles, the chemistry variation with heat-treatment shown in the present study appears to be consistent with what one would expect from equilibrium considerations. In Zr-rich alloys of the Zr-Fe system, the equilibrium precipitate is Zr$_2$Fe or Zr$_4$Fe. This is consistent with the observations made with the high α-annealed (800°C) Zr-Sn-Fe-Cr samples which shows precipitates predominantly of the type Zr$_2$(Fe, Cr) and α+β annealed samples with mostly Zr$_4$(Fe, Cr) precipitates. Lower temperature annealing may have less opportunity to attain equilibrium and that is why highest number density of Zr(Fe, Cr)$_2$ precipitates form at 700° C.

From the accelerated oxidation experiment, it has been observed that both the alloys with 1.35 wt.% Sn and 1.53 wt.% Sn in as quenched condition, show similar oxidation resistance.While alloy 2 with lower Sn content shows more resistance to oxidation as compared to alloy 1 in all the α annealed heat treated conditions. GIXRD study indicated that the oxide in as quenched 1.53 wt. % Sn alloy contains relatively higher fraction of tetragonal phase with respect to as quenched 1.35 wt. % alloy which is consistent with the fact that Sn stabilizes tetragonal phase. This can be concluded that the beneficial effect of Sn in stabilizing tetragonal phase may be counteracted or overpowered by deleterious effect of Sn on increasing the oxygen anion vacancies which can facilitate diffusion of oxygen ions through oxide at high temperature steam. XPS analysis of outer surface of the oxide formed at 500° C steam clearly indicated +2 ionization state of Sn in oxide which can increase significant amount of oxygen ion vacancies in the oxide and subsequently oxygen diffusion. The absence of Sn 3d5/2 peak in XPS spectra of oxide formed at 415° C may be due to the lower rate of oxidation of Sn at 415°C as compared to 500° C and hence is below detectable limit.

Initially, with shorter duration (15 mins.) α-annealing of parent metal, the tetragonal fraction present in the oxide layer at 415° C, reduced but again increases with longer duration α-annealing (10 hrs.) as measured by GIXRD technique. With shorter duration annealing (~15

mins.) at 700°C, oxidation resistance of the alloys degrades. In as quenched condition microstructure consists of mostly precipitate free widmanstatten lath formed by diffusional transformation. With annealing for 15 mins. at 700°C very fine precipitates are forming and matrix alloying elements may in-homogeneously reduce. In this condition alloy shows poorest oxidation resistance. Surface to volume ratio of the fine particles present in the matrix is very high, and can lead to more stored energy in the material causing poor oxidation resistance. These fine precipitates may also not be sufficient to generate required strain in the lattice to stabilize the tetragonal form of oxide as measured in GIXRD. With longer duration annealing at same temperature, alloying element content in matrix reduces, simultaneously precipitates are growing in size and oxidation resistance of the alloys improves and tetragonal fraction increases. So a minimum size of precipitates is required to get good uniform corrosion resistance of the alloy. 700°C 10 hrs.α annealing treated sample showed the best oxidation resistance. In this condition, the material is having the highest number density of parallelepiped precipitates (Avg. side length 70 nm with aspect ratio 3.5) which are Zr lean hexagonal $Zr(Fe\ Cr)_2$ and these were uniformly distributed. The corresponding CAP value is CAP of 14×10^{-18}. EDS analysis of samples in this condition also indicates the presence of few fine parallelepiped precipitates that were enriched with Sn. And its surrounding matrix is void of Sn. When annealing was carried out at still higher temperatures (800° C for shorter duration), number density and volume fraction of Zr rich $Zr_2(FeCr)$ globular precipitates (with Avg. diameter 80 nm) increases as compared to $Zr(FeCr)_2$ precipitates. But spacing between the precipitates was non uniform and wide size range of $Zr_2(FeCr)$ precipitates was present which may be responsible for higher weight gain during autoclaving. With longer duration annealing at same temperature lead to formation of uniformly spaced narrow range of coarser precipitates and improved the resistance to oxidation.

5.4 Summary

> Complete Recrystallized microstructure was observed in α annealed (700°C/10 hrs.) Zr-Sn-Fe-Cr alloys. Globular $Zr_2(Fe_{0.7}Cr_{0.3})$, parallelepiped like $Zr(Fe_{0.6}Cr_{0.4})_2$ and a few fine Sn rich parallelepiped Zr-Sn precipitates in α annealed Zircaloy-4 were revealed by TEM/STEM with EDS. Significant resistance to oxidation appears after 10 hrs. of annealing at 700°C. TEM and SANS confirmed that at this condition the alloy contains the highest number density of uniformly distributed relatively coarser parallelepiped

precipitates. To get good uniform oxidation resistance of the alloy a threshold size of precipitates with uniform size distribution are required. Even high temperature shorter duration annealing did not lead to good oxidation resistance. Longer duration annealing is beneficial for improving uniform resistance of the alloy.

➢ Initially with shorter duration (15 mins.) α-annealing of parent metal, the tetragonal fraction present in the oxide layer at 415°C, reduces but again increases with longer duration α-annealing (10 hrs.). With longer duration annealing at same temperature alloying element content in matrix reduces, simultaneously precipitates are growing in size and oxidation resistance of the alloys improves.

➢ High α annealing leads to formation of $Zr_2(FeCr)$ precipitates.

➢ TEM/STEM with EDS indicates the presence of $Zr_4(Fe_{0.7}Cr_{0.3})$ precipitates in α+β annealed state.

➢ Cross sectional TEM diffraction pattern indicates presence of nanocrystalline oxide grains near oxide metal interface.

➢ GIXRD indicates presence of relatively higher fraction of tetragonal phase in oxide of as quenched Zr-1.56 wt. % Sn-Fe-Cr alloy compared to Zr-1.35 wt. % Sn-Fe-Cr alloy which confirms Sn stabilizes tetragonal structure of oxide.

➢ As both the alloys behave similarly in as quenched condition, where second phase precipitates are not present, the beneficial effect of Sn in stabilizing tetragonal phase may be counteracted by deleterious effect of Sn on increasing the oxygen anion vacancies which can facilitate diffusion of oxygen ions through oxide at high temperature steam.

➢ GIXRD also showed presence of hexagonal sub-oxide Zr_3O along with monoclinic ZrO_2 oxide. Near the interface tetragonal ZrO_2 was detected.

➢ XPS analysis of oxide formed at 500° C clearly indicates +2 ionization state of Sn in both oxide, the black lustrous oxide as well as white nodular oxide. This +2 ionization state can increase significant amount of oxygen ion vacancies in the oxide and subsequently oxygen diffusion. The absence of Sn 3d5/2 peak in XPS spectra of oxide formed at 415° C may be due to the lower rate of oxidation of Sn at 415°C compared to 500° C and hence is below detectable limit.

➢ GIXRD study of nodular oxide formed during 500°C autoclaving, indicated absence of tetragonal phase up to 10° grazing angle reflection whereas the black oxide formed at

same temperature contained tetragonal oxide. The orientations of oxide crystallites formed at 500°C is significantly different from oxide formed during 415°C autoclaving.

5.5 References:

[5.1] G.P. Sabol, Gerald R. Kilp, Malcolm G. Balfour, Elwyn Roberts, Zirconium in Nuclear Industry, 8th Inter. Symp., ASTM STP 1023, 227-245.

[5.2] Garde A.M., Smith G.P., Pirek R.C., Zirconium in the Nuclear Industry: 13th Inter. Symp., ASTM STP 1423, G.D. Moan and P. Rudling, Eds., ASTMInternational, West Conshohocken, PA, 2002, 490-506.

[5.3]Waterside corrosion of zirconium alloys in nuclear power plants, IAEA TECHDOC-996, 124-169.

[5.4] Bossis P., Pêcheur D., Hanifi K., Thomazet J., Blat M., Zirconium in the Nuclear Industry: 14th   Inter. Symp., STP1467-EB, 2005.

[5.5] David G. Franklin and P.M. Lang, 9th Int. Symp. on Zirconium in Nuclear Industry, ASTM-STP-1132(1991), 3-32.

[5.6] Adamson R. B., Cox B., Garzarolli F., Strasser A., Rudling P. and Wikmark G., Special Topical Report on "Corrosion of Zirconium Alloys", ZIRAT-7, Dec., 2002.

[5.7] B. Cox,J. Nucl. Mater. 336 (2005) 331‾368.

[5.8] C.T.Wang, C.M.Eucken and R.A.Graham, Zirconium in the Nuclear Industry, 9th Inter. Symp., ASTM STP1132.Philadelphia,1990, 319-345.

[5.9] KuwaeR., J. Nucl. Mater., 1983, Vol.119, 229-239.

[5.10] Schemel, J.H, Zirconium in the Nuclear Industry, 7th Inter. Symp., ASTM STP 551, 1987, 243-256.

[5.11] E.R.Bradley, J.H. Schemel, and A.L. Nystrom, Zirconium in the Nuclear Industry, 9th Inter. Symp.,, ASTM STP1132.Philadelphia,1990, 304-316.

[5.12] W.J.S.Yang , R.P.Tucker, B.Cheng, R.B.Adamson,J. Nucl. Mater., 138 (1986) 185-195.

[5.13] Goll, W. and Ray L., Zirconium in the Nuclear Industry: 13th Inter. Symp., ASTM STP 1423, G.D. Moan and P. Rudling, Eds., 2002, 80-95.

[5.14] S.Mazumder, D. en, T. Sarvanan, P.R. Vijayraghavan, J. Neutron Res. 9 (2001)39.

[5.15] J. A. Lake, Acta Cryst. (1967). 23, 191-194

[5.16] Aschroft, N. W.; Lekner, J. Phys. Re . 1966, 145,83- 90.

[5.17] Pedersen, J. S. J. Appl. Cryst. Sci. 1994, 7, 595- 608.

[5.18] Martensitic Transformation, Phase Transformations: Examples from Titanium and Zirconium Alloys, S.Banerjee and P. Mukhopadhyay, Pergamon Materials Series, Vol.12, 260-335.

[5.19] Diffusion less Transformation, Phase Transformations in Metal and Alloys, by David A. Porter and K. E. Easterling, 382-426.

[5.20] D. Shaltiel, Jacob and D. Davidov, J. Less-Common Metals 53 (1977) 117.

[5.21] N. (Rao) V. Bangaru, J. Nucl. Mater.,131 (1985) 260-290

[5.22] W.J.S. Yang, R.P. Tucker, B. Cheng and R.B. Adamson, J. Nucl. Mater., 138 (1986)185-195.

[5.23] J.B. Vandersande , A.L. Bement, J. Nucl. Mater., 52 (1974) 115.

[5.24] P. Mukhopadhyay, V. Raman, S. Banejee and R. Krishnan, J. Mater. Sci. 14,(1979) 1398.

Chapter 6

Influence of Fe content and β-phase on Corrosion and Hydrogen pick up behaviour of Zr-2.5Nb pressure tube material

This chapter describes the effects of alloying element (Fe) and heat treatment on microstructure evolution in Zr-2.5Nb alloy and its importance on oxidation behaviour of the alloy.

The effects of Fe addition in the range of 300-1250 ppm in cold worked stress-relieved Zr-2.5Nb pressure tube on oxidation and hydrogen pick up behaviour have been studied after 415°C steam autoclaving. The effect of β-phase on the corrosion performance of the alloy has also been studied. Microstructure and micro chemistry of second phase and precipitates were characterized using electron microscope. The chemical state of oxide has been determined by X-ray photo electron spectroscopy. The phase fraction and distribution of stress in oxide in all the three alloys has been studied using Grazing Incidence X-ray Diffraction.

6.1. Introduction

Fe is considered an alloying element in Zircaloy [6.1] and Zirlo [6.2] and is a beta phase stabilizer. In α phase, Fe solubility is very low [6.3], (maximum solubility of 120 ppm at 700°C). At usual concentrations in Zr base alloys, Fe is fully soluble in β phase but precipitates out in α-phase as Zr_3Fe, Zr_2Fe, $ZrFe_2$ [6.3-6.13]. Some studies indicated that Fe may be attached with silicide particles and may be mistaken for Zr-Fe particles [6. 14]. After complete decomposition of β phase (500°C /750 hrs. heat treatment) to β-Nb (Zr - 80% Nb), Fe has been seen to be associated with Nb in a form which is interpreted as $(ZrNb)_3FeCr$ where Cr is an additional impurity [6.14, 6.15]. These intermetallic precipitates depending on their composition and crystal structure play an important role in controlling microstructure, corrosion and hydriding behavior of the Zr base alloys [6.1, 6.4, 6.16, 6.17, 6.18, 6.19].

Cold worked and stress-relieved Zr-2.5Nb is used for pressure tubes in pressurized heavy water reactors (PHWRs). Fabrication flow sheet of these Zr-2.5Nb pressure tubes mainly consists of vacuum arc melting, forging and extrusion at 800°C followed by 2-stage cold drawing to obtain 20 - 30% cold work in the final product [6.20]. The final step is autoclaving at 400°C to produce

a protective black lustrous oxide layer [6.20, 6.21] and to relieve the internal stresses. In place of hot extrusion and cold drawing route, hot extrusion followed by a 2-stage cold - pilgering with intermediate annealing at 550°C ± 10° C for 6 hrs.has also been established [6.22]. This route is being followed for pressure tube fabrication for the Indian PHWRs. Stress relieving of the finished tubes takes place during steam autoclaving (400°C for 36 hrs.) [6.23]. The microstructure of the tube consists of flat, elongated α-Zr grains containing about 1 at.% Nb and a high dislocation density with β phase sandwiched between α-lamellae having composition ~20 at.% Nb [6.22, 6.23]. Generally, α grain size in radial direction is 0.3 - 0.5 µm keeping the aspect ratio 1:5:50 (radial: transverse: axial direction). This grain morphology gives strength and prevents formation of radial hydrides during reactor operation [6.22]. The β-Zr phase present in pressure tube is meta-stable at reactor operating temperature (260-300˚C), being much below the monotectoid temperature (610˚C) and on heating, progressively decomposes to α-Zr phase and β phase enriched with Nb and ultimately forms β-Nb (Zr - 85 wt. %Nb). Meta-stable ω-phase precipitates as an intermediate step during decomposition depending on the heat treatment schedule as shown in equation 6.1 [6.23]. This transformation (β Zr to α + β Nb) is very sluggish at lower temperature and complete transformation does not occur. For this reason β stringer and partially decomposed β particle are retained in α/α grain boundary and Nb content is found to be varying from 7- 22 at.% depending upon extent of decomposition.

$$\beta_{Zr} \rightarrow \alpha + \beta_{Nb\ enriched} \rightarrow \alpha + \omega + \beta_{Nb\ enriched} \rightarrow \alpha + \beta_{Nb\ enriched} \rightarrow \alpha + \beta_{Nb} - - - (6.1)$$
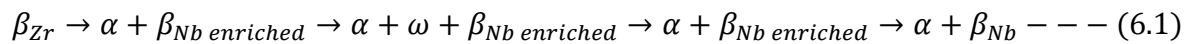
The oxidation and hydrogen pick up behaviour of the alloy is controlled by the characteristics of the oxide formed on the base alloy. The oxide formed on base metal is very much sensitive to its matrix microstructure and micro-constituents [6.18]. So the study of matrix as well as oxide formed near metal - oxide interface is important. The oxide of pure Zr metal is not protective at all. With addition of small amount of alloying elements protective oxide forms and oxidation behaviour of the alloys is improved. It is well known that for Zr base alloys slight differences in composition with or without any appreciable change in microstructure lead to significant difference in oxidation and hydrogen pick up behaviour. Even during ageing at reactor operation, corrosion resistance of Zr–2.5Nb improves [6.1]. The improved corrosion resistance has been attributed to the radiation-enhanced precipitation of fine β Nb particles and the concomitant reduction of the Nb concentration in the α-Zr during irradiation. However, full mechanistic

understanding of oxide formation in alloy with different matrix microstructure or having different micro-constituents has not been achieved so far.

Fe is considered as an impurity element in pressure tube and its specified limit is 650 ppm (max.). This limit has been specified on the premise that increased density of Zr-Fe intermetallic precipitates may increase the deuterium pick up rate. Recent in-service inspection results indicated lower axial elongation in pressure tubes that contained higher Fe impurity [6.24]. Axial creep of 6.64 mm was observed during 3340 effective full power days in tubes containing mainly higher Fe content (>800 ppm) compared to 32.24 mm in tubes containing lower Fe content (< 300 ppm) [6.24, 6.25]. This study was undertaken to assess the scope of relaxation in Fe impurity limit in pressure tube material.

The material used in the present study is the off-cuts of Indian PHWR's pressure tubes manufactured by Nuclear Fuel Complex, Hyderabad by a process of extrusion followed by two stage pilgering with intermediate annealing. Three compositions of dilute Zr-2.5Nb alloys were selected having Fe 300 ppm, 800 ppm, 1250 ppm. Samples were received after 400°C / 24 hrs. stress relieving in steam autoclave. The out of pile oxidation test were carried out and philosophy behind choosing the time and temperature are described in section 3.2.2. In-reactor uniform corrosion performance of the Zr-2.5Nb alloys with varying Fe content, has been ranked from the results of short term (3 days) accelerated out of pile autoclaving at 415° C. Correspondingly hydrogen intake behaviour of all the three alloys during 3 days autoclaving test has been evaluated. XPS analysis was carried out to establish the chemical state of oxide formed during accelerated autoclaving at 415° C high pressure steam. To get the distribution of phases and stresses in through thickness, GIXRD was done. Results of corrosion tests, hydrogen pick up and their correlation to matrix microstructure and distribution of phases, stress in oxide and its morphology as well as chemical state of oxide of the alloys are discussed in the paper.

6 .2 Results:

6.2.1 Microstructures and characteristics of the precipitate or second phase.

Two phase lamellar structure of α and β phases were observed in all the three alloys in as received condition as shown in fig. 6.1a, 6.2a, 6.3a respectively. The average volume fraction of

β phase in alloy 3 and 4 was 2.0 %. The width of α grain size in alloy 3 was 0.18 - 0.24 μm with aspect ratio greater than 10. Heterogeneous distribution of β phase was found.

Fig. 6. 1a: Transmission electron micrographs Zr-2.5Nb pressure tube material in alloy 3, showing elongated α-Zr grains surrounded by β-phase.
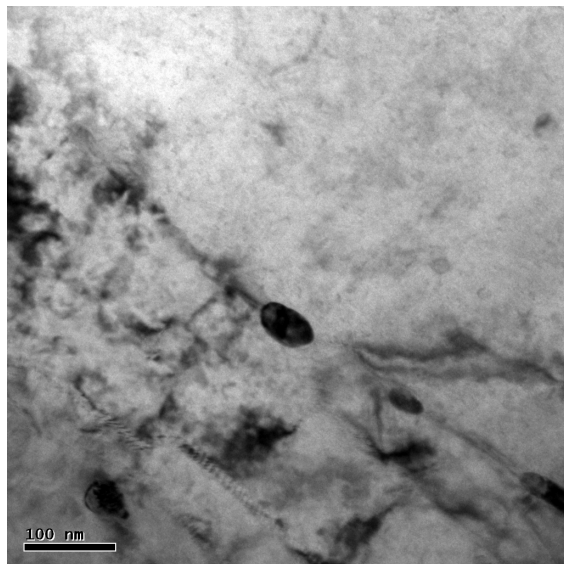
Fig. 6. 1b: Bright field transmission electron micrographs of Zr-2.5Nb pressure tube material in alloy 3, showing discontinuous β at α-α grain boundary as well as within α grain.
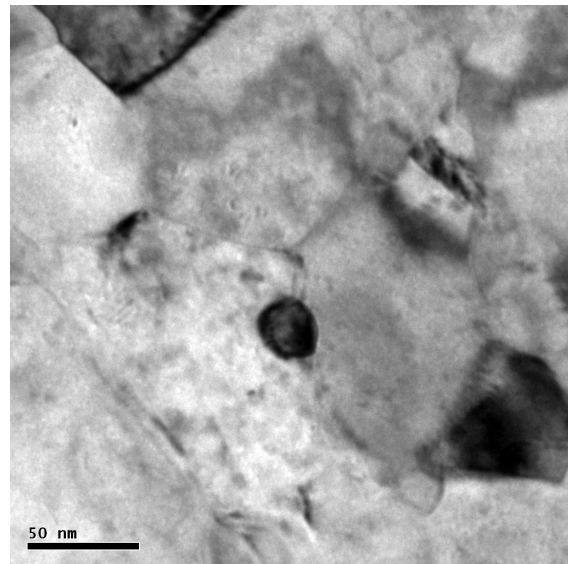
Fig. 6. 1c: Discontinuous globular as well as stringer shape β-phase at α-α grain boundary in alloy 3.
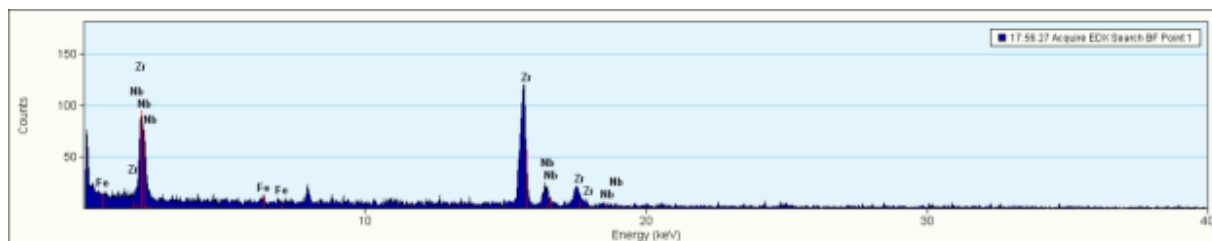
Fig. 6. 1d: EDS scan of β phase present at grain boundary in alloy 3.

The β phase was mostly observed at α / α interface (fig. 6.1b, fig. 6.1 c) although certain α / α interfaces did not contain any β phase. Majority of β phase present at α/α grain boundaries were continuous (stringer form) where-as certain amount of β was discontinuous and were elliptical in shape with width 40 nm and aspect ratio 1.65. EDS spectrum (fig. 6.1d) indicated that Nb content in the β phase present at α / α interface was 3 to 18 wt. %. Maximum Fe content in this phase was measured to be 0.76 wt. %. All these observations indicated that these were meta-stable β-Zr. Small fraction of fine size (20-25 nm) β phase in globular form was also present in the α phase and they are termed as grain body β. Nb content in these β phase was higher (45-50 wt. %).

Most of the β phase in alloy 4 was present at α / α grain boundary (fig. 6.2b) and was discontinuous and elliptical in morphology. The Nb and Fe contents were not detected in the α-matrix. The Nb content in α / α grain boundary β phase varied in a wide range (7 wt. % to 22 wt. %). Lower Nb content in these phases confirmed the presence of β-Zr. Maximum Fe content in these phases was found to be 0.62 wt. %. Apart from β phase at α-α grain boundaries, β phase was also present inside the α grains. Grain body β phase was rich in Nb (up to 47 wt. % Nb) and were elliptical in shape (width 25 nm, aspect ratio 1.6). Very small amount of Fe (0.03 wt. %) was also found to be attached to these grain body β phase. These grain body β particles may form from the supersaturated solid solution of Nb present in the α-phase [6.26] during subsequent processing after extrusion of the as-fabricated components.

Certain coarser (fig.6.2c) Fe and Nb bearing parallelepiped precipitates of (140 nm x 30 nm) were found along with β phase. EDS analysis of these precipitates indicated that they contained ~54 at.% Zr, ~30.20 at.% Nb, ~15.80 at.% Fe. Volume fraction of these Nb, Fe bearing

precipitates was measured to be around 0.5%. The EDS spectrum of one of these precipitates is given in Fig.6.2e. Presence of Fe and Nb enriched precipitates reduced the Fe and Nb contents in α-Zr matrix to below detectable limit of EDS.

Fig. 6. 2a: Microstructure of Zr-2.5Nb pressure tube material in alloy 4, showing stringer form β phase and discontinuous β particles at α/α boundary and β particles within α grain.
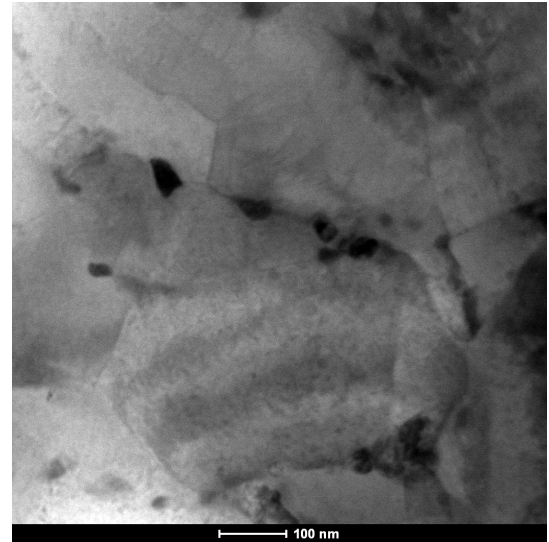
Fig. 6. 2b: Enlarged view of grain boundary β phase particles in alloy 4.
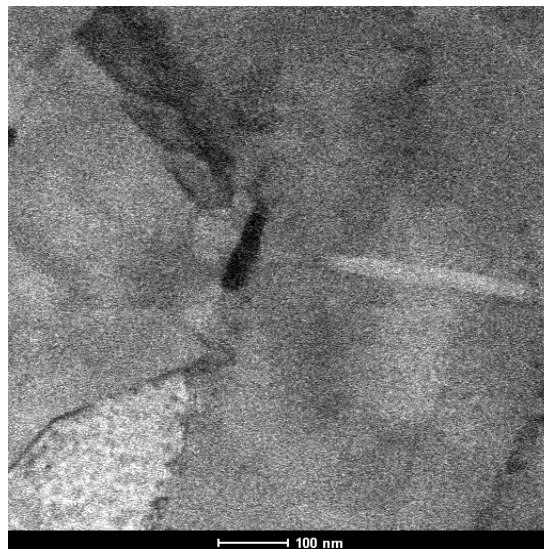
Fig. 6. 2c: Fe, Nb and Zr bearing parallelepiped precipitates in alloy 4.
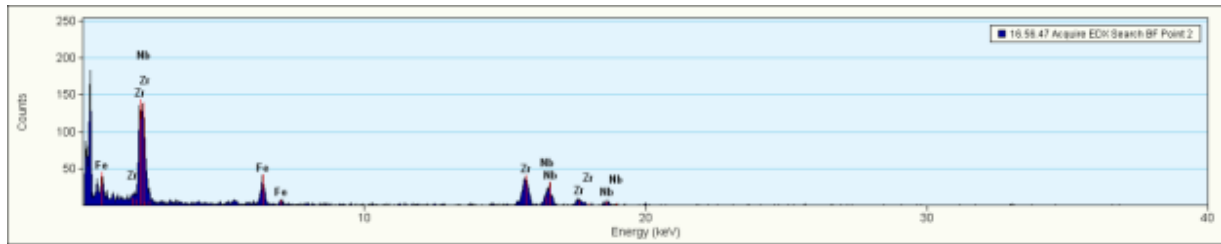
Fig. 6. 2d: EDS scan shows Fe enrichment in the precipitates in alloy 4

The volume fraction of β phase in alloy 5 was 3.2 - 4 %. Average α grain size was 0.16 μm x 1.22 μm with aspect ratio 7.7. The EDS analysis indicated that matrix was α-Zr with Fe content 0.01 wt.%. No Nb was detected in the α-Zr matrix. The β phase was observed at α / α interfaces (fig. 6.3a, 6.3b) as well as within α grains (fig. 6.3d). Certain α / α interfaces did not contain any β. At grain boundaries β phases were not continuous and formed a chain like morphology. The morphology of β phase was elliptical. These chain like precipitates contained Nb up to 22 wt. % with 0.25 wt% Fe (fig. 6.3c). Grain body β phase contained a lower level of Fe. The Nb content in grain body β phase varied from 22 to 75 wt. % (fig. 6.3e). These precipitates were nearly globular shaped with diameter 25 nm and distributed inhomogenously. Certain grains showed higher concentration of grain body precipitates whereas certain grains were devoid of grain body precipitates and contained such α / α grain boundary precipitates.

From the microstructural and micro chemical analysis of all the three alloys, it can be clearly concluded that β phase was present in two distinct morphologies: i) β phase with particle morphology present within α grain which contained higher amount of Nb and lower amount of Fe, and ii) chain like precipitates or filament (stringer) morphology at α / α interface and contained relatively less Nb and higher amount of Fe.

Another type of spherical or ellipsoidal precipitates scattered within α matrix were observed which contained only Zr and Fe, with no detectable amount of Nb (fig. 6.3f). Due to small size of these particles, these were completely embedded within the matrix, thus it was difficult to make a quantitative analysis of their chemical composition from EDS scan without interference from α-Zr matrix. Volume fraction of these precipitates was around 0.1 % with 15-60 nm in diameter. These are Zr-Fe intermetallic precipitates. Due to presence of these Zr-Fe intermetallic precipitates Fe content in β phase is also less compared to alloy 3.

Fig. 6. 3a: Bright field TEM micrograph of alloy 5, showing lamellar structure.

500 nm
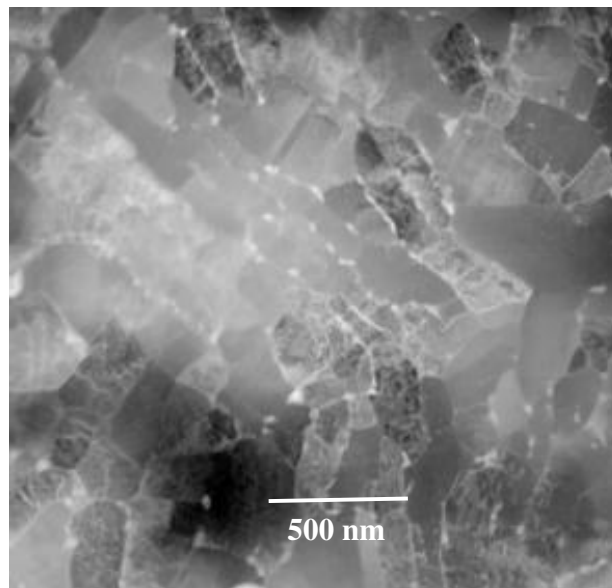
Fig. 6. 3b: Dark field TEM micrograph of alloy 5, showing elongated α-zirconium grains

surrounded by discontinuous β-phase.
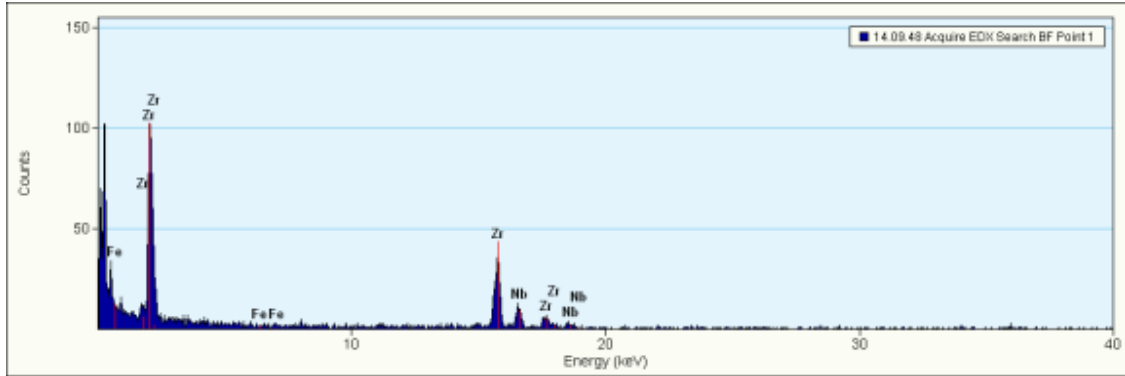
Fig. 6. 3c: EDS profile of Zr rich grain boundary β.
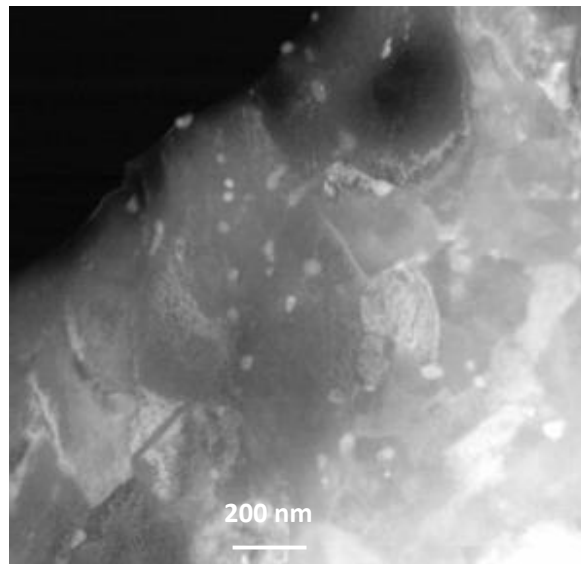
Fig. 6. 3d: Dark field TEM micrographs of globular grain body β phase.
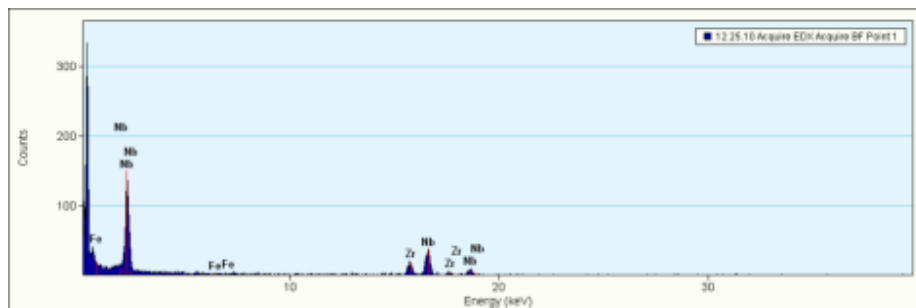
Fig. 6. 3e: EDS profile of Nb rich grain body β phase in alloy 5.
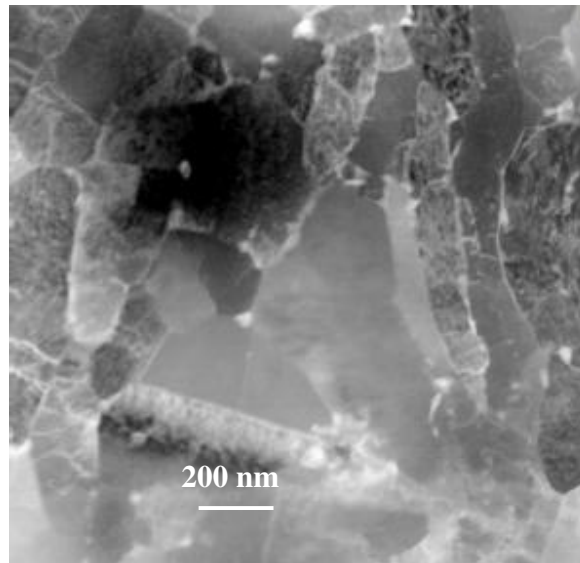
Fig. 6. 3f: Dark field TEM micrographs of scattered Zr-Fe rich grain body precipitates in alloy 5.

Alloy 5 when heat treated at 680° C for 2 hrs in He environment and after air-cooling it contains higher volume fraction of β-phase compare to as received material. The SEM microstructure of heat treated alloy-5 is given in fig. 6.3g clearly indicated significantly higher fraction of β-phase.
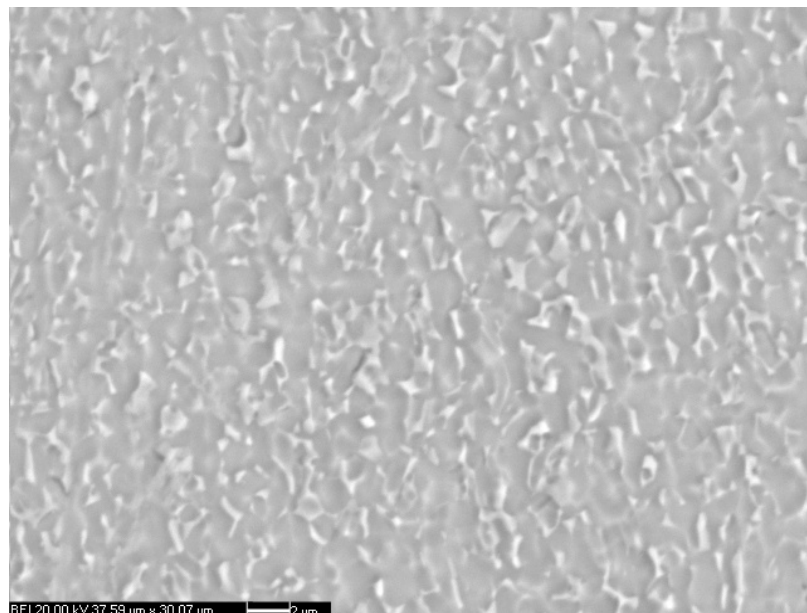
Fig. 6. 3g: Backscattered SEM image shows of higher fraction of β-phase α-matrix of heat-treated alloy-5.

6.2.2 Micro hardness Measurement:

The alloy 3 and alloy 4 showed same range of hardness 211-220 HV whereas alloy 5 was slightly harder 222-230 HV.

6.2.3 Oxidation Behaviour:

After accelerated steam autoclaving of the alloys, weight gains for each heat treatment conditions were measured and mentioned in table 6.1. It has been observed from table 6. 1 that alloy 4 and alloy 5 (in as received condition) which contained a high level of Fe, showed lower weight gain or good oxidation resistance. Alloy 3 containing lower Fe and slightly higher Nb content showed much higher weight gain or poor oxidation resistance. If we consider that the effect of variation of Nb content in this range has negligible effect on oxidation resistance of the alloy and plot the Fe content in the respective alloys vs. weight gain after autoclave testing, a relationship is obtained with Fe variation as shown in fig. 6. 4.

Table: 6.1 Oxidation behaviour of the alloys with different Fe content during accelerated autoclaving at 415°C, 10.3 MPa, 3 days.

Sl. No.	Alloy	Fe Content (ppm)	Avg. Weight Gain (mg/dm^2)	Avg. Oxide Layer Thickness (um)
1.	Alloy-3	300	29.10	2.04
2.	Alloy-4	800	22.75	1.55
3.	Alloy-5	1250	21.63	1.47
4.	Heat treated Alloy-5	1250	38.5	2.62

This relationship indicates that the Fe addition is beneficial for improving oxidation resistance. The alloy which shows best corrosion resistance (alloy 5), if we heat treat it to increase the

fraction of β-Zr, then this alloy shows the worst corrosion resistance (as marked by point *A in fig. 6.4. That is holding above monotectoid temperature lead to poor corrosion performance of the alloy.
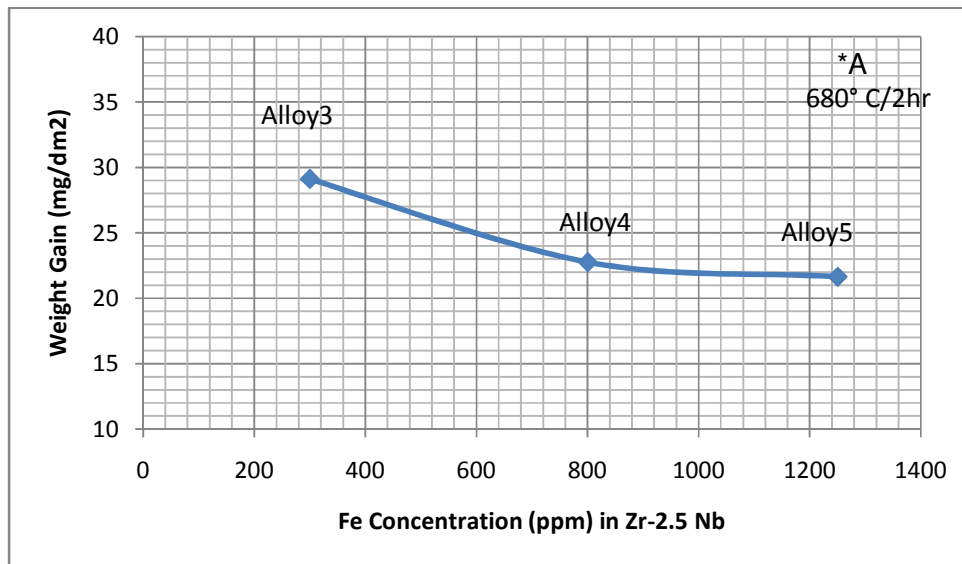
Fig. 6. 4:Relationship between Fe content in Zr-2.5Nb alloy and weight gain after 415° C, 10.3 MPa,3 days steam autoclave testing showing beneficial effect of Fe in improving oxidation resistance.

6.2.4 Hydrogen pick up behaviour

Measured values of hydrogen pick up during autoclaving is given in table 6.2 and the correlation between hydrogen pick up and Fe content in the alloys is plotted in fig. 6.5a. It has been observed that H-pick up is less in alloy 3 and alloy 4. Alloy 5 showed the highest H pick up during autoclaving compared to alloy 3 and 4. Hydrides were also seen in the matrix (fig. 6. 5).

Table: 6. 2 Hydrogen intake after accelerated autoclaving after 415°C, 10.3 MPa, 3 days.

	Fe Content (ppm)	Nb Content (wt %)	H content Before Autoclaving (ppm)	H content After Autoclaving (ppm)	H pick up during autoclaving (ppm)
Alloy-3	300	2.60	11.12	15.72	4.60
Alloy-4	800	2.47	14.20	19.16	4.96
Alloy-5	1250	2.49	13.35	23.64	10.29
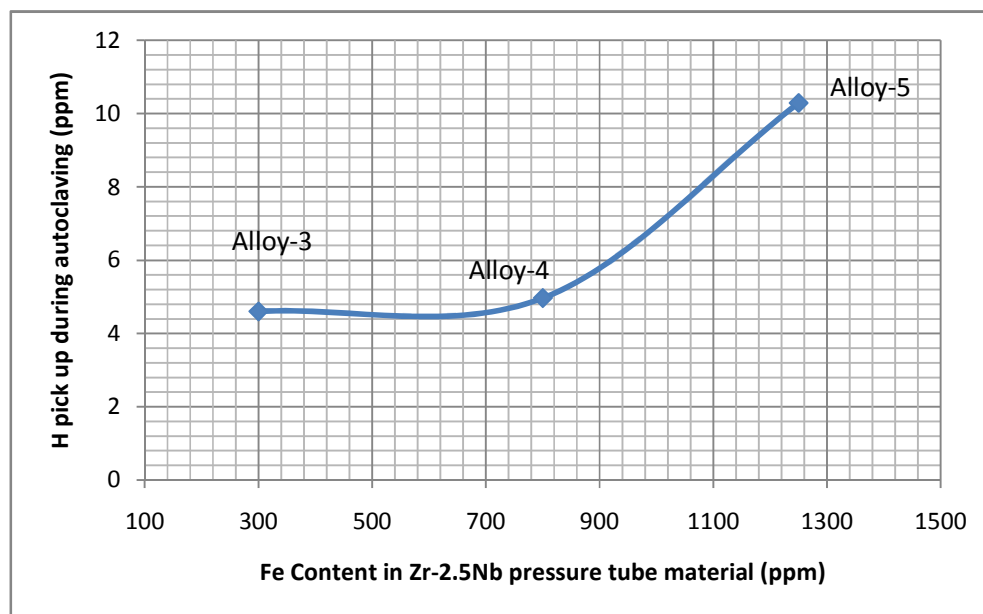
Fig. 6.5a: Relationship between Fe content in Zr-2.5Nb alloy with Hydrogen pick up during 415°C, 10.3MPa, 3 days steam autoclave testing showing detrimental effect of Fe in H intake.
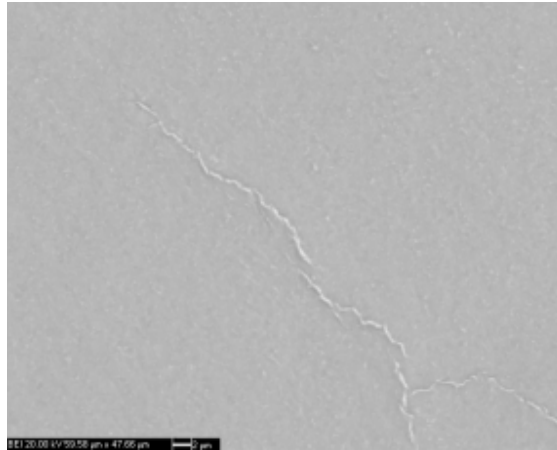
Fig. 6. 5b: Hydrides were observed under SEM in alloy 5 after 72 hours autoclaving at 415° C.

6.2.5 SEM Observation of oxide:

Representative areas of oxide and oxide - metal interface are shown in fig. 6. 6 , fig.6. 7 and fig. 6.8 for alloy 3, alloy 4, alloy 5 respectively. In case of alloy 3, the oxide layer thickness was very much non uniform in nature (fig. 6.6a) and was 1.44 - 2.50 µm thick. Cracks were seen in the regions of oxide layer (fig. 6.6b) where there was a large variation of oxide thickness.
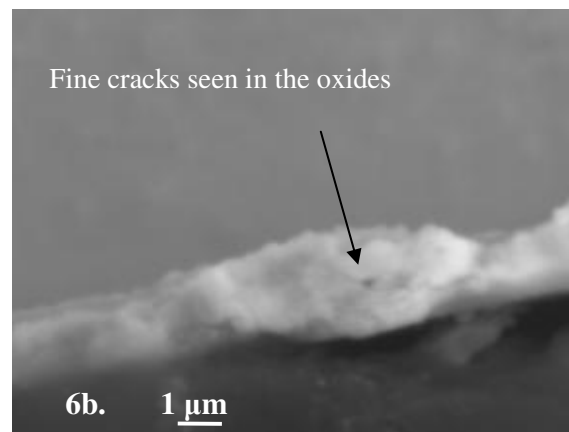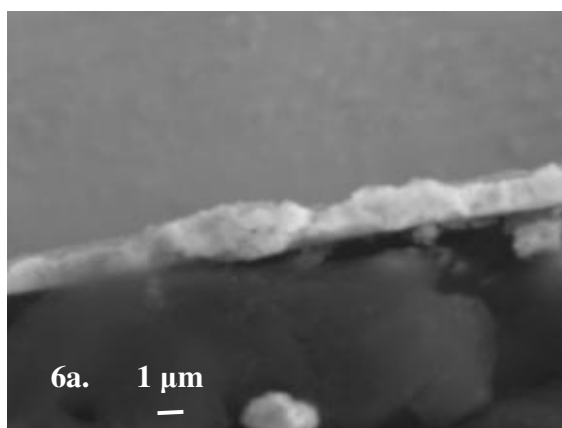
Fig. 6. 6a: Floppy and cracked oxides with its wavy interface observed under SEM in alloy 3 after 72 hrs. autoclaving at 415° C. Fig. 6. 6b: Enlarged View of the oxide.

The regions where oxide thickness was on higher side of the range, had a layer morphology with fine cracks in between the layers nearly parallel to the interface. First cracks were observed 500 nm away from the oxide-coolant interface. Sometimes cracks were in the middle of the layer and divided the oxide layer into two parts. The oxide near the outer surface had pores and cracks whereas oxide at metal oxide interface was free from pores and cracks. The oxide metal interface was undulated in nature and the region which showed heavy oxidation, the degree of undulation of the oxide metal interface was having average 220 nm amplitude oscillation and periodicity of 400 nm (average).

For alloy 4, the oxide thickness was very homogenous (1.3 - 1.8 μm) compared to alloy 3 (fig. 6.7). Very fine, hair- line type cracks appeared 500 nm from the outer surface of oxide. Frequency of appearance of the cracks in oxide was less and oxide was dense. The interface was wavy in nature with amplitude of waviness 222 nm (average) and periodicity 600 nm (average).
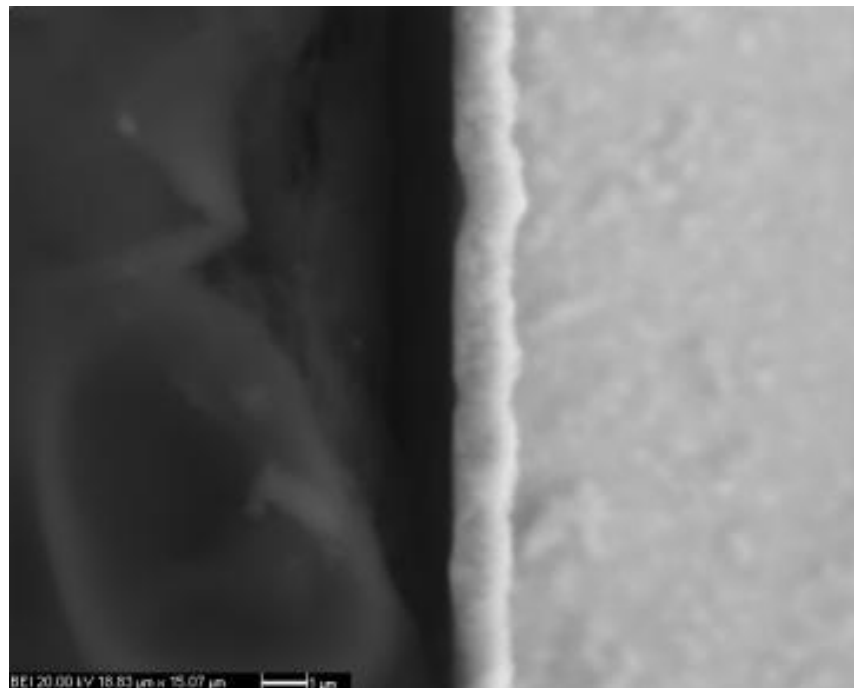
Fig. 6. 7: Cracks or pore free oxide and its wavy interface observed under SEM in alloy 4 after 72 hrs. autoclaving at 415° C.

Oxides in alloy 5 were also very homogeneous (1.26 to 1.50 µm) and dense in nature (fig. 6.8a). Cracks were not observed in SEM. The interface of oxide was undulated with 160 nm amplitude oscillation and periodicity of 470 nm. Amplitude of undulation was smaller when oxide thickness was less as in case of alloy 5. Similar observations [6.27] were reported in case of Zircaloy-2 where 1 µm thick oxide showed periodicity of 1µm and an amplitude of around 100 nm and when oxide thickness increased to 2 µm, the amplitude of the interface undulations was larger.
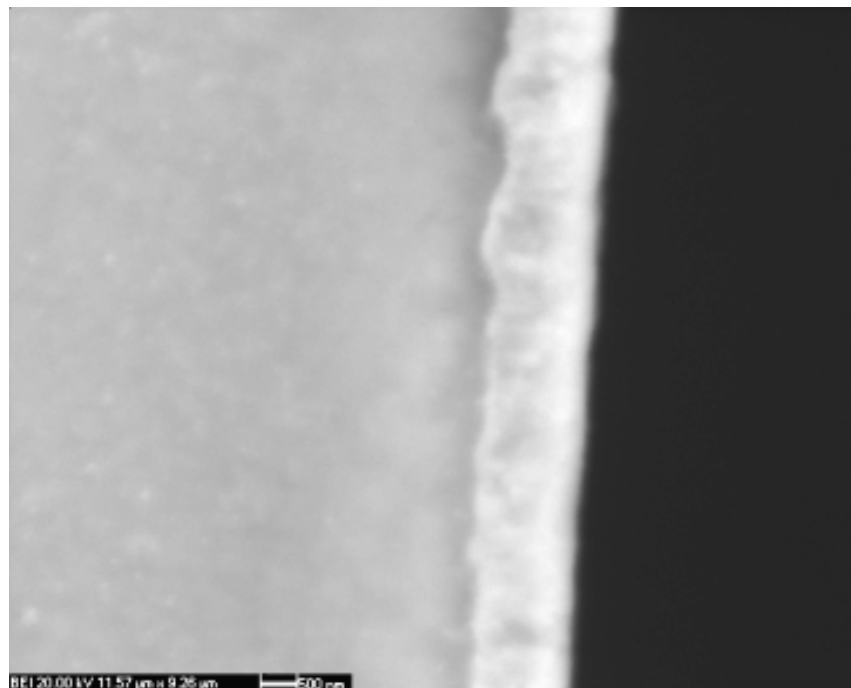
Fig. 6. 8a: Dense oxide and its wavy interface observed under SEM in alloy 5 after 72 hrs. autoclaving at 415° C

Cross sectional SEM image oxide of heat treated alloy-5 shows porous morphology with frequent presence of cracks (fig. 6.8b and fig. 6.8c). The picture clearly indicates that oxidation is progressed inward preferentially through β-phase. The α phase is oxidized at last stage. The β-Zr surrounding α-Zr matrix is oxidized progressively leaving behind the α-matrix which ultimately oxidizes at later stage. The oxide in very much inhomogeneous and average oxide thickness is varying in the range of 1.91 - 3.34 µm. First cracks were observed 600 nm away from the oxide-coolant interface.The oxide metal interface was undulated in nature and the region which
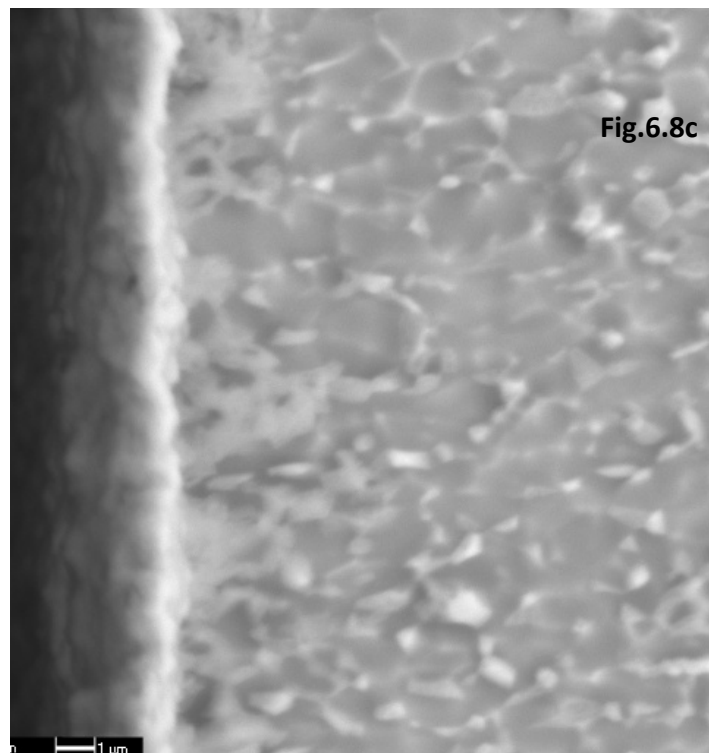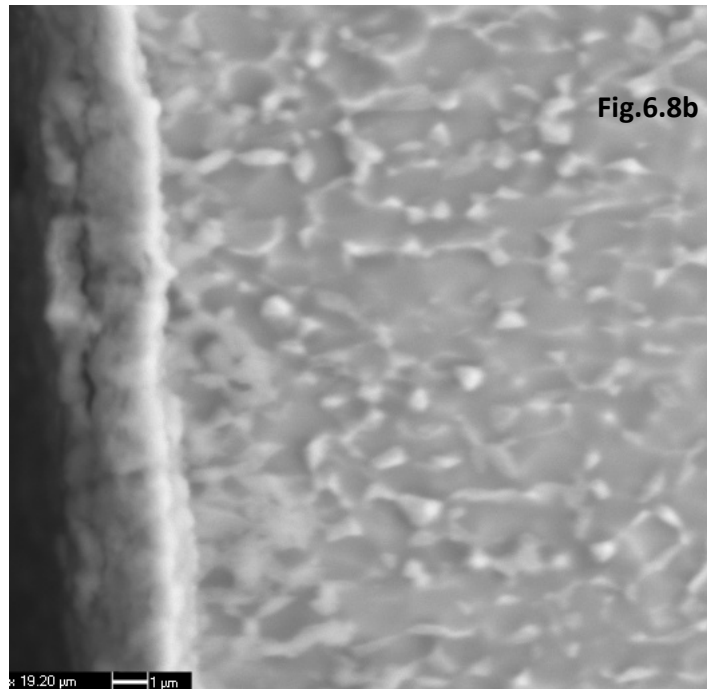
Fig. 6. 8b: Floppy and porous oxides with its wavy interface observed under SEM in heat treated alloy 5 after 72 hrs. autoclaving at 415° C. Fig. 6. 8c: Enlarged View of the oxide.

showed heavy oxidation, the degree of undulation of the oxide metal interface was having average 220 nm amplitude oscillation and periodicity of 300 nm (average). When oxidized surface is observed under SEM (fig. 6.8d), the effect of differential oxidation rate can easily be identified. The bright region is the oxide which undergone heavy oxidation while the dark region shows delayed oxidation.
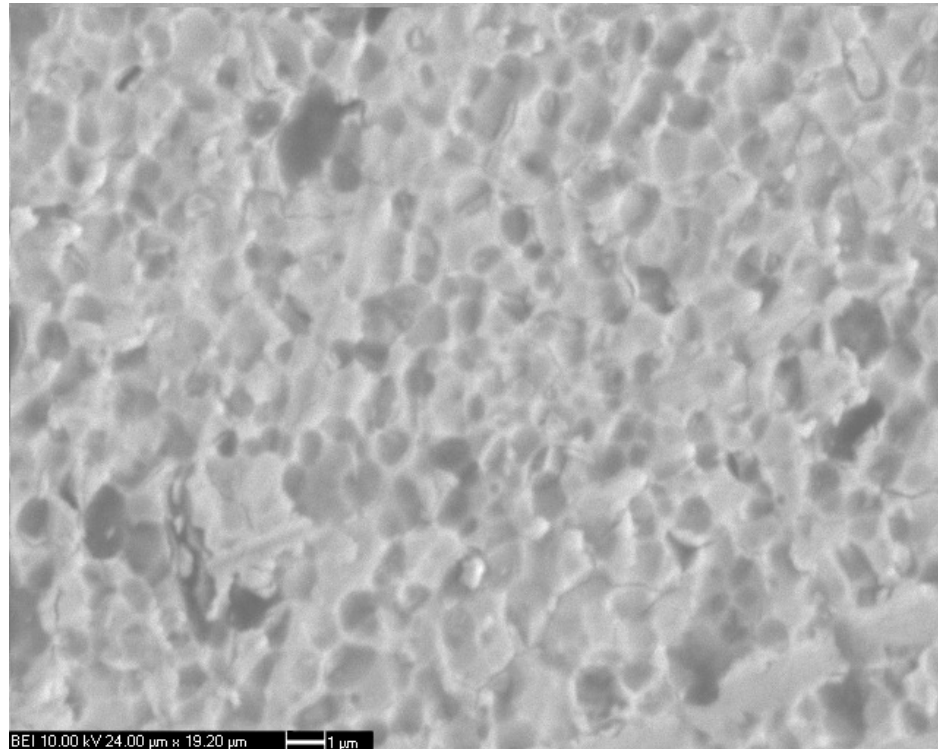
Fig. 6. 8d: The oxide surface observed under SEM in heat treated alloy 5 after 72 hrs. autoclaving at 415° C.

6.2.6 XPS Analysis : XPS analysis indicated the presence of Zr, Nb and oxygen (fig. 6.9a) in the analyzed layers from the surface of oxide. The formation of Zr sub-oxide was investigated by Y. Nishini *.et al.* [6.28] in the initial oxidation state in Zr and Zircaloy-2 with oxygen and water vapour at room temperature using Auger and X ray photo electron spectroscopy. The binding energy values for Zr 3 d 5/2 used in their study were for Zr in ZrO_2, 182.9eV, for Zr in Zr_2O_3, 181.8 eV. Olsson [6.29] suggests that the binding energy 3 d 5/2 of tetravalent Zr is at 182.2 eV and [6.29, 6.30] 3d 5/2 for Nb in Nb_2O_5, 207 ev and doublet is separated by 2.8eV.
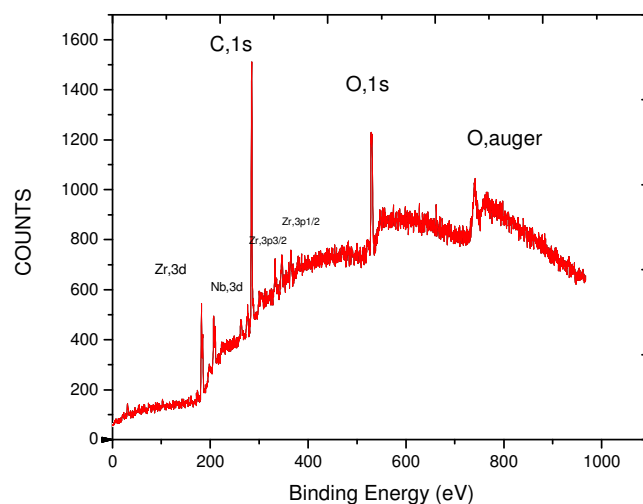
Fig. 6. 9 a: XPS spectra of the oxidized Zr-2.5Nb with 1200 ppm Fe after exposure to accelerated steam at 415°C.
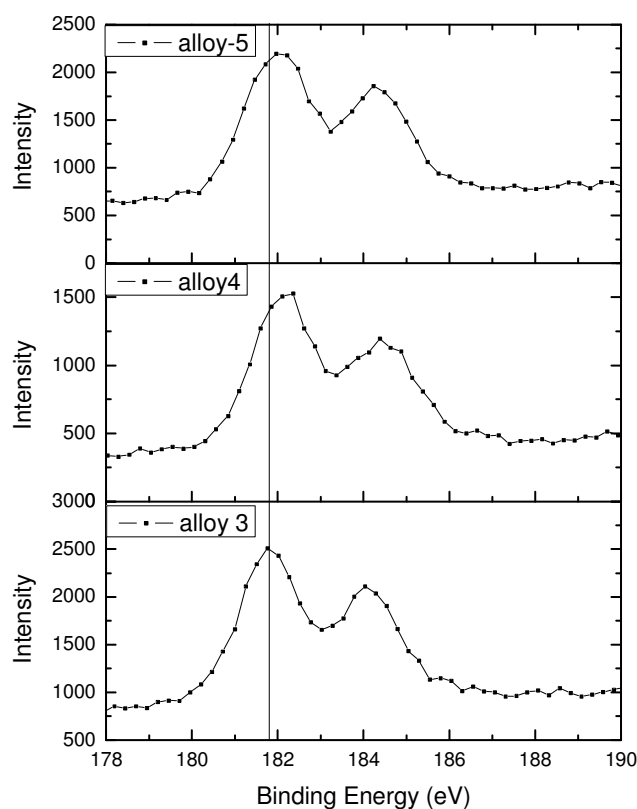
Fig. 6. 9 b: Intensity of XPS lines in Zr 3d spectra of the oxidized Zr-2.5Nb with different content of Fe after exposure to accelerated steam showing Zr 3d5/2 binding energy peak for all the alloy in within 181.9-182.2 ev.
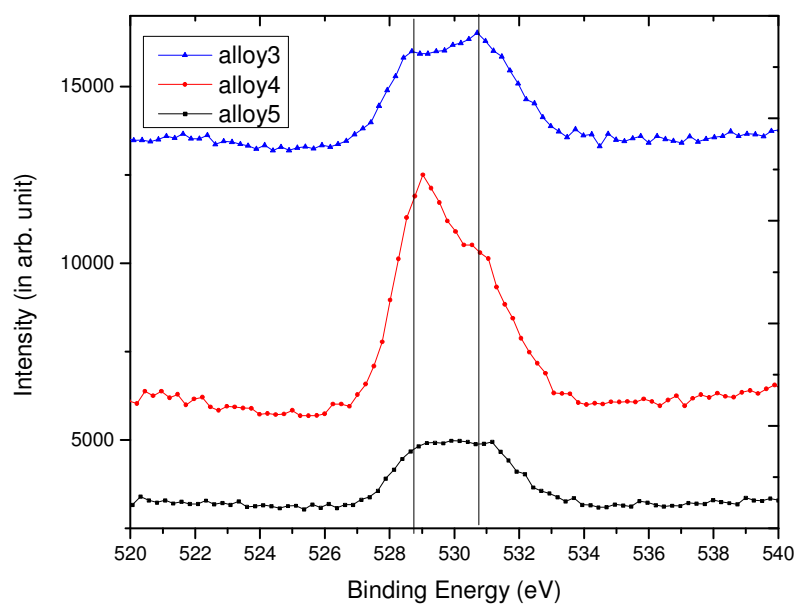
Fig. 6. 9 c: Intensity of XPS lines in O 1S spectra of the oxide of Zr-2.5Nb with different content of Fe after exposure to accelerated steam, showing 1s oxygen peak of Zr at 530.6 eV and the other 1s oxygen for Nb was at 528.6 eV indicating presence of both the oxide.
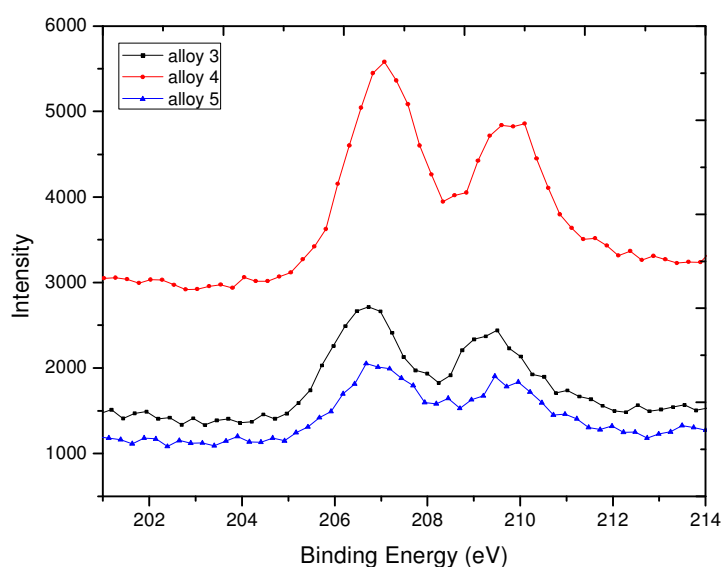
Fig. 6. 9 d: Intensity of XPS lines in Nb 3d spectra of the oxidized Zr-2.5Nb with different content of Fe after exposure to accelerated steam showing Nb 3d5/2 binding energy peak for all the alloys in within 206.7 - 206.9 eV.

From the XPS spectra of alloy 3, a well resolved doublet of Zr 3d5/2, 3d 3/2 were observed with 3d5/2 binding energy peak at 181.9 eV and for alloy 4 and 5 peaks were shifted to 182.2 eV and 182.1 eV respectively (fig. 6.9b). These were for Zr^{+4}. From the oxygen 1s spectra two peaks could be fitted in all the alloys. Alloy 3 and 4 showed oxygen 1s peak for Zr at 530.6 eV and for alloy 5 it was at 531.0 eV. The other peak of 1s oxygen for Nb was at 528.6 eV for all the alloys (fig.6.9c). For all the alloys, irrespective of Fe content Nb 3 d5/2 peak was at 206.7 eV, 206.9 eV and 206.9 eV respectively which confirmed presence of Nb_2O_5 oxide apart from Zr oxide (fig. 6.9d). Due to low concentration of Fe in the alloy, no detectable signal of Fe 2p could be found from outer surface of the oxide. Using atomic sensitivity factor of Zr 3d 5/2: 0.8, Nb 3d5/2: 1 and oxygen 1s: 0.66, atomic fraction of Zr, Nb and oxygen were calculated. O / M ratio was found to be 1.86 for alloy 5 with 1250 ppm Fe, 1.93 for alloy 4 (with 800 ppm Fe) whereas highest O / M ratio was obtained for alloy 3 containing 300 ppm Fe. The ratio of relative intensity of 3d 5/2 spectra (after normalization with atomic sensitivity factor) of Nb and Zr for alloy 4 was lower (0.38) than 0.50 for alloy 5 which indicated that presence of relatively higher fraction of Nb_2O_5 in alloy 5. From the XPS spectra of heat treated alloy 5, a well resolved doublet of Zr 3d5/2, 3d 3/2 were observed with 3d5/2 binding energy peak at 181.85 eV and Zr 3d3/2 binding energy peak at 184.2 eV (Fig.6.9e). These were for Zr^{+4}.
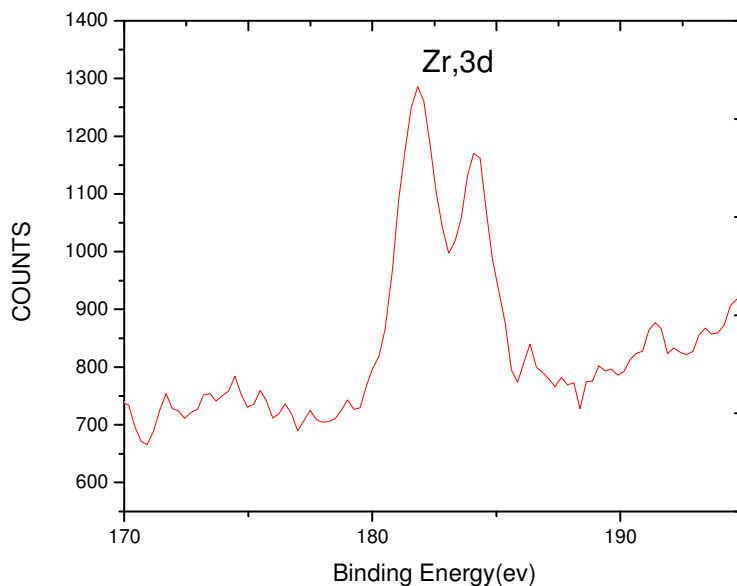
Fig. 6. 9 e: Well resolved doublet of Zr 3d spectra of the oxidized heat treated Zr-2.5Nb observed after exposure to accelerated steam showing Zr 3d5/2 binding energy peak at 181.79 eV.

From the oxygen 1s spectra only one peak is found at 530.6 eV (fig. 6.9f) which corresponds to ZrO_2 whereas in as received Zr-2.5Nb alloys (fig. 6.9c) two peaks could be fitted in all the alloys (one for ZrO_2 at 530.6 eV and other for Nb_2O_5 at 528.6 eV). No peak of any oxide of Nb like Nb2O5 (Nb 3 d5/2 peak was at 207 eV) or NbO was found in oxide of Zr-2.5Nb alloy after heat treatment in $\alpha + \beta$ Zr region. As XPS spectra is restricted only at the outer surface layer of the oxide, it clearly indicates that the Nb_2O_5 is absent in the outer surface in oxide of heat treated Zr-2.5Nb alloy.
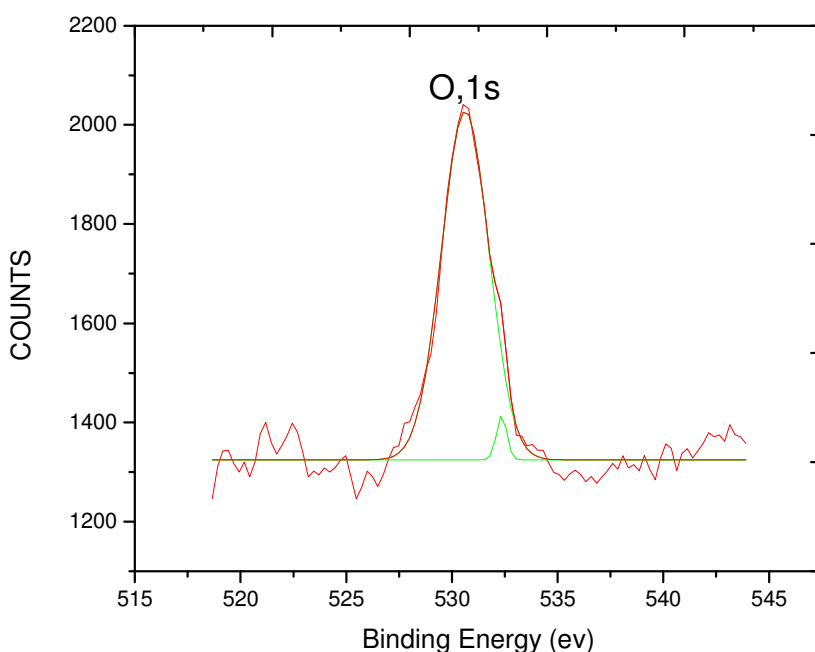
Fig. 6. 9 f: Intensity of XPS lines in O 1S spectra of the oxide of heat treated Zr-2.5Nb after exposure to accelerated steam, showing only 1s oxygen peak of Zr at 530.6 eV.

As received pressure tube material irrespective Fe content, has certain fraction of grain body β apart from grain boundary continuous β-Zr (section 6.2.1). These grain body β phase contains higher fraction of Nb (45 wt. % or more) compared to grain boundary β (7-14 wt. %). These Nb enrich regions when exposed to steam during autoclaving may form Nb_2O_5 along with ZrO_2. When heat treatment was carried out in $\alpha + \beta$-Zr region, volume fraction of β-Zr phase increases compared to as received pressure tube material with Nb content is around 12-14 wt.%. Localized Nb rich β would not be present which may lead to absence of Nb_2O_5 in the oxide.

6.2.7 GIXRD results:

The results of GIXRD study on the oxides of alloy 3 and alloy 4 are given in fig. 6.10 a, b, c. From the GIXRD scan on oxide of alloy 3, grazing angle X- ray reflection up to 0.5° showed presence of monoclinic ZrO_2 oxide only with peaks of ($\bar{1}1$ 1)m, (0 2 0)m at 28.25° and 34.24° respectively. With increase in grazing angle (1°) depth of penetration of X-ray increased and a peak at 30.28° was found which is of tetragonal phase (1 0 1)t [6.31, 6.32, 6.33]. With further increase in angle of incidence to 5°, matrix α Zr peaks of (1 0 0)$_{hcp}$, (0 0 2)$_{hcp}$,(1 0 1)$_{hcp}$ were seen at 32.17°, 34.82°, 36.51°respectively [6.34, 6.35]. Using relative intensity ratio method of tetragonal and monoclinic phase, alloy 3 showed maximum 6.4% tetragonal phase and the rest being monoclinic phase. In this determination, texture effect [6.36] has not been considered as texture will affect the both alloys in same way. For alloy 4, at 0.5°grazing angle reflection tetragonal peak (101)t was observed at 30.28°and the volume fraction of tetragonal phase was found to be 5%along with monoclinic. When angle of incidence increased to 5°, matrix α Zr peaks were found in all the three alloys. At 5°grazing angle tetragonal fraction in alloy 4 and 5 oxide was much higher (12%) compared to alloy 3.
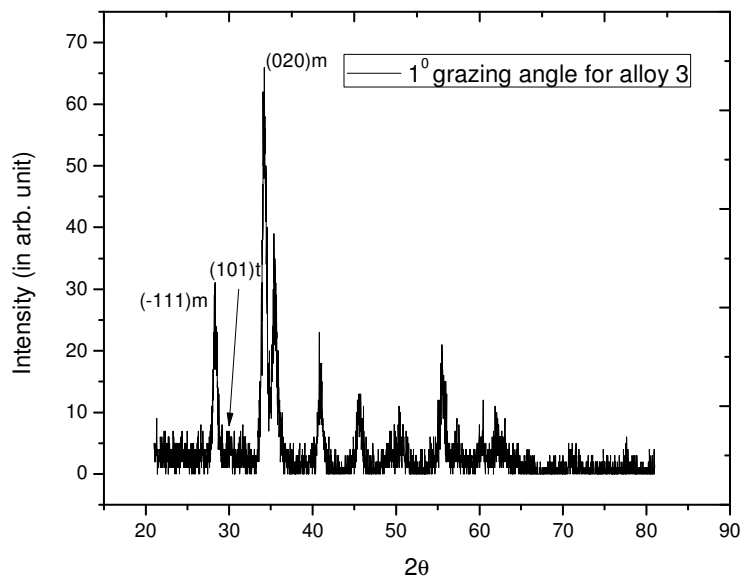
Fig. 6. 10 a: GIXRD scan of the oxide at 1 degree incidence angle in alloy 3 after exposure to accelerated steam at 415°C showing presence of small fraction of tetragonal Zirconia along with monoclinic structure of oxide.
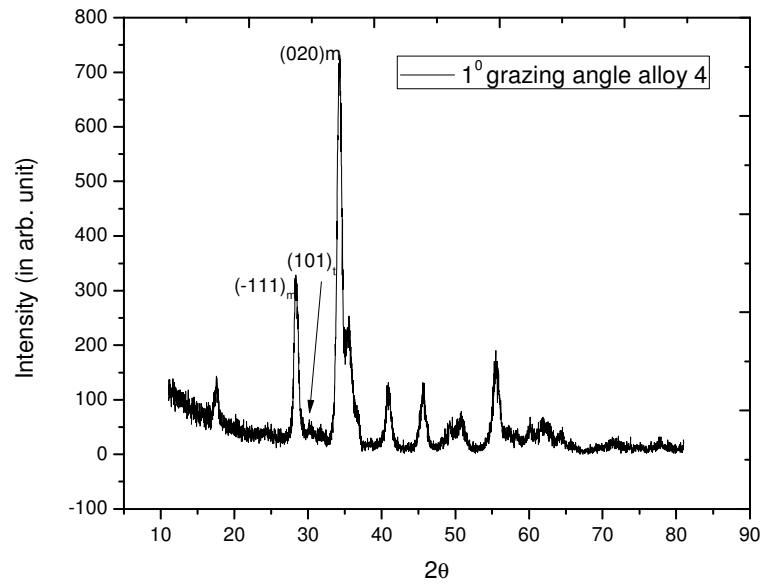
Fig. 6. 10 b : GIXRD scan on the oxide 1 degree incidence angle in alloy 4 after
exposure to accelerated steam at 415°C showing presence of relatively higher fraction
of tetragonal Zirconia along with monoclinic structure of oxide.
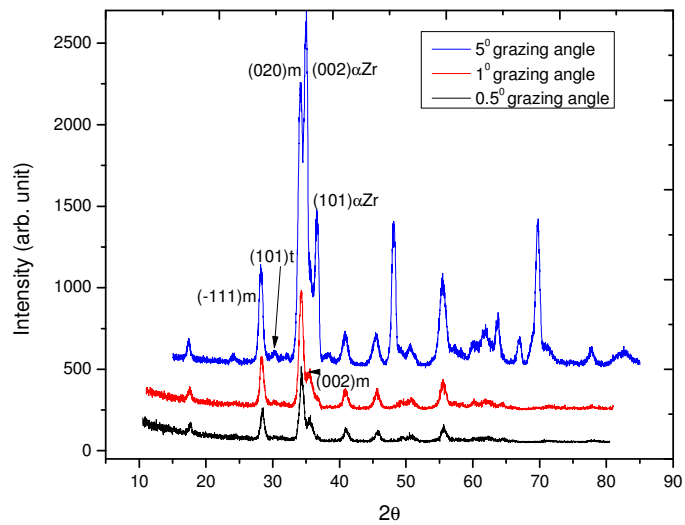
Fig. 6. 10 c: GIXRD scan on the oxide showing presence of tetragonal zirconia along with
monoclinic structure of oxide as well as α-Zr peaks with increasing grazing angle of incidence
alloy 4 after exposure to accelerated steam at 415°C.

As the depth of penetration increased peak broadening became significantly higher (fig. 6.10c). This broadening may be due to presence of higher and higher stresses near the oxide-metal interface as well as small grain size near the oxide-metal interface [6.37- 6.42]. In order to obtain reliable oxide stress values, the focus was placed on diffraction peaks that display no overlap with other reflections.

Peak broadening was determined from the full-width half maximum (FWHM) value obtained from the line profile analysis (LPA) [6.43]. Two sources of line broadening need to be considered: (1) broadening due to strain and (2) broadening due to small grain size.

The correction for instrumental broadening which is the most important step in estimation of material properties from line profile analysis was done using standard Si sample provided with the instrument. The FWHM (b) is a function of Bragg's diffraction angle (θ) as shown in equation.6.2,

$$b^2 = U \, tan^2\theta + V \, tan\theta + W \: - - - -(6.2)$$

This equation was used for calculating instrumental broadening (b) at any given angle θ. The high degree of fit (adjusted R^2=0.989) ensured proper correction due to instrumental effects. Then the corrected (without instrumental broadening) FWHM at any angle was calculated by equation 6.3,

$$\beta = B - \frac{b^2}{B} - - - - - (6.3)$$

where B is the total broadening which includes instrumental as well as broadening due to grain size as well as strain. To separate the effect of broadening of X-ray line due to small grain size D and strain ε, following equation was used

$$\frac{\beta cos\theta}{\lambda} = \frac{1}{D} + \frac{4\varepsilon sin\theta}{\lambda} - - - - - (6.4)$$

where β=instrumental corrected broadening in radians

    θ=Bragg's diffraction angle

    D=The grain size (Å)

ε = micro-strain

λ = wave length (Å)

The plot of $\frac{\beta cos\theta}{\lambda}$ vs. $\frac{sin\theta}{\lambda}$ was a straight line (fig. 6.10d). From the plot D and ε were calculated using the following equations, Intercept $= \frac{1}{D}$, slope $= 4\varepsilon$.

The grain size was determined from broadening of monoclinic peaks of alloy 3 at a grazing angle of incidence of 1°, was in the range of 13 nm and at 0.5°angle of incidence it was 17 nm. Finer grain structure (7 nm) was indicated towards the oxide -metal interface. For alloy 4 and alloy 5, the grain size was uniform (7 - 9 nm for alloy 4 and 12 - 13 nm for alloy 5). Accuracy in determination of grain size for monoclinic structure is more because the tetragonal phase is a minor fraction of the oxide, so that the diffraction peaks are weak and width measurements would not be accurate enough. The negative slope of the straight line in fig. 6.10d indicated that strain associated in oxide was compressive in nature. For alloy 3 compressive strain calculated from oxide peaks at 0.5°and at 1°incidence angle was 0.00262 and 0.00294 where as for alloy 4 it was 0.00631 at a grazing angle of 0.5° and 0.0065 at grazing angle incidence of 1° and 0.0109 at a grazing angle of 5°. For alloy 5 compressive strain was 0.00675 at a grazing angle of 0.5° and 0.007 at grazing angle incidence of 1°.
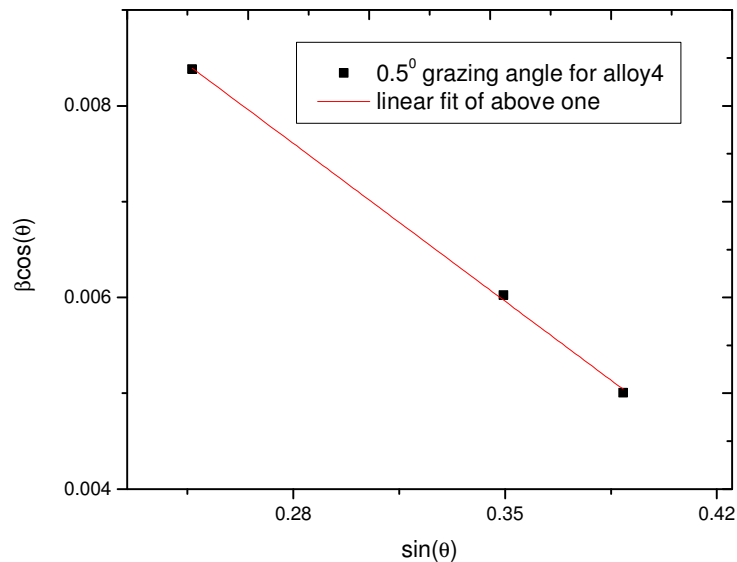
Fig. 6. 10d: The negative slope of β cos (θ) vs. sin(θ) indicated presence of compressive stress in oxide at a 0.5° grazing angle incidence in case of alloy 4.

The dark field cross sectional TEM image indicates presence of columnar grains (fig.6.10e) and diffraction pattern indicates textured nanocrystalline grains (fig.6 .10f) in the oxide.
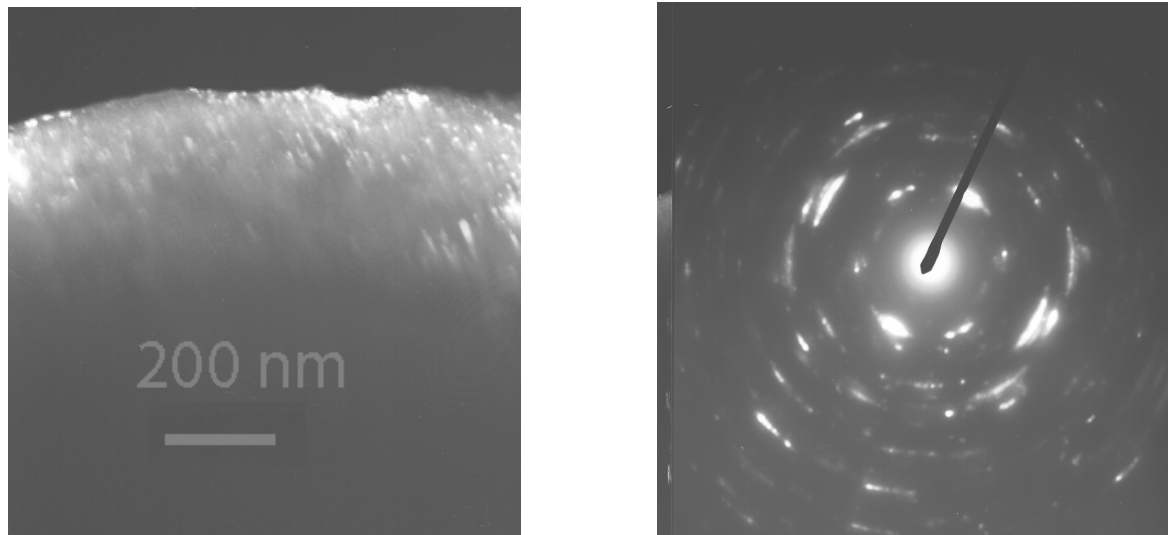
Fig. 6. 10e. Dark field TEM image of oxide in cross sectional sample indicating columnar grains, f. Selected area diffraction pattern of oxide indicates presence of nanocrystallinetextured grains.

In case of α+ β heat treated samples, GIXRD reflection from 0.5°, 1°, 5° and 10° reflection
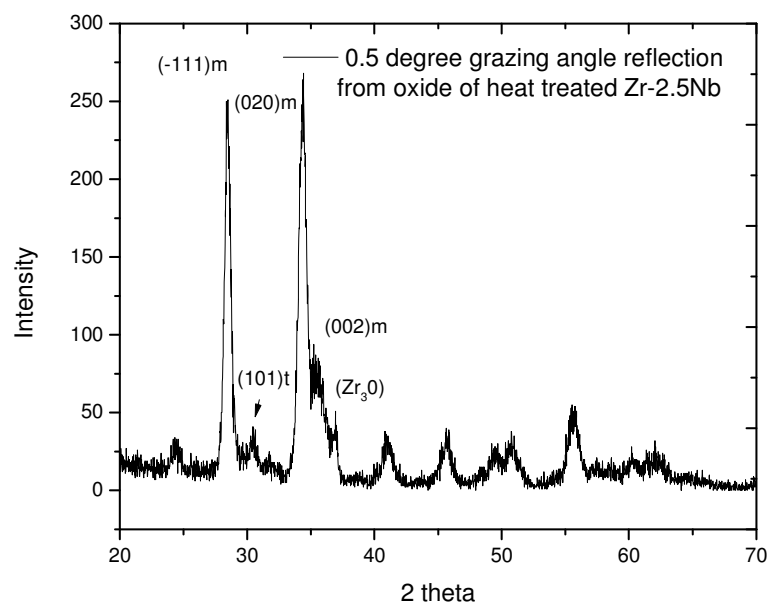
Fig. 6. 10 g: GIXRD scan on the oxide showing presence of significant tetragonal zirconia along with monoclinic structure of oxide as well as Zr_3O peakat 0.5° grazing angle of incidence heat treated alloy after exposure to accelerated steam at 415°C.

showed significant tetragonal reflection along with monoclinic reflection as shown in fig. 6.10 g and h. 0.5° and 1° reflection showed peaks from hexagonal Zr_3O which were absent in oxide formed in as received pressure tube material. 5 ° grazing angle reflection showed presence of (101)α Zr as well as (116) hexagonal Zr_3O reflection at 36.5° and 36.75° respectively. 10° reflection showed predominately reflection from matrix α-Zr.
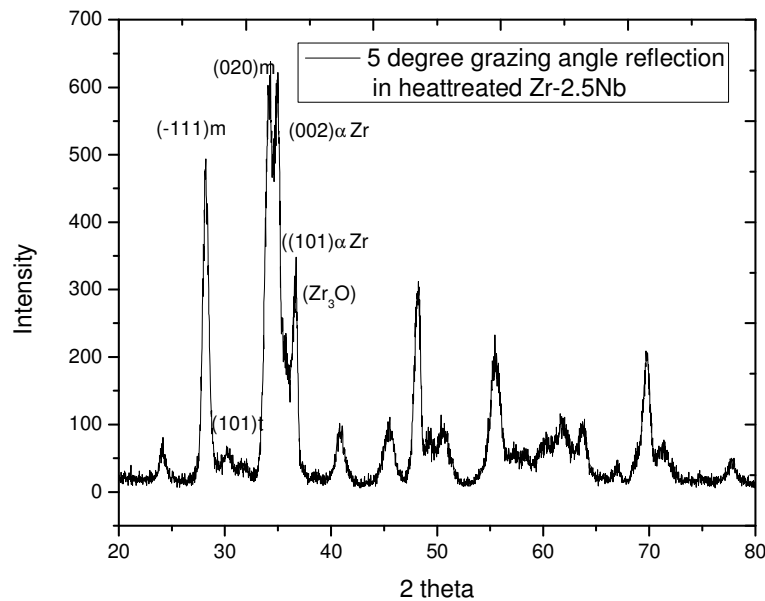
Fig. 6. 10 h: GIXRD scan on the oxide showing presence of significant tetragonal zirconia along with monoclinic structure of oxide as well as Zr_3O peakat 5° grazing angle of incidence heat treated alloy after exposure to accelerated steam at 415°C.

6.3 Discussions:

Chemical reaction of Zr with water (equation 6.5) results in the formation of zirconium oxide and hydrogen.

$$Zr + 2\,H_2O \rightarrow ZrO_2 + 2\,H_2 \qquad \text{-------- (6.5)}$$
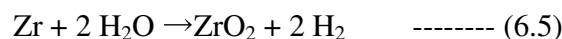
This reaction can be divided into 3 partial reactions [6.1, 6.17], *viz*.,
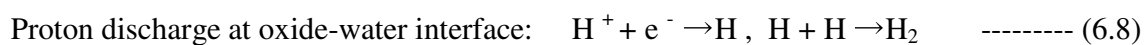
Anodic Reaction at metal-oxide interface: $\quad Zr + 2\,O^{-2} \rightarrow ZrO_2 + 2\,Vo^{++} + 8e^{-}$ ------- (6.6)

Cathodic Reaction at oxide-water interface: $Vo^{++} + 2e^{-} + H_2O \rightarrow 2\,H^{+} + O^{-2}$ -------- (6.7)

Proton discharge at oxide-water interface: $\quad H^{+} + e^{-} \rightarrow H,\ H + H \rightarrow H_2$ --------- (6.8)

A negatively charged oxygen ion (O^{-2}) diffuses through the ZrO_{2-x} to the oxide- metal interface to oxidize the Zr metal and release two electrons. These electrons must diffuse back through the oxide until they meet a hydrogen containing radical, reducing the H^+ ion to atomic H^o. It is widely accepted mechanism that when atomic hydrogen is generated at or close to the oxide - water interface, oxide grows uniformly and atomic hydrogen either recombines and hydrogen gas is liberated to the water or it diffuses into the metal through the oxide [6.1, 6.46]. Thus, the oxide characteristics e.g., pore, small cracks, and the dense barrier layer thickness are key factors affecting the hydrogen uptake behavior. Higher hydrogen uptake of zirconium alloys having porous oxide may be due to reduced diffusion distance through the thin barrier layer coupled with the increased difficulty involved in diffusing out of the pores of oxide. Based on this assumption, the hydrogen uptake of zirconium alloys from corrosion reaction should have a direct corresponding relationship with the corrosion resistance. That is to say, the hydrogen content in the specimen with superior corrosion resistance should be less than that in the specimen with inferior corrosion resistance because on onehand, the specimen with superior corrosion resistance generates less hydrogen and on the other hand, the specimen with superior corrosion resistance possesses less pores and cracks in the oxide. Thus, it is more difficult for hydrogen to be transported through the oxide. From the steam autoclaving results (fig. 6. 4) it has been observed that with increasing Fe content from 300 ppm to 800 ppm, oxidation resistance improved and with further addition up to 1250 ppm of Fe content no further improvement of oxidation resistance occurred whereas hydrogen intake drastically increased. Composition wise alloy 4 and alloy 5 contain similar level of Nb but only Fe content is on higher side in alloy 5. When Fe content is low, rate of oxidation is high and the oxide formed has pores as well as cracks but hydrogen intake in these samples is less, *i.e.* although high amount of hydrogen is generated through corrosion reaction, but H pick up fraction is less. With increasing Fe content, oxidation resistance improved with dense oxide without frequent presence of cracks but H pick up is enhanced, *i.e.* although less amount of hydrogen is generated through corrosion reaction, H pick up fraction is more. This indicates that the porous cracked morphology of oxide is not responsible for high H intake. Similar observation in Zircaloy-2 and Zircaloy-4 was also pointed out by Yao *et al.* [6.45].

Fe is a fast diffusing element in α-Zr and its diffusivity is nine order magnitude [6.46] faster than α-Zr self diffusion over a range of temperatures and traces of Fe may have a critical influence on the mass transport in α-Zr. An ab initio study [6.47] indicated that the presence of Fe induces the formation of neighbour vacancies, thereby increasing the number of vacancies with respect to those in pure α-Zr at a given temperature. Solubility of Fe [6.48] in α Zr is less compared to β Zr and high diffusivity of Fe allow it to be partitioned between α, β and Zr-Fe-Nb bearing precipitates. When alloy contains very low amount of Fe (alloy 3: 300 ppm Fe), Zr-Fe or Zr-Nb-Fe bearing intermetallic precipitates were not observed and Fe is mostly found in β phase (0.75 wt.%). With increasing Fe content (800 ppm in alloy 4) Zr-Nb-Fe rich intermetallic precipitates start forming, reducing Fe and Nb content in α-Zr matrix to below detectable limit. Still the β phase present at α / α interface has Fe content 0.62 wt. % and grain body β contains 0.03 wt. % Fe. Lower Nb content in α-Zr matrix may reduce the c-component dislocation density and lead to decrease in irradiation growth [6.25]. With further increasing Fe content (1250 ppm in alloy 5), Zr-Fe intermetallic precipitates were observed apart from Zr-Nb-Fe bearing intermetallic precipitates. The α-Zr matrix in alloy 5 contains around 0.01 wt% Fe and its β phase has less Fe compared to β phase in alloy 3 and alloy 4. These measurements indicate that the presence of Fe rich intermetallic precipitates reduces Fe content in β phase also. The presence of Zr_2Fe in extruded Zr-2.5Nb pressure tube material with 0.1 wt% Fe was also confirmed by analytical electron microscope as well as Mossbauer spectroscopy [6.49]. Mossbauer measurements [6. 50] and ab initio calculations [6.47] also ruled out a simple substitutional position for Fe atoms, causing considerable distortion of the hcp Zr lattice.

Nb content of the β phase present within α grain is more (maximum 75 wt. % Nb) compared to β present at α / α interface (22 wt. % Nb). The high Nb content in grain body β phase may significantly reduce matrix Nb content as well as improve corrosion resistance of the alloy. When β phase is present as β-Zr then corrosion property degrades to a great extent [6.50, 6.51]. XPS analysis of oxide indicated presence of slightly higher fraction of Nb_2O_5 in alloy 5. Although presence of Nb_2O_5 [6. 1] results in lower H pick up due to reduction of solubility of H [+] but alloy 5showed higher H intake. This indicates that the effect of Fe in enhancing H intake in Zr-2.5Nb alloy is more prominent than the relative higher fraction of presence of Nb_2O_5 in oxide. Fe enhanced the formation of Zr-Fe bearing intermetallic precipitates. The microstructure of Zr-2.5Nb alloy with higher Fe content has higher fraction of fine size second phase precipitates (Zr-

Fe bearing) apart from β phase. The higher volume fraction of the Zr-Fe bearing precipitates along with smaller size may lead to creation of very large interface area through which hydrogen absorption is taking place.

The oxidation of zirconium alloys at high temperatures is controlled by matrix microstructure and its micro constituent as well as the characteristic of oxide formed at metal oxide interface formed by inward diffusion of the oxidizing species [6.1, 6.17]. Monoclinic structure is the room temperature equilibrium phase. The tetragonal phase is neither stable at room temperature and atmospheric pressure nor at the corrosion test conditions (about 415°C and 10 to 17 MPa). The tetragonal phase can be stabilized in three ways:

1) Grain size [6.37,6.38]: from surface energy considerations, it has been suggested [6.37] that the tetragonal phase is stable for grain sizes smaller than about 20 to 30 nm, depending on temperature.

2) Point defects: The tetragonal phase can be stabilized by addition of dopants (Y, Ca, Mg, Fe [6.41]), or oxygen vacancies (oxide films are non-stoichiometric). The H^+ is considered as a destabilizing species and could lower the critical grain size of the tetragonal to monoclinic transformation [6.41].

3) Stresses: Due to the high Pilling Bed-worth ratio (1.56 for zirconium), compressive stresses developed in oxide and metal at the interface is under tension [6.40].

According to the pressure - temperature phase diagram of Zirconia [6.52] and based on measurement of stresses in oxide films, several authors [6.19, 6.38, 6.40] take these stresses to be responsible for the tetragonal phase stabilization. The compressive stress in oxide decreases when it moves away from the interface. The point where the stresses in the oxide have decreased below the critical stress to stabilize the tetragonal phase, a martensitic phase transformation occurs in which the tetragonal phase transforms to monoclinic [6.1]. The volume expansion during the martensitic transformation is approximately ~5% [6.21] and micro-cracks and or pores may form. The origin of pores and micro cracks in oxides of alloy 3 may be due to this phase transformation.

Although compressive stress are beneficial in stabilizing the tetragonal structure of oxide at interface but very high compressive stress may lead to mechanical failure of the oxide. Presence of linear oxide - metal interface in the case of pure zirconium [6.1] will lead to very large compressive stresses, and mechanical failure of the oxide is frequently observed. It is known

that the undulation observed at the interface of most zirconium alloys reduces compressive stress to a reasonable level so that mechanical failure of oxide is avoided. All the three alloys showed undulated interface. But the degree of waviness is more in thick region of oxide formed in alloy 3 compared to alloy 4 and 5. This allows the stress distribution to be optimized since increase of volume due to oxide formation will be distributed over a larger volume of metal. The stress build up will therefore be much less than in others. GIXRD study indicated that the presence of strain in oxide is compressive in nature and this negative strain in oxide is relatively more for alloy 5 and alloy 4 compared to alloy 3. GIXRD study also showed that the oxide formed on the alloy 4 and alloy 5 (having higher Fe content) had higher fraction of tetragonal oxide. This is consistent with the fact that tetragonal crystal structure is stabilized in presence of Fe. Presence of relatively lower fraction of tetragonal oxide in case of alloy 3 (6.4 %) compared with 12% for alloy 4 and alloy 5 and the early transformation of tetragonal to monoclinic transformation as well as presence of large number of pores or cracks/micro cracks in oxide are responsible for the poor oxidation resistance of alloy 3. When the alloy is heat treated in α+ β phase field, the oxidation resistance deteriorated although significant fraction of tetragonal phase observed from 0.5° grazing angle reflection up to 10° grazing angle reflection. Presence of β -phase is responsible for poor resistance of oxidation as oxygen diffusivity in β-phase is significantly high. Oxidation progresses preferentially along the β phase.

6.4 Summary

➢ The change in microstructure and micro chemistry of β phase and intermetallic precipitates with increasing Fe content in three pressure tube Zr-2.5Nb alloys have been studied using TEM/STEM with EDS. The oxidation and hydrogen pick up behaviour of the three alloys have also been analyzed after 415 °C steam autoclaving. The following can be concluded from the oxidation studies and hydrogen pick up determination:

➢ With increasing Fe content, Zr-Nb-Fe bearing intermetallic started to precipitate out. At 1250 ppm Fe most of the precipitates were Zr-Fe intermetallic.

➢ With increase in Fe content up to 800 ppm, oxidation resistance improved. With further addition of Fe, no significant change in oxidation resistance occurred but resistance to hydrogen pick - up deteriorated.

- The α + β heat treated material showed poor oxidation resistance during autoclaving which clearly indicates deleterious effect of β-Zr.

- XPS analysis indicated that irrespective of Fe content in pressure tube material, Nb was present as Nb_2O_5 along with ZrO_2 in the oxide formed during steam autoclaving. Fe was not detected in oxide during XPS analysis.

- When heat treatment was carried out in α+β region Nb_2O_5 was not detected in the outer surface of the oxide formed during autoclaving at 415°C which indicates local Nb rich β-phase is responsible for formation of Nb_2O_5 in as received pressure tube material.

- When Fe content in the alloy was low, the rate of oxidation was high and the oxide formed had pores as well as cracks but H pick up fraction was less. With increasing Fe content, oxidation resistance improved with dense oxide formation without frequent presence of cracks but H pickup was enhanced, *i.e.* although less amount of hydrogen was generated through corrosion reaction, *i.e.* H pick up fraction was more. This indicates that the pores or cracks in oxide are not responsible for high H intake .

- Presence of higher fraction of fine Zr-Fe intermetallic is responsible for high hydrogen intake of the alloy containing 1250 ppm Fe.

- The oxide formed with high Fe content pressure tube material had a higher fraction of tetragonal oxide as compared to low Fe content pressure tube material. Therefore, the higher fraction of tetragonal oxide is responsible for better oxidation resistance of pressure tube with high Fe content.

- When the alloy is heat treated in α+ β phase field, the oxidation resistance deteriorated although significant fraction of tetragonal phase was observed from 0.5° grazing angle reflection up to 10° grazing angle reflection. Presence of higher volume fraction of β - phase may be responsible for poor resistance of oxidation as oxygen diffusivity in β-phase is significantly high. SEM observation also indicated that the oxidation progresses preferentially along the β phase.

6.5 References

[6.1] *Waterside corrosion of zirconium alloys in nuclear power plants, IAEA TECHDOC- 996, 124-169.*

[6.2] Sabol G. P., Gerald R. Kilp, Malcom G. B., Elwyn R., ASTM STP 1023 (1989) 227-245.

[6.3] Borrelly R., Merle P., Adami L., J. Nucl. Mater., 170 (1990) 147-156.

[6.4] B.D. Warr, M.W. Hardie, V.F. Urbanic and D.O. Northwood, Proc. Pacific Corrosion '87 November 1987, Vol. 1.

[6.5] M. Griffiths, J. Nucl. Mater. 159 (1988) 190-218.

[6.6] X. Meng and D. O. Northwood, ASTM-STP 1023 (1989) 478-486.

[6.7] M. Griffiths and R.A. Holt, ASTM-STP 1132 (1992) 172-176.

[6.8] C.K. Chow, C.E. Coleman, R.R. Hosbons, P.H. Davies, M. Griffiths and R. Choubey, ASTM-STP 1132 (1991) 246-275.

[6.9] A. Perovic, V. Perovic, G.C. Weatherly, G.R. Purdy and R.G. Fleck, J. Nucl. Mater. 199 (1993) 102-111.

[6.10] V. Perovic, A. Perovic, G.C. Weatherly, L.M. Brown,G.R. Purdy, R.G. Fleck and R.A. Holt, J. Nucl. Mater. 205 (1993) 251-257.

[6.11] O.T. Woo, G.J.C. Carpenter, J.A. Sawicki and S.R. MacEwen, J. Nucl. Mater. 172 (1990) 71-76.

[6.12] M Griffiths, R W Gilbert and V. Fidleris, ASTM-STP1023 (1989) 658-677.

[6.13] D.O. Northwood, X. Meng-Burany and B.D. Warr, ASTM-STP 1132 (1992) 156-172.

[6.14] M. Griffiths, W. Phythian,S Dumbill, J. Nucl. Mater. 207 (1993) 353-356.

[6.15] B.A. Cheadle and S.A. Aldridge, J. Nucl. Mater. 47(1973) 255-258.

[6.16] G.Choudhuri, S.Neogy, D.Sen, S Majumder, D Srivastava, G K Dey, BK Shah, J. Nucl. Mater. 430 (2012) 205–215.

[6.17] G.Choudhuri, K R Gurumurthy,B K Shah, J. Met. Mater. & Process, (2006)18 (1) 95-106.

[6.18] Hyun-Gil Kim, Jeong Yong Park, Yong Hwan Jeong, J. Nucl. Mater., 345(2005) 1-10.

[6.19] H. J. Beie, A. Mitwalsky, F. Garzarolli, H. Ruhmann, H.-J. Sell, ASTM STP 1245 (1994) 615-641.

[6.20] D.O. Northwood, W.L. Fong, Metallography 13 (1980) 97-201.

[6.21] D. Warr, V. Perovic, Y.P. Lin, A.C. Wallace, in: ASTM STP 1423 (2002) 313-338.

[6.22]] Srivastava, D., Dey, G. K., and Banerjee S., Metall. Mater. Trans. A, 26 (1995) 2707-2718.

[6.23] Gargi Choudhuri, D. Srivastava, K.R. Gurumurthy, B.K. Shah , J. Nucl. Mater., 383 (1-2) (2008) 178-182.

[6.24] S. K. Sinha, R.K.Sinha, IAEA Workshop on Prediction of axial and radial creep of HWR pressure tubes, (2011) Nov.16-18.

[6.25] R. G. Fleck, J. E. Elder, A. R. Causey, R. A. Holt, ASTM STP 1245(1993)168-181.

[6.26] M. Griffith, H. Mullejans, Micron, 26 (6) (1995) 555-557.

[6.27] P. Tejland, M. Thuvander, H.O. Andrén, S. Ciurea, M. Dahlbäck, L.Hallstadius, J. ASTM Int., 8 (6) (2011).

[6.28] Y.Nishini, A. R. Krauss,Y. Lin,D .M. Gruen, , J. Nucl. Mater., 228 (1996) 346-353.

[6.29] C. O. A. Olsson, D. Landolt, Corros. Sci., 46 (2004) 213–224.

[6.30] Y.S. Li, K.C. Wong,P.C Wong,KAR Mitchell, Appl. Surf. Sci., 103 (1996) 389-393.

[6.31] Jianlong Lin, Hualong Li, J.A. Szpunar, R. Bordoni, A.M. Olmedo, M. Villegas, A.J.G. Maroto, Mater. Sci. and Eng. A, 381 (2004) 104–112.

[6.32] A. Yilmazbayhan, A.T. Motta, R.J. Comstock, G.P.Sabol, B. Lai, Z. Cai, J. Nucl. Mater., 324 (2004) 6-22.

[6.33] Jeong-Yong Park , Hyun-Gil Kim, Yong Hwan Jeong, Youn-Ho Jung, J. Nucl. Mater., 335 (2004) 433–442.

[6.34] Y. Li, R. Rogge, R.A. Holt, Mater. Sci. and Eng. A, 437 (2006) 10–20.

[6.35] M. KiranKumar, C. Vanitha, I. Samajdar, G.K. Dey, R. Tewari, D. Srivastava, S. Banerjee,J. Nucl. Mater., 335 (1) (2004) 48-58.

[6.36] N. Petigny, P. Barberis, C. Lemaignan, Ch. Valot, M. Lallemant, J. Nucl. Mater. 280 (2000) 318-330.

[6.37] R.C. Garvie, J. Phys. Chem., 60 (4) (1966) 1238-1243.

[6.38] P. Barberis, J. Nucl. Mater. 226 (1995) 34-43.

[6.39] R.C. Garvie and PJ. Nicholson, J. Am. Ceram. Soc. 55 (6) (1972) 303-305.

[6.40] J. Godlewski, , ASTM-STP 1245 (1994) 663-683.

[6.41] D. PScheur, F. Lefebvre, A.T. Motta, C. Lemaignan and D. Charquet, ASTM-STP 1245 (1994) 687-705.

[6.42] Jianlong Lin, Hualong Li, Cheol Nam, Jerzy A. Szpunar, J. Nucl. Mater. 334 (2004) 200–206.

[6.43] P. Mukherjee, A. Sarkar, P. Barat, S.K. Bandyopadhyay, Pintu Sen, S.K. Chattopadhyay, P. Chatterjee, S.K. Chatterjee, M.K. Mitra, Acta Mater. 52 (2004) 5687–5696.

[6.44] Cox, B., AECL, Report No. AECL-8702, 1985.

[6.45] M. Y. Yao, J. H. Wang, J. C. Peng, B. X. Zhou, and Q. Li, J. of ASTM Int., 8 (2) Paper ID JAI102948.

[6.46] G.M. Hood, R.J. Schultz, Philos. Mag. 26 (1972) 329.

[6.47] Rodolfo Ariel Pe´rez, Mariana Weissmann, J. Nucl. Mater. 374 (2008) 95–100.

[6.48] H. Zhou, G.M. Hood, J.A. Roy, R.J. Schultz, J.A. Jackman, J. Nucl. Mater. 210 (1994) 239-243.

[6.49] Y. Yoshida, M. Menningen, R. Sielemann, G. Vogl, G. Weyer, K.Schro¨ der, Phys. Rev. Lett. 61 (1988) 195.

[6.50] Yong Hwan Jeong, Kyoung Ok Lee, Hyun Gil Kim, J. Nucl. Mater. 302 (2002) 9–19.

[6.51] Yong Hwan Jeong, Hyun Gil Kim, Dae Jung Kim, Byung Kwon Choi, Jun Hwan Kim, J. Nucl. Mater. 323 (2003) 72–80.

[6.52] S. Block, J.A.H. Da Jornada and G.J. Piermarini, J. Am.Ceram. Soc. 68(9) (1985) 497-499.

Chapter7

Effect of irradiation on Oxide

This chapter describes the effect of irradiation viz., ion as well as neutron on oxide and compares the results with oxide formed during in pile irradiation in PHWR.

7.1 Introduction

Zr base alloys are the main material of core components of Pressurized Heavy water reactor (PHWR). The excellent corrosion resistance of these alloys in PHWRs environment is due the presence of adherent black lustrous thin protective sub-stoichiometric oxide (ZrO_{2-x}, where x<0.44) [7. 1].With increase in temperature and neutron dose, corrosion resistance deteriorates as well as new corrosion mechanism sets in, which results in formation of stoichiometric (ZrO_2) oxide [7. 2]. For high burn up and high temperature advanced reactor applications, it is important to minimize the corrosion rate of the alloys which is mainly controlled by the characteristics of the oxide formed in the reactor. The room temperature equilibrium phase is monoclinic crystal structure. But the high temperature cubic or tetragonal structure can be stabilized in the oxide of Zr bases alloys by either presence of compressive stress, or the addition of alloying elements or lowering the grain size below 30 nm. These tetragonal to monoclinic phase transformation in the oxide is associated with volume change and simultaneously generation of pores or cracks which deteriorate the protective properties of the oxide. Irradiation can also induce crystalline to crystalline phase transformation through the generation of defects viz. vacancies and interstitials and can significantly change the corrosion rate. The damage profile caused by neutron in reactor is often simulated in short term by varying out of pile irradiation conditions. So a systematic study on the effect of ion irradiation (heavy ion as well as proton) on crystalline phase transformation of already formed oxide on the two important materials, Zr-Sn-Fe-Cr and Zr-2.5Nb alloys and correlating the results with the in-pile oxide formedin actual fuel tube material are required.

In the present study, 306 KeV Ar [9+]has been used to irradiate zirconium-oxide which formed on Zr-2.5Nb (as received alloy 4) and alpha annealed heat-treated Zr-Sn-Fe-Cr alloys (alloy-1 700°C /10 hrs.) during 3 days accelerated autoclaving at 415°C 10.3 MPa. 3.5 MeV proton has

also been used to irradiate oxide of αannealed Zr-Sn-Fe-Cr alloy (alloy-2 800° C /10 hrs.) at a fluence of 5×10^{16} p/cm^2.The details of experimental procedure have been described in section 3. 2. 13. The effect of Ar ion irradiation on crystalline to crystalline phase transformation at a fluence of 3×10^{15} Ar^{+9} /cm^2 has been studied using GIXRD technique. This technique has been elaborated in section 3. 2. 11. The results of heavy ion irradiation were compared with that from proton irradiation.The Transport of Ions in matter (TRIM-96) /The Stopping and Range of Ions in Matter (SRIM-2008) computer program was used to simulate the distribution and damage level of ions.

To study the distribution of phases along the thickness directionin actual oxide of fuel tube formed during in-pile exposure, fuel tube after 7670 MWd/T burn up was received and samples were prepared without disturbing the outer surface. GIXRD study upto 5° grazing angle reflection was carried out. The distribution of phases along the thickness direction was evaluated and compared with that of out of pile as well as heavy ion irradiation. After GIXRD study samples were prepared for measurement of oxide thickness in optical microscope.

7.2 Damage profile using TRIM programme:

The displacement per atom (dpa) in the case of heavy ion and proton irradiation, were calculated using TRIM-96 programme. The damage profile and the range of 306 KeV Ar^{+9} ions in oxide of Zr calculated by SRIM-2008 are shown in fig.7.1a and fig.7. 1b respectively. Damage level can be calculated in terms of displacement per atom (dpa) using the following formula [7. 3, 7. 4].

$$dpa = \frac{\varphi \times 10^8 \times Damage - rate}{N}$$

where φ is the fluence in ions/cm^2, the damage - rate is in vacancies/(ion-A°) obtained with SRIM, and N is the atomic density in atoms/cm^3 (0.2776×10^{23} taking ρ=5.68 g/cm^3). The maximum damage occurred during heavy ion irradiation in oxide is 9.46 dpa. Range of Ar (fig. 7. 1b) with 306 KeV ion with the given energy is∼193 nm and the damage is maximum around a target depth of 125 nm.

In case of proton irradiation as the depth of penetration is more than the thickness of oxide, the multilayer target was considered during SRIM calculation. The damage profile and the range of 3.5 MeV protonions calculated by SRIM 2008 are shown in fig.7. 2 a and fig.7. 2b respectively.

Range of proton with given energy is ~ 69.4 µm and the damage is maximum around that location. Maximum dpa in α-Zr matrix is 0.015 dpa and in oxide it is further less.

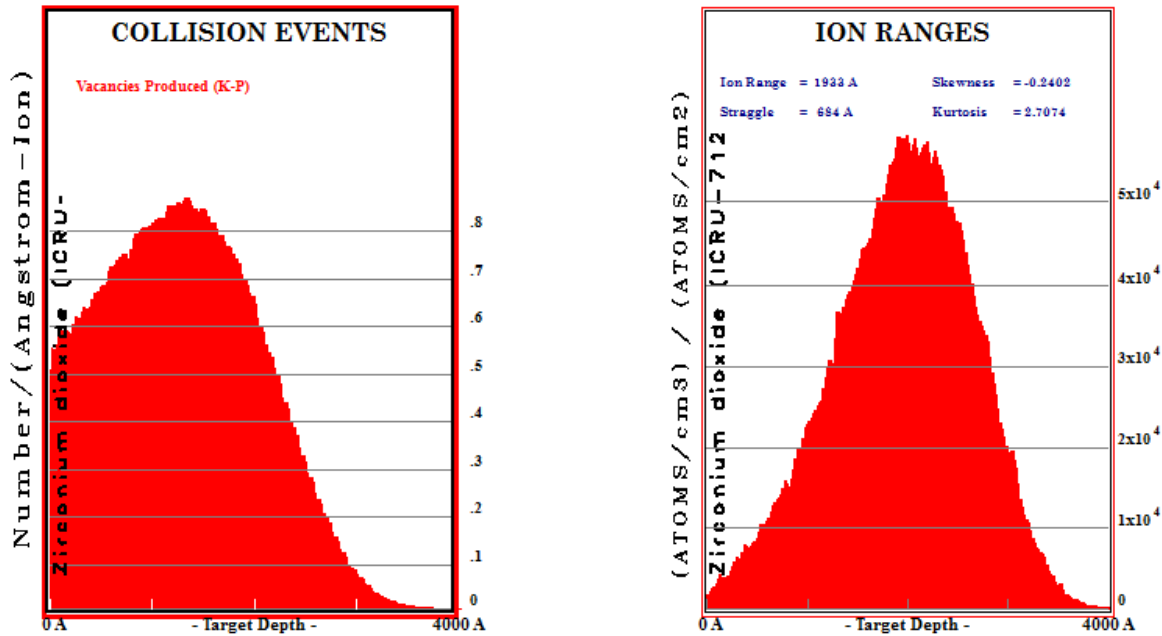Fig.7. 1. (a) Damage profile of 306 KeV Ar^{+9} ions in oxide of Zirconium calculated by SRIM-2008. (b) Plot showing the range of ions (193 nm) in target, whereas oxide is having thickness 1200 nm.
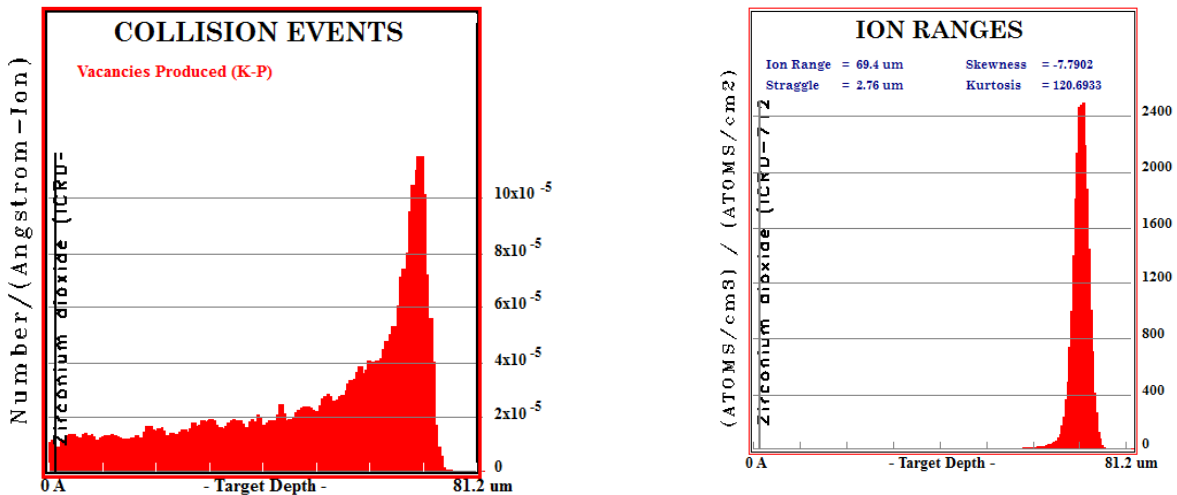

Fig.7. 2. (a) Damage profile of 3.5 MeV proton ions in oxide of Zirconium calculated by SRIM-2008. (b) Plot showing the range of ions (69.4 µm) in target, whereas oxide is having thickness 1.2 µm.

The grazing incident angles of 0.5°, 1°, 2°, 5°and 10° were used to study the oxide structure along the thickness direction. The depth of penetration (τ) of X-ray during GIXRD, were calculated at 0.5°, 1°, 5°and 10° and are given in table 3.4 of section 3.2.11. Range of Ar with 306 KeV ion with the given energy is~193 nm and the damage is maximum at a target depth of 125 nm. So grazing angle reflection at 0.5° will show the effect of heavy ion irradiation. In case of proton irradiation, up to 10° grazing angle will cover very low damage (~0.0035 dpa). Maximum damage (0.015 dpa) occurs at 69.5 μm inside the surface of the target which anyhow GIXRD is not probing. The GIXRD on the fuel tube material was performed upto 5° grazing angle which corresponds to 1.5 μm thickness in oxide. To establish the chemical state of elements in the oxide film the outermost surface of all the three alloys were analyzed with XPS using hemispherical Thermo VG Clam2 analyzer. Detailed scans of C 1S, Zr 3d, Nb 3d, Fe, O 1S were obtained with monochromatic Mg Kα X- ray source. The area of analysis was approximately 100 mm^2.The binding energy of O1s, Zr 3d and Nb 3d was corrected taking C 1S peak at 284.5eV.

7.3 Characteristics of Oxide:

After accelerated steam autoclaving of the alloys, weight gains for all the samples were measured. When the weight gain values were converted into thickness of oxide (1 μm = 14.7 mg/dm^2), the avg. oxide layer thickness of Zr-2.5Nb alloy was 1.55 μm.Oxide thickness was also measured in SEM and it has been observed that the oxide layer thickness is varying in a close range of 1.3-1.8 μm for Zr-2.5Nb alloy. In case of both alpha annealed Zr-Sn-Fe-Cr alloys the oxide thickness is in the range of 1 - 1.2 μm. From the calculation as given in table 3.4 of section 3.2.11, it is seen that up to grazing angle incidence 1°, X-ray reflection is only from the oxide , in all the three oxidized samples. At 5° grazing angle incidence, significant contribution fromα-Zr matrix will present for Zr-Sn-Fe-Cr alloys, but relatively less contribution from matrix α-Zr for Zr-2.5Nb alloy due to higher thickness of oxide.

7.4 GIXRD Results

7.4.1 Heavy Ion Irradiation:

7.4.1.1 Zr-2.5 Nb alloy

The results of GIXRD study on the oxides of Zr-2.5Nb before and after heavy ion irradiation are shown in fig. 7.3 a, b, c, d and fig. 7.4 a, b, c, d respectively. From the GIXRD scan onas received oxide of Zr-2.5Nb, (fig. 7.3a) 0.5°grazing angle X- ray reflectionshowed presence of low intensity (101)t reflection of tetragonal phase at 30.28°with peaks of monoclinic ZrO_2 oxide of (001)m, (-11 1)m, (111)m , (0 2 0)m and (002)m at 17.4°, 28. 3°, 31.46°, 34.3°and 35.3° respectively. With increase in grazing angle (1°) depth of penetration of X-ray increased and intensity of tetragonal peak 30.28°was found to increase (fig.7.3b) [7.5, 7. 6, 7. 7, 7. 8]. With further increase in angle of incidence to 5°,(fig. 7.3c) matrix α Zr peaks of (1 0 0)$_{hcp}$, (0 0 2)$_{hcp}$,(1 0 1)$_{hcp}$ were seen at 32.17°, 34.82°, 36.51°respectively. At 10° grazing angle reflection (fig. 7.3d) depth of penetration of X-ray is high and majority of the peaks are from matrix α Zr peaks of (1 0 0)$_{hcp}$, (0 0 2)$_{hcp}$,(1 0 1)$_{hcp}$along with monoclinic reflections from ($\bar{1}$11)m and (200)m. At 5° and 10° ($\bar{1}$11)m reflection was seen at 28.17° compared to 28.3° at 0.5°grazing angle. This shifting of peak towards higher angle may be due to the smaller grazing angle or presence of uniform stress at the interface location. No peak of sub-oxide was found.The volume fraction of tetragonal phase can be determined from Garvie and Nicholson formula [7. 9]

$$f_T = \frac{I^T_{101}}{I^M_{-111} + I^M_{111} + I^T_{101}} - - - - - - 7.1$$

where the I^T_{101} is the integrated intensity under the (101) tetragonal peak and the $I^M_{\bar{1}11}$ and I^M_{111} are the integrated intensity of ($\bar{1}$11) and (111)m peaks of monoclinic phase. The tetragonal fraction calculated using the above formula equation 7.1 is for powder sample, with no texture. In random samples maximum intensities are from ($\bar{1}$11)m planes for monoclinic and (101)t planes for tetragonal. In this case maximum intensity is from (020)m planes for the monoclinic and (101)t planes for the tetragonal. There are no significant reflections from (111)m monoclinic planes. In this work, for only comparison purpose, the above formula has been used. This formula will not provide absolute fraction of tetragonal phase. The above formula indicated that the oxide contained a very small fraction (< 5%) of tetragonal phase at 0.5° grazing angle incidence and the rest being monoclinic phase. At 1°grazing angle reflection, the volume fraction of tetragonal phase was found to be 5%. At 5°grazing angle, tetragonal fraction was much higher

(11%) compared to 1° grazing angle reflection.Texture effect has not been considered during this phase fraction determination.

After heavy ion irradiation tetragonal fraction calculated using equation 7.1, at 0.5°grazing angle incidence (fig. 7.4 a) increased significantly ($\approx$ 47 %). Intensity of reflection of (101)t at 30.34° tetragonal increased and simultaneously reflection from monoclinic phase ($\bar{1}$11) m at 28.4°, (020)m at 34.36° reduces . The reflection of (002)t at 34.6 ° and (110)t at 35.28 ° were also observed. Due to presence of monoclinic and tetragonal phase, reflection at 35.3° ((110)t at 35.28 ° and (002)m at 35.31°) is maximum. With increase in grazing angle reflection at 1°, (fig. 7.4 b) tetragonal fraction remained high (($\approx$ 40 %) compared to as received condition (5 %). The reflection of (002)t at 34.6°, (110)t at 35.28 ° (112)t at 50.5°, (103)t at 59.3°, (211)t at 60.22° were also present. At 5° grazing angle reflection (fig. 7.4 c) tetragonal fraction is still high (($\approx$ 26.4 %) compared to unirradiated oxide (11%)). From this observation, it can be inferred that at 5° grazing angle reflection, irradiation induces monoclinic to tetragonal phase transformation but the extent of transformation is less as unirradiated oxide at same grazing angle had 11% tetragonal phase fraction. At 10° grazing angle reflection after irradiation, tetragonal reflection observed at 30.22°, is similar to unirradiated oxide. This clearly indicates that heavy ion induced phase transformation is not significant at this depth. 306 KeV Ar+9 ion at a dose of 3x10 ^{15} Ar^{+9}/cm^2 is capable of crystalline to crystalline phase transition in oxide of Zr-2.5Nb alloys and the effect of heavy ions irradiation is mostly confined to the surface of the sample.
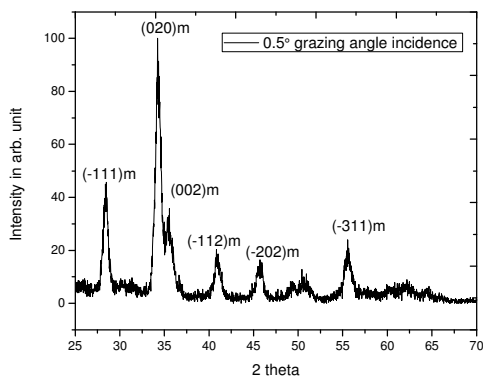
Fig. 7. 3a : Before Irradiation 0.5° grazing angle reflection from oxide of Zr-2.5Nb alloy shows mostly reflection from monoclinic phase.
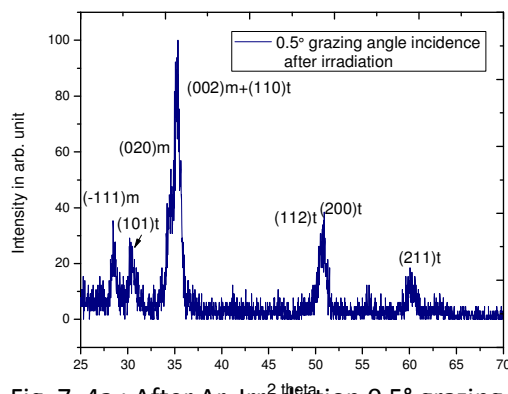
Fig. 7. 4a : After Ar Irradiation 0.5° grazing angle reflection from oxide of Zr-2.5Nb alloy shows significant tetragonal reflection. Reflection intensity from monoclinic phases reduces.
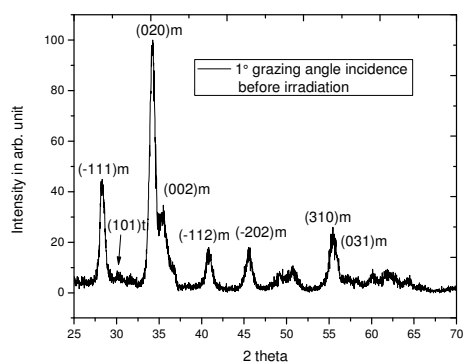
Fig. 7. 3b : Before Irradiation 1° grazing angle reflection from oxide of Zr-2.5Nb alloy shows mostly reflection from monoclinic phase.
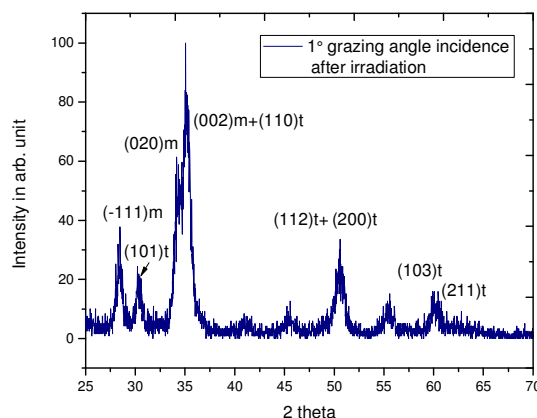
Fig. 7. 4b : After Ar Irradiation 1° grazing angle reflection from oxide of Zr-2.5Nb alloy shows significant tetragonal reflection. Reflection intensity from monoclinic phases reduces.

Fig. 7. 3c : Before Irradiation 5° grazing angle reflection from oxide metal interface of Zr-2.5Nb alloy shows reflection from tetragonal, monoclinic oxide and α-Zr phase.

Fig. 7. 4c : After Ar Irradiation 5° grazing angle reflection from oxide metal interface of Zr-2.5Nb alloy shows reflection of tetragonal, monoclinic oxide and α-Zr phase.

Fig. 7. 3d : Before Irradiation 10° grazing angle reflection from oxide metal interface of Zr-2.5Nb alloy shows reflection of mostly α-Zr phase and monoclinic oxide phase.
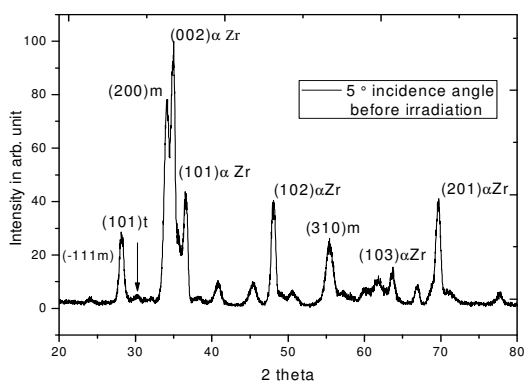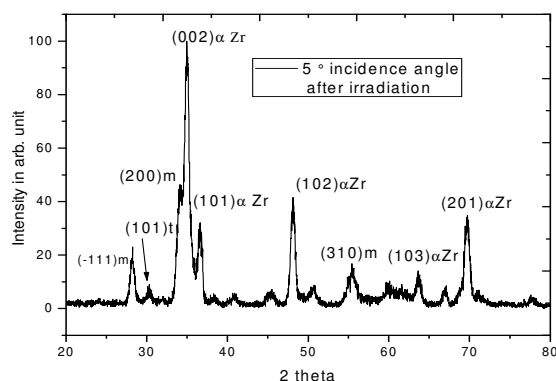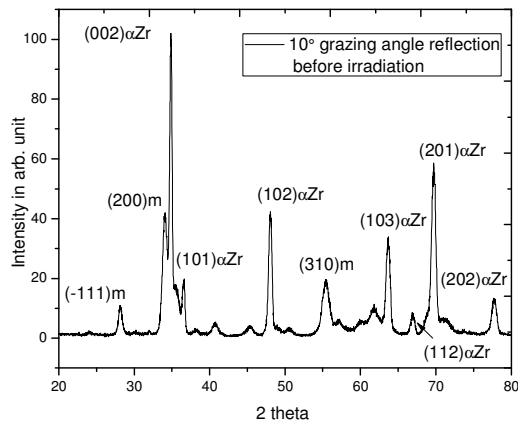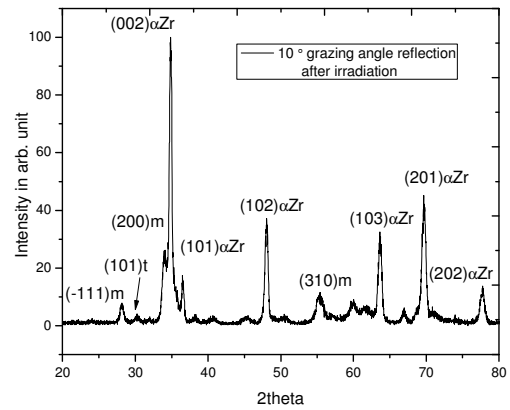
Fig. 7. 4d : After Irradiation 10° grazing angle reflection from oxide metal interface of Zr-2.5Nb alloy shows reflection of mostly α-Zr phase and monoclinic oxide phase. Tetragonal reflection at 30.24 ^{0} is also found.

7.4.1.2 Zr-Sn-Fe-Cr alloy

The results of GIXRD study on the oxides of alpha annealed (700° C/10 hrs.) Zr-Sn-Fe-Cr series alloy 1 before and after heavy ion irradiation are tabulated in table 7. 2 and also given in fig. 7.5 a, b, c, d and fig. 7.6 a, b, c, d respectively. From the GIXRD scan on as received oxide (fig. 7.5a), 0.5°grazing angle X- ray reflection showed presence of (101)t reflection of tetragonal at 30.4° with peaks of monoclinic ZrO_2 oxide of (001)m, ($\bar{1}$11)m, (111)m, (020)m and (002)m at 17.4°, 28.4°, 31.4°, 34.35°and 35.4° respectively. With increase in grazing angle (1°) depth of penetration of X-ray increased and intensity of tetragonal peak 30.28° was found to increase (fig. 7.5b). With further increase in angle of incidence to 5°, (fig. 7.5c) matrix α Zr peaks of (1 0 0)$_{hcp}$, (1 0 1)$_{hcp}$ were seen at 32.17° and 36.51° along with monoclinic peaks and tetragonal peaks. The characteristic peaks of sub-oxide Zr_3O was found at 5° grazing angle incidence as shown in fig. 7.5c. At 10° grazing angle (002)hcpreflection of α Zr peaks at 34.8° were clearly visible along with other ones similar to previous one including Zr_3O peaks. This observation clearly indicates that at or near the oxide metal interface hexagonal Zr_3O is present in alpha annealed Zr-Sn-Fe-Cr series alloy. The alloy showed very small fraction (R < 5%) tetragonal phase at 0.5° and 1° grazing angle incidence and the rest being monoclinic phase. At 5°grazing angle tetragonal fraction was higher (≈ 11%) compared to 1° grazing angle reflection.

If we compare the intensity vs. 2 theta profile from the outer layer of oxide (i.e. at 0.5°grazing angle incidence - fig. 7. 3a, fig. 7. 5a and 1°grazing angle incidence - fig. 7. 3b, fig. 7. 4b) for textured Zr-2.5Nb alloy and α-annealed Zr-Sn-Fe-Cr alloy in unirradiated material, 100% peak corresponds to the reflection from (020)m of monoclinic structure but not from ($\bar{1}$11)m. (002)m reflection is also present significantly. (111)m reflection is nearly absent in both the cases. This indicates that the outer layer of oxide is highly textured irrespective of base metal orientation. When grazing angle incidence increased to 5° and 10°, maximum reflection from oxide of Zr-Sn-Fe-Cr alloy is from (200)m plane at 34.16° whereas maximum intensity of matrix α-Zr is from (101)hcp reflection at 36.6°. But when base metal is having different texture with maximum intensity is from (002)hcp α-Zr for both the grazing angle reflection (as in case of Zr-2.5Nb alloy), oxide again shows maximum reflection from (200)m plane. The texture of oxide forms at or near the oxide/metal interface is also independent on base metal texture. And outer surface has predominantly (020)m, (002)m reflection along with ($\bar{1}$11)m reflection whereas near oxide metal interface oxide reflection changed to (200)m.($\bar{1}$11)m reflection is also present. From these observations it can be inferred that the oxide away from the interface is preferentially oriented with (200)m plane aligned parallel to the oxide metal interface i.e. the pole of (200)m is perpendicular to the oxide metal interface and near the interface (200)m plane is nearly perpendicular to the oxide metal interface. The tetragonal oxide present in as oxidized samples is also highly textured with reflection from (101)t in all the grazing angle reflection conditions. This indicates that (101) planes of tetragonal oxide are perpendicular to the oxide metal interface i.e. the pole of this plane is parallel to the oxide metal interface.

Oxide peaks of particular interest are the triplet of peaks, (200)$_m$, (020)$_m$, and (002)$_m$ [7.10] . These poles are oriented in three widely separated directionsand helping in qualitatively monitoring the oxide texture. It is observed [7. 2,7. 10] that the growth direction in the oxide is approximately normal to the ($\bar{4}$01)m planes, which are parallel to the oxide-metal interface. The angles between the pole of ($\bar{4}$01)m plane (parallel to the growth direction) are oriented 14.9°, 90.0°, and 95.6° from the (200)$_m$, (020)$_m$, and (002)$_m$ poles, respectively. The dominant peaks from diffraction of the oxide away from the oxide-metal interface are the (020)$_m$ and (002)$_m$ reflections. Given the predominant ($\bar{4}$01) m oxide growth direction, these (the (020)$_m$ and

$(002)_{m)}$poles are approximately normal to the oxide growth direction and therefore are expected to be the primary diffraction peaks when the oxide is analyzed in grazing angle geometry.

Some studies suggested that the formation of oxide texture is mainly due to the epitaxialorientation relationship between ZrO_2 and α-Zr substrate. The epitaxial relations observed [7. 2] for very thin oxide films on the(11$\bar{2}$0) face of Zr are a mixture of :

$$(100)[001]m//(0001)[11\bar{2}0] \text{ and}$$

$$(100) [010]m //(0001) [11\bar{2}0]$$

However, nounique epitaxial relationship exists for thermal oxide films on Zr [7. 2]. The epitaxial relationship cannot explain the oxide texture formed on the samples made from different surfaces of the pressure tube or the same type of oxide reflection in annealed Zr-Sn-Fe-Cr alloy compared to textured Zr-2.5Nb pressure tube alloy. This indicates the complexity involved in the formation of oxide film. As the process of oxidation is associated with generation of huge amount of stresses, those oxide orientations only develop which significantly minimize the compressive stresses in the plane of the surface. Previous studies have shown that the predominant texture in the oxide layer has the ($\bar{4}$01)m pole perpendicular to the oxide surface [7. 11]. It has been seen that such orientation of the ($\bar{4}$01)m pole minimized the stresses generated from oxide growth.

The crystal orientationrelationship between the monoclinic and the tetragonal phases was found to be (103)m ‖ (100)tor (103)m ‖ (101)t and [100]t ‖ [010]m. Work done by Lin et al. [7. 4] on the characteristics of oxide of Zr-2.5Nb alloy formed during exposure in staticautoclaves at 623 K in lithiated heavy water showed that thetetragonal Zirconia is highly textured and no change in texture in monoclinic or tetragonal phase was observed with respect to the oxidation time. Lin et al. [7. 4] also showed that the main texture component is the growth mode texture. XRD studies of Lin et al. [7. 4] on Zr-2.5Nb and Zircaloy-4 oxidized in static autoclaves at 623K show that the ideal orientations of monoclinic Zr oxide grown on the Zr-2.5Nb are (10$\bar{3}$) [0$\bar{1}$ 0] and (10$\bar{4}$) [401], while the ideal orientation for the monoclinic Zr oxide formed on the Zircaloy-4 is the (10$\bar{4}$) fiber.

After heavy ion irradiation tetragonal fraction at 0.5°grazing angle incidence (fig.7.6a) increased significantly (49.5 %). Intensity of reflection of (101)t at 30.4° tetragonal increased and simultaneously peak intensity of monoclinic phase (-111) m at 28.4°, (020)m at 34.4° reduced. The reflection of (002)t at 34.6°, (110)t at 35.28 ° (112)t at 50.5°, (211)t at 60.22° were also present. Due to presence of monoclinic and tetragonal phases, reflection at 35.3° ((110)t at 35.28° and (002)m at 35.31°) is maximum just as similar to Zr-2.5Nb. With increase in grazing angle reflection at 1°, (fig. 7.6 b) tetragonal fraction remained high (37.4 %) compared to as received condition. At 5° grazing angle reflection (fig. 7.6 c) (002)α-Zr peak is clearly distinguishable from (200)m due to lowering of intensity of (200)m and tetragonal fraction is 16%. For 10° grazing angle reflection (fig.7.6 d) depth of penetration of X-ray is high and peaks from matrix α Zr peaks were found along with monoclinic and tetragonal peaks. The peak at 36.75° is from hexagonal Zr_3O (5.563 Å, 31.185Å) along with (101) α-Zr peak is at 36.55°. This sub-oxide peak is only detected at 5° and 10° grazing angle which indicates that it is present in the interface location and it was present before irradiation also. So heavy ion irradiation does not have any effect on sub-oxide formation. It can be concluded that 306 KeV Ar^{+9} ion at a dose of 3×10^{15} Ar^{+9}/cm^2 is capable of crystalline to crystalline phase transition near the outer surface of the oxide of Zr-Sn-Fe-Cr alloys and Zr-Nb alloy.

Fig. 7. 5 a : Before Irradiation 0.5° grazing angle reflection from oxide of Zr-Sn-Fe-Cr alloy shows mostly reflection of monoclinic phase.

Fig. 7. 6 a : After Ar Irradiation, 0.5° grazing angle reflection from oxide of Zr-Sn-Fe-Cr alloy shows significant tetragonal reflection. 100% intensity in peak was shifted to an angle where both tetragonal and monoclinic peaks present.
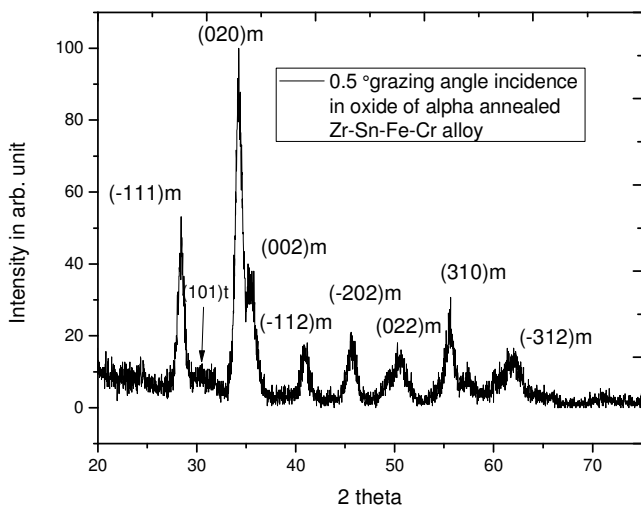
Fig. 7. 5 b : Before Irradiation 1° grazing angle reflection from oxide of Zr-Sn-Fe-Cr alloy shows mostly reflection from monoclinic phase.
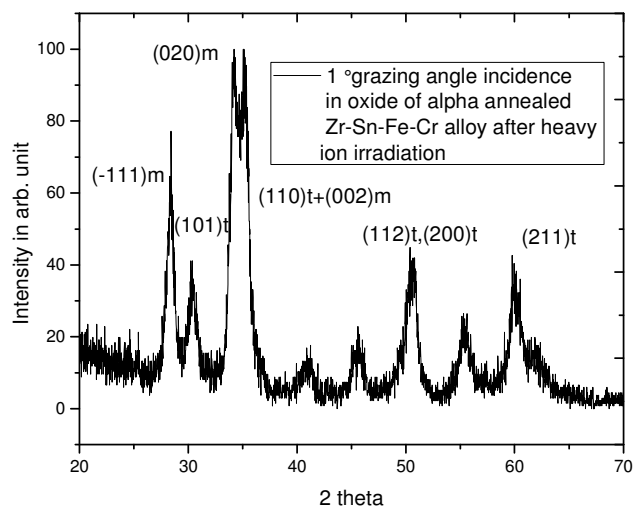
Fig. 7. 6 b : After Ar Irradiation 1° grazing angle reflection from oxide of Zr-Sn-Fe-Cr alloy shows significant tetragonal reflection.
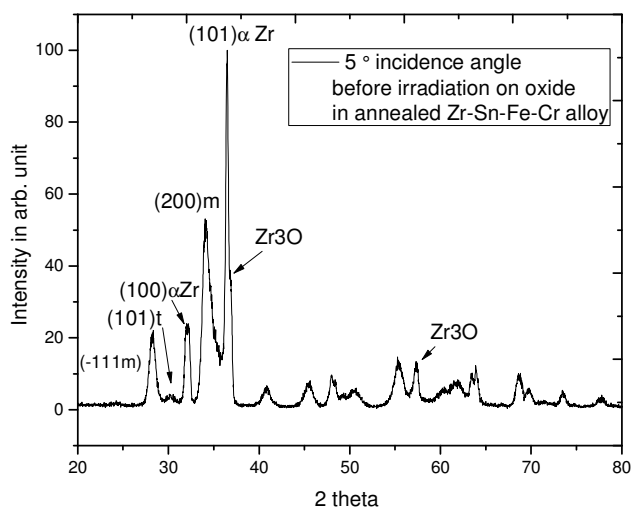
Fig. 7. 5 c : Before Irradiation 5° grazing angle reflection from oxide metal interface of Zr-Sn-Fe-Cr alloy shows reflection from tetragonal, monoclinic oxide and α-Zr phase.
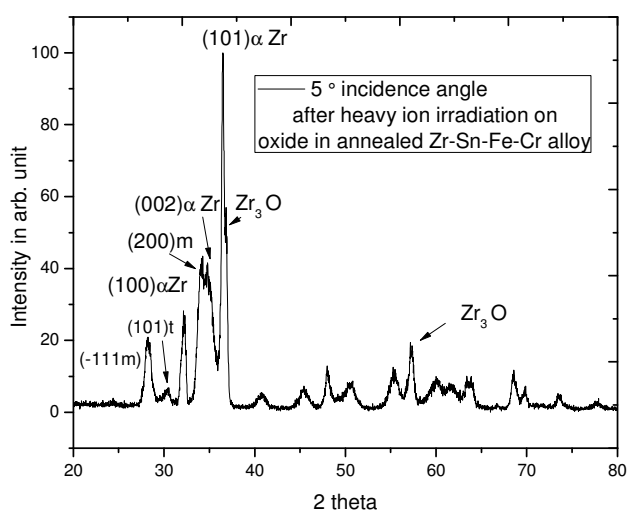
Fig. 7. 6 c : After Ar Irradiation 5° grazing angle reflection from oxide metal interface of Zr-Sn-Fe-Cr alloy shows reflection from tetragonal, monoclinic oxide and α-Zr phase.
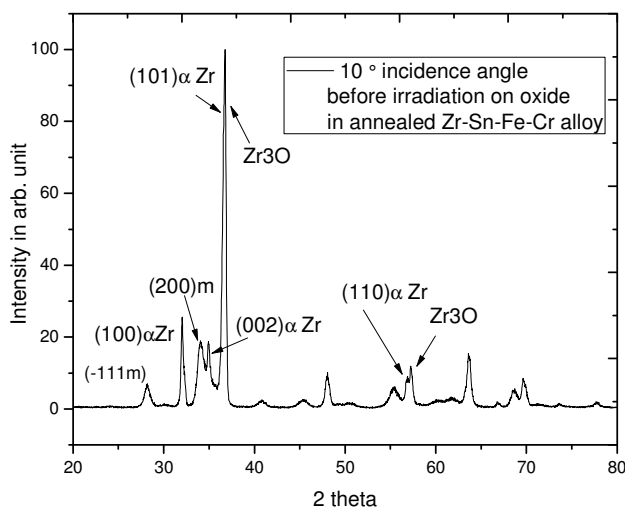
Fig. 7. 5 d : Before Irradiation 10° grazing angle reflection from oxide metal interface of Zr-Sn-Fe-Cr alloy shows reflection from mostly α-Zr phase and monoclinic oxide phase.

Fig. 7. 6 d : After Irradiation 10° grazing angle reflection from oxide metal interface of Zr-Sn-Fe-Cr alloy shows reflection from mostly α-Zr phase and monoclinic oxide phase. Tetragonal reflection at 30.24°is also found.

7.4.2 Proton Irradiation

7.4.2.1 Zr-Sn-Fe-Cr alloy

The results of GIXRD study on the oxides of αannealed Zr-Sn-Fe-Cr alloys before and after proton ion irradiation are given in fig. 7.7 a, b, c, d and fig. 7.8 a, b, c, d respectively. From the GIXRD scan on as received oxide (fig. 7.7 a) 0.5 grazing angle X- ray reflection showed presence of peaks of monoclinic ZrO_2 oxide of $(001)m$, $(\bar{1}11)m$, $(020)m$ and $(002)m$ at 17.5°, 28.4°, 34.35°and 35.4° respectively. With increase in grazing angle (1°) depth of penetration of X-ray increased and reflection from $(101)t$ tetragonal structure at 30.28° was found (fig. 7.7 b). With further increase in angle of incidence to 5°, (fig.7.7 c) very sharp reflection from (100) α Zr at 31.94° was seen along with monoclinic reflections and sub-oxide hexagonal (5.63 Å, 15.59 Å) Zr_3O_{1-x} reflection from (113). At 10° grazing angle, clearly defined characteristics peak of (113) Zr_3O_{1-x} peak was found at 36.27°. (002)hcp reflection of α Zr peaks at 34.8° were also visible along with other reflections.

After proton irradiation, no significant change in Intensity vs. 2theta profile was observed (fig. 7.7a , fig. 7.8 a and fig. 7.7 b, fig. 7.8 b, fig. 7. 7 c , fig. 7. 8 c and fig. 7. 7 d, fig. 7. 8 d).

Fig. 7. 7a : Before Irradiation 0.5° grazing angle reflection from oxide of Zr-Sn-Fe-Cr alloy shows mostly reflection from monoclinic phase.
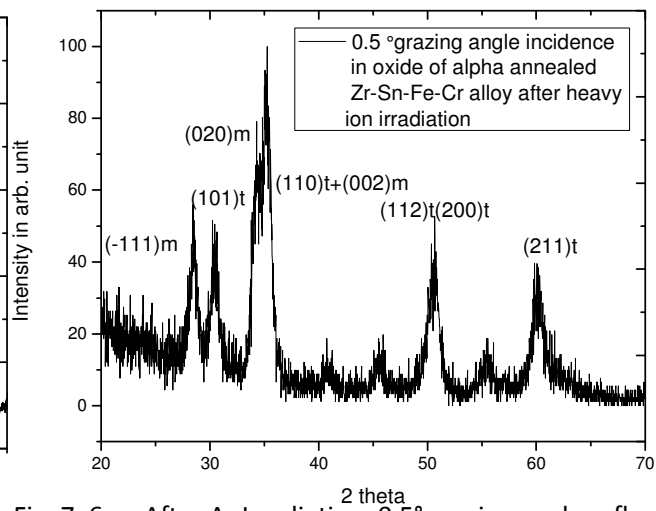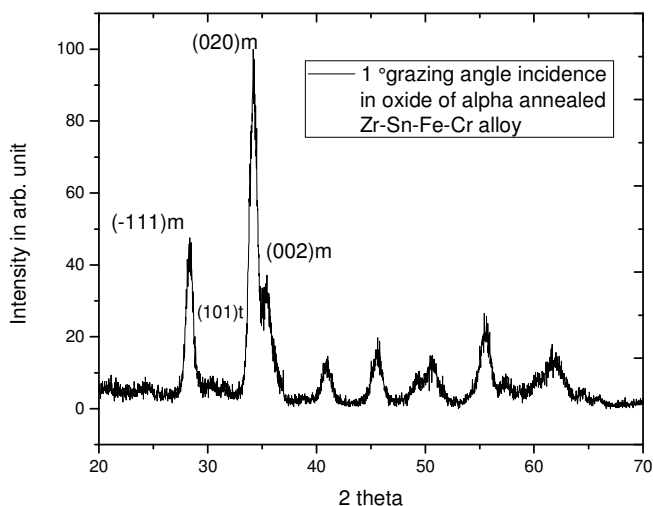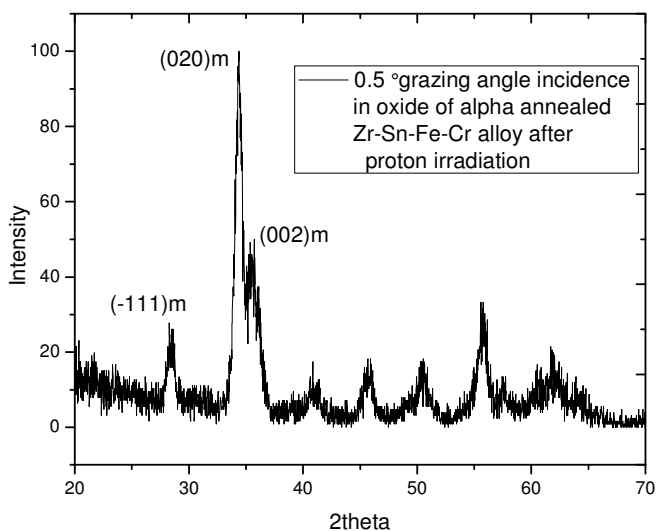

Fig. 7. 8a : After proton Irradiation 0.5° grazing angle reflection from oxide of Zr-Sn-Fe-Cr alloy shows no tetragonal reflection. Reflection intensity is only from monoclinic phases.
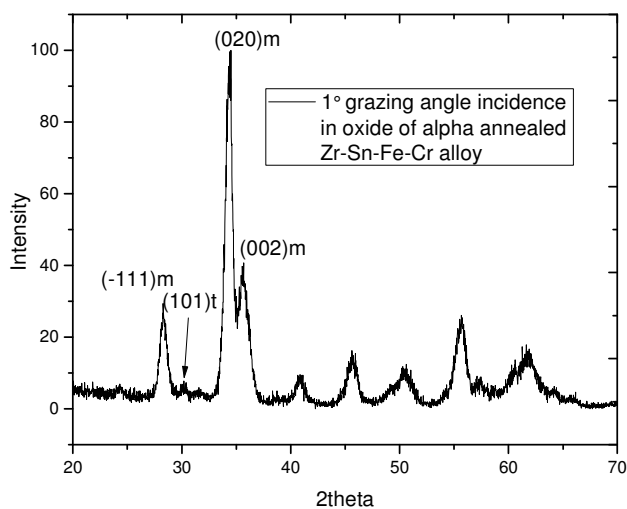
Fig. 7. 7 b : Before Irradiation 1° grazing angle reflection from oxide of Zr-Sn-Fe-Cr alloy shows mostly reflection from monoclinic phase with very small fraction of tetragonal reflection.
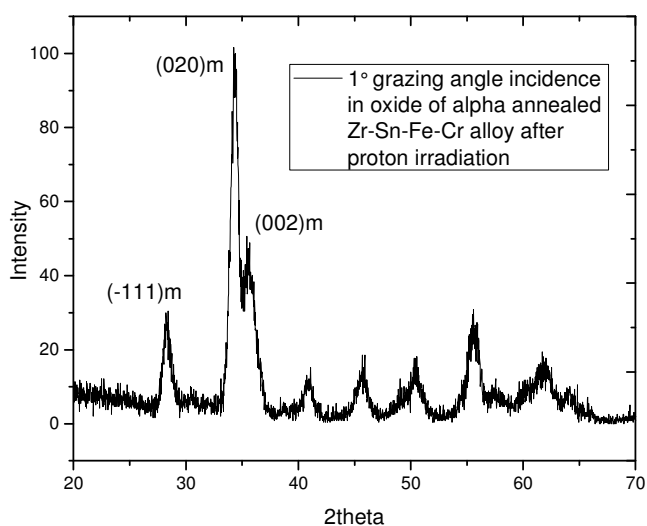
Fig. 7. 8 b : After proton Irradiation 1° grazing angle reflection from oxide metal interface of Zr-Sn-Fe-Cr alloy shows no change in GIXRD reflection.
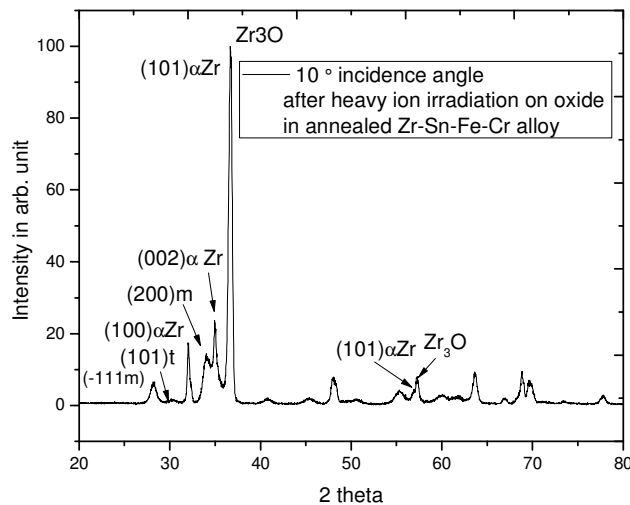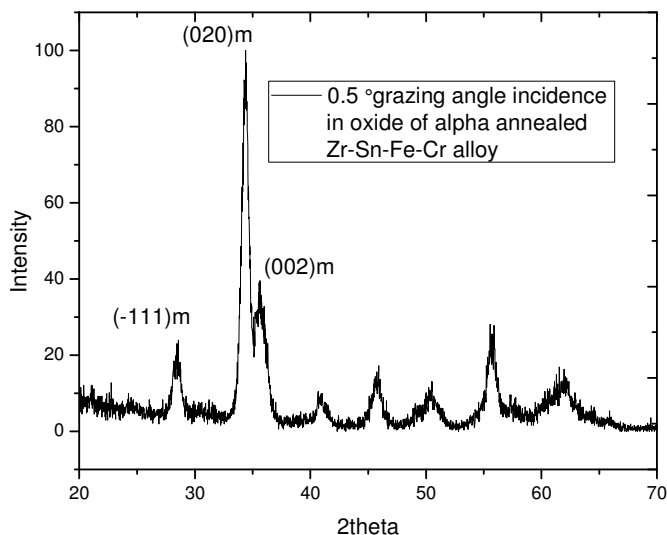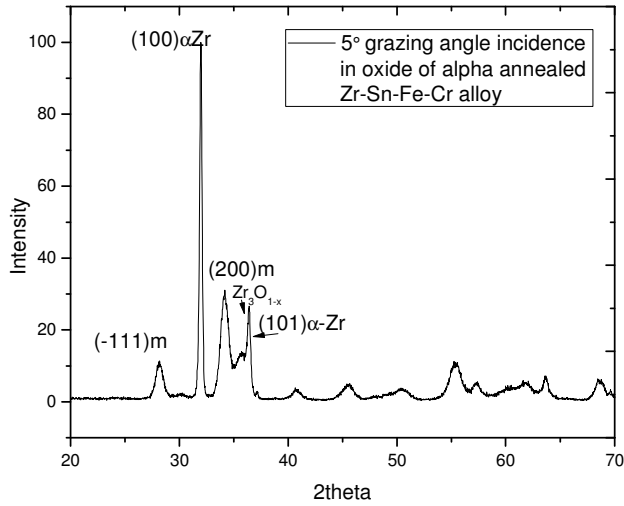
Fig. 7. 7 c : Before Irradiation 5° grazing angle reflection from oxide metal interface of Zr-Sn-Fe-Cr alloy shows reflection from tetragonal, monoclinic oxide and α-Zr phase.
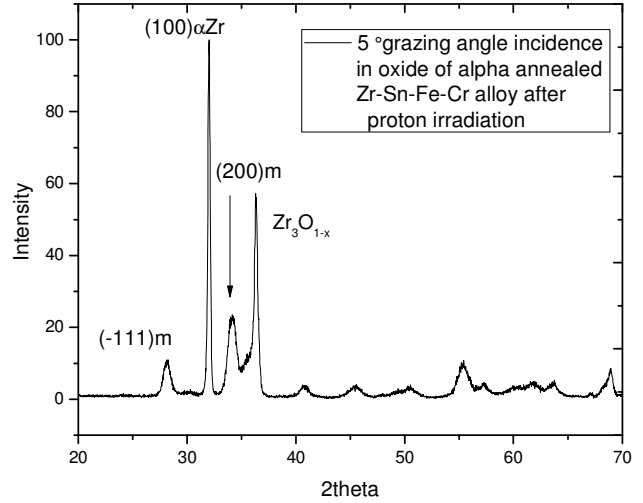
Fig. 7. 8 c : After proton Irradiation 5° grazing angle reflection from oxide metal interface of Zr-Sn-Fe-Cr alloy shows reflection from tetragonal, monoclinic oxide and α-Zr phase.
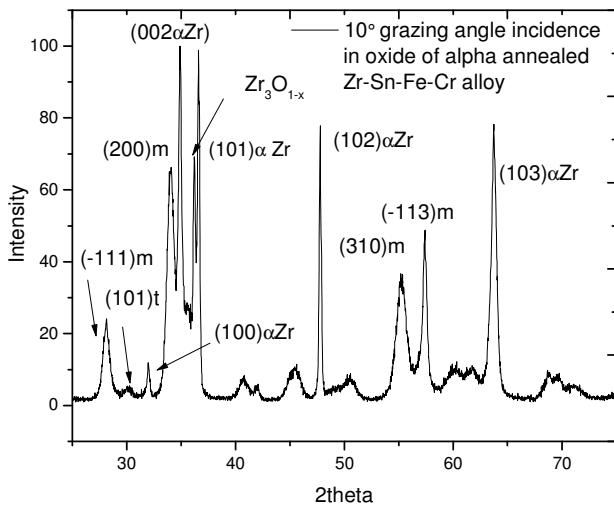
Fig. 7. 7 d : Before Irradiation 10° grazing angle reflection from oxide metal interface of Zr-Sn-Fe-Cr alloy shows reflection from mostly α-Zr phase and monoclinic oxide and small amount of tetragonal oxide.
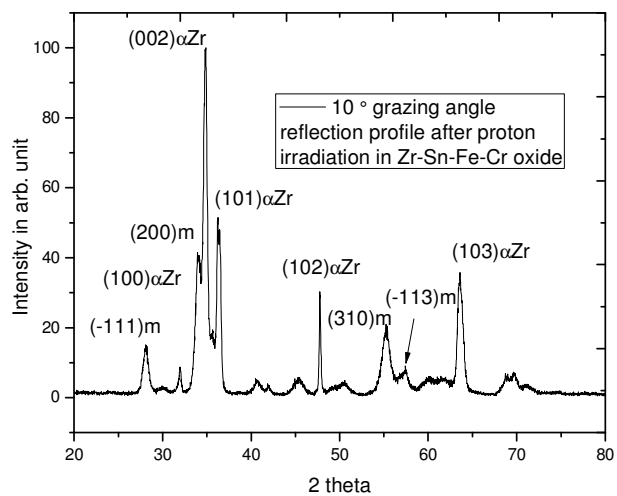
Fig. 7. 8 d : After proton Irradiation 10° grazing angle reflection from oxide metal interface of Zr-Sn-Fe-Cr alloy shows reflection from mostly α-Zr phase and monoclinic oxide and small amount of tetragonal oxide.

At 5°grazing angle reflection (fig. 7. 8 c) (100) and (101) α-Zr peaks are clearly visible along with (200)m and ($\bar{1}$11)m. In case of 10° grazing angle reflection (fig. 7. 8 d) depth of penetration of X-ray is highest and majority of the peaks are from matrix α Zr peaks along with monoclinic

and tetragonal peaks. The proton irradiation does not cause any significant change in oxide. The maximum damage imparted by 3.5 MeV protons is 0.015 dpa and it is in the α-Zr matrix. In oxide the damage is much less than 0.015 dpa. When depth of penetration increases to 10° grazing angle, niether new peaks of other oxide were found nor the reflections from tetragonal oxide changed significantly. Up to 10° grazing angle, characteristic peak of β-Zr phase was absent implying that proton irradiation did not induce any phase transformation near the surface and subsurface (up to 10°grazing angle) which could be detectable using rotating anode GIXRD. The profile at 10°grazing angle showed preferred orientation on certain crystallographic planes of Zr- matrix (002)α-Zr, (101)α-Zr, (102)α-Zr, (103)α-Zr.

7.5 In pile oxide formed in fuel tube:

The 0.5°, 1°, 2°and 5°grazing angle reflection from oxide of fuel tube with burn up 7670 MWd/t is given in fig. 7.9 b, c, d. Due to small size of the sample background noise is high. The optical microscopy reveals the thickness of the oxide after GIXRD scan and was found to vary from 2.9 -3.5 μm (fig. 7.9 a).Thus up to 5° grazing angle reflection, the oxide metal interface region was not accessible. The GIXRD scan probed only up to 1.5 μm thickness from the outer surface of the oxide. Wavy oxide metal interface was observed.
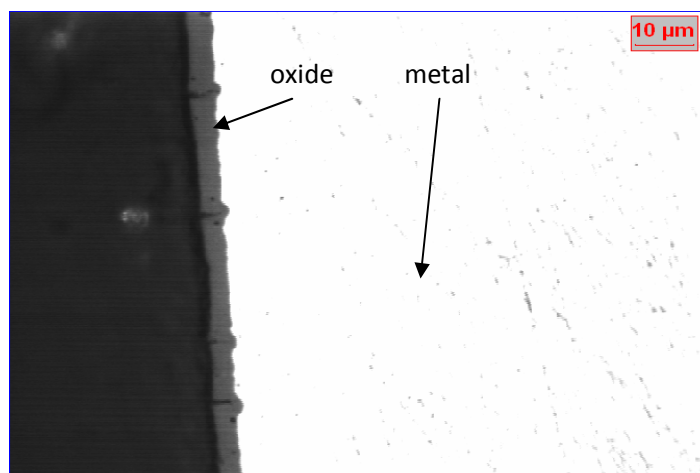
Fig. 7. 9 a Oxide layer formed in reactor on the outer surface of the fuel clad . Oxide thickness 2.9 - 3.5μm.

The 0.5° grazing angle reflection (fig. 7. 9 b) showed tetragonal, monoclinic as well as reflection from sub-oxide Zr_3O. The prominent reflection from monoclinic oxide is from (002)m, (020)m and ($\bar{1}$11)m up to 5° grazing angle. (200)m reflections are absent in all grazing angle scans and in normal XRD scan it was present which indicates that (200)m plane is parallel to the interface, i.e. the pole of this plane is perpendicular to the interface.

Fig. 7. 9 b : 0.5° grazing angle reflection from oxide of Zr-Sn-Fe-Cr fuel tube alloy shows significant tetragonal reflection as well as reflection from Zr_3O along with monoclinic phase.

Similar profile was found for 1° , 2° and 5° grazing angle reflections (fig. 7.9c, d , e). The reflection profile from heavy ion irradiated oxide at 0.5°, 1° grazing angle is similar to the in-pile oxide reflection except Zr_3O reflection. Zr_3O reflection was found from 0.5° up to 5° grazing angle in irradiated fuel tube material (oxide thickness 2.9 - 3.5μm) whereas 0.5° and 1° grazing angle reflection from after heavy ion irradiation of autoclaved oxide (1.0 - 1.1 μm) did not show the Zr_3O reflection. The Zr_3O reflection at 5° and 10° grazing angle incidence angles were present before heavy ion irradiation which indicates presence of sub oxide at oxide metal interface region in out of pile oxidation whereas in pile oxidation, sub oxide present even near the oxide coolant surface, far away from oxide metal interface.
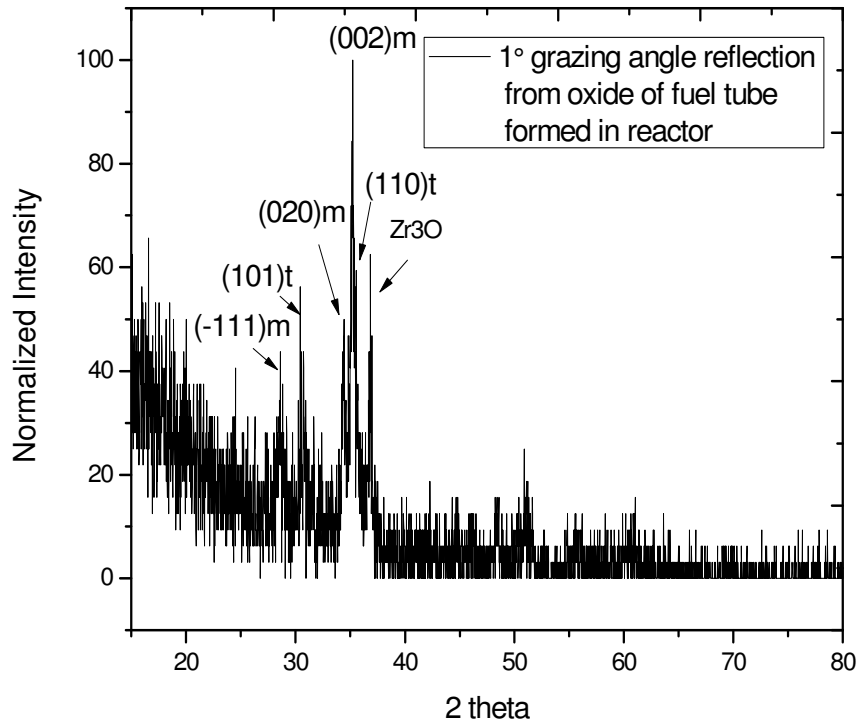
Fig. 7. 9 c : 1° grazing angle reflection from oxide of Zr-Sn-Fe-Cr alloy shows significant tetragonal reflection as well as reflection from hexagonal Zr_3O along with monoclinic phase.
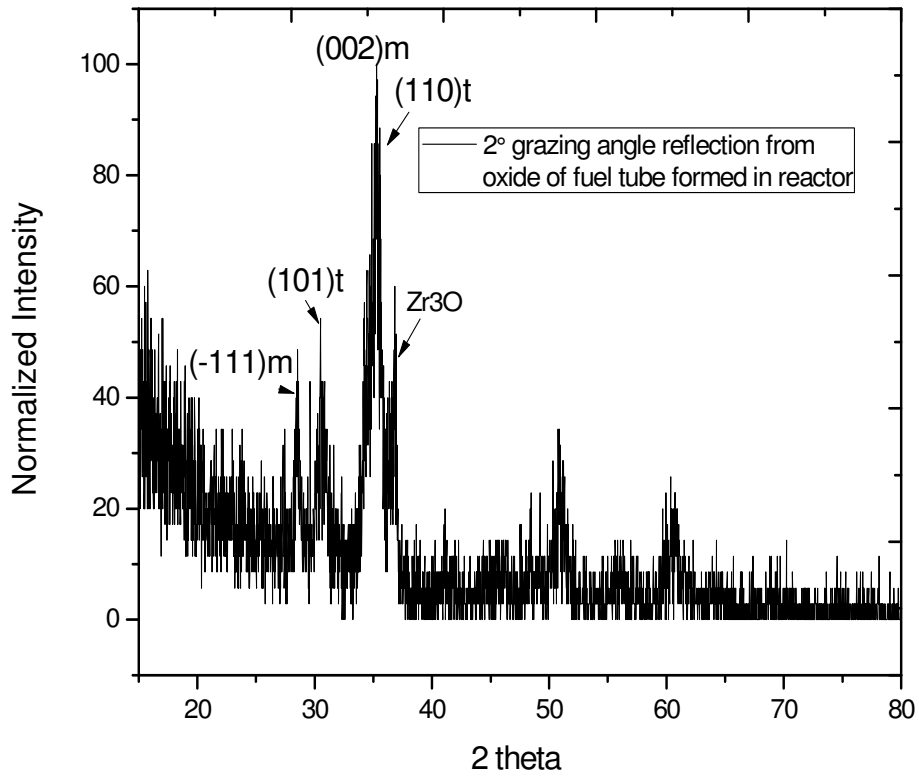
Fig. 7. 9 d : 2° grazing angle reflection from oxide of Zr-Sn-Fe-Cr alloy shows significant tetragonal reflection along with monoclinic phase and reflection from hexagonal Zr_3O.
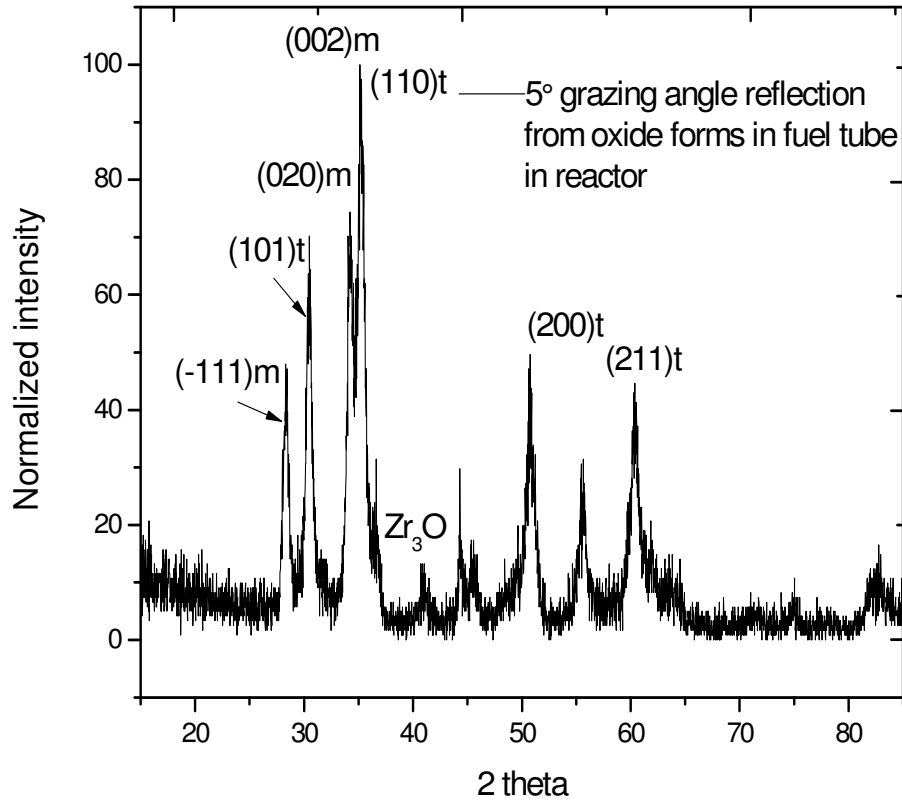
Fig. 7. 9 e : 5° grazing angle reflection from oxide of Zr-Sn-Fe-Cr alloy shows significant tetragonal reflection along with monoclinic and Zr_3O phase.

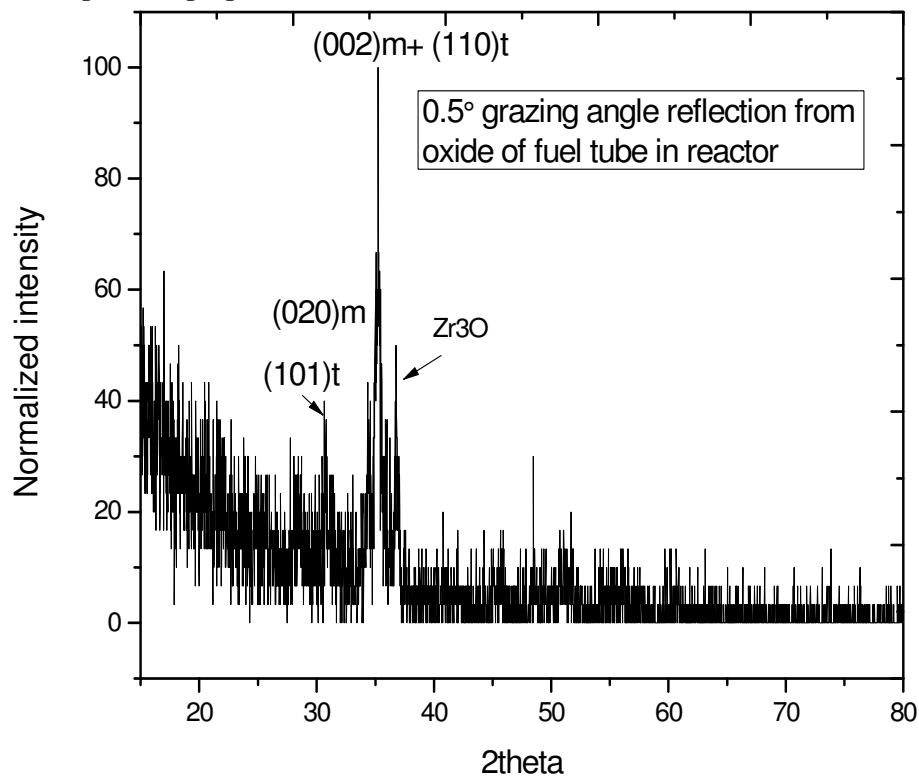Significant tetragonal reflection was found throughout the oxide formed under neutron irradiation. At 5° grazing angle tetragonal fraction calculated using equation 7.1 was 58.65%. At 2° grazing angle highest tetragonal reflection wasfound (64%). Whereas at 1° and 0.5° grazing angle reflections showed 56% and 54 % tetragonal fraction respectively. The tetragonal fraction is higher in pile oxide compared to heavy ion irradiated oxide (table 7.1). As the penetration of probing X-ray beam is restricted to 1.5 μm during GIXRD study, the significant fraction of tetragonal formation is due to irradiation only as the effect of stress on tetragonal stabilization is limited to near oxide metal interface region.

GIXRD study indicated that out of pile oxide, formed during 415° C steam autoclaving has higher tetragonal fraction and sub-oxide Zr_3O near oxide metal interface in α annealed Zr-Sn-Fe-Cr alloys. The study also indicated that the presence of tetragonal phases near oxide metal interface of the oxide formed during autoclaving at 415° C,in Zr-2.5Nb alloy but the sub-oxide

was absent. After heavy ion irradiation, the tetragonal fraction increased near outer surface of oxide. As damage during heavy ion irradiation is restricted near the outer surface of the oxide, this monoclinic to tetragonal phase transformation near outer surface is due to heavy ion irradiation which creates significant number of oxygen vacancies. Creation of anion vacancies is responsible for changing the local coordination number i.e. symmetry of the structure and lead to formation of tetragonal structure. These anion vacancies can also be created by addition of Sn and Fe in Zr base alloys and favours tetragonal formation. No peak of Zr_3O was detected at 0.5° or 1° grazing angle reflection after heavy ion irradiation.

In case of fuel cladding, oxide thickness is higher compared to autoclaved oxide. Up to 5° grazing angle reflection, X ray penetration is restricted to only 1.5 μm from outer surface of the oxide. So oxide metal interface region has not been analyzed. Presence of monoclinic, tetragonal as well as Zr_3O up to 5° grazing angle was identified. In reactor wide range of neutrons are available.Oxidation and irradiation occurs simultaneously at 300° C. Monoclinic phase formed during in pile oxidation. Creations of oxygen vacancies through displacement damage mechanism may be responsible for transformation of this monoclinic phase to tetragonal phase. Low oxygen potential in the environment in combination of irradiation may have caused the formation of sub-oxide Zr_3O but this sub oxide formation was not detected in the outer surface of oxide during heavy ion irradiation. Formation of anion vacancies, phase transformation (as associated with volume change) as well as sub oxide formation may increase the rate of in pile oxidation several folds compared with out of pile oxidation. The effects of heavy ion, proton and neutron irradiation on oxide phase transformation are tabulated in table 7.1.

Table 7.1 Results of GIXRD study of oxide of Zr-Sn-Fe-Cr alloy

GIXRD incidence angle (°)	Main reflections	Tetragonal fraction (%)		
		Unirradiated Autoclaved oxide	Ar irradiation	In-pile oxide
0.5	(001)m, ($\bar{1}$11)m, (111)m, (020)m, (002)m (101)t Zr$_3$O*	<5	49.5	54
1	(001)m, ($\bar{1}$11)m, (111)m, (020)m, (002)m (101)t Zr$_3$O*	5	37.4	56
2	(001)m, ($\bar{1}$11)m, (111)m, (020)m (002)m (101)t, (110)t Zr$_3$O*			64
5	(001)m,($\bar{1}$11)m, (111)m, (020)m (002)m (101)t (1 0 0)hcp, (1 0 1)hcp (116) Zr$_3$O	11	16	58.65

*in pile only

7.6 XPS analysis of Heavy ion irradiated oxide of Zr-2.5Nb alloy

XPS spectra of Zr and Nb 3d received from the outer surface of the oxide after heavy ion irradiation are given in fig. 7.10. The position of 3d 5/2 peak of Zr at 182.2 eV indicates +4 oxidation states of Zr. Nb 3d 5/2 peaks are at 206.2 eV and 206.8 eV indicates +4 as well as +5 oxidation state of Nb. Before irradiation out of pile autoclaved oxide contains only +5 oxidation state for Nb (fig. 6. 9d). During interactions of heavy ion with oxide, +4 oxidation state of Nb is formed. Whether this +4 oxidation states formed from Nb+5 after absorbing electrons or from zero valence states need further study.
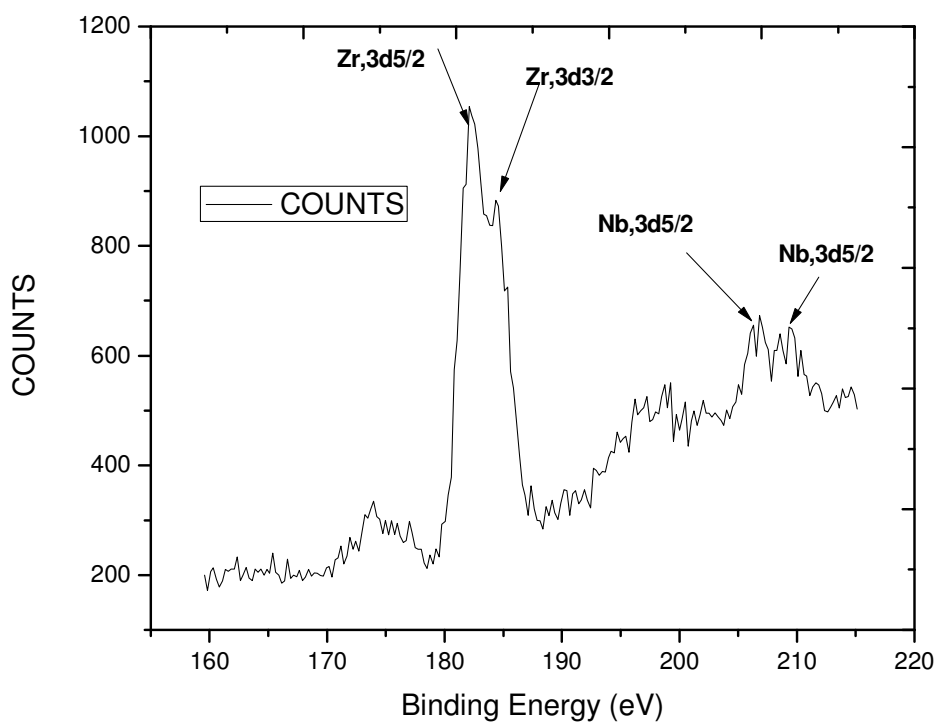

Fig. 7. 10 Intensity of XPS lines in Zr and Nb 3d spectra of heavy ion irradiated oxidized Zr-2.5Nb showingZr 3d5/2 binding energy peak is at 182.2evand Nb 3d5/2 binding energy peaks are at 206.2 corresponds to NbO_2 and 206.8 eV corresponds to Nb_2O_5.

7.7 Summary

- The majority of oxide formed in out of pile oxidation test in Zr-2.5Nb and Zr-Sn-Fe-Cr alloys, is the monoclinic phase. The oxide away from the metal oxide interface has different texture than from near oxide metal interface. Away from the metal oxide interface (200)m plane is approximately parallel to the oxide-metal interface (as in grazing angle geometry significant reflection from (020)m and (002)m present and (200)m reflection is absent), so that the overall growth direction of the oxide is consistent with the (40$\bar{1}$) orientation observed by Lin et. al.[7.4]. Near the interface (200)m plane becomes perpendicular to the oxide metal interface as highest reflection of this plane was observed in grazing angle geometry at 10°.

- The structure of the autoclaved oxide at the oxide-metal interface is different from that in the bulk of the oxide. Near the oxide metal interface higher fraction of tetragonal oxide was found in both the alloys compared to bulk of oxide. Near the oxide metal interface (5° and 10° grazing angle reflection) in Zr-Sn-Fe-Cr alloy, sub-oxide Zr_3O and Zr_3O_{1-x} were found but in case of oxide -metal interface of Zr-2.5Nb alloy these were not found.

- When the Zr-2.5Nb alloy is heat treated in α+ β phase field, presence of Zr_3O was confirmed in 0.5°, 1°, 5° (fig. 6.10g and h) grazing angle reflections from oxide which was formed during 415° C autoclaving.

- 306 KeV heavy Ar^{+9} ion is capable of introducing crystalline to crystalline phase (i.e. monoclinic to tetragonal) transformation in the outer surface of oxides of both Zr-2.5Nb and Zr-Sn-Fe-Cr alloys.

- The damage caused by heavy ion is restricted to 400 nm depth (within oxide) from the surface with maximum damage at a depth of 193 nm, calculated using SRIM-2008.

- 0.5° and 1° grazing angle X ray reflection shows significant fraction of tetragonal oxide after Ar ion irradiation compared to unirradiated one for both the alloys. At 5° and 10° this is not significant which indicates that the damage is restricted in the outer surface of oxide.

- Proton irradiation does not cause any phase transformation in the oxide layer. Maximum damage (0.015 dpa) occurs at a depth of 69 μm which is well away from oxide.

- In case of oxide formed in fuel tube during its residence in reactor, significant tetragonal reflection was found throughout the oxide along with hexagonal sub-oxide Zr_3O. The (200)m plane of monoclinic oxide formed in reactor is predominately parallel to the oxide metal interface.
- The phase transformation from monoclinic to tetragonal phase during irradiation may be due to generation of oxygen vacancies in the oxide. And this transformation along with anion vacancies may be responsible for higher rate of in reactor oxidation.

7.8 References

7.1. H. Okamoto, Journal of Phase Equilibria and Diffusion Vol. 28 No. 5 2007.

7.2. Waterside corrosion of zirconium alloys in nuclear power plants, IAEA TECHDOC- 996, 124-169.

7.3. Jianlong Lin , Hualong Li, Cheol Nam, Jerzy A. Szpunar, J of Nucl. Mater, 334 (2004) 200– 206.

7.4. Jianlong Lin, Hualong Li, J.A. Szpunar, R. Bordoni, A.M. Olmedo, M. Villegas, A.J.G. Maroto, Mater. Sci. and Eng. A, 381 (2004) 104–112.

7.5. A. Yilmazbayhan, A.T. Motta, R.J. Comstock, G.P.Sabol, B. Lai, Z. Cai, J. Nucl. Mater., 324 (2004) 6-22.

7.6. Jeong-Yong Park , Hyun-Gil Kim, Yong Hwan Jeong, Youn-Ho Jung, J. Nucl. Mater., 335 (2004) 433–442.

7.7. R.C. Garvie, P.S. Nicholson, J. Am. Ceram. Soc. 55 (1972) 303.

7.8. Arthur T. Motta, Aylin Yilmazbayhan, Robert J. Comstock, Jonna Partezana, George P. Sabol, Barry Lai, and Zhonghou Cai, Journal of ASTM International, May 2005, Vol. 2, No. 5 Paper ID JAI12375.

7.9. Petigny, N., Barberis, P., Lemaignan, C., Valot, C., and Lallemant, M., J of Nucl. Mater, Vol. 280, 2000, pp. 318–330.

7.10 A. Sarkar, P. Mukherjee , P. Barat, J of Nucl. Mater. 372 (2008) 285–292.

7.11. M. Griffiths, J of Nucl. Mater. 205 (1993) 225-241.

7.12. D.Q. Peng, X.D. Bai, F. Pan, Physica B 391 (2007) 72–78 (XPS).

Chapter 8

Conclusions & Scope for further research

8.1. Conclusions:

Present study aims at development of phase field model for Zr-Nb system to predict microstructure evolution during β to α diffusional solid phase transformation using Gibb's free energy and experimentally found diffusivity data. Apart from this modeling work, few experimental works have also been undertaken to study the following important issues related to Zr bases alloys for nuclear applications.

➢ Effect of α-annealing heat treatment on the microstructure evolution in Zr-Sn-Fe-Cr alloys, mainly precipitates size and its distribution along with micro-chemistry.

➢ Effect of precipitate size and distribution on oxidation behavior in Zr-Sn-Fe-Cr alloys.

➢ Effect of Sn content on the oxidation behavior of Zr-Sn-Fe-Cr alloys for fuel tube applications.

➢ Influence of Fe content and β-phase on Corrosion and Hydrogen pick up behaviour of Zr 2.5Nb pressure tube material.

➢ Effect of ion irradiations (heavy ion as well as proton) on crystalline to crystalline phase transformation in oxide layer and the scope of simulation of simultaneous oxidation and irradiation damage caused by in reactor neutron has been studied.

(a) The growth of α-phase from equilibrated nucleus has been modeled using phase field method for Zr-Nb series alloys with different Nb content. Using this simulation the microstructure evolution during β to α diffusional phase transformation can be predicted for Zr-Nb substitutional alloy system. The model shows that for Zr-2.5%Nb alloy with low under-cooling, the driving force for plate growth decreases and at 1054 K it shows formation of allotriomorphs α through classical diffusional transformation. Higher undercooling favours Widmanstatten lath formation. The growth velocity of the Widmanstatten plate is constant. The change in alloy composition changes the effective super-saturation at the α/β interface and leads to a different tip

velocity. The model also predicts that when Nb content reduces below 200 ppm, lath morphology does not develop and the interface remains planar only.

(b) Significant resistance to oxidation appears in Zr-Sn-Fe-Cr alloys after long duration (10 hrs) annealing at 700°C. TEM and SANS confirmed that at this condition the alloy contains the highest number density of uniformly distributed relatively coarser parallelepiped $Zr(Fe_{0.6}Cr_{0.4})_2$ precipitates and the oxide is also having the higher fraction of tetragonal oxide compared to oxide formed in shorter duration annealed samples.GIXRD indicates presence of relatively higher fraction of tetragonal phase in oxide of as quenched Zr-1.56 wt.% Sn-Fe-Cr alloy compared to Zr-1.35 wt.% Sn-Fe-Cr alloy which confirms Sn stabilizes tetragonal structure of oxide. As both the alloys behave similarly in as quenched condition, where second phase precipitates are not present, the beneficial effect of Sn in stabilizing tetragonal phase may be counteracted by deleterious effect of Sn on increasing the oxygen anion vacancies which can facilitate diffusion of oxygen ions through oxide at high temperature steam.

(c) XPS analysis of oxide formed at 500° C clearly indicates +2 ionization state of Sn in both oxide, the black lustrous oxide as well as white nodular oxide. This +2 ionization state can increase significant amount of oxygen ion vacancies in the oxide and subsequently oxygen diffusion. The absence of Sn 3d5/2 peak in XPS spectra of oxide formed at 415° C may be due to the lower rate of oxidation of Sn at 415°C compare to 500° C and hence is below detectable limit. GIXRD study of nodular oxide formed during 500°C autoclaving, indicated absence of tetragonal phase up to 10° grazing angle reflection whereas the black oxide formed at same temperature contains tetragonal oxide. The orientations of oxide crystallites formed at 500°C is significantly different from oxide formed during 415°C autoclaving which indicates that the mechanism of oxidation are different.

(d) With increase in Fe content up to 800 ppmin Zr-2.5Nb pressure tube material, oxidation resistance improved. Further addition of Fe, lead to no significant change in oxidation resistance but resistance to hydrogen pick -up deteriorated. When Fe content in the alloy was low, the rate of oxidation was high and the oxide formed had pores as well as cracks but H pick up fraction was less. With increasing Fe content, oxidation resistance improved with dense oxide formation without frequent presence of cracks but H pickup was enhanced, i.e. although less amount of

hydrogen was generated through corrosion reaction, i.e. H pick up fraction was more. This indicates that the pores or cracks in oxide are not responsible for high H intake.

(e) The microstructure of the pressure tube consists of flat, elongated α-Zr grains containing about 1 at.% Nb and a high dislocation density with β phase sandwiched between α-lamellae having composition ~20 at. % Nb. With increasing Fe content in Zr-2.5Nb alloy, Zr-Nb-Fe bearing intermetallic started to precipitate out. At 1250 ppm Fe most of the precipitates were Zr-Fe intermetallic. These Zr-Fe intermetallic precipitates are responsible for high hydrogen intake of the alloy containing 1250 ppm Fe. The oxide formed with high Fe content pressure tube material had a higher fraction of tetragonal oxide as compared to low Fe content pressure tube material. Therefore, the higher fraction of tetragonal oxide is responsible for better oxidation resistance of pressure tube with high Fe content. XPS analysis also indicated that irrespective of Fe content in pressure tube material, Nb was present as Nb_2O_5 along with ZrO_2 in the oxide formed during steam autoclaving. The selected area diffraction pattern obtained from cross-sectional TEM samples showed oxide are nanocrystalline.

(f) The α + β heat treated pressure tube material showed poor oxidation resistance during autoclaving although significant fraction of tetragonal phase was found in the oxide.which clearly indicates deleterious effect of β-Zr. Presence of higher volume fraction of β -phase in α + β heat treated alloy may be responsible for poor resistance of oxidation as oxygen diffusivity in β-phase is significantly high compared with α-phase. SEM observation also indicated that the oxidation progresses preferentially along the β phase. In this condition, Nb_2O_5 was not detected in the outer surface of the oxide formed which confirms that the local Nb rich β-phase is responsible for formation of Nb_2O_5 in as received pressure tube material.

(g) The majority of oxide formed in out of pile oxidation test in Zr-2.5Nb and Zr-Sn-Fe-Cr alloy,is the monoclinic phase. The structure of the oxide at the oxide-metal interface is different from that in the bulk of the oxide. Near the oxide metal interface in Zr-Sn-Fe-Cr alloys, sub-oxide Zr_3O and Zr_3O_{1-x} were found but was not found in oxides of Zr-2.5Nb alloy. When the Zr-2.5Nb alloy is heat treated in α+ β phase field, presence of Zr_3O was confirmed in0.5°, 1°, 5° grazing angle reflections from oxide formed during 415° C autoclaving.

(h) 306 KeV heavy Ar^{+9} ion is capable of introducing crystalline to crystalline phase (i.e. monoclinic to tetragonal) transformation in the outer surface of oxide of both Zr-2.5Nb and Zr-Sn-Fe-Cr alloys. The damage occurred by heavy ion is restricted to only 400 nm depth (within oxide only) from the surface with maximum damage at a depth of 193 nm, calculated using SRIM-2008. Proton irradiation does not cause any phase transformation in the oxide layer. Maximum damage (0.015 dpa) in our case occurs at a depth of 69 μm which is well away from oxide.

(i) In case of oxide formed in fuel tube during its residence in reactor, significant tetragonal reflection was found throughout the oxide along with hexagonal sub-oxide Zr_3O. The (200)m plane of monoclinic oxide formed in reactor is predominately parallel to the oxide metal interface. The phase transformation from monoclinic to tetragonal phase during irradiation may be due to generation of oxygen vacancies in the oxide. And this transformation along with anion vacancies may be responsible for higher rate of in reactor oxidation.

8.2. Scope for further research

The present study opens up many directions for further research in the field of development of Zr based alloys for nuclear applications. Some of the important issues are as listed below:

1. Detailed cross sectional transmission electron microscopy of the irradiated as well as unirradiated oxide can gives significant information on microstructure, local crystal structure as well as microchemistry from the oxide coolant interface to deep inside the metal matrix.

2. XPS studies with simultaneous depth profiling on oxide formed during out of pile as well as heavy ion exposure can improve understanding of chemical state of oxide along the thickness direction.

3. Study of anion vacancies in autoclaved oxide as well as heavy ion irradiated oxide in Zr-Sn-Fe-Cr and Zr-2.5Nb alloys using positron annihilation spectroscopy can provide better mechanistic understanding of oxidation phenomena under irradiation.

4. Incorporation of stress in the phase field model for prediction of microstructure evolution during diffusional phase transformation under high undercooling and the effect of stress on the morphology of the Widmanstatten lath can provide complete understanding of plate formation mechanism during diffusional phase transformation.

5. Development of phase field model to predict Martensitic phase transformation in Zr based alloys.

Appendix

Thermodynamic Description of Zr-Nb system [4. 39, 4. 40]

$$°G_{Zr}^{\beta} = -526.9 + +124.9457 * T - 25.607406 * T * \log(T) - 0.00034008415 * T^2$$
$$- 9.72897347 * .1 * 10^{-8} * T^3 - .761428942 * 10^{-10} * T^4$$
$$+ \left(\frac{25233}{T}\right) \qquad\qquad ------------1)$$

$$°G_{Nb}^{\beta} = -8519.35 + 142.048 * T - 26.4711 * T * \log(T) - 0.000203475 * T^2 - 3.50119$$
$$* 0.0000001 * T^3 + \left(\frac{93398.8}{T}\right) ------2)$$

Interaction parameters in β phase,

$$L_0^{\beta} = 15911 + 3.35 * T ------3)$$
$$L_{0i}^{\beta} = 3919 - 1.091 * T ------4)$$

$$iG_m^{\beta} = c * °G_{Nb}^{\beta} + (1 - c) * °G_{Zr}^{\beta} + R * T * c * \log(c) + R * T * (1 - c) * \log(1 - c) + c$$
$$* (1 - c) * (L_0^{\beta} + L_{0i}^{\beta} * (2 * c - 1)) -----5)$$

$$°G_{Zr}^{\alpha} = -7829 + 125.649 * T - 24.1618 * T * \log(T) - 0.00437791 * T^2$$
$$- \left(\frac{34971}{T}\right) \qquad ------6)$$

$$°G_{Nb}^{\alpha} = 1480.65 + 144.448 * T - 26.4711 * T * \log(T) + 0.000203475 * T^2 - 3.50119$$
$$* 0.0000001 * T^3 + \left(\frac{93398.8}{T}\right) -------7)$$

Interaction parameter in α phase

$$L_0^{\alpha} = 24411 ----- 8)$$

$$iG_m^\alpha = c * {}^\circ G_{Nb}^\alpha + (1 - c) * {}^\circ G_{Zr}^\alpha + R * T * c * log(c) + R * T * (1 - c) * log(1 - c) + c$$
$$* (1 - c) * L_0^\alpha - - - - - - - - - - - - 9)$$

PDF-code of the phases present in oxide and matrix of different Zr based alloys:

Name	Formula	Crystal System	Space group	Cell Parameters (Å)	PDF-Card No.
α-Zr	Zr	Hexagonal	P63/mmc(194)	a=b=3.2318, c=5.1483 α=β=90°, γ=120°	01-089-4791
β-Zr	Zr	Cubic	Im-3m(229)	a=b=c=3.5453 α=β=γ=90°	00-034-0657
Baddeleyite	ZrO_2	Monoclinic	P21/a(14)	a=5.3129,b=5.2125,c=5.1471 α=γ=90°, β=99.218°	00-037-1484
Zirconia (nanocrystalline)	ZrO_2	Tetragonal	P42/nmc(137)	a=b=3.5948,c=5.1824 α=β=γ=90°	01-070-6627
Zirconium Oxide	Zr_3O	Trigonal	R32(155)	a=b=5.5630,c=31.1850 α=β=90°, γ=120°	01-073-0958
Zirconium Oxide	Zr_3O_{1-x}	Trigonal	R-3c(167)	a=b=5.63,c=15.59 α=β=90°,γ=120°	00-021-1498